August 2016

Observation of J/psi p resonances consistent with pentaquark states in Lambda_b^0 to J/psi K^- p decays

Nathan Philip Jurik
Syracuse University

Abstract

The observation of structures consistent with charmonium-pentaquark states decaying to $J/\psi p$ in $\Lambda_b^0 \to J/\psi K^- p$ decays is presented. The data sample analyzed corresponds to an integrated luminosity of 3 fb^{-1} acquired with the LHCb detector from 7 and 8 TeV pp collisions. An amplitude analysis was performed which utilized all six kinematic degrees of freedom in the decay. It was shown that adequate descriptions of the data are unattainable with only $K^- p$ resonances in the amplitude model. For satisfactory fits of the data, it was found to be necessary to include two $J/\psi p$ resonances, with each having significances of over 9 standard deviations. One has a mass of $4449.8 \pm 1.7 \pm 2.2$ MeV and a width of $39 \pm 5 \pm 16$ MeV, while the second is broader, with a mass of $4380 \pm 8 \pm 29$ MeV and a width of $205 \pm 18 \pm 87$ MeV. The J^P assignments could not be uniquely determined, though there is a preference for one to have spin 3/2 and the other spin 5/2 with an opposite parity to the first. The data sample was also inspected in a model-independent way for the presence of $J/\psi p$ or $J/\psi K^-$ contributions. It was demonstrated at more than 9 standard deviations that the data cannot be described with $K^- p$ contributions alone, and that $J/\psi p$ contributions play a dominant role in this incompatibility. These model-independent results support the model-dependent evidence for $P_c^+ \to J/\psi p$ charmonium-pentaquark states provided by the amplitude analysis.

Observation of $J/\psi\, p$ resonances consistent with pentaquark states in $\Lambda_b^0 \to J/\psi K^- p$ decays

by

Nathan Jurik

B.S., University of Illinois at Urbana-Champaign, 2011

Dissertation

Submitted in partial fulfillment of the requirements for the degree of

Doctor of Philosophy in Physics

Syracuse University

August 2016

Acknowledgements

A great number of people have contributed in some form or another to helping this work be completed, and so many thanks are due.

A great deal of thanks go to my advisor, Tomasz Skwarnicki. The help and knowledge he has shared have been invaluable, and I have learned much from him over the years. As an advisor, he always managed to provide enough guidance without being overwhelming, and enough freedom without being inattentive. He has been great to work with, and I couldn't have asked for a better advisor.

To the Syracuse High Energy Physics group, I give many thanks. In particular I would like to thank Sheldon Stone. It was a lot of fun to work with him during the pentaquark amplitude analysis, and I've learned a lot from him as well. I would also like to extend special thanks to JC Wang, for his guidance and patience as we navigated some tremendously frustrating electronics projects. He helped make them easier, and I've learned a lot from him. Thanks also to Steve Blusk, Marina Artuso, and Ray Mountain, all of whom were great to work with and always approachable about any random question which came up over the past 5 years. Thanks also to the many past and present graduate students and postdoctoral researchers. In particular, I offer my thanks to Thomas Britton, whose own work helped provide a base off of which to develop the software used in the amplitude analysis.

Special thanks are also due to Liming Zhang, whom I worked alongside to complete the amplitude analysis. He was a pleasure to work with, and I benefited greatly from it. I learned a lot, and constantly had to challenge myself in trying to keep up with his pace. Liming was also directly responsible for some of the work which is presented in this thesis. He performed the event selections shown in Sec. 4, which also involved Appendices A and C. He was responsible for the weights given to the Monte Carlo sample (Appendix B) as well. In general, Liming performed fits using the "*sFit*" method, which is described in Sec. 6.3. We both had our own implementations of the *sFit* method, and they were cross-checked with each other. The cross-check studies which used the *sFit* method in Sec. 14 were done by Liming, as were the systematic studies which used *sFit* in Sec. 15.

The work shown in Appendix E correspond to the *sFit* versions of many of the fits shown in the main body of the thesis, and were also performed by Liming.

I'd also like to say thank you to my friends from all over who have given me support, as well as things to do other than physics. Originally, I tried to start naming people, but the fear of leaving anyone out has made me decide against this route. Anyway, you know who you are. Still, I can't help but give special thanks to TJ and Mary Massinger, who have not only been fun friends to spend time with, but have also helped me out in several tough situations over the past 5 years.

Finally, I would like to thank my family. A lot can occur in five years. Through the good times and the bad, it has been worth more than I can say to know that even if it all went bad and I failed, I'd still have them. I thank my brothers for being there to talk to, and help keep me sane on a day-to-day basis. I thank my parents for their being a constant source of support. They've believed in me ever since I declared as a young boy that I wanted to be a professional baseball player when I grew up. However, I'll always remember sitting on the front porch with my father, at an age where I probably had no business still saying I wanted to be a baseball player, when he told me it might be a good idea to have a backup plan. I should thank him for that. I think things turned out well for a "backup plan".

Contents

List of Figures

List of Tables

1 Introduction

The existence of hadrons beyond the conventional quark-antiquark ($q\bar{q}$) mesons and three-quark baryons (qqq) have been hypothesized since the birth of the quark model. In fact, the possibility of mesons with quark content $qq\bar{q}\bar{q}$ and baryons with quark content $qqqq\bar{q}$ was explicitly mentioned in the original papers published by Gell-Mann [1] and Zweig [2] back in 1964. Such $qq\bar{q}\bar{q}$ mesons are commonly referred to as tetraquarks, and $qqqq\bar{q}$ baryons are commonly referred to as pentaquarks. At the time, only the lighter mass quarks (u, d, s) were known, and searches for "exotic" mesons and baryons consisting of these light quarks are almost as old as the quark model itself. While there have been several claims of finding such states, there has been no lasting experimental evidence for the existence of exotic hadrons with only light valence quarks.

Pentaquarks searches have focused mainly on the baryons with strangeness quantum number equal to +1. Such states can't be accommodated by only three quarks, and so are unambiguously identifiable as pentaquark states. These states were looked for in a number of kaon-nuclean scattering experiments, and various partial wave analyses of the data reported possible pentaquark resonances, denoted at the time as Z baryons. For a review of these measurements, see the 1976 Particle Data Group (PDG) status summary [3]. Despite these early hints at pentaquarks, there was still nothing conclusive when, in 1992, the PDG's review called for higher standards of proof and predicted it would take another 20 years to sort out whether or not these states exist [4].

Interest in pentaquarks waned for a period. However, there were theoretical predictions made [5, 6] suggesting that a Z baryon could be found at 1530 MeV with a width of less than 15 MeV.[1] While there was no statistically significant evidence of any pentaquarks at this mass, the data were not able to rule them out as, being only 100 MeV above the K^+p threshold, there were challenges from requiring a low-momentum K^+ beam. Thus, the mass was low enough that it could have evaded searches. Such a narrow state was also attractive in terms of experimental detectability, as broader states are much more easily able to hide under backgrounds. A second wave of interest in pen-

[1] Natural units with $c = 1$ are used throughout this dissertation

taquarks came, and a number of claims of evidence for this state, referred to as the Θ^+ particle, proceeded to come out around the same time. While only a very brief summary is given here, a more thorough review of the history can be found at Ref. [7]. The first four experiments which reported evidence are listed in Table 1. Note the agreement in

Table 1: The first four experiments with positive evidence for the Θ^+ [7].

Experiment	Reaction	Mass (GeV)	Significance
LEPS [8]	$\gamma C \to K^+K^-X$	1.54±0.01	4.6σ
DIANA [9]	$K^+Xe \to K^0_{\rm S}pX$	1.539±0.002	4.4σ
CLAS [10]	$\gamma d \to K^+K^-pn$	1.542±0.005	$(5.2\pm0.6)\sigma$
SAPHIR [11]	$\gamma p \to K^0_{\rm S}K^+n$	1.540±0.004	4.8σ

mass, and how high of significances are claimed. Searches for other pentaquarks were also carried out, and indeed claims were made that they were found, as well. However, the Θ^+ and other candidates all suffered similar fates. Many of the claims were controversial, and were contradicted by other experiments. Ultimately, no candidates survived searches from higher statistics analyses. Currently there is no obvious explanation of the positive results, as it is extremely unlikely all these signals appearing at the same mass were results of statistical fluctuations. Possibly, this may be a case of "pathological science" [12]. Regardless, the 2006 pentaquark update by the PDG ended with a rather pessimistic note, stating that "The conclusion that pentaquarks in general, and the θ^+, in particular, do not exist, appears compelling" [13].

Though the exotic baryon searches have gone poorly and caused much controversy, the exotic meson searches have found some success in recent years. In particular, an abundance of charmonium- and bottomonium-like tetraquark candidates have been found, which are often referred to as XYZ states. This is not the place to give a full review, so just a few examples will be mentioned. The first instance was the $X(3872)$, which was discovered by Belle [14], and had its quantum numbers uniquely determined by LHCb [15, 16]. Similarly, the $Z(4430)^+$ state was discovered by Belle [17, 18] and confirmed by LHCb [19, 20]. Evidence for the $X(4140)$ in $B^+ \to J/\psi\,\phi K^+$ decays was originally published by CDF [21]. LHCb recently confirmed this state (although with a much larger width) along with three other $J/\psi\,\phi$ resonances, all of whose quantum numbers

were also measured [22, 23]. The history of these states is much more complicated and interesting, and the recent LHCb publications can be consulted for an overview [22, 23]. The natures of all these tetraquark candidates are still unclear, and some of them may not be resonances at all, but a result of rescattering of known mesons. The presence of tetraquarks would not mandate the presence of pentaquarks, though the existence of strong tetraquark candidates lends support to the hypothesis that pentaquarks exist. That the strongest tetraquark candidates have only appeared in recent years, and contain heavy quarks is certainly note-worthy. It could be that more pentaquark candidates with heavy quark content will be showing up, as more copious amounts of heavy baryons are being produced at the LHC.

In this dissertation, the observation of $J/\psi p$ resonances consistent with pentaquark states in $\Lambda_b^0 \to J/\psi K^- p$ decays is presented. [2] This decay mode was first observed and reported by LHCb in the precision measurement of the Λ_b^0 lifetime [24]. In fact, it was through this analysis, and not a dedicated pentaquark search, that these structures were first seen, though it was not known at the time what they were. The observed invariant mass distribution of the $K^- p$ system (m_{Kp}) and $J/\psi p$ system ($m_{J/\psi p}$) in $\Lambda_b^0 \to J/\psi K^- p$ decays are both shown in Fig. 1. The observed structures in the m_{Kp} distribution proceed

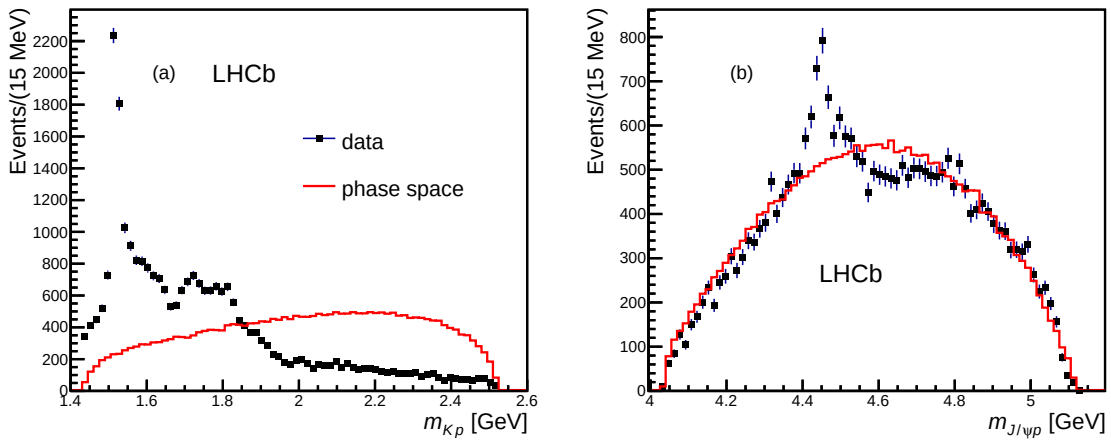

Figure 1: The (a) m_{Kp} and (b) $m_{J/\psi p}$ for the background-subtracted $\Lambda_b^0 \to J/\psi K^- p$ candidates. The solid (red) histogram shows the phase space expectations.

through the Feynman diagram shown in Fig. 2(a). These are expected, and correspond

[2] Charge-conjugate states are implied throughout this dissertation.

to conventional resonances. The prominent peak shown in the $m_{J/\psi p}$ system is not expected, and is indicative of a pentaquark resonance. This decay would proceed through the Feynman diagram shown in Fig. 2(b), with the prospective pentaquark state denoted by P_c to reflect the $c\bar{c}$ quark pair. While the structure in $m_{J/\psi p}$ is quite striking, the

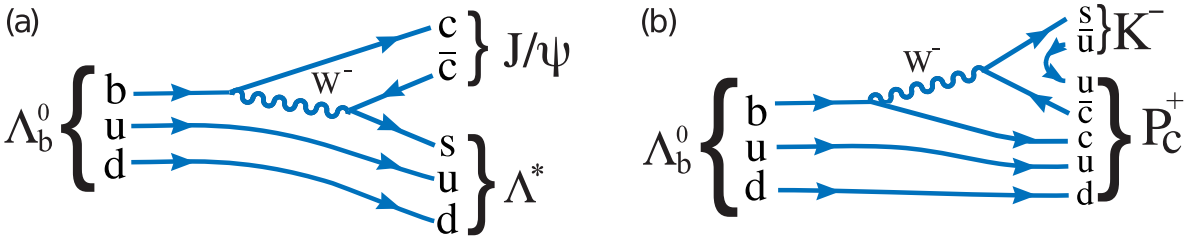

Figure 2: Feynman diagrams for (left) $\Lambda_b^0 \to J/\psi\Lambda^*$ and (right) $\Lambda_b^0 \to P_c K^-$ decay.

history of pentaquark searches has made it clear that caution should be practiced when making claims about new candidates, and so great effort has gone into studying these signals. Two complementary analyses which demonstrate that the observed structures can't be the result of conventional sources have been performed. The first analysis is a six-dimensional amplitude analysis which, in addition to showing the data can't be described by known conventional resonances, resulted in the announcement of the observation of the pentaquark candidates, $P_c(4380)$ and $P_c(4450)$. The second analysis assessed in a model-independent way the compatibility of the data with the hypothesis that only conventional components are present. It demonstrated with high significance that the data isn't compatible with this hypothesis, and did so without making any assumptions about the number of conventional resonant or nonresonant components, nor about their lineshapes, masses, widths, or possible interference patterns. The first and second analyses resulted in the publications of Ref. [25] and Ref. [26], respectively. Both of these will be presented in this dissertation.

Prior to the aforementioned pentaquark candidate studies, work was done on the analysis of semileptonic decays of the B_c meson. As this does not fit into the main narrative of this dissertation, it is briefly summarized in Appendix N.

2 The Quark Model

2.1 Overview

The quantum field theory of the strong interaction, Quantum Chromodynamics (QCD), describes the interactions between quarks and gluons. Within it, hadrons are viewed as being made of valence quarks and a "sea" of gluons and quark-antiquark pairs. The quark model, proposed independently in 1964 by Murray Gell-Mann [1] and George Zweig [2], is a successful scheme for classifying hadrons in terms of their valence quarks and anti-quarks. While the complete picture is more complicated, the valence quarks determine the quantum numbers of the hadron, and the quark model has been tremendously successful in predicting properties of hadrons. From this point, when the quark content is spoken of, it can be assumed that it refers to the valence quark content.

There are 6 flavors of quarks: up (u), down (d), charm (c), strange (s), top (t), bottom (b). Each has spin 1/2 and has positive parity (P). Additionally, they carry an electric charge of either $-1/3$ or $2/3$, as specified in Table 2. The quark masses [27] are also listed, where it can be seen that the u, d, and s quarks are all significantly lighter than the c, b, and t quarks. Thus these two groups are often referred to as the light and heavy quarks, respectively. Each flavor also has an associated flavor quantum number, with the sign of this quantum number following the sign of the electric charge. The flavor quantum numbers of each species of quark are also listed in Table 2. These quantum numbers are conserved quantities in the strong interaction[3]. There is also an antiquark for each of the quark flavors, which of course carries all the opposite quantum numbers.

In Table 2, the flavor quantum numbers for the up and down quarks are the third components of a quantum number called "isospin". Both the up and down quarks have total isospin $I = 1/2$. While isospin is just a more specific case of the larger flavor symmetry which is conserved by the strong interaction, the similarity of the up and down quark masses makes representing their flavor quantum numbers with isospin be useful. In particular, this makes the strong interaction be approximately invariant under rotations

[3]This is an important point in this analysis, when it comes to determining the minimum quark content of the P_c states in the $P_c \to J/\psi\, p$ decay.

Table 2: Quarks and their mass [27], charge (Q), and flavor quantum numbers: third isospin component (I_z), charmness (C), strangeness (S), topness (T), bottomness (B)

Name	Mass (MeV)	Q (e)	I_z	C	S	T	B
First Generation							
up (u)	$2.3^{+0.7}_{-0.5}$	$+2/3$	$+1/2$	0	0	0	0
down (d)	$4.8^{+0.5}_{-0.3}$	$-1/3$	$-1/2$	0	0	0	0
Second Generation							
charm (c)	1275 ± 25	$+2/3$	0	$+1$	0	0	0
strange (s)	95 ± 5	$-1/3$	0	0	-1	0	0
Third Generation							
top (t)	$173210 \pm 510 \pm 710$	$+2/3$	0	0	0	$+1$	0
bottom (b)	4180 ± 30	$-1/3$	0	0	0	0	-1

in isospin space. Isospin symmetry was originally proposed by Werner Heisenberg to explain the nearly degenerate masses of the *uud* proton and *udd*. It has since become a useful tool for classifying hadrons and predicting behavior of decays involving particles which carry isospin. While isospin actually has nothing to do with spin, the mathematical formalism used to describe it is very similar. Indeed, isospin is an approximate SU(2) symmetry. This symmetry can be extended to SU(3) symmetry with the inclusion of the s quark, though this symmetry is badly broken due to the significantly heavier s quark mass. Further extensions with the heavier quarks are even more badly broken and are essentially useless.

Quarks carry the color charge, which is exchanged via interactions with gluons. In contrast to the electric charge, the color charge can take three different values: red, green, and blue. Antiquarks then carry the anti-colors: anti-red, anti-green, anti-blue. QCD is invariant under rotations in color space, leading to an exact SU(3) color symmetry. The color charge adds in such a way that the combined addition of all three colors results in a colorless net charge, *i.e.* it is white. Similarily all three anticolors added together are white, and a color added with its anticolor is white. Due to a feature of QCD called color confinement, isolated color charged particles do not exist by themselves in nature. That is, quarks are never found by themselves, and are only found in combinations in which the total composite particle is colorless.

Another quantum number of the quarks called "baryon" number ($\mathcal{B}$) is useful for

classifying the types of colorless hadrons which can be built. Each quark has $\mathcal{B} = +1/3$, and each antiquark has $\mathcal{B} = -1/3$. Baryon number is also a conserved quantity, and were it not for its role in classifying hadrons, it would be more suitably referred to as quark number. The simplest ways to obtain a colorless composite state would be to combine a quark and an antiquark with the respective anticolor, or three quarks of different color. These two possibilities have $\mathcal{B} = 0$ and $\mathcal{B} = 1$, and are referred to as mesons and baryons, respectively. There are of course other configurations which lead to $\mathcal{B} = 0$ and $\mathcal{B} = 1$, and these are the subject of the next subsection.

2.2 Exotic Hadrons

While the simplest colorless combinations of quarks are the $q\overline{q}$ and qqq configurations, which correspond to the conventional mesons and hadrons, there is no known reason within QCD why other combinations should not exist. Nature tends to prefer the simplest ways to do things, and in the present discussion this is clearly manifested in that these configurations of mesons and baryons dominate the known hadrons. However, unless something is strictly forbidden, nature will also utilize all possibilites, even if it is only some small fraction of the time. Unless there is something prohibiting their existence, colorless configurations of quarks beyond the conventional hadrons ought to exist.

As was mentioned in the introduction, quark combinations beyond the conventional ones have been hypothesized since the quark model was first proposed [1, 2]. It should be noted that since the development of QCD, other types of exotic particles consisting of bound states of valence gluons ("glueballs") or hybrid states with both valence quarks and gluons have been hypothesized. The proposal of such states is based on the fact that gluons carry the very charge to which they couple. The rest of this dissertation, however, will only mention the "multi-quark" exotic hadron candidates of exotic mesons and exotic baryons, which include most prominently the $qq\overline{qq}$ tetraquarks, and the $qqqq\overline{q}$ pentaquarks, respectively.

Following the original suggestion that such configurations of quarks might exist, a quantitative model for tetraquarks was developed in 1976 [28], and the idea was soon

expanded upon to include pentaquarks [29,30]. The name pentaquark itself wasn't coined until 1987 [31]. Throughout the years, a number of theoretical predictions for various states consisting of light quarks have been made, for which all experimental searches have failed. To some degree, their production is expected to be suppressed with regards to the conventional hadrons. Furthermore, multiquark states which consist of only light quarks may also have broad widths, which would make their identification be experimentally difficult. The fairly recent arrival of several tetraquark candidates with heavy quark content has also been taken as possible evidence that heavy quarks play an important role in having stable multiquark states [32–34]. It should also be noted that the internal structure of exotic hadrons is an active area of research. There are a number of models which have been proposed, which cover a range of internal structures. For example, there are tightly bound states, in which all quarks are contained within the same color confinement volume, and there are loosely bound states in which conventional hadrons are bound by meson exchange. This is a topic which will be revisited in Sec. 26, and is in need of experimental input.

3 Detector Description

This dissertation uses data collected from proton-proton collisions with the LHCb detector. The proton-proton collisions are provided by the Large Hadron Collider, for which a very brief overview will be given. Next, the LHCb Experiment and the components of the detector will be discussed. A more detailed description of the detector can be found at Ref. [35], and its performance in Run 1 is presented in Ref. [36]

3.1 The Large Hadron Collider

The Large Hadron Collider (LHC), located at the European Organization for Nuclear Research (CERN) on the France-Switzerland border, is the world's highest energy particle accelerator. It was constructed to be capable of colliding beams of protons at a center-of-mass energy of up to $\sqrt{s} = 14$ TeV. An overview of the collider, which spans a 27-kilometer ring, is given in Fig. 3. The acceleration to the collision energy occurs in a number of steps, utilizing accelerators from previous experiments. The linear particle accelerator, LINAC2, delivers 50 MeV protons into the Proton Synchotron Booster (PBS), where they are further accelerated to 1.4 GeV. The next step is the Proton Synchotron (PS) followed by the Super Proton Synchotron (SPS), where they reach energies of 26 GeV and 450 GeV, respectively. After the SPS, the protons are injected into the main LHC rings, where two proton beams move in opposite directions in separate beampipes. The beampipes are kept at ultrahigh vacuum, and the protons are accelerated and guided by strong magnetic fields maintained by superconducting magnets operating at $-271.3°$C. The beams which circulate the collider are not actually continuous, but spaced in bunches of roughly 10^{11} protons each. Each bunch is separated in time by about 25 ns, leading to a bunch-crossing rate of 40MHz. The beams will circulate and collide at predesignated points for several hours until the proton bunches grow depleted. After a certain point, the beams are dumped and replenished beams are reaccelerated. While the main use of the machine is for proton-proton collisions, it also receives limited use for proton-lead and lead-lead collisions.

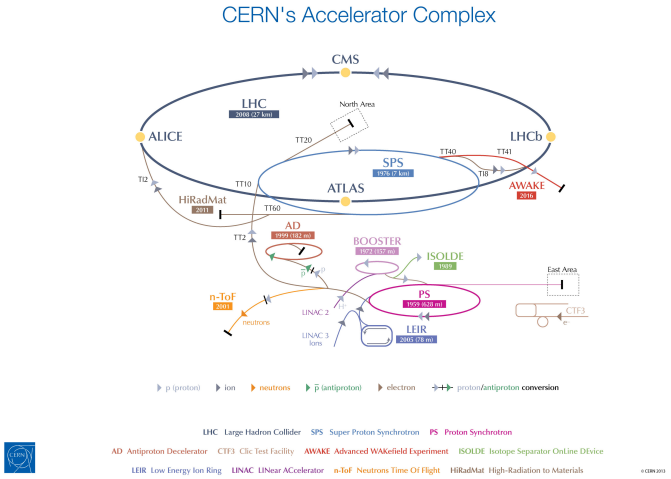

Figure 3: Layout of CERN's accelerator complex and LHC experiments. [37]

There are four interaction points along the collider, where the beams are made to collide. Located at these four large interaction points are the large LHC experiments. The CMS [38] and ATLAS [39] experiments are general-purpose detectors, which cover a wide range of goals, such as studying the Higgs Boson and searching for physics beyond the Standard Model. ALICE [40] collects heavy ion collision data in order to study strongly interacting matter at extreme energy densities, for purposes such as understanding color confinement in QCD. Finally, LHCb [35] was designed for precision measurements of CP violation and bottom and charm quark decays.

While the machine is capable of colliding beams at $\sqrt{s} = 14$ TeV, it has not yet done so. In 2011, it ran at 7 TeV, and in 2012 it was increased to 8 TeV. The data collected during 2011-2012 constitutes the Run 1 data set, which this dissertation is based off of. During this period, LHCb collected $\sim 3\,\text{fb}^{-1}$ of data. This is considerably less than the $25\,\text{fb}^{-1}$ collected by both ATLAS and CMS, for reasons which will be described in the next section. Note that after two years of maintenance and upgrades, the LHC began collisions again in 2015 and reached 13 TeV collisions for the first time.

3.2 The LHCb Experiment

The LHCb detector is a single-arm forward spectrometer, designed for precision measurement of CP violation and of bottom and charm quark decays. An overview of the

detector is shown in Fig. 4, and each of the subdetector systems will be summarized in the following sections. The angular acceptance is 10-300 mrad in the magnet bending

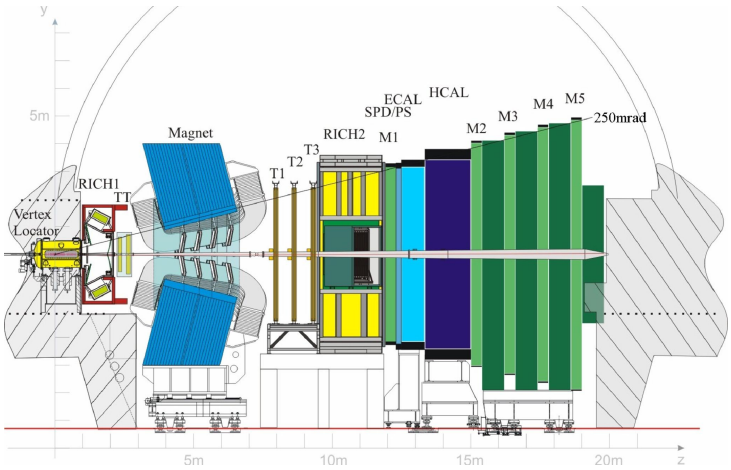

Figure 4: Overview of the LHCb detector. [35]

plane, and up to 250 mrad in the vertical plane, corresponding to a pseudorapidity range of $1.8 < \eta < 4.9$. This particular geometry of the detector was chosen as the production of b and $\bar{b}$ quarks at LHC energies is such that their directions will tend to be along the beam line. The polar angles of the b and $\bar{b}$-hadrons produced for $\sqrt{s} = 8$ TeV collisions are shown in Fig. 5, as predicted from PYTHIA [41] simulations.

The detector was designed to operate at a luminosity of $\mathcal{L} = 2 \times 10^{32}\text{cm}^{-2}\text{s}^{-1}$, in comparison to the LHC's design maximum luminosity of $10^{34}\text{cm}^{-2}\text{s}^{-1}$. A lower luminosity is used essentially to make for less "busy" events. Higher luminosities mean more interactions per bunch crossing, which results in a larger number of points where proton-proton collisions take place. A proton-proton collision point is referred to as a primary vertex, and the identification of primary vertices is essential in many analyses in order to accurately reconstruct the paths of decaying particles. A high number of primary vertices in an event makes it much more difficult to identify the primary vertex from which a particle originated. The higher track multiplicity events, which would result from more collisions, would also make event reconstruction more difficult. Finally, operating at lower luminosities also limits the radiation damage and detector occupancy. To achieve the lower luminosity, a method referred to as "luminosity leveling" is used. This is done by shifting the beams relative to each other, effectively changing the area of the beam overlap so as

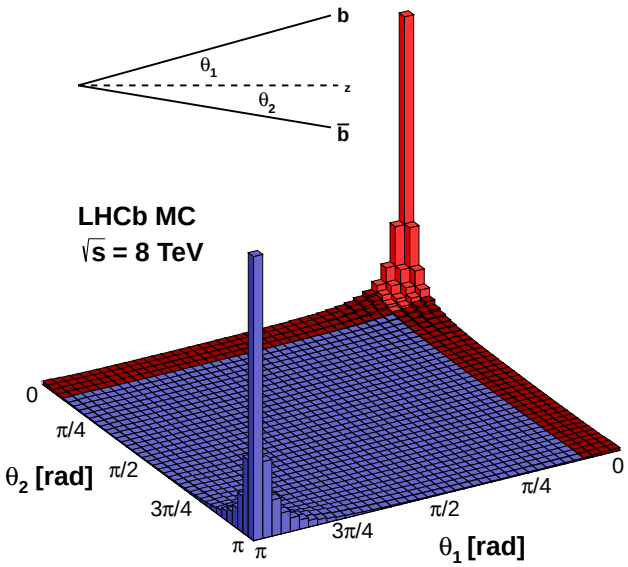

Figure 5: Display of $\bar{b}b$ production angles as simulated with PYTHIA8. The LHCb acceptance is shown in red.

to achieve a lower luminosity. As the number of proton bunches goes down, the beams can be made to overlap more in small increments so that the luminosity is also kept constant.

3.3 Tracking

The tracking system makes use of the Vertex Locater (VELO), dipole magnet, and tracking stations. There are four tracking stations, which are referred to as the TT, T1, T2, and T3. The TT is placed directly upstream from the magnet, while the rest are downstream. Figure 6 shows the interplay of the different tracking elements in reconstructing different types of tracks. The tracking system plays critical roles in the LHCb detector. Reconstructed tracks allow for determing the locations of primary or secondary vertices. They also allow for determining the bending of charged particles in the magnetic field, which allows for measuring the particle's momentum and charge. Reconstructed tracks are also essential for gathering information from the other subdetectors. The different tracking components will now be discussed.

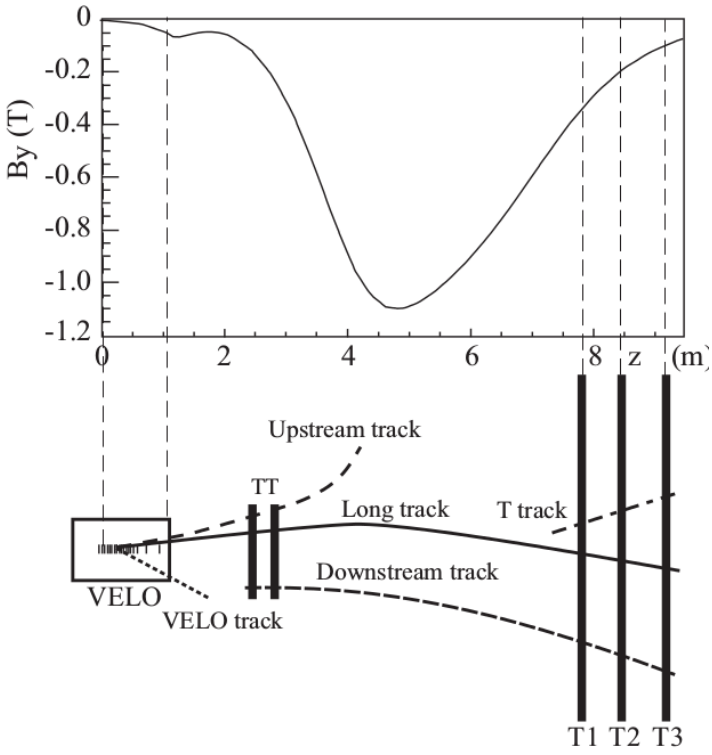

Figure 6: Schematic of the tracking components with different types of track definitions. The main B-field component (B_y) as a function of the z coordinate is plotted above. [36]

3.3.1 Vertex Locater

The Vertex Locater (VELO) immediately surrounds the interaction point and is used to obtain precise measurement of track coordinates near the interaction region. This is crucial for reconstructing the production and decay vertices of b and c-hadrons, and for measuring the impact parameter of particles with respect to the primary vertices. Detached vertices also play an important role in the High Level Trigger, which is to be discussed in Sec. 3.5.2.

The VELO consists of 2×21 silicon modules placed along the beam in stations, and enclosing the beampipe. They are arranged such that tracks inside the acceptance of the detector cross at least three stations. An overview is given in Fig. 7. The stations located farthest upstream and labeled "pileup VETO stations" were envisioned to be used to veto events with a large number of primary vertices, though they have instead been used for luminosity measurements. The radial distance from the beampipe is smaller than the aperture required during the injection of the proton beams, and so the stations are

required to be retractable, as shown with the open and closed configurations in Fig. 7. Each of the stations has two semicircular silicon strip sensors which are mounted back-to-back, and measure the cylindrical coordinates (r, ϕ) of a track. For this purpose, each station has two types of sensors consisting of silicon strips which separately determine the two coordinates. The radial sensors are arranged in constant radii and centered around the beam axis, while the ϕ sensors are straight and arranged nearly radially around the module. Figure 7 also shows the arrangement of the r and ϕ sensors. The particular VELO station then returns the z-coordinate of a particular point in the track, completing the 3 dimensional measurement of a track point.

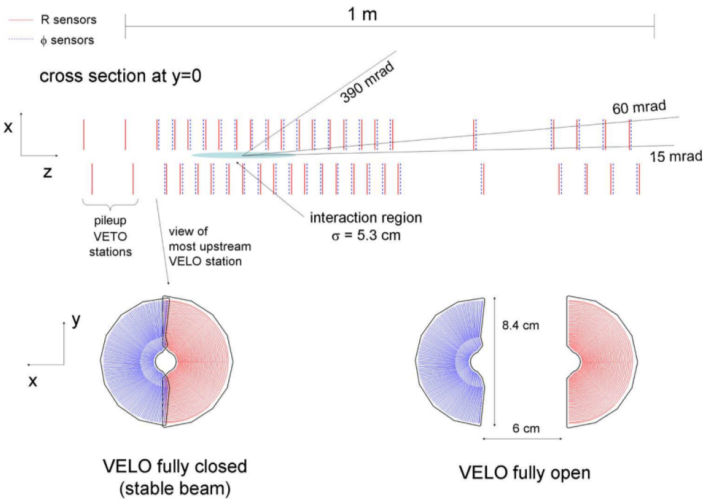

Figure 7: On top is an overview of the VELO as seen in the (x, z) plane. The bottom two figures show the front face of the modules in the (x, y) plane, for both open and closed positions. [35]

3.3.2 Dipole Magnets

A dipole magnet is used for the measurement of the momentum of charged particles. It consists of two separate aluminum coils, shaped like a saddle and mounted symmmetrically in a window-frame magnetic yoke. An overview of the magnet can be seen in Fig. 8. The magnetic field is vertically oriented (in the y-direction), and covers ± 250 mrad vertically and ± 300 mrad horizontally. The integrated magnetic field for tracks of 10 m in length is 4 Tm. In order to obtain the desired momentum resolution, the integrated magnetic field must be known with a precision on the order of 10^{-4}. This pre-

cision was achieved using arrays of Hall probes, with which the components of the field were measured in a fine grid spanning from the interaction point to the RICH2 detector. The polarity of the magnet is also able to be reversed, which is important for studies of detector asymmetry which have an impact on CP violation measurements.

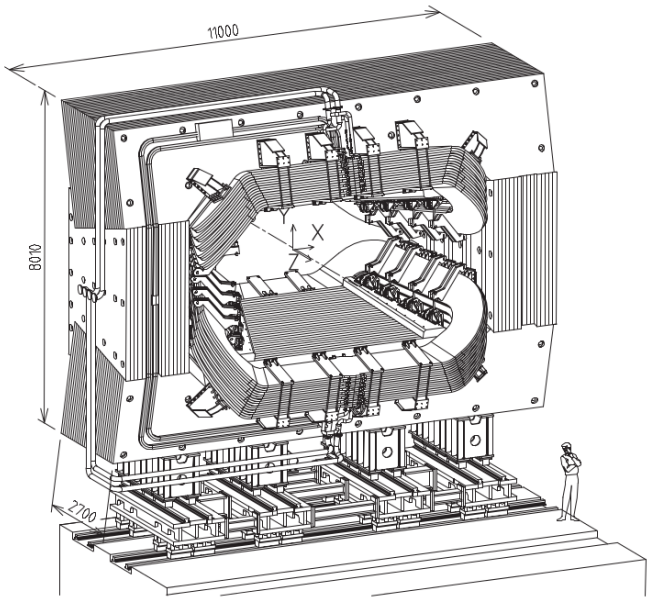

Figure 8: An overview of the dipole magnet [35]

3.3.3 Silicon Tracker

The Silicon Tracker (ST) consists of the Tracker Turicensis (TT), located upstream from the magnet, and the Inner Tracker (IT), located downstream from the magnet. Both components use silicon microstrip sensors with a strip pitch of about 200 μm. The TT covers the full acceptance of the detector, while the IT covers a 120 cm wide and 40 cm high cross-shaped area in the center of the three downstream tracking stations. The four ST stations consist of four detection layers which are placed in an $(x-u-v-x)$ arrangment, in which the outer layers have vertical strips, and the second and third layers have strips rotated by a stereo angle of -5° and $+5^\circ$, respectively. The TT is especially useful in reconstructing long lived particles that are not detected by the VELO, as well as low momentum tracks which will be bent out of the acceptance by the magnet. The IT tracker helps in reconstructing tracks which have passed through the magnetic field and lie near the beam axis.

The basic building blocks of the TT layers are half modules, which cover half of the acceptance and are joined together end-to-end in order to create the full module. The half modules are made up of seven silicon sensors, which are organized into either two or three readout sectors, depending on the proximity to the beampipe. The read-out sectors have one, two, three, or four sensors bonded together, such that the sectors closer to the beampipe, which encounter the higher particle flux, have the lower number of sensors bonded together. The space above and below the beampipe are each covered by a half module, and the regions to the sides are covered by rows of seven full modules in the first two layers and eight full modules in the last two layers. To avoid acceptance gaps, adjacent modules are staggered by about 1 cm in z to allow overlap by a few millimeters in x. For the u and v layers, individual modules are rotated by the respective stereo angle. An overview of the third layer can be seen in Fig 9.

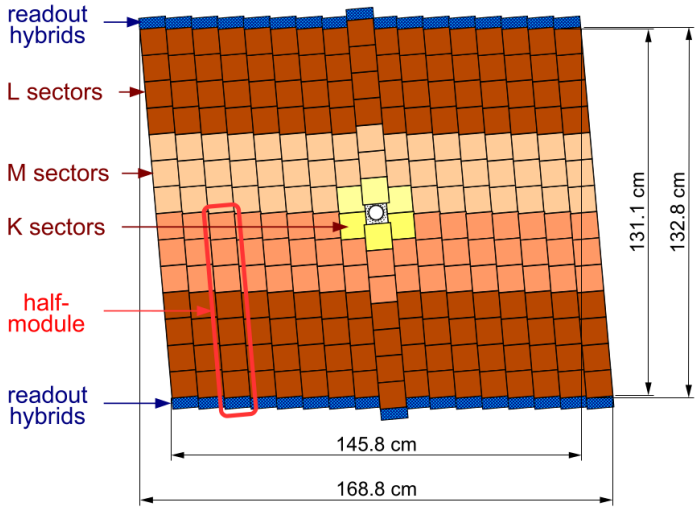

Figure 9: Layout of the third TT detection layer. Different readout sectors are indicated by different shadings. [35]

The three IT stations consist of four detector boxes arranged around the beampipe, as in Fig. 10. A detector box contains four detection layers which are arranged in the same $(x-u-v-x)$ configuration as the TT. Each of the detection layers has seven silicon modules. Acceptance gaps are avoided by having adjacent modules staggered by 4 mm in the z direction and an overlap by 3 mm in the x direction. The modules in the top and bottom boxes consist of a single silicon sensor, while the modules in the side boxes

consist of two silicon sensors. An x detection layer of the second IT station is shown in Fig. 11.

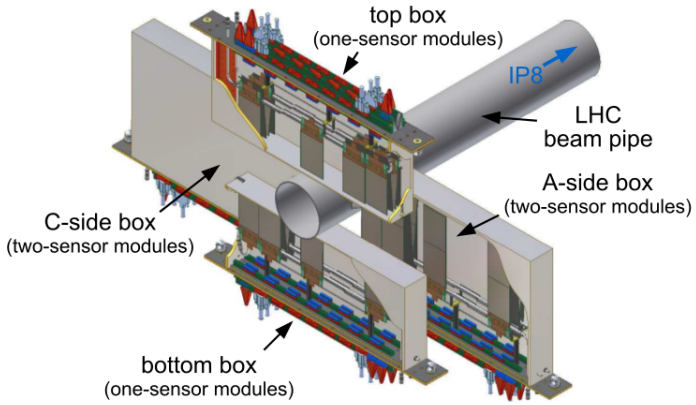

Figure 10: Layout of the four detector boxes of an IT station arranged around the beampipe. [35]

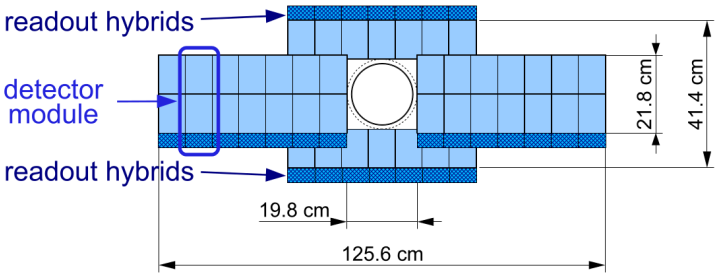

Figure 11: Layout of a second IT station detection layer. [35]

3.3.4 Outer Tracker

The Outer Tracker (OT) is a drift time detector, which is built around the IT and outwards to cover the full acceptance. It consists of three gas-tight straw-tube stations, positioned at T1, T2, and T3. An overview of the OT stations and their relation to the ST is shown in Fig. 12.

Each station is built out of four layers, having the same $(x-u-v-x)$ arrangement as the ST. Each of the modules then contains two staggered layers of drift-tubes with inner diameters of 4.9 mm, as shown in Fig. 13. The counting gas is chosen as a mixture of Argon (70%) and CO_2 (30%). This mixture guarantees a drift time below 50 ns, and a drift-coordinate resolution of about 200 μm.

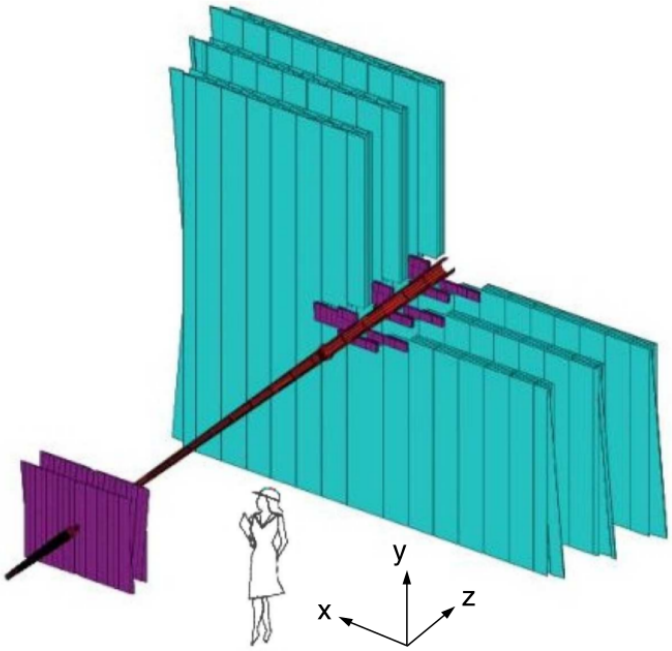

Figure 12: The three OT stations (light blue) surrounding the three IT stations (purple), along with the TT (purple) [35]

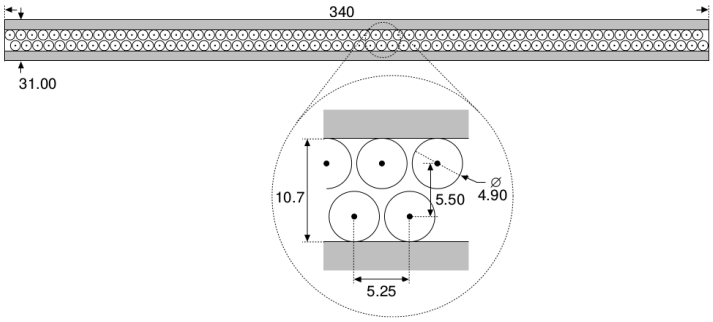

Figure 13: A cross section view of a straw-tubes module [35]

3.4 Particle identification

Particle identification is crucial to many of the analyses done at LHCb. It is performed by two Ring-Imaging Chernkov (RICH) detectors, calorimeters, and a muon system. Using the combined information from all systems, probablities of being different particle species are assigned.

3.4.1 RICH

The ability to separate hadrons from each other is very important, and is provided through the RICH detectors. These utilize the fact that a charged particle moving through a

dielectric medium will emit electrogmagnetic radiation if its speed is greater than the phase velocity of light in the medium. The radiation is emitted in a cone, and the opening angle at which these photons are radiated, θ_c, depends on the speed of light c, the refractive index n of the material, and the particle's velocity v, via the relation $\cos\theta_c = \frac{c}{nv}$. Knowledge of the particle's momentum from the other subdetectors then allows for the prediction of the velocity for different particle types, which allows for the calculation of θ_c for different hypotheses. These can then be compared to the measured value.

The momentum spectrum is typically softer for particles with larger polar angles, and the spectrum is harder for particles with smaller polar angles. It is important to be able to cover a wide momentum range, and thus two RICH detectors are used which utilize different radiator materials which are chosen to be better suited for the targeted momentum spectrum. The RICH 1 lies upstream of the magnet in order to detect low momentum particles and covers the full LHCb acceptance. It uses aerogel and C_4F_{10} radiators, and covers a momentum range of $1 - 60\,\text{GeV}$. RICH 2 is located downstream of the magnet and has a more limited angular acceptance of $\sim \pm 15$ mrad to ± 120 mrad (horizontal) and ± 100 mrad (vertical). This covers the regions where high momentum particles are expected. It uses a CF_4 radiator, and covers a momentum range of $\sim 15 - 100\,\text{GeV}$. The Cherenkov angles obtained for the radiator material used in the two detectors for a range of momentum values are show in Fig. 14.

For both RICH detectors, a combination of spherical and flat mirrors are used to focus the radiated light and reflect the image out of the acceptance. RICH 1 utitlizes a vertical optical layout, whereas RICH 2 has a horizontal layout. These layouts can be seen in Fig. 15. Hybrid Photon Detectors (HPDs) are used to detect the photons in a wavelength range of $200 - 600$ nm. In order to permit operation of the HPDs in magnetic fields up to 50 mT, they are surrounded by external iron shields and placed in MuMetal cylinders.

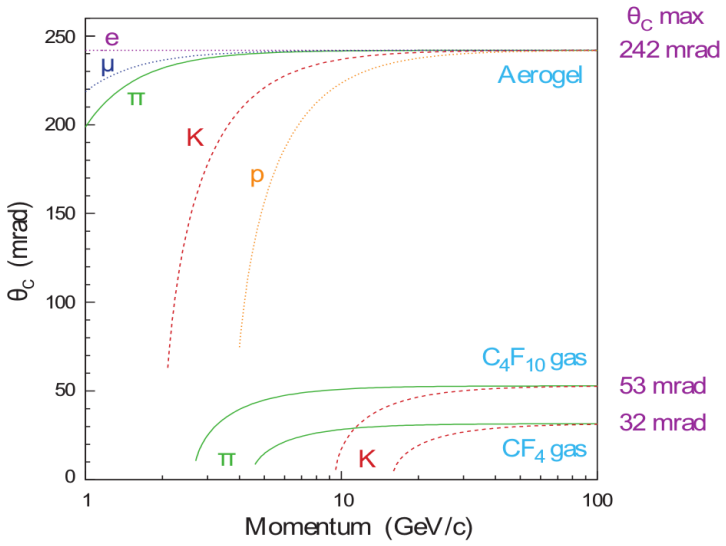

Figure 14: The Cherenkov angle dependence on particle momentum shown for the different RICH radiators [35].

3.4.2 Calorimeters

The calorimeter system is located upstream of the RICH 2, and between the first and second muon stations. It provides the transverse energy of hadron, electron, and photon candidates for the first trigger level, to be described in Sec. 3.5. It is also used for the identification of electrons, photons, and hadrons, as well as measurements of their positions. Moving from upstream to downstream, the calorimeter system consists of a scintillating pad detector (SPD), a pre-shower (PS), an electromagnetic calorimeter (ECAL), and a hadronic calorimter (HCAL). All of the components use scintillating materials in order to detect showers as particles pass through. The scintillation light is then transmitted to a photo-multiplier by wavelength-shifting fibers. The different detectors are segmented in the $x - y$ plane, with higher channel density nearer to the beampipe. This segmentation can be seen in Fig. 16. The segmentation of the HCAL into two zones with larger sizes is due to the dimensions of hadronic showers.

The SPD/PS detector consists of two nearly identical planes of high granularity scintillator pads separated by a lead converter. Since no showers are initiated before the SPD, it will only detect charged tracks. On the other hand, electromagnetic showers can be created in the lead converter and detected in the PS. Thus backgrounds from neutral pions can be reduced by checking for hits in the SPD. In order to reduce the background from

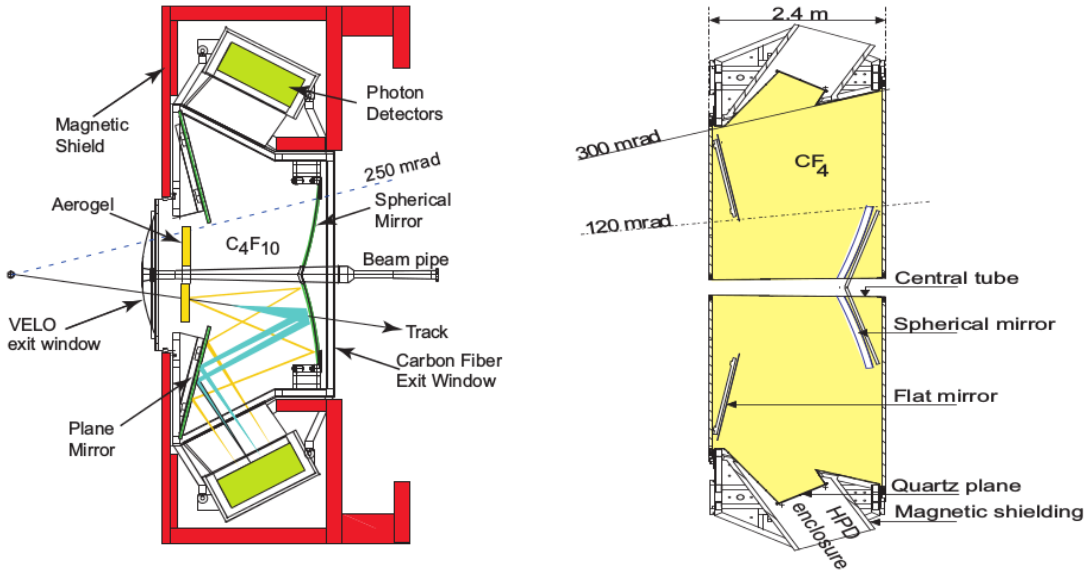

Figure 15: (left) Sideview of the RICH 1 detector and (right) top view of the RICH 2 detector [35].

charged pions, longitudinal segmentation of electromagnetic shower detection is needed, which is provided by the PS followed by the ECAL.

The ECAL and HCAL are both sampling calorimeters. The ECAL records the rest of the electromagnetic shower after the PS. It uses alternating 4 mm thick scintillator and 2 mm thick lead absorber layers over a distance of 42 cm, and contains the full electromagnetic shower. The HCAL also uses a 4 mm thick scintillator, but with a thicker 16 mm iron absorber layer. The scintillating tiles run parallel to the beam axis. The interaction length of the HCAL is not large enough to contain the full hadronic shower, and thus it can only provide an estimate of the hadron energy.

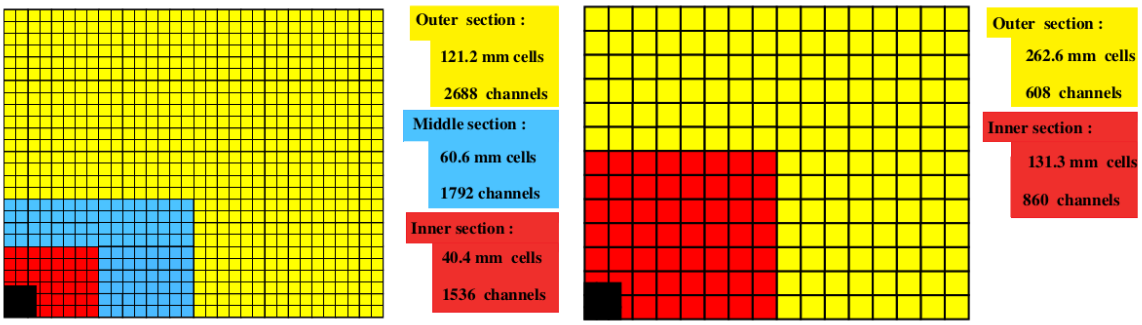

Figure 16: The Lateral segmentation of the SPD/PS and ECAL (left) and the HCAL (right), for a quarter of the detector front. The cell dimensions listed in the left are given for the ECAL. [35]

3.4.3 Muon system

The muon system is capable of providing fast information for high-p_{T} muon triggers, as well as muon identification information for the higher-level trigger and use in offline analysis. Many of the analyses, including the one presented in this dissertation, greatly rely on these capabilities.

A side view of the muon system is shown in Fig. 17. It consists of five rectangular stations placed along the beam axis, and denoted by M1 through M5. The acceptance of the muon system is 20-306 mrad in the bending plane, and 16-258 mrad in the non-bending plane. Stations M2 through M5 are located downstream from the calorimeters, and have 80 cm thick iron absorbers placed between them. These help to only let through muons, and require muons with momentum of at least 6 GeV to traverse the five stations. The M1 station is placed upstream from the calorimeters in order to improve the p_{T} measurements available to the trigger.

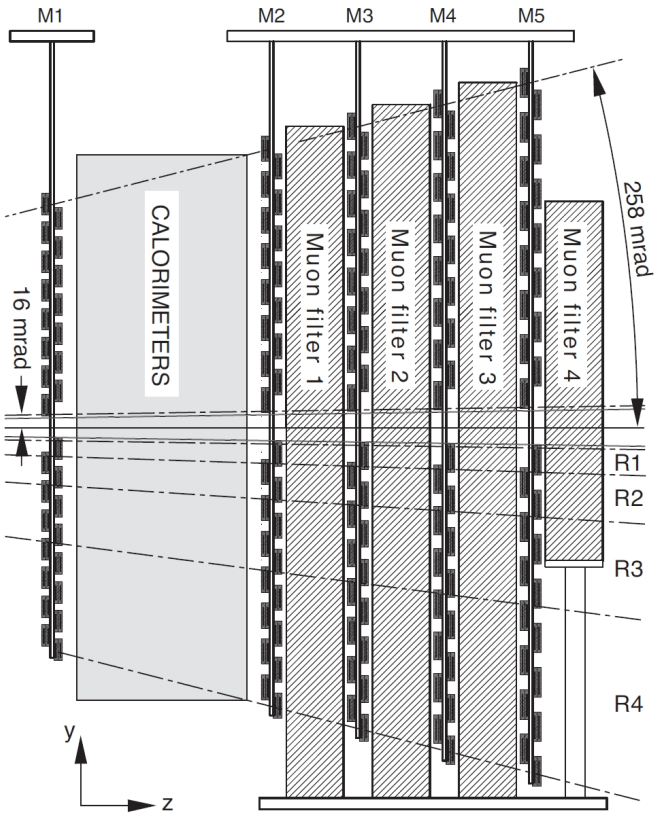

Figure 17: Side view of the muon system [35]

A muon detector is partitioned into rectangular logical pads with varying dimensions which will define the x, y resolution. The logical pads make point measurements of the tracks, and provide a binary yes/no signal to the trigger processor and DAQ. The M1 through M3 stations have higher spatial resolution in the bending plane, and define the track direction. The last two stations have worse resolution, and are mainly for identifying penetrating particles. The stations are split up into regions R1 through R4, with increasing distance from the beampipe, as shown in Fig. 18. The linear dimensions of the regions, as well as the segmentation of each region into "chambers", scales as 1:2:4:8. With this configuration, the particle flux and channel occupancy are predicted to be approximately the same in the four regions. The chambers in the different regions also have different segmentations into the logical pads, and this is shown for the M1 chambers in Fig. 18 as well. While the x, y spatial resolution deteriorates far from the beam axis, it is anyway limited by the increase of multiple scattering at large angles.

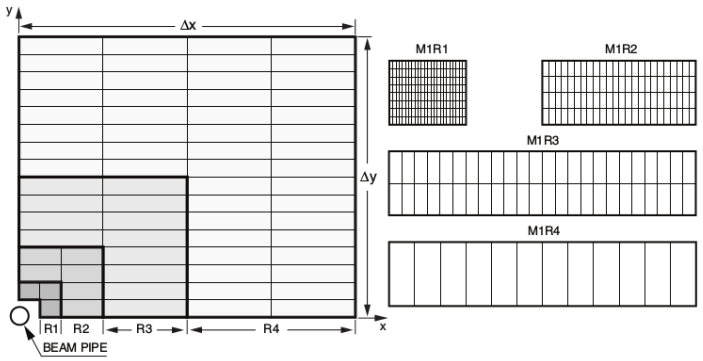

Figure 18: (left) The front view of a quadrant of a muon station, with each rectangle representing one chamber. (right) The division of four chamber types into logical pads for station M1. Stations M2 and M3 have double the pad columns per chamber, and M4 and M5 have half. The number of pad rows per chamber is the same for all stations [35]

Multi-wire proportional chambers (MWPC) are used for all regions except for R1 of station M1, which uses triple Gas Electron Multiplier (GEM) detectors. The use of GEMs is due to their high radiation tolerance, which is necessary in this region. In the MWPCs, the gas used is an $Ar/CO_2/CF_4$ mixture in a 40/55/5 proportion. The same mixture is used in the GEM detectors, but with a 45/15/40 proportion.

3.5 Trigger System

For the nominal instantaneous luminosity of $2 \times 10^{32}\text{cm}^{-2}\text{s}^{-1}$, the rate of events with collisions that produce at least two charged particles with enough VELO and T1-T3 hits to allow for their reconstruction is roughly 10 MHz. These events are referred to as visible interactions, and it is not possible to save them all to disk. In fact, the rate at which events can be written to storage is about 2-5kHz. The necessary reduction in rate is achieved by the trigger system, which attempts to select only interesting events. An intial reduction down to 1 MHz comes from the Level-0 (L0) hardware trigger, which uses custom electronics and runs synchronously with the 40 MHz bunch crossing frequency. This is followed by a software-based High Level Trigger (HLT), which runs asynchronously on a processor farm and reduces the rate to the desired range. More details will be given on each stage in the following sections.

3.5.1 L0 Trigger

The L0 trigger is responsible for reducing the rate to 1 MHz, at which information from the entire detector can be read out and used. It is divided into three independent triggers: the L0-Calorimeter trigger, the L0-Muon trigger, and the L0-PileUp trigger. The L0-PileUp trigger was originally meant to reject events with several visible interactions. However, as the experiment is running with a higher average number of visible interactions per bunch crossing than was expected, events with pile-up are not rejected. The L0-PileUp trigger is instead being used for luminosity measurements.

The L0-Calorimeter trigger brings together information from the different calorimeter components. The transverse energy E_T which is deposited in the calorimeters is calculated in clusters of 2×2 cells. Three types of candidates are defined. An L0Hadron candidate is the highest E_T HCAL cluster, with the E_T of the matched ECAL cluster also associated with it. An L0Photon candidate is constructed from the highest E_T ECAL cluster, which also has 1 or 2 PS hits and no hits in the corresponding SPD cells. An L0Electron candidate is the same as the L0Photon, but instead requiring that there is an SPD hit in the cell matching the PS cell. If an event has any of these candidates with E_T above

some set threshold, the L0 trigger is fired. The L0-Calorimeter trigger is also used to reject events which would take too much processing time in the HLT by vetoing events which have a number of SPD hits above some threshold. The E_T and number of SPD hit thresholds are given in Table 3.

Table 3: Typical minimum p_T or E_T values given in GeV and maximum number of SPD hits used for different types of candidates in the Run 1 L0 trigger.

	p_T or E_T		SPD
Candidate	2011	2012	2011/2012
single muon	1.48	1.76	600
dimuon $p_{T_1} \times p_{T_2}$	$(1.30)^2$	$(1.60)^2$	900
hadron	3.50	3.70	600
electron	2.50	3.00	600
photon	2.50	3.00	600

The L0-Muon trigger looks for the two highest p_T tracks in each quadrant of the muon stations. Measurements of the p_T with a resolution of 25% can be obtained by the first two stations. The trigger is fired if either the largest value p_{T_1} is greater than some threshold, or the product of the two highest values $p_{T_1} \times p_{T_2}$ is greater than some threshold. Values used for these thresholds are given in Table 3.

The L0 Decision Unit (L0DU), collects all the information from the calorimeter, muon, and pile-up trigger systems at 40 MHz. The various trigger decisions are logically OR-ed to deliver the L0 decision. The decision is sent to the Readout Supervisor, which makes the final decision of whether to accept an event or not. The output rate from the L0 is approximately 400 kHz for muon triggers, 500 kHz for hadron triggers, and 150 kHz for electron/photon triggers. Note that the different triggers will have an overlap of about 10%.

3.5.2 HLT

The HLT runs on the events passing the L0 trigger, and thus recieves events at a 1 MHz rate. It is software based, and consists of C++ applications running on CPUs comprising the Event Filter Farm. The HLT has access to all of the data available in each event. Thus, if given enough computing resources, it could execute offline selection algorithms.

However, given the limited CPU resources, the HLT attempts to reject the bulk of the uninteresting events by using only part of the full event data. An approximate flow diagram of the trigger sequences is shown in Fig. 19. The HLT is split into two steps,

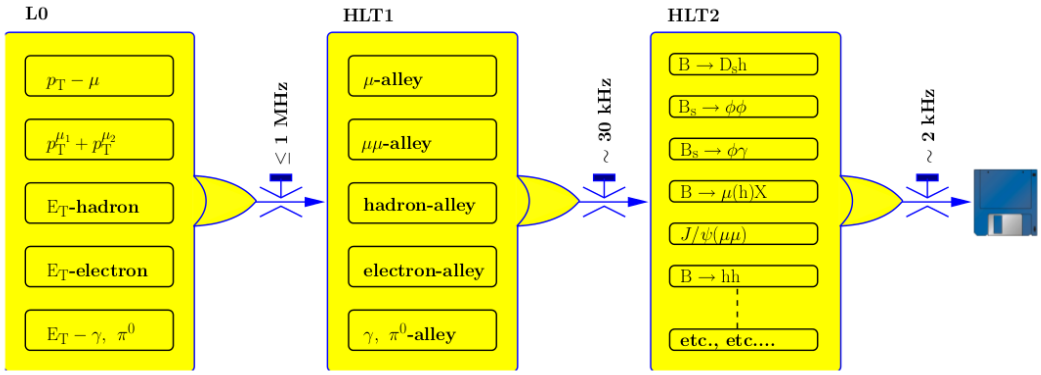

Figure 19: A flow diagram of trigger sequences. [35]

HLT1 followed by HLT2. A partial reconstruction is done in HLT1, and the complete event is reconstructed in HLT2.

VELO tracks are reconstructed for all events entering the HLT1, as the offline VELO reconstruction algorithm for performing a full 3D pattern recognition is sufficiently fast. Vertices are constructed from a minimum of five intersecting VELO tracks, and any vertex within a 300 μm radius of the mean pp-interaction position is considered to be a primary vertex. Not all VELO tracks are passed through the "forward tracking" algorithm, which looks for matching hits in the tracking stations. Only tracks which have a significant impact parameter with respect to all primary vertices or which match muon chamber hits are passed through the forward tracking. Furthermore, the algorithm is only performed for events that triggered an L0 muon trigger. The forward track search also has a minimum momentum requirement which varied from 3 to 6 GeV in Run 1, and VELO tracks without matching muon hits had a minimum p_T requirement which varied from 0.5 to 1.25 GeV. The reconstructed forward tracks are fitted with a Kalman filter using a simplified detector geometry and also fewer iterations relative to the offiline usage. Tracks identified as muons are further purified using a basic muon identification algorithm.

Inclusive beauty and charm trigger lines require a single quality track candidate,

which satisfies a p_T threshold of around 1.6-1.7 GeV and is sufficiently displaced from the primary vertex with an impact parameter greater than ~ 0.1 mm. These lines account for a large fraction of the HLT1 output rate. Inclusive one-track triggers for electron or photon candidates found in the L0 trigger also exist with reduced thresholds.

Single muon trigger lines are also used for quality tracks which match hits in the muon chambers, satisfy $p_T > 1$ GeV, and are displaced from the primary vertex. A variation of this muon line exists for for muon candidates with $p_T > 4.8$ GeV and no primary vertex separation requirement. Dimuon triggers require either mass requirements of $m_{\mu\mu} > 2.5$ GeV and no displacement requirement, or a displacement requirement without a mass requirement.

Additional trigger lines consist of dedicated lines for events with high p_T electrons, proton pairs, displaced vertices, and high E_T jets. Finally, a number of technical trigger lines exist for luminosity and beam-gas measurements.

The rate after HTL1 is small enough that forward tracking algorithms can be ran for all VELO tracks subject to the requirements of $p > 3$ GeV and $p_T > 0.3$ GeV. Muon identification is done with the offline algorithm, and electrons are identified by associating tracks to ECAL clusters. Photon and neutral pion candidates are also built from the calorimeter clusters created in the L0 trigger.

A large contribution to the output rate comes from the "topological" trigger lines. These are designed for partially reconstrcted b-hadron decays, and cover all such decays with at least two charged final state particles and a displaced vertex. The tracks are selected based on their track fit χ^2 per degree of freedom, impact parameter, and muon/electron identification. Vertices for two, three, or four body decays are built with tracks which satisfy a distance of closest approach (DOCA) requirement. An n-body combination of the tracks can have requirements on $\sum |p_T|$, $p_T^{\min}$, the invariant mass, DOCA, impact parameter to the primary vertex, and flight distance.

There are several lines for selecting events with one or two muons. Single muon candidates can be selected if the candidate passes a tight $p_T > 10$ GeV requirement, or if it is a quality track, displaced from the primary vertex, and with a transverse momentum

satisfying $p_T > 1.3$ GeV. Dimuon candidates without a mass requirement can be selected if the vertex is sufficiently separated from the primary vertex. There are a number of J/ψ trigger lines for dimuon pairs satisfying $|m_{J/\psi} - m_{\mu\mu}| < 100$. There are two "prompt" lines which have no requirements for detachment from the primary vertex, one with a $p_T > 2\,\text{GeV}$ requirement and the other with no p_T requirement, but only passing a fraction of events. There is also a detached line, which requires separation of the J/ψ candidate from the primary vertex.

There is a huge rate for $c\bar{c}$ pairs to be produced in the LHCb acceptance, and so tight, exclusive trigger lines are used for selecting charm particles. A number of trigger lines are used for a variety of D-meson and Λ_c^+ decays.

Additional lines also exist for a large number of exclusive lines, as well as lines dedicated to decays with electrons or photons in the final state, electroweak measurements, jets, *etc.*. A number of technical lines are also used for things such as monitoring and luminosity measurements.

Events which pass the HLT2 trigger requirements are then written to disk. The data is later processed with more accurate alignment and calibrations of the sub-detectors. Note that since the HLT is fully implemented in software, it is very flexible and evolves in order to adapt to the data and changing priorities, or the evolution of the reconstruction and selection software.

4 Data samples and event selection

This section will detail the selection criteria which $\Lambda_b^0 \to J/\psi K^- p$ candidates were required to fulfill. The Λ_b^0 signal, and two-body invariant mass distributions will then be shown. Some preliminary considerations on the structures observed in the mass distributions will also be given.

4.1 Event selection

The data sample corresponds to the ~ 3.0 fb^{-1} of pp collision data collected during Run 1 with the LHCb detector. Along with the data sample, 2×10^6 $\Lambda_b^0 \to J/\psi p K^-$ Monte Carlo (MC) events are used that were generated uniformly in decay phase space with $J/\psi \to \mu^+\mu^-$ decays required to occur within the LHCb acceptance. The events are generated using Pythia [41] with a special LHCb parameter tune [42]. The LHCb detector simulation is based on Geant4 [43], and is described in Ref. [44]. The simulated signal sample is passed through the reconstruction and selection procedure, after which the number of surviving events is about 10 times larger than the number of signal events found in data. This MC sample is used for many purposes throughout this analysis, such as parametrizing the reconstruction and selection efficiency and performing integrations.

A quick explanation of the types of criteria which the selected events must pass will be given in order to give a brief overview and to set the notation. Particle identification is crucial to this analysis, and uses information from several parts of the detector, as was discussed in the section cover the description of the detector (Sec. 3). Likelihoods are formed for the various hypotheses of a particle belonging to a certain species, *i.e.* proton, kaon, pion, muon. Likelihood ratio test variables are then formed, *e.g.* $DLL(p - \pi)$ is the log of the likelihood ratio of the proton and the pion hypotheses. Often times it is desired for a track to either point towards or away from the pp interaction point, or the primary vertex (PV). For example, the Λ_b^0 in this analysis should come from a PV. On the other hand the proton should come from the decay vertex of the Λ_b^0, which is often well-separated from the PV due to the weak decay of the Λ_b^0 allowing it to travel an

appreciable distance before decaying. Meanwhile, there are many protons coming from the PV, and so it is desirable to select protons which don't point to the PV. A variable which is often used for this purpose is $\chi^2_{\rm IP}$ which is the χ^2 of the impact parameter (IP) from the PV. When multiple tracks are required to form a vertex, cuts are applied to ensure that they actually are consistent with forming a vertex together. This is performed with a χ^2 of the vertex: $\chi^2_{\rm vtx}$. This cut is usually normalized by the number of degrees of freedom (ndf). Similarily, the χ^2 per degree of freedom from the track fit, $\chi^2_{\rm trk}/{\rm ndf}$, is used to ensure that quality tracks are selected by quantifying how well a reconstructed trajectory matches measured hits in the detector.

The selection of the J/ψ candidates will now be discussed. Each of the opposite signed muons is required to have a transverse momentum $p_{\rm T} > 550$ MeV, an $\chi^2_{\rm IP} > 4$, a $DLL(\mu^\pm - \pi^\pm) > 0$, and a $\chi^2_{\rm trk}/{\rm ndf} < 4$. The two muons are combined to form a J/ψ candidate, which has its own set of selection criteria. The J/ψ candidate is required to be separated from the PV, which is enforced by selecting candidates with a decay length significance χ^2 with respect to the PV of greater than 3. The two muons must form a good vertex together, through the $\chi^2_{\rm vtx}/{\rm ndf} < 16$ requirement. Finally, only $(\mu^+\mu^-)$ candidates are taken which are in the invariant mass window of $-48 < m_{\mu^+\mu^-} - m_{J/\psi} < 43$ MeV, where the asymmetry in the window is to account for final-state electromagnetic radiation. Candidate $\mu^+\mu^-$ combinations are constrained to the J/ψ mass for subsequent use in event selection.

The above requirements give a clean J/ψ sample which is then combined with a p and a K^- track. Each of these tracks is required to satisfy $p_{\rm T} > 250$ MeV, $\chi^2_{\rm IP} > 9$, and $\chi^2_{\rm trk}/{\rm ndf} < 4$. In terms of particle identification, the K^- must satisfy $DLL(K - \pi) > 0$ and $DLL(p - K) < 3$, while the p must satisfy $DLL(p - \pi) > 10$ and $DLL(p - K) > 3$. In the track reconstruction, during the pattern recognition, pseudo-random combinations of hits can form a track. These are refered to as ghosts, and the probability of a track being from a ghost is required to be less than 0.2. It is also required that the K^- and p tracks are consistent with forming a vertex, via the direction of closest approach $\chi^2 < 16$ requirement. The full Λ_b^0 candidate must satisfy the following requirements:

$\chi^2_{\rm IP} < 25$, $\chi^2_{\rm vtx}/{\rm ndf} < 10$, and having a flight distance of over 1.5 mm. Further, the cosine of the angle between the Λ_b^0 momentum vector and the vector between the PV and Λ_b^0 decay vertex must be greater than 0.999 (DIRA$>$ 0.999). The selection criterion are summarized in Table 4.

Table 4: Selection criteria for $\Lambda_b^0 \to J/\psi K^- p$ candidates. Not listed are the BDTG requirement and b-hadron vetos.

Selection variables	Requirements
All tracks χ^2/ndf	< 4
Muon PID	DLL$(\mu - \pi) > 0$
$p_{\rm T}$ of muon	> 550 MeV
J/ψ vertex χ^2	< 16
J/ψ χ^2/ndf DLS	> 3
J/ψ mass window	$-48 < m(\mu^+\mu^-) - m(J/\psi) < 43$ MeV
$p_{\rm T}$ of hadron	> 250 MeV
Hadron $\chi^2_{\rm IP}$	> 9
K^- ID	DLL$(K - \pi) > 0$ and DLL$(p - K) < 3$
p ID	DLL$(p - \pi) > 10$ and DLL$(p - K) > 3$
Clone track rejection on hadron	Ghost probability < 0.2
pK^- vertex	DOCA $\chi^2 < 16$
Λ_b^0 $\chi^2_{\rm IP}$	< 25
Λ_b^0 vertex χ^2/ndf	< 10
Λ_b^0 flight distance	> 1.5 mm
Λ_b^0 pointing	DIRA> 0.999

Despite the excellent particle identification provided by the LHCb detector, particles are still misidentified. It is thus necessary to worry about decays from other b-hadrons feeding into the Λ_b^0 mass range due to one of the final-state hadrons being misidentified. In particular, the $\overline{B}{}_s^0 \to J/\psi K^- K^+$ decay with the K^+ misidentified as a p, as well as the $\overline{B}{}^0 \to J/\psi K^- \pi^+$ decay with the π^+ misidentified as a p, can both feed into the Λ_b^0 mass range. Contributions from these decays can be checked for by reassigning the proton track as either a kaon or a pion, and then calculating either the $m_{J/\psi K^- K^+}$ or $m_{J/\psi K^- \pi^+}$ invariant mass. The candidate is then vetoed if the calculated $m_{J/\psi K^- K^+}$ or $m_{J/\psi K^- \pi^+}$ falls within 30 MeV of the $\overline{B}{}_s^0$ or $\overline{B}{}^0$, respectively. This procedure effectively removes reflections from these potential backgrounds. More details, and the effect of the veto, can be seen in Appendix A.

The final background reduction is performed using a multivariate classifier. Specifi-

cally, a Boosted Decision Tree (BDT), using gradient boosting, was employed. Hereafter it will be referred to as the BDTG, reflecting the particular boosting algorithm. Muon identification is used in the BDTG via one of the variables being the smaller value of the two discriminants DLL($\mu^+ - \pi^+$) and DLL($\mu^- - \pi^-$) in the candidate. Two variables pertain to the K^- and p tracks: the smaller value of $\chi^2_{\rm IP}(K)$ and $\chi^2_{\rm IP}(p)$, along with their scalar $p_{\rm T}$ sum. The rest of the variables are for the full Λ^0_b candidate. One such variable is the DIRA variable, which is already required to be greater than 0.999: the cosine of the angle between the Λ^0_b momentum vector and the vector from the primary vertex to the Λ^0_b decay vertex. In addition the $\chi^2_{\rm IP}$, flight distance, $p_{\rm T}$, and $\chi^2_{\rm vtx}$ of the Λ^0_b candidate are used. A detailed discussion of the training and variables used can be found in Appendix C.

As was mentioned, the MC sample goes through this full selection criteria, including the BDTG. A caveat to this is that no selections are actually applied to the MC for the hadron particle identification. It is well-known that the simulation procedure mismodels this, and so instead of explicitly cutting on the variables, data-driven methods are used to apply weights to the MC which statistically replicate the effect of applying these cuts. The selected MC events must also receive corrections resulting from mismodeling of the kinematics of the decay, which are also applied via further event weights. The full weighting procedure is described in Appendix B.

4.2 The $\Lambda^0_b \to J/\psi\, pK^-$ signal

The $m_{J/\psi pK}$ distribution for events which have passed the full selection criteria are shown in Fig 20. The combinatorial background is modeled with an exponential function and the Λ^0_b signal shape is parameterized by a double-sided Hypatia function [45], where the radiative tail parameters are fixed to the Monte Carlo prediction. The fit returns $n_{sig} = 27546 \pm 176$ $\Lambda^0_b \to J/\psi\, pK^-$ signal events, with the Λ^0_b peak having a mass and width of $M_0 = 5620.77 \pm 0.04$ MeV and $\sigma = 7.54 \pm 0.05$ MeV, respectively. The background is smooth and small, contributing only 5.4% of events with the mass range $M_0 \pm 2\sigma$.

The Dalitz plot [46] for the K^-p and $J/\psi\, p$ systems, showing the distribution over the

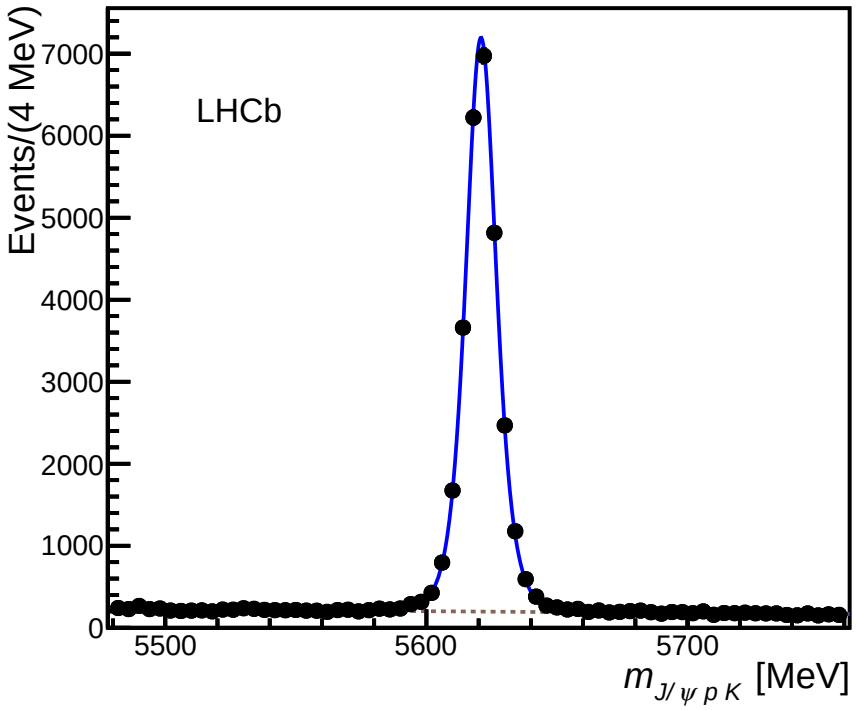

Figure 20: The invariant mass spectrum of $J/\psi pK^-$ combinations, fit with a double-sided Hypatia function to model the signal and an exponential function to model the background.

$(m^2_{Kp}, m^2_{J/\psi p})$ plane, is shown in Fig. 21 for all candidates which lie within 15 MeV of the Λ_b^0 signal peak. The most prominent feature is a distinct vertical band clearly seen in the pK^- system near 2.3 GeV^2 and corresponding to the $\Lambda(1520)$. Further inspection shows other vertical bands, also corresponding to other Λ excitations (hereafter denoted Λ^*). These are all expected and are conventional resonances. However there is a distinct horizontal band near 19.5 GeV^2 which is not expected, as a resonance in the $J/\psi p$ system would correspond to a pentaquark.

The Dalitz plots of $(m^2_{Kp}, m^2_{J/\psi K})$ and $(m^2_{J/\psi p}, m^2_{J/\psi K})$ are shown in Fig. 22. For $(m^2_{Kp}, m^2_{J/\psi K})$, there are no clear horizontal bands which would indicate a resonance in the $J/\psi K^-$ system. These would indicate an exotic tetraquark contribution, and are not expected to be present, since there are no known tetraquark candidates decaying to $J/\psi K^-$. Similarily, there are no horizontal bands seen in the $(m^2_{J/\psi p}, m^2_{J/\psi K})$ plane. There is however a vertical band, again indicating the presence of something in the $J/\psi p$ system near 19.5 GeV^2. One might have also noted that there a diagonal band in the

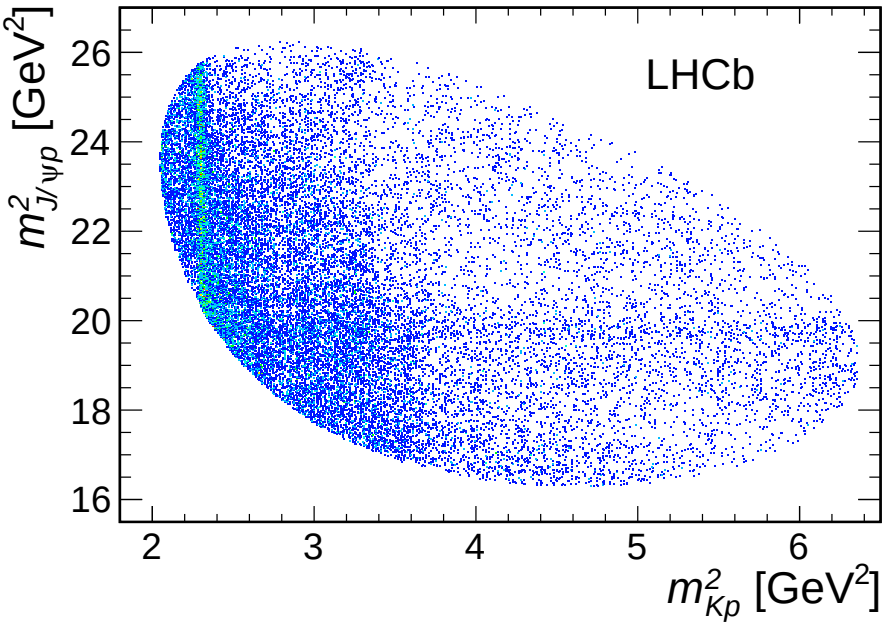

Figure 21: The $(m^2_{Kp}, m^2_{J/\psi p})$ plane for candidates within ± 15 MeV of the Λ_b^0 mass.

$(m^2_{Kp}, m^2_{J/\psi K})$ plane. It can be seen in a side-by-side comparison that it covers the same $m^2_{J/\psi K}$ range as the vertical band in the $(m^2_{J/\psi p}, m^2_{J/\psi K})$ plane, thus indicating that the diagonal band is the result of activity in the $J/\psi p$ system. This is similar to how the conventional $K^- p$ resonances reflect into the $(m^2_{J/\psi p}, m^2_{J/\psi K})$ plane as a diagonal band.

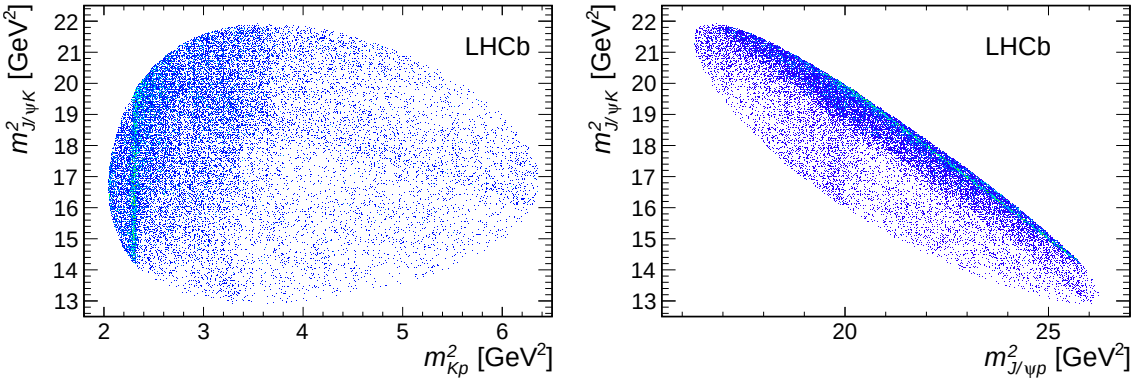

Figure 22: The $(m^2_{Kp}, m^2_{J/\psi K})$ (left) and $(m^2_{J/\psi p}, m^2_{J/\psi K})$ (right) planes for candidates within ± 15 MeV of the Λ_b^0 mass.

Figure 23 shows the individual distributions of the three invariant masses: m_{Kp}, $m_{J/\psi p}$, and $m_{J/\psi K}$. The background has been subtracted using the *sPlot* technique [47] (see also Sec 6.3 for more details). Shown in the same figures are the expectations from the MC sample, which represents the expectations for phase space events after going through the

reconstruction and selection procedure. As was seen in the Dalitz plots, there is a rich spectrum of resonances in the K^-p system. There is also a prominent peak in $m_{J/\psi p}$, corresponding to the unexpected structure seen in the $J/\psi p$ system. Clearly, there is significant deviation of $m_{J/\psi K}$ from the phase space expectations as well. However the Dalitz plot distributions show that this is likely due to the activity in the K^-p and $J/\psi p$ systems reflecting into the $J/\psi K^-$ system.

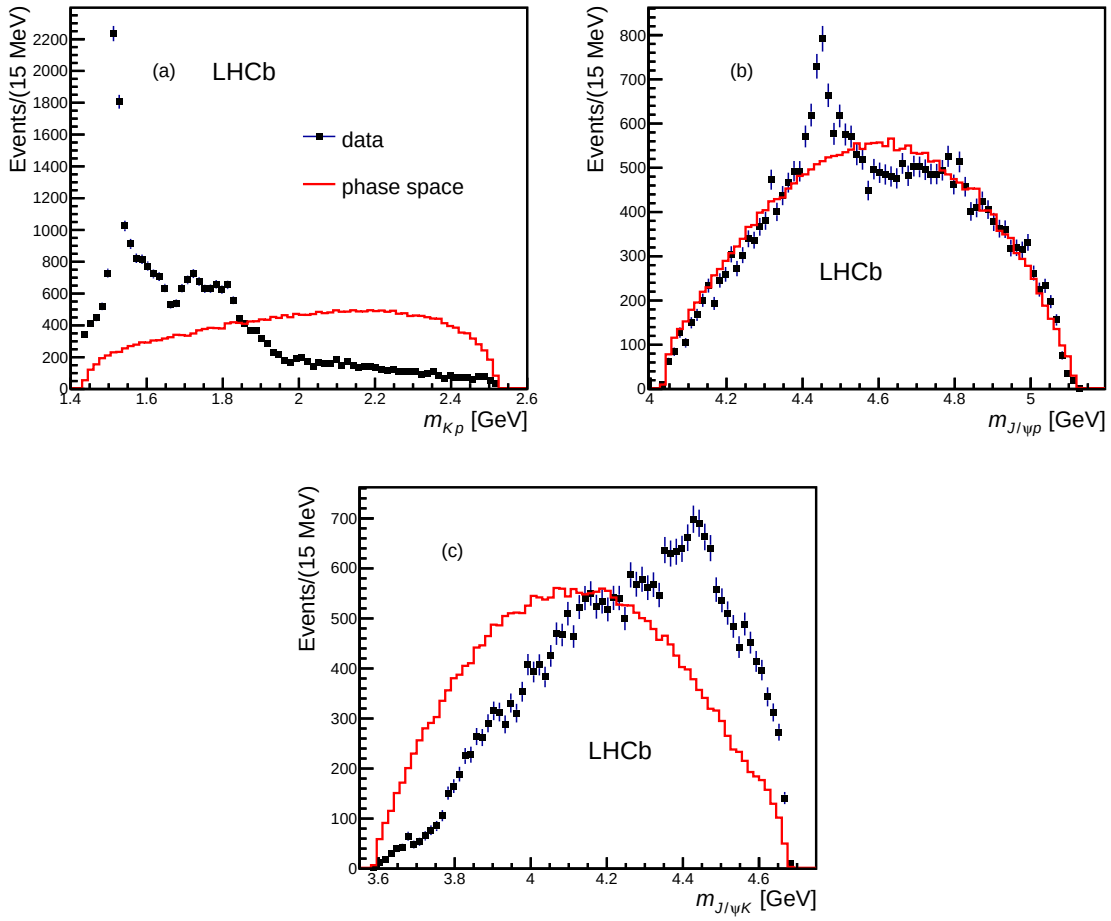

Figure 23: The (a) m_{Kp}, (b) $m_{J/\psi p}$, and (c) $m_{J/\psi K}$ distributions for the background-subtracted $\Lambda_b^0 \to J/\psi K^- p$ candidates. The solid (red) histogram shows the phase space expectations.

4.3 Preliminary Considerations

The Dalitz plots and mass projections all indicate that there is activity in the $J/\psi p$ system, for which pentaquarks are one possible explanation. However, given the history of past pentaquark searches, making such a claim is not something to be taken lightly.

It is worth noting that this situation is significantly different from the past cases, as the statistics are much better. From examining the structure in the $m_{J/\psi p}$ distribution, it is easy to convince oneself that this is not the result of statistical fluctuations. It is also worth noting that this structure was not being sought after, and that it was observed by multiple LHCb teams which were using their own data selection criteria after the original sighting. Still, there are a number of considerations that should be investigated before bringing pentaquarks into the picture.

It is important to check whether or not the peaking structure could be the result of decays from other b-hadrons. As stated earlier all $B_s \to J/\psi K^- K^+$ and $B^0 \to J/\psi K^- \pi^+$ decays were explicitly vetoed. Another possible source could be decays from some higher mass state such as $\Xi_b^- \to J/\psi K^- p \pi^-$. To check this, the event selection was repeated as before, but requiring also that a π forms a vertex with the $J/\psi K^- p$. It is required that the π satisfy $DLL_K(\pi) > -10$, $\chi^2_{\rm IP} > 9$, $p_{\rm T} > 250$ MeV, and have a Ghost probability< 0.2. Further, the new $J/\psi K^- p \pi^-$ vertex must satisfy $\chi^2_{vtx} < 30$ (with 7 degrees of freedom). Figure 24 shows the $m_{J/\psi K^- p \pi^-}$ versus $m_{J/\psi K^- p}$ distribution for the selected events. The dark vertical band corresponds to the $\Lambda_b^0 \to J/\psi K^- p$ decays. With no visible structures in the $(J/\psi K^- p \pi^-)$ system, there is no evidence for contributions from Ξ_b^- or any other higher mass state.

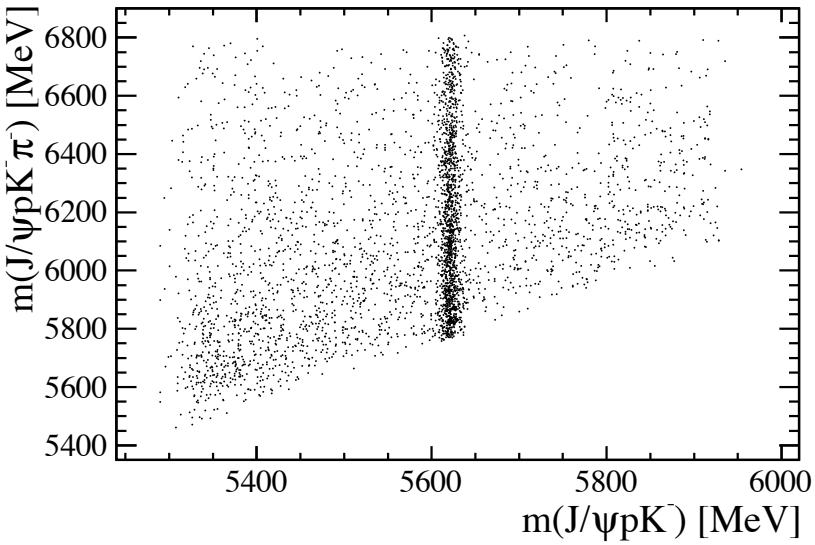

Figure 24: $m(J/\psi K^- p \pi^-)$ versus $m(J/\psi K^- p)$ for selected $J/\psi p K \pi$ combinations.

Additionally, it was carefully checked that the peaking structure could not be the

result of any fake tracks which were artificially created by the track reconstruction procedure. Also, efficiency effects from the selection criteria would not create such a structure. This can be seen from the distribution of the phase space MC after the selection (Fig. 23); there were no such structures created. The efficiency over the Dalitz plane can also be seen ahead in Fig. 31. Various sanity checks were also performed. For example, the data set was split in various ways, to check for consistency and any unexpected effects. In Fig. 25, the $m_{J/\psi p}$ distribution is shown for data taken in the year 2011, along with data taken in the year 2012 split by the polarity of the magnet during data taking. All three are consistent with each other. Also shown is the data split into separate $P_c^+ \to J/\psi p$ and $P_c^- \to J/\psi \overline{p}$ samples. No visible differences are observed.

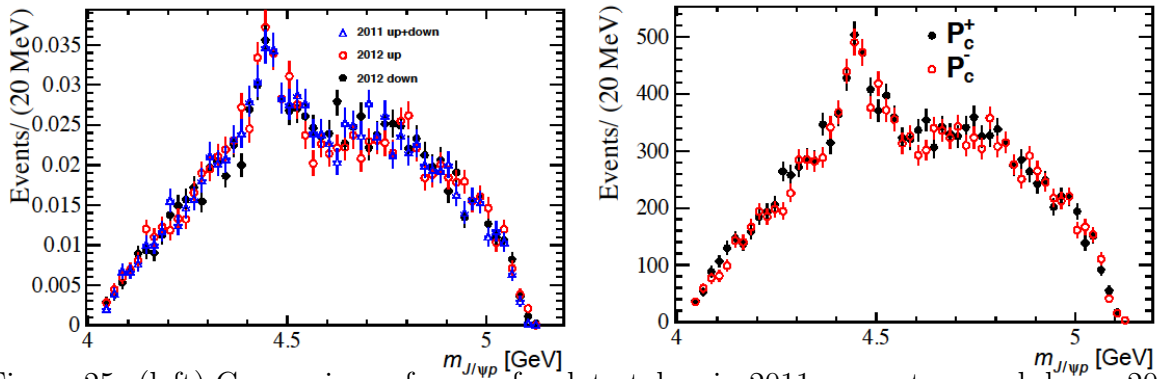

Figure 25: (left) Comparison of $m_{J/\psi p}$ for data taken in 2011 magnet up and down, 2012 magnet up, and 2012 magnet down. (right) Comparison of $m_{J/\psi p}$ for separate $P_c^+ \to J/\psi p$ and $P_c^- \to J/\psi \overline{p}$ samples.

All tests and checks performed indicate that the unexpected structures are the result of real physics effects present in true $\Lambda_b^0 \to J/\psi K^- p$ decays. However, before concluding that the structure is from activity in the $J/\psi p$ system, it is necessary to rule out the possibility it is a result of reflections from $K^- p$ contributions. Despite the narrowness of the peak, it is still important to check whether or not interferring $K^- p$ resonances are capable of creating the observed features. In order to do this, an amplitude analysis is performed. Later, the same question is approached in a model-independent way.

5 Amplitude analysis formalism

An amplitude analysis allows for testing whether or not interferring Λ^* resonances are responsible for the peaking structure seen in the $m_{J/\psi p}$ distribution. If it is shown they are not responsible, an amplitude analysis will also allow for testing if the inclusion of $P_c \to J/\psi p$ decays in the amplitude model can reproduce the structure. It then would allow for determining any P_c parameters. In this analysis, the helicity formalism is used to parametrize the decay dynamics, and the Isobar approximation is used to sum up Breit-Wigner amplitudes from all contributing resonances. The full $\Lambda_b^0 \to J/\psi K^- p$, $J/\psi \to \mu^+\mu^-$ decay chain is studied in order to maximize sensitivity. Analyzing the data in the full set of dimensions which completely specify the decay also helps avoid biases due to non-uniform efficiency.

In this section, a brief outline is given of the helicity formalism and the notation which will be used in the rest of the section. The matrix element for the $\Lambda_b^0 \to \Lambda^*\psi$, $\Lambda^* \to K^- p$, $\psi \to \mu^+\mu^-$ decay sequence is then derived[4], followed by the matrix element for the $\Lambda_b^0 \to P_c^+ K^-$, $P_c^+ \to \psi p$, $\psi \to \mu^+\mu^-$ decay sequence. These decay sequences are hereafter referred to as the Λ^* and P_c decay chains, respectively. The coherent combination of the matrix elements for these two decay chains, so as to obtain a correct description of their intereference, is also shown. Finally, a discussion of the relationship of the helicity and LS couplings is presented, along with how it can be utilized to reduce the number of parameters which need to be determined from the data.

5.1 Helicity formalism and notation

For each two-body decay $A \to B\,C$, a coordinate system is set up in the rest frame of A, with $\hat{z}$ being[5] the direction of quantization for its spin. This coordinate system is denoted as $(x_0^{\{A\}}, y_0^{\{A\}}, z_0^{\{A\}})$, where the superscript "$\{A\}$" means "in the rest frame of A", while the subscript "0" means the initial coordinates. For the first particle in the

[4]For the rest of this section J/ψ is denoted as ψ.

[5]The "hat" symbol denotes a unit vector in a given direction.

decay chain (Λ_b^0), the choice of these coordinates is arbitrary.[6] However, once defined, these coordinates must be used consistently between all decay sequences described by the matrix element. For subsequent decays, *e.g.* $B \to D\,E$, the choice of these coordinates is already fixed by the transformation from the A to the B rest frames, as discussed below. Helicity is defined as the projection of the spin of the particle onto the direction of its momentum, and is denoted as λ.

In using the helicity formalism, a transformation is required which aligns the z axis of the initial coordinate system with the direction of momentum of one of the daughter particles, *e.g.* the B. The physical meaning of the transformation will be made clear later. A generalized rotation operator can be formulated in three-dimensional space, $\mathcal{R}(\alpha, \beta, \gamma)$, that uses Euler angles. Applying this operator results in a sequence of rotations: first by the angle α about the $\hat{z}_0$ axis, followed by the angle β about the rotated $\hat{y}_1$ axis and then finally by the angle γ about the rotated $\hat{z}_2$ axis. The subscript on the axes is used to specify the rotations which have already been performed on the coordinates. The spin eigenstates of particle A, $|J_A, m_A\rangle$, in the $({x_0}^{\{A\}}, {y_0}^{\{A\}}, {z_0}^{\{A\}})$ coordinate system can be expressed in the basis of its spin eigenstates, $|J_A, m'_A\rangle$, in the rotated $({x_3}^{\{A\}}, {y_3}^{\{A\}}, {z_3}^{\{A\}})$ coordinate system with the help of Wigner's $D-$matrices

$$|J_A, m_A\rangle = \sum_{m'_A} D^{J_A}_{m_A, m'_A}(\alpha, \beta, \gamma)^* \, |J_A, m'_A\rangle, \tag{1}$$

where

$$D^J_{m,\,m'}(\alpha, \beta, \gamma)^* = \langle J, m|\mathcal{R}(\alpha, \beta, \gamma)|J, m'\rangle^* = e^{i\,m\alpha}\; d^J_{m,m'}(\beta)\; e^{i\,m'\gamma}, \tag{2}$$

and where the small-d Wigner matrix contains known functions of β that depend on J, m, m'. To achieve the rotation of the original $\hat{z}_0^{\{A\}}$ axis onto the B momentum ($\vec{p}_B^{\{A\}}$), it is sufficient to rotate by $\alpha = \phi_B^{\{A\}}$, $\beta = \theta_B^{\{A\}}$, where $\phi_B^{\{A\}}$, $\theta_B^{\{A\}}$ are the azimuthal and polar angles of the B momentum vector in the original coordinates *i.e.* $(\hat{x}_0^{\{A\}}, \hat{y}_0^{\{A\}}, \hat{z}_0^{\{A\}})$. This is depicted in Fig. 26, where the quantization axis for the spin of A is its momentum

[6] When designing an analysis to be sensitive (or insensitive) to a particular case of polarization, the choice is not arbitrary, but this does not change the fact that one can quantize the Λ_b^0 spin along any well-defined direction. The Λ_b^0 polarization may be different for different choices.

in some initial reference frame. As the third rotation is not necessary, the convention $\gamma = 0$ is chosen.[7] The angle $\theta_B^{\{A\}}$ is usually called "the A helicity angle", thus to simplify the notation it is denoted as θ_A. Also in the spirit of compact notation, $\phi_B^{\{A\}}$ is denoted as ϕ_B. These angles can be determined from[8]

$$\begin{aligned}
\phi_B &= \text{atan2}\left(p_B^{\{A\}}{}_y,\, p_B^{\{A\}}{}_x\right) \\
&= \text{atan2}\left(\hat{y}_0^{\{A\}} \cdot \vec{p}_B^{\{A\}},\, \hat{x}_0^{\{A\}} \cdot \vec{p}_B^{\{A\}}\right) \\
&= \text{atan2}\left((\hat{z}_0^{\{A\}} \times \hat{x}_0^{\{A\}}) \cdot \vec{p}_B^{\{A\}},\, \hat{x}_0^{\{A\}} \cdot \vec{p}_B^{\{A\}}\right), \qquad (3) \\
\cos\theta_A &= \hat{z}_0^{\{A\}} \cdot \hat{p}_B^{\{A\}}. \qquad (4)
\end{aligned}$$

where $p_B^{\{A\}}{}_i$ denotes the i-th component of the momentum vector (of particle B in the rest frame of A).

Angular momentum conservation in the decay requires $m'_A = m'_B + m'_C = \lambda_B - \lambda_C$ (since $\vec{p}_C^{\{A\}}$ points in the opposite direction to $\hat{z}_3^{\{A\}}$, $m'_C = -\lambda_C$). Each two-body decay contributes a multiplicative term to the matrix element as

$$\mathcal{H}^{A\to BC}_{\lambda_B,\lambda_C}\, D^{J_A}_{\lambda_A,\,\lambda_B-\lambda_C}(\phi_B, \theta_A, 0)^*, \qquad (5)$$

where the helicity couplings $\mathcal{H}^{A\to BC}_{\lambda_B,\lambda_C}$ are complex constants. The modulus-squared of this term can be thought of as the probability of a particle A with spin J_A and helicity λ_A to decay to two particles with spin projection $\lambda_B - \lambda_C$ in the direction given by $(\phi_B, \theta_A, 0)$. The helicity couplings contain the dynamics of the decay, and must be determined from the data. Parity must be conserved when the decay proceeds via the strong or electromagnetic interaction, requiring that the helicity couplings satisfy the relation

$$\mathcal{H}^{A\to BC}_{-\lambda_B,-\lambda_C} = P_A\, P_B\, P_C\, (-1)^{J_B+J_C-J_A}\, \mathcal{H}^{A\to BC}_{\lambda_B,\lambda_C}, \qquad (6)$$

[7] An alternative convention is to set $\gamma = -\alpha$. The two conventions lead to equivalent formulae.

[8] The function atan2(x, y) is the $\tan^{-1}(y/x)$ function with two arguments. The purpose of using two arguments instead of one is to gather information on the signs of the inputs in order to return the appropriate quadrant of the computed angle.

where P stands for the intrinsic parity of a particle.

To account for the subsequent decay of a daughter, $B \to D\,E$, a similar procedure is repeated. However the four-vectors of all particles must first be Lorentz boosted to the rest frame of B, along the $\vec{p}_B^{\,\{A\}}$ *i.e.* $\hat{z}_3^{\,\{A\}}$ direction. Again, this is the z axis in the rest frame of A after the Euler rotations (since the $\gamma = 0$ convention is used, the $\hat{z}_3^{\,\{A\}} = \hat{z}_2^{\,\{A\}}$). This can be visualized in Fig. 26, with the $B \to D\,E$ particle labels replacing the $A \to B\,C$ labels. This transformation does not change vectors that are perpendicular to the boost direction. Thus the transformed coordinates become the initial coordinate system quantizing the spin of B in its rest frame,

$$\begin{aligned} \hat{x}_0^{\,\{B\}} &= \hat{x}_3^{\,\{A\}}, \\ \hat{y}_0^{\,\{B\}} &= \hat{y}_3^{\,\{A\}}, \\ \hat{z}_0^{\,\{B\}} &= \hat{z}_3^{\,\{A\}}. \end{aligned} \tag{7}$$

In practice, there are two equivalent ways to determine the $\hat{z}_0^{\,\{B\}}$ direction. It can be set to the direction of the B momentum in the A rest frame

$$\hat{z}_0^{\,\{B\}} = \hat{z}_3^{\,\{A\}} = \hat{p}_B^{\,\{A\}}. \tag{8}$$

Alternatively, the fact that B and C are back-to-back in the rest frame of A can be used, $\vec{p}_C^{\,\{A\}} = -\vec{p}_B^{\,\{A\}}$. Since the momentum of C is antiparallel to the boost direction from the A to B rest frames, the C momentum in the B rest frame will be different, but it will still be antiparallel to this boost direction

$$\hat{z}_0^{\,\{B\}} = -\hat{p}_C^{\,\{B\}}. \tag{9}$$

After the first rotation by ϕ_B about $\hat{z}_0^{\,\{A\}}$, the $\hat{x}_1^{\,\{A\}}$ axis is along the component of $\vec{p}_B^{\,\{A\}}$

which is perpendicular to the $\hat{z}_0^{\{A\}}$ axis

$$\begin{aligned}
\vec{a}_{B\perp z_0}^{\{A\}} &\equiv (\vec{p}_B^{\{A\}})_{\perp \hat{z}_0^{\{A\}}} = \vec{p}_B^{\{A\}} - (\vec{p}_B^{\{A\}})_{||\hat{z}_0^{\{A\}}}, \\
&= \vec{p}_B^{\{A\}} - (\vec{p}_B^{\{A\}} \cdot \hat{z}_0^{\{A\}})\, \hat{z}_0^{\{A\}}, \\
\hat{x}_1^{\{A\}} &= \hat{a}_{B\perp z_0}^{\{A\}} = \frac{\vec{a}_{B\perp z_0}^{\{A\}}}{|\,\vec{a}_{B\perp z_0}^{\{A\}}\,|}.
\end{aligned} \tag{10}$$

The $\hat{y}_1^{\{A\}}$ can then be uniquely determined from the unchanged $\hat{z}_1^{\{A\}} = \hat{z}_0^{\{A\}}$ direction and $\hat{x}_1^{\{A\}}$. After the second rotation by θ_A about $\hat{y}_1^{\{A\}}$, $\hat{z}_2^{\{A\}} = \hat{z}_3^{\{A\}} = \hat{p}_B^{\{A\}}$, and $\hat{x}_2^{\{A\}} = \hat{x}_3^{\{A\}}$ is antiparallel to the component of the $\hat{z}_1^{\{A\}} = \hat{z}_0^{\{A\}}$ vector that is perpendicular to the new z axis *i.e.* $\hat{p}_B^{\{A\}}$. Thus

$$\begin{aligned}
\vec{a}_{z_0\perp B}^{\{A\}} &\equiv (\hat{z}_0^{\{A\}})_{\perp \vec{p}_B^{\{A\}}} = \hat{z}_0^{\{A\}} - (\hat{z}_0^{\{A\}} \cdot \hat{p}_B^{\{A\}})\, \hat{p}_B^{\{A\}}, \\
\hat{x}_0^{\{B\}} &= \hat{x}_3^{\{A\}} = -\,\hat{a}_{z_0\perp B}^{\{A\}} = -\,\frac{\vec{a}_{z_0\perp B}^{\{A\}}}{|\,\vec{a}_{z_0\perp B}^{\{A\}}\,|}.
\end{aligned} \tag{11}$$

Then $\hat{y}_0^{\{B\}}$ is obtained as $\hat{y}_0^{\{B\}} = \hat{z}_0^{\{B\}} \times \hat{x}_0^{\{B\}}$.

If C also decays, $C \to F\,G$, then the coordinates for the quantization of C spin in the C rest frame are defined by

$$\hat{z}_0^{\{C\}} = -\hat{z}_3^{\{A\}} = \hat{p}_C^{\{A\}} = -\hat{p}_B^{\{C\}}, \tag{12}$$

$$\hat{x}_0^{\{C\}} = \hat{x}_3^{\{A\}} = -\,\hat{a}_{z_0\perp B}^{\{A\}} = +\hat{a}_{z_0\perp C}^{\{A\}}, \tag{13}$$

$$\hat{y}_0^{\{C\}} = \hat{z}_0^{\{C\}} \times \hat{x}_0^{\{C\}}, \tag{14}$$

i.e. the z axis is reflected compared to the system used for the decay of particle B (it must point in the direction of C momentum in the A rest frame), but the x axis is kept the same, since the particle B was chosen for the rotation used in Eq. (5).

The processes of rotation and subsequent boosting can be repeated until the final-state particles are reached, and all factors of Eq. (5) have been accumulated. After multiply all such factors, they must be summed up coherently over the helicity states of intermediate particles, and incoherently over the helicity states of the initial and final-

state particles. The possible helicity values which are summed over are constrained by angular momentum conservation. In the case of $A \to B\,C$, the constraints are $|\lambda_B| \leq J_B$, $|\lambda_C| \leq J_C$ and $|\lambda_B - \lambda_C| \leq J_A$. When there are multiple different decay chains that can be taken to arrive at the same set of final-state particles, care must be taken in the coherent addition of contributions from different chains. This will be discussed in the context of the present use-case in the following sections.

5.2 Matrix element for the Λ^* decay chain

First, the portion of the matrix element describing the conventional $\Lambda_b^0 \to \Lambda_n^*\psi$, $\Lambda_n^* \to Kp$ decays (*i.e.* Λ^* decay chain) will be discussed. Here Λ_n^* denotes various possible excitations of the Λ, *e.g.* $\Lambda(1520)$, Unless an n-dependent quantity is being labeled, Λ_n^* will often be written just as Λ^*, for simplicity.

Analogously to Eq. 5, the decay of $\Lambda_b^0 \to \Lambda_n^*\psi$ is described by

$$\mathcal{H}^{\Lambda_b^0 \to \Lambda_n^* \psi}_{\lambda_{\Lambda^*}, \lambda_\psi}\; D^{\frac{1}{2}}_{\lambda_{\Lambda_b^0}, \lambda_{\Lambda^*} - \lambda_\psi}(\phi_{\Lambda^*}, \theta_{\Lambda_b^0}, 0)^*, \tag{15}$$

where $\mathcal{H}^{\Lambda_b^0 \to \Lambda_n^* \psi}_{\lambda_{\Lambda^*}, \lambda_\psi}$ are resonance (*i.e.* n) dependent helicity couplings to be determined by a fit to the data. There are 4 different complex values of these couplings to be determined for each Λ_n^* resonance with spin $J_{\Lambda_n^*} = \frac{1}{2}$, and 6 values for higher spins. Note that this is a weak decay, and so all couplings must be independent of each other. The couplings are complex parameters; thus each independent coupling contributes 2 free parameters (taken to be real and imaginary parts) to the fit. Since the ψ and Λ^* are intermediate particles in the decay chain, the matrix element terms for different values of λ_ψ and λ_{Λ^*} must be added coherently.

The choice of the $\hat{z}_0^{\{\Lambda_b^0\}}$ direction for the Λ_b^0 spin quantization is arbitrary, and it is taken to be the Λ_b^0 momentum in the lab frame, giving its spin projection onto this axis the meaning of the Λ_b^0 helicity ($\lambda_{\Lambda_b^0}$). In the Λ_b^0 rest frame, this direction is defined by

the direction of the boost from the lab frame (Eq. (8)),

$$\hat{z}_0^{\{\Lambda_b^0\}} = \hat{p}_{\Lambda_b^0}^{\{\text{lab}\}}, \tag{16}$$

as depicted in Fig. 27. With this choice, the Λ_b^0 helicity angle ($\theta_{\Lambda_b^0}$) can be calculated as

$$\cos\theta_{\Lambda_b^0} = \hat{p}_{\Lambda_b^0}^{\{\text{lab}\}} \cdot \hat{p}_{\Lambda^*}^{\{\Lambda_b^0\}}. \tag{17}$$

Longitudinal polarization of the Λ_b^0 via strong production mechanisms is forbidden due to parity conservation in strong interactions, causing $\lambda_{\Lambda_b^0} = +\frac{1}{2}$ and $-\frac{1}{2}$ to be equally likely. Terms with different $\lambda_{\Lambda_b^0}$ values must be added incoherently. The choice of $\hat{x}_0^{\{\Lambda_b^0\}}$ direction in the Λ_b^0 rest frame is also arbitrary. The $\Lambda_b^0 \to \Lambda^*\psi$ decay plane in the lab frame is used to define it, which makes the ϕ_{Λ^*} angle zero by definition.

The strong decay $\Lambda_n^* \to Kp$ is described by a term

$$\mathcal{H}_{\lambda_p}^{\Lambda_n^* \to Kp}\ D^{J_{\Lambda_n^*}}_{\lambda_{\Lambda^*},\lambda_p}(\phi_K, \theta_{\Lambda^*}, 0)^*\ R_{\Lambda_n^*}(m_{Kp}). \tag{18}$$

Since the K^- meson is spinless, the resonance-dependent helicity coupling $\mathcal{H}_{\lambda_p}^{\Lambda_n^* \to Kp}$ depends only on proton helicity, $\lambda_p = \pm\frac{1}{2}$. As strong decays conserve parity, the two helicity couplings are related

$$\mathcal{H}_{-\lambda_p}^{\Lambda_n^* \to Kp} = -P_{\Lambda_n^*}\,(-1)^{J_{\Lambda_n^*}-\frac{1}{2}}\ \mathcal{H}_{\lambda_p}^{\Lambda_n^* \to Kp}, \tag{19}$$

where $P_{\Lambda_n^*}$ is the parity of Λ_n^*. Since the overall magnitude and phase of $\mathcal{H}_{+\frac{1}{2}}^{\Lambda_n^* \to Kp}$ can be absorbed into a redefinition of the $\mathcal{H}_{\lambda_{\Lambda^*},\lambda_\psi}^{\Lambda_b^0 \to \Lambda_n^*\psi}$ couplings, it is possible to set $\mathcal{H}_{+\frac{1}{2}}^{\Lambda_n^* \to Kp} = (1, 0)$ and $\mathcal{H}_{-\frac{1}{2}}^{\Lambda_n^* \to Kp} = (P_{\Lambda_n^*}\,(-1)^{J_{\Lambda_n^*}-\frac{3}{2}}, 0)$, where the values in parentheses give the real and imaginary parts of the couplings.

The angles ϕ_K and θ_{Λ^*} are the azimuthal and polar angles of the kaon in the Λ^* rest frame (see Fig. 27). The $\hat{z}_0^{\{\Lambda^*\}}$ direction is defined by the boost direction from the Λ_b^0 rest frame, which coincides with the $-\vec{p}_\psi^{\{\Lambda^*\}}$ direction in this frame (Eq. (9)). This leads to

$$\cos\theta_{\Lambda^*} = -\hat{p}_\psi^{\{\Lambda^*\}} \cdot \hat{p}_K^{\{\Lambda^*\}}, \tag{20}$$

with both vectors in the Λ^* rest frame. As explained in Sec. 5.1, the $\hat{x}_0^{\{\Lambda^*\}}$ direction is defined by the choice of coordinates in the Λ_b^0 rest frame discussed above. Following Eq. (11) and (16),

$$\begin{aligned} \vec{a}_{z_0\perp\Lambda^*}^{\{\Lambda_b^0\}} &= \hat{p}_{\Lambda_b^0}^{\{\text{lab}\}} - (\hat{p}_{\Lambda_b^0}^{\{\text{lab}\}} \cdot \hat{p}_{\Lambda^*}^{\{\Lambda_b^0\}})\, \hat{p}_{\Lambda^*}^{\{\Lambda_b^0\}}, \\ \hat{x}_0^{\{\Lambda^*\}} &= \hat{x}_3^{\{\Lambda_b^0\}} = -\frac{\vec{a}_{z_0\perp\Lambda^*}^{\{\Lambda_b^0\}}}{|\,\vec{a}_{z_0\perp\Lambda^*}^{\{\Lambda_b^0\}}\,|}\,. \end{aligned} \tag{21}$$

The azimuthal angle of the K^- can now be determined in the Λ^* rest frame from (Eq. (3))

$$\phi_K = \text{atan2}\left(-(\hat{p}_\psi^{\{\Lambda^*\}} \times \hat{x}_0^{\{\Lambda^*\}}) \cdot \hat{p}_K^{\{\Lambda^*\}},\, \hat{x}_0^{\{\Lambda^*\}} \cdot \hat{p}_K^{\{\Lambda^*\}}\right). \tag{22}$$

The term $R_{\Lambda_n^*}(m_{Kp})$ describes the Λ_n^* resonance that appears in the invariant mass distribution of the kaon-proton system,

$$R_{\Lambda_n^*}(m_{Kp}) = B'_{L_{\Lambda_b^0}^{\Lambda_n^*}}(p, p_0, d) \left(\frac{p}{M_{\Lambda_b^0}}\right)^{L_{\Lambda_b^0}^{\Lambda_n^*}} \text{BW}(m_{Kp}|M_0^{\Lambda_n^*}, \Gamma_0^{\Lambda_n^*})\, B'_{L_{\Lambda_n^*}}(q, q_0, d) \left(\frac{q}{M_0^{\Lambda_n^*}}\right)^{L_{\Lambda_n^*}}. \tag{23}$$

Here, p is the Λ^* momentum in the Λ_b^0 rest frame ($p = |\vec{p}_{\Lambda^*}^{\{\Lambda_b^0\}}|$). Similarly, q is the K^- momentum in the Λ^* rest frame ($q = |\vec{p}_K^{\{\Lambda^*\}}|$). The symbols p_0 and q_0 denote values of these quantities at the resonance peak ($m_{Kp} = M_0^{\Lambda_n^*}$). The orbital angular momentum between the Λ^* and ψ particles in the Λ_b^0 decay is denoted as $L_{\Lambda_b^0}^{\Lambda_n^*}$. Similarly, $L_{\Lambda_n^*}$ is the orbital angular momentum between the p and K^- in the Λ_n^* decay. The Blatt-Weisskopf

functions [48],

$$
\begin{aligned}
B'_0(p,p_0,d) =& 1\,,\\
B'_1(p,p_0,d) =& \sqrt{\frac{1+(p_0\,d)^2}{1+(p\ \ d)^2}}\,,\\
B'_2(p,p_0,d) =& \sqrt{\frac{9+3(p_0\,d)^2+(p_0\,d)^4}{9+3(p\ \ d)^2+(p\ \ d)^4}}\,,\\
B'_3(p,p_0,d) =& \sqrt{\frac{225+45(p_0\,d)^2+6(p_0\,d)^4+(p_0\,d)^6}{225+45(p\ \ d)^2+6(p\ \ d)^4+(p\ \ d)^6}}\,,\\
B'_4(p,p_0,d) =& \sqrt{\frac{11025+1575(p_0\,d)^2+135(p_0\,d)^4+10(p_0\,d)^6+(p_0\,d)^8}{11025+1575(p\ \ d)^2+135(p\ \ d)^4+10(p\ \ d)^6+(p\ \ d)^8}}\,,\\
B'_5(p,p_0,d) =& \sqrt{\frac{893025+99225(p_0\,d)^2+6300(p_0\,d)^4+315(p_0\,d)^6+15(p_0\,d)^8+(p_0\,d)^{10}}{893025+99225(p\ \ d)^2+6300(p\ \ d)^4+315(p\ \ d)^6+15(p\ \ d)^8+(p\ \ d)^{10}}}\,,
\end{aligned}
\tag{24}
$$

are used for the orbital angular momentum barrier factors, $p^L\,B'_L(p,p_0,d)$, to account for the difficulty in creating the orbital angular momentum L. These depend on the momentum of the decay products p (in the rest frame of the decaying particle) and on the size of the decaying particle given by the constant d. This size parameter is set as $d = 3.0$ GeV^{-1} $\sim$0.6 fm, and is varied in the studies of systematic uncertainties. The relativistic Breit-Wigner amplitude is given by

$$
\mathrm{BW}(m|M_0,\Gamma_0) = \frac{1}{M_0^2 - m^2 - iM_0\Gamma(m)}\,, \tag{25}
$$

where

$$
\Gamma(m) = \Gamma_0 \left(\frac{q}{q_0}\right)^{2\,L_{\Lambda^*}+1} \frac{M_0}{m} B'_{L_{\Lambda^*}}(q,q_0,d)^2\,. \tag{26}
$$

In the case of the $\Lambda(1405)$ resonance, which peaks below the K^-p threshold, a two-component width equivalent to the Flatté parameterization [49] is used. A width for its decay to the dominant $\Sigma^+\pi^-$ channel is added to the width in the K^-p channel, $\Gamma(m) = \Gamma(m)_{K^-p}+\Gamma(m)_{\Sigma\pi}$, where q in the second term and q_0 in both terms are calculated assuming the decay to $\Sigma^+\pi^-$. Assuming that both channels are dynamically equally likely and differ only by the phase space factors Γ_0 is set to the total width of $\Lambda(1405)$ in both terms. For nonresonant (NR) terms, $\mathrm{BW}(m) = 1$ is used with $M_{0\,\mathrm{NR}}$ set to the midrange

mass.

Angular momentum conservation limits $L_{\Lambda_n^*}$ to $J_{\Lambda_n^*} \pm \frac{1}{2}$, which is then uniquely defined by parity conservation in the Λ_n^* decay, $P_{\Lambda_n^*} = (-1)^{L_{\Lambda_n^*}+1}$. Angular momentum conservation also requires $\max(J_{\Lambda_n^*} - \frac{3}{2}\,,\, 0) \leq L^{\Lambda_n^*}_{\Lambda_b^0} \leq J_{\Lambda_n^*} + \frac{3}{2}$. The minimal value of $L^{\Lambda_n^*}_{\Lambda_b^0}$ is assumed in $R_{\Lambda_n^*}(m_{Kp})$, and is varied in systematic uncertainty studies.

The electromagnetic decay $\psi \to \mu^+\mu^-$ is described by a term

$$D^1_{\lambda_\psi,\,\Delta\lambda_\mu}(\phi_\mu, \theta_\psi, 0)^*, \tag{27}$$

where $\Delta\lambda_\mu \equiv \lambda_{\mu^+} - \lambda_{\mu^-} = \pm 1$, and ϕ_μ, θ_ψ are the azimuthal and polar angles of μ^+ for $\overline{\Lambda}_b^0$ (μ^- for Λ_b^0 decays) in the ψ rest frame (see Fig. 27). There are no helicity couplings in Eq. (27), since they are all equal due to conservation of C and P parities. Therefore, this coupling can be set to unity as its magnitude and phase can be absorbed into the other helicity couplings which are left free in the fit. The calculation of the ψ decay angles is analogous to that of the Λ^* decay angles described above (Eqs. (20)–(22))

$$\cos\theta_\psi = -\,\hat{p}_{\Lambda^*}^{\{\psi\}} \cdot \hat{p}_\mu^{\{\psi\}}, \tag{28}$$

$$\phi_\mu = \mathrm{atan2}\left(-(\hat{p}_{\Lambda^*}^{\{\psi\}} \times \hat{x}_0^{\{\psi\}}) \cdot \hat{p}_\mu^{\{\psi\}},\, \hat{x}_0^{\{\psi\}} \cdot \hat{p}_\mu^{\{\psi\}}\right), \tag{29}$$

with

$$\hat{x}_0^{\{\psi\}} = \hat{x}_0^{\{\Lambda^*\}} = \hat{x}_3^{\{\Lambda_b^0\}} \tag{30}$$

and $\hat{x}_3^{\{\Lambda_b^0\}}$ given by Eq. (21).

Collecting terms from the subsequent decays together, the matrix element connecting different helicity states of the initial and the final-state particles for the entire Λ^* decay chain can be written as

$$\begin{aligned}\mathcal{M}^{\Lambda^*}_{\lambda_{\Lambda_b^0},\,\lambda_p,\,\Delta\lambda_\mu} = &\sum_n R_{\Lambda_n^*}(m_{Kp})\, \mathcal{H}^{\Lambda_n^* \to Kp}_{\lambda_p} \sum_{\lambda_\psi} e^{i\,\lambda_\psi \phi_\mu}\; d^1_{\lambda_\psi,\Delta\lambda_\mu}(\theta_\psi) \\ &\times \sum_{\lambda_{\Lambda^*}} \mathcal{H}^{\Lambda_b^0 \to \Lambda_n^* \psi}_{\lambda_{\Lambda^*},\,\lambda_\psi}\; e^{i\,\lambda_{\Lambda^*}\phi_K}\; d^{\frac{1}{2}}_{\lambda_{\Lambda_b^0},\,\lambda_{\Lambda^*}-\lambda_\psi}(\theta_{\Lambda_b^0})\; d^{J_{\Lambda_n^*}}_{\lambda_{\Lambda^*},\,\lambda_p}(\theta_{\Lambda^*}).\end{aligned} \tag{31}$$

Terms with different helicities of the initial and final-state particles (λ_p, $\Delta\lambda_\mu$) must be added incoherently

$$\left|\mathcal{M}^{\Lambda^*}\right|^2 = \frac{1+\mathrm{P}^{\Lambda_b^0}}{2}\sum_{\lambda_p}\sum_{\Delta\lambda_\mu}\left|\mathcal{M}_{(\lambda_{\Lambda_b^0}=+1/2),\,\lambda_p,\,\Delta\lambda_\mu}\right|^2 + \frac{1-\mathrm{P}^{\Lambda_b^0}}{2}\sum_{\lambda_p}\sum_{\Delta\lambda_\mu}\left|\mathcal{M}_{(\lambda_{\Lambda_b^0}=-1/2),\,\lambda_p,\,\Delta\lambda_\mu}\right|^2, \tag{32}$$

where $\mathrm{P}^{\Lambda_b^0}$ is the Λ_b^0 polarization, defined as the difference of probabilities for $\lambda_{\Lambda_b^0} = +1/2$ and $-1/2$ [50]. For the given choice of quantization axis for Λ_b^0 spin, no polarization is expected ($\mathrm{P}^{\Lambda_b^0} = 0$), due to parity conservation in strong interactions which dominate Λ_b^0 production at LHCb.

5.3 Matrix element for the P_c^+ decay chain

Next, the $\Lambda_b^0 \to P_{cj}K^-$, $P_{cj} \to \psi p$ decays will be discussed, in which more than one pentaquark state is allowed, $j = 1, 2, \ldots$. Superscripts containing the P_c decay chain name without curly brackets, *e.g.* ϕ^{P_c}, will denote quantities belonging to this decay chain and should not be confused with the superscript "$\{P_c\}$" denoting the P_c^+ rest frame, *e.g.* $\phi^{\{P_c\}}$. With only a few exceptions, the Λ^* decay chain label is omitted.

The weak decay $\Lambda_b^0 \to P_{cj}K^-$ is described by the term,

$$\mathcal{H}_{\lambda_{P_c}}^{\Lambda_b^0 \to P_{cj}K}\; D^{\frac{1}{2}}_{\lambda_{\Lambda_b^0},\,\lambda_{P_c}}(\phi_{P_c}, \theta^{P_c}_{\Lambda_b^0}, 0)^*, \tag{33}$$

where $\mathcal{H}_{\lambda_{P_c}}^{\Lambda_b^0 \to P_{cj}K}$ are resonance (*i.e.* j) dependent helicity couplings. The helicity of the pentaquark state, λ_{P_c}, can only take values of $\pm\frac{1}{2}$, regardless of its spin, $J_{P_{cj}} = \frac{1}{2}, \frac{3}{2}, \ldots$. Therefore, there are two independent helicity couplings to be determined for each P_{cj} state. The above mentioned ϕ_{P_c}, $\theta^{P_c}_{\Lambda_b^0}$ symbols refer to the azimuthal and polar angles of P_c in the Λ_b^0 rest frame (see Fig. 28).

Similar to Eq. (17), the Λ_b^0 helicity angle in the P_c decay chain can be calculated as,

$$\cos\theta^{P_c}_{\Lambda_b^0} = \hat{p}_{\Lambda_b^0}^{\{\mathrm{lab}\}} \cdot \hat{p}_{P_c}^{\{\Lambda_b^0\}}. \tag{34}$$

The ϕ_{P_c} angle cannot be set to zero, since the $\hat{x}_0^{\{\Lambda_b^0\}}$ axis in the Λ_b^0 rest frame has

already been defined by the $\phi_{\Lambda^*} = 0$ convention. Analogous to Eq. (10),

$$\begin{aligned} \vec{a}_{\Lambda^* \perp z_0}^{\{\Lambda_b^0\}} &= \vec{p}_{\Lambda^*}^{\{\Lambda_b^0\}} - (\vec{p}_{\Lambda^*}^{\{\Lambda_b^0\}} \cdot \hat{p}_{\Lambda_b^0}^{\{\text{lab}\}})\, \hat{p}_{\Lambda_b^0}^{\{\text{lab}\}}, \\ \hat{x}_0^{\{\Lambda_b^0\}} &= \frac{\vec{a}_{\Lambda^* \perp z_0}^{\{\Lambda_b^0\}}}{|\, \vec{a}_{\Lambda^* \perp z_0}^{\{\Lambda_b^0\}}\,|}. \end{aligned} \tag{35}$$

The ϕ_{P_c} angle can be determined in the Λ_b^0 rest frame from

$$\phi_{P_c} = \text{atan2}\left((\hat{p}_{\Lambda_b^0}^{\{\text{lab}\}} \times \hat{x}_0^{\{\Lambda_b^0\}}) \cdot \hat{p}_{P_c}^{\{\Lambda_b^0\}},\, \hat{x}_0^{\{\Lambda_b^0\}} \cdot \hat{p}_{P_c}^{\{\Lambda_b^0\}} \right). \tag{36}$$

The strong decay $P_{cj} \to \psi p$ is described by a term

$$\mathcal{H}^{P_{cj}\to\psi p}_{\lambda_\psi^{P_c}, \lambda_p^{P_c}}\; D^{J_{P_{cj}}}_{\lambda_{P_c},\, \lambda_\psi^{P_c} - \lambda_p^{P_c}}(\phi_\psi, \theta_{P_c}, 0)^*\; R_{P_{cj}}(m_{\psi p}), \tag{37}$$

where $\phi_\psi^{P_c}, \theta_{P_c}$ are the azimuthal and polar angles of the ψ in the P_c rest frame (see Fig. 28). They are defined analogously to Eqs. (20)−(22). The $\hat{z}_0^{\{P_c\}}$ direction is defined by the boost direction from the Λ_b^0 rest frame, which coincides with the $-\vec{p}_K^{\{P_c\}}$ direction. This leads to

$$\cos\theta_{P_c} = -\hat{p}_K^{\{P_c\}} \cdot \hat{p}_\psi^{\{P_c\}}. \tag{38}$$

The azimuthal angle of the ψ can now be determined in the P_c rest frame (see Fig. 28) from

$$\phi_\psi^{P_c} = \text{atan2}\left(-(\hat{p}_K^{\{P_c\}} \times \hat{x}_0^{\{P_c\}}) \cdot \hat{p}_\psi^{\{P_c\}},\, \hat{x}_0^{\{P_c\}} \cdot \hat{p}_\psi^{\{P_c\}} \right). \tag{39}$$

In Eq. (37), the $\hat{x}_0^{\{P_c\}}$ direction is defined by the convention that was used in the Λ_b^0 rest frame. Thus, similar to Eq. (21),

$$\begin{aligned} \vec{a}_{z_0 \perp P_c}^{\{\Lambda_b^0\}} &= \hat{p}_{\Lambda_b^0}^{\{\text{lab}\}} - (\hat{p}_{\Lambda_b^0}^{\{\text{lab}\}} \cdot \hat{p}_{P_c}^{\{\Lambda_b^0\}})\, \hat{p}_{P_c}^{\{\Lambda_b^0\}}, \\ \hat{x}_0^{\{P_c\}} &= -\frac{\vec{a}_{z_0 \perp P_c}^{\{\Lambda_b^0\}}}{|\, \vec{a}_{z_0 \perp P_c}^{\{\Lambda_b^0\}}\,|}. \end{aligned} \tag{40}$$

The ψ and p helicities, $\lambda_\psi^{P_c}$ and $\lambda_p^{P_c}$, have been labeled with the P_c superscript to make it clear that the spin quantization axes are different than in the Λ^* decay chain. Since the

ψ is an intermediate particle, this has no consequences after summing (coherently) over $\lambda_\psi^{P_c} = -1, 0, +1$. The proton, however, is a final-state particle. Before the P_c terms in the matrix element can be added coherently to the Λ^* terms, the $\lambda_p^{P_c}$ states must be rotated to λ_p states (defined in the Λ^* decay chain). The proton helicity axes are different, since the proton comes from a decay of different particles in the two decay sequences, the Λ^* and P_c. The quantization axes are along the proton direction in the Λ^* and the P_c rest frames, thus antiparallel to the particles recoiling against the proton: the K^- and ψ, respectively. These directions are preserved when boosting to the proton rest frame (see Fig. 29). Thus, the polar angle between the two proton quantization axes (θ_p) can be determined from the opening angle between the K^- and ψ mesons in the p rest frame,

$$\cos\theta_p = \hat{p}_K^{\{p\}} \cdot \hat{p}_\psi^{\{p\}}. \tag{41}$$

(A similar problem is discussed in Ref. [51], where the two different χ_{c1} helicity frames in $B^0 \to K^+\pi^-\chi_{c1}$ decays, in the interference of $B^0 \to K^*\chi_{c1}$, $K^* \to K^+\pi^-$ and of $B^0 \to Z^-K^+$, $Z^- \to \chi_{c1}\pi^-$ contributions, are realigned.) The dot product above must be calculated by operating on the $\vec{p}_K^{\{p\}}$ and $\vec{p}_\psi^{\{p\}}$ vectors in the proton rest frame obtained by the same sequence of boost transformations, either according to the Λ^* or P_c decay chains, or even by a direct boost transformation from the lab frame.[9]

No azimuthal rotation is needed to align the two proton helicity frames, since the decay planes of the Λ^* and the P_c are the same (see Fig. 29). Therefore, the relation between λ_p and $\lambda_p^{P_c}$ states is

$$|\lambda_p\rangle = \sum_{\lambda_p^{P_c}} D^{J_p}_{\lambda_p^{P_c},\,\lambda_p}(0,\theta_p,0)^* |\lambda_p^{P_c}\rangle = \sum_{\lambda_p^{P_c}} d^{J_p}_{\lambda_p^{P_c},\,\lambda_p}(\theta_p) |\lambda_p^{P_c}\rangle. \tag{42}$$

[9]Numerical values of momentum vector components, (p_x, p_y, p_z), depend on the boost sequence taken and are related between different boosts via the rotation matrix. However, the dot product between the two vectors remains independent of the boost sequences.

Thus, the term given by Eq. (37) must be preceded by

$$\sum_{\lambda_p^{P_c}=\pm\frac{1}{2}} d^{\,J_p}_{\lambda_p^{P_c},\,\lambda_p}(\theta_p). \tag{43}$$

Parity conservation in $P_{cj} \to \psi p$ decays leads to the following relation

$$\begin{aligned}\mathcal{H}^{P_{cj}\to\psi p}_{-\lambda_\psi^{P_c},-\lambda_p^{P_c}} &= P_\psi\, P_p\, P_{P_{cj}}\,(-1)^{J_\psi+J_p-J_{P_{cj}}}\,\mathcal{H}^{P_{cj}\to\psi p}_{\lambda_\psi^{P_c},\,\lambda_p^{P_c}} \\ &= P_{P_{cj}}\,(-1)^{\frac{1}{2}-J_{P_{cj}}}\,\mathcal{H}^{P_{cj}\to\psi p}_{\lambda_\psi^{P_c},\,\lambda_p^{P_c}},\end{aligned} \tag{44}$$

where $P_{P_{cj}}$ is the parity of the P_{cj} state. This relation reduces the number of independent helicity couplings to be determined from the data to 2 for $J_{P_{cj}} = \frac{1}{2}$ and 3 for $J_{P_{cj}} \geq \frac{3}{2}$. Since the helicity couplings enter the matrix element formula as a product, $\mathcal{H}^{\Lambda_b^0\to P_{cj}K}_{\lambda_{P_c}}\,\mathcal{H}^{P_{cj}\to\psi p}_{\lambda_\psi^{P_c},\,\lambda_p^{P_c}}$, the relative magnitude and phase of these two sets must be fixed by a convention. For example, $\mathcal{H}^{\Lambda_b^0\to P_{cj}K}_{\lambda_{P_c}=-\frac{1}{2}}$ can be set to $(1,0)$ for every P_{cj} resonance, in which case $\mathcal{H}^{\Lambda_b^0\to P_{cj}K}_{\lambda_{P_c}=+\frac{1}{2}}$ develops a meaning of the complex ratio of $\mathcal{H}^{\Lambda_b^0\to P_{cj}K}_{\lambda_{P_c}=+\frac{1}{2}}/\mathcal{H}^{\Lambda_b^0\to P_{cj}K}_{\lambda_{P_c}=-\frac{1}{2}}$, while all $\mathcal{H}^{P_{cj}\to\psi p}_{\lambda_\psi^{P_c},\,\lambda_p^{P_c}}$ couplings should have both real and imaginary parts free in the fit.

The term $R_{P_{cj}}(m_{\psi p})$ describes the ψp invariant mass distribution of the P_{cj} resonance and is given by Eq. (23) after appropriate substitutions as

$$R_{P_{cj}}(m_{\psi p}) = B'_{L^{P_{cj}}_{\Lambda_b^0}}(p,p_0,d)\left(\frac{p}{M_{\Lambda_b^0}}\right)^{L^{P_{cj}}_{\Lambda_b^0}}\mathrm{BW}(m_{\psi p}|M_0^{P_{cj}},\Gamma_0^{P_{cj}})\,B'_{L_{P_{cj}}}(q,q_0,d)\left(\frac{q}{M_0^{P_{cj}}}\right)^{L_{P_{cj}}}. \tag{45}$$

Angular momentum conservation limits $L^{P_{cj}}_{\Lambda_b^0}$ in $\Lambda_b^0 \to P_{cj}K^-$ decays to $J_{P_{cj}} \pm \frac{1}{2}$. The angular momentum conservation also imposes $\max(J_{P_{cj}} - \frac{3}{2}\,,\,0) \leq L_{P_{cj}} \leq J_{P_{cj}} + \frac{3}{2}$, which is further restricted by the parity conservation in the P_{cj} decays, $P_{P_{cj}} = (-1)^{L_{P_{cj}}+1}$. The minimal values of $L^{P_{cj}}_{\Lambda_b^0}$ and $L_{P_{cj}}$ are assumed in $R_{P_{cj}}(m_{\psi p})$.

The electromagnetic decay $\psi \to \mu^+\mu^-$ in the P_c decay chain contributes a term

$$D^{\,1}_{\lambda_\psi^{P_c},\,\Delta\lambda_\mu^{P_c}}(\phi_\mu^{P_c},\theta_\psi^{P_c},0)^*, \tag{46}$$

which is the same as Eq. (27), except that since the ψ meson comes from the decay of

different particles in the two decay chains, the azimuthal and polar angle of the muon in the ψ rest frame, $\phi_\mu^{P_c}$, $\theta_\psi^{P_c}$, are different from ϕ_μ, θ_ψ introduced in the Λ^* decay chain. The ψ helicity axis is along the boost direction from the P_c to the ψ rest frames, which is given by

$$\hat{z}_0^{\{\psi\}\ P_c} = -\hat{p}_p^{\{\psi\}}, \tag{47}$$

and so

$$\cos\theta_\psi^{P_c} = -\hat{p}_p^{\{\psi\}} \cdot \hat{p}_\mu^{\{\psi\}}. \tag{48}$$

The x axis is inherited from the P_c rest frame (Eq. (11)),

$$\begin{aligned} \vec{a}_{z_0\perp\psi}^{\{P_c\}} &= -\vec{p}_K^{\{P_c\}} + (\vec{p}_K^{\{P_c\}} \cdot \hat{p}_\psi^{\{P_c\}})\, \hat{p}_\psi^{\{P_c\}} \\ \hat{x}_0^{\{\psi\}\ P_c} = \hat{x}_3^{\{P_c\}} &= -\frac{\vec{a}_{z_0\perp\psi}^{\{P_c\}}}{|\,\vec{a}_{z_0\perp\psi}^{\{P_c\}}\,|}, \end{aligned} \tag{49}$$

which leads to

$$\phi_\mu^{P_c} = \mathrm{atan2}\left(-(\hat{p}_p^{\{\psi\}} \times \hat{x}_0^{\{\psi\}\ P_c}) \cdot \hat{p}_\mu^{\{\psi\}},\ \hat{x}_0^{\{\psi\}\ P_c} \cdot \hat{p}_\mu^{\{\psi\}}\right). \tag{50}$$

Since the muons are final-state particles, their helicity states in the P_c decay chain, $|\lambda_\mu^{P_c}\rangle$, need to be rotated to the muon helicity states in the Λ^* decay chain, $|\lambda_\mu\rangle$, before the P_c matrix element terms can be coherently added to the Λ^* matrix element terms. The situation is simpler than for the rotation of the proton helicities discussed above, as the muons come from the ψ decay in both decay chains. This makes the polar angle θ_μ (analogous to θ_p in Eq. (43)) equal to zero, which leads to $d^{\frac{1}{2}}_{\lambda_\mu^{P_c},\,\lambda_\mu}(0) = \delta_{\lambda_\mu^{P_c},\,\lambda_\mu}$, where $\delta_{i,j}$ is the Kronecker symbol. However, the muon helicity states are not identical since the x axes are offset by the azimuthal angle α_μ. Since the boost to the μ rest frame is the same for both decay chains (*i.e.* always from the ψ rest frame), α_μ can be determined in the ψ rest frame

$$\alpha_\mu = \mathrm{atan2}\left((\hat{z}_3^{\{\psi\}} \times \hat{x}_3^{\{\psi\}\ P_c}) \cdot \hat{x}_3^{\{\psi\}\ \Lambda^*},\ \hat{x}_3^{\{\psi\}\ P_c} \cdot \hat{x}_3^{\{\psi\}\ \Lambda^*}\right), \tag{51}$$

where $\hat{z}_3^{\{\psi\}} = \hat{p}_\mu^{\{\psi\}}$, and from Eq. (11)

$$\hat{x}_3^{\{\psi\}\ P_c} = -\,\hat{a}_{z_0\perp\mu}^{\{\psi\}\ P_c}, \tag{52}$$

$$\vec{a}_{z_0\perp\mu}^{\{\psi\}\ P_c} = -\,\hat{p}_p^{\{\psi\}} + (\hat{p}_p^{\{\psi\}}\cdot\hat{p}_\mu^{\{\psi\}})\,\hat{p}_\mu^{\{\psi\}}, \tag{53}$$

as well as

$$\hat{x}_3^{\{\psi\}\ \Lambda^*} = -\,\hat{a}_{z_0\perp\mu}^{\{\psi\}\ \Lambda^*}, \tag{54}$$

$$\vec{a}_{z_0\perp\mu}^{\{\psi\}\ \Lambda^*} = -\,\hat{p}_{\Lambda^*}^{\{\psi\}} + (\hat{p}_{\Lambda^*}^{\{\psi\}}\cdot\hat{p}_\mu^{\{\psi\}})\,\hat{p}_\mu^{\{\psi\}}. \tag{55}$$

The term aligning the muon helicity states between the two reference frames is given by

$$\sum_{\lambda_\mu^{P_c}} D^{\,J_\mu}_{\lambda_\mu^{P_c}\,\lambda_\mu}(\alpha_\mu,0,0)^* = \sum_{\lambda_\mu^{P_c}} e^{i\,\lambda_\mu^{P_c}\alpha_\mu}\delta_{\lambda_\mu^{P_c},\,\lambda_\mu} = e^{i\,\lambda_\mu\alpha_\mu}. \tag{56}$$

The transformation of μ^- states will be similar to that of the μ^+ states, except that since $\hat{z}_\psi$ will have the opposite direction, $\alpha_{\mu^+} = -\alpha_{\mu^-}$. The transformation of $|\lambda_{\mu^+}^{P_c}\rangle|\lambda_{\mu^-}^{P_c}\rangle$ to $|\lambda_{\mu^+}\rangle|\lambda_{\mu^-}\rangle$ states will require multiplying the terms for the P_c decay chain by

$$e^{i\,\lambda_\mu\alpha_\mu}e^{i\,\lambda_{\bar{\mu}}\alpha_{\bar{\mu}}} = e^{i\,(\lambda_\mu-\lambda_{\bar{\mu}})\alpha_\mu} = e^{i\,\Delta\lambda_\mu\alpha_\mu}. \tag{57}$$

An alternative derivation of Eq. (57) is discussed in Ref. [18] (Eqs. (20)−(22) therein) for the interference of $B^0\to K^*\psi$, $K^*\to K\pi$ and of $B^0\to ZK^-$, $Z\to\psi\pi$ ($\psi\to\ell^+\ell^-$) terms, which are analogous to the two decay chains discussed here with the substitution $B^0\to\Lambda_b^0$, $K^*\to\Lambda^*$, $Z\to P_c$ and $\pi\to p$. The rotation by α_μ about the ℓ^+ direction in the ψ rest frame in the Z decay chain is incorporated by setting $\gamma=\alpha_\mu$, instead of $\gamma=0$ in Eq. (46). This leads to the same formulae since

$$D^{\,1}_{\lambda_\psi^{P_c},\,\Delta\lambda_\mu}(\phi_\mu^{P_c},\theta_\psi^{P_c},\alpha_\mu)^* = D^{\,1}_{\lambda_\psi^{P_c},\,\Delta\lambda_\mu}(\phi_\mu^{P_c},\theta_\psi^{P_c},0)^*\,e^{i\,\Delta\lambda_\mu\alpha_\mu}. \tag{58}$$

The more generic derivation is used here to demonstrate that the methods of transforming

the muon and proton helicity states between the two decay chains are the same.

Collecting terms from the three subsequent decays in the P_c chain together,

$$\mathcal{M}^{P_c}_{\lambda_{\Lambda_b^0},\lambda_p^{P_c},\Delta\lambda_\mu^{P_c}} = e^{i\,\lambda_{\Lambda_b^0}\phi_{P_c}} \sum_j R_{P_cj}(M_{\psi p}) \sum_{\lambda_\psi^{P_c}} e^{i\,\lambda_\psi^{P_c}\phi_\mu^{P_c}}\; d^{\,1}_{\lambda_\psi^{P_c},\,\Delta\lambda_\mu}(\theta_\psi^{P_c}) \times \sum_{\lambda_{P_c}} \mathcal{H}^{\Lambda_b^0\to P_cjK}_{\lambda_{P_c}}\; e^{i\,\lambda_{P_c}\phi_\psi^{P_c}}\; d^{\,\frac{1}{2}}_{\lambda_{\Lambda_b^0},\lambda_{P_c}}(\theta^{P_c}_{\Lambda_b^0}) \mathcal{H}^{P_{cj}\to\psi p}_{\lambda_\psi^{P_c},\lambda_p^{P_c}}\; d^{\,J_{P_cj}}_{\lambda_{P_c},\lambda_\psi^{P_c}-\lambda_p^{P_c}}(\theta_{P_c}), \tag{59}$$

and adding them coherently to the Λ^* matrix element, via appropriate relation of $|\lambda_p\rangle|\lambda_{\mu^+}\rangle|\lambda_{\mu^-}\rangle$ to $|\lambda_p^{P_c}\rangle|\lambda_{\mu^+}^{P_c}\rangle|\lambda_{\mu^-}^{P_c}\rangle$ states as discussed above, leads to the final matrix element squared

$$|\mathcal{M}|^2 = \sum_{\lambda_{\Lambda_b^0}=\pm\frac{1}{2}} \sum_{\lambda_p=\pm\frac{1}{2}} \sum_{\Delta\lambda_\mu=\pm1} \left| \mathcal{M}^{\Lambda^*}_{\lambda_{\Lambda_b^0},\lambda_p,\Delta\lambda_\mu} + e^{i\,\Delta\lambda_\mu\alpha_\mu} \sum_{\lambda_p^{P_c}} d^{\,\frac{1}{2}}_{\lambda_p^{P_c},\lambda_p}(\theta_p)\, \mathcal{M}^{P_c}_{\lambda_{\Lambda_b^0},\lambda_p^{P_c},\Delta\lambda_\mu} \right|^2, \tag{60}$$

where $\mathrm{P}^{\Lambda_b^0} = 0$ is set. As a cross-check, fitting the Λ_b^0 polarization to the data with the default Λ^* and P_c^+ model yields a value consistent with zero, $\mathrm{P}^{\Lambda_b^0} = (-2.0 \pm 2.3)\%$ (statistical error only).

Assuming approximate *CP* symmetry, the helicity couplings for Λ_b^0 and $\overline{\Lambda}_b^0$ can be made equal, but the calculation of the angles requires some care, since parity (P) conservation does not change polar (i.e. helicity) angles, but does change azimuthal angles. Thus, not only must $\vec{p}_{\mu^+}$ be used instead of $\vec{p}_{\mu^-}$ for $\overline{\Lambda}_b^0$ candidates (with K^+ and $\bar{p}$ in the final-state) in Eqs. (28), (29), (48), (50) and (51), but also all azimuthal angles must be reflected before entering the matrix element formula: $\phi_K \to -\phi_K$, $\phi_\mu \to -\phi_\mu$, $\phi_{P_c} \to -\phi_{P_c}$, $\phi_\psi^{P_c} \to -\phi_\psi^{P_c}$, $\phi_\mu^{P_c} \to -\phi_\mu^{P_c}$ and $\alpha_\mu \to -\alpha_\mu$ [18].

It is clear from Eq. (60) that various Λ_n^* and P_c resonances interfere in the differential distributions. By integrating the matrix element squared over the entire phase space the interferences cancel in the integrated rates unless the resonances belong to the same decay chain and have the same quantum numbers.[10]

[10]For $\Lambda_n^* - P_c$, the $\lambda_{\Lambda_b^0} = +1/2$ interference terms have the opposite effect to the $\lambda_{\Lambda_b^0} = -1/2$ interference terms.

5.4 Reduction of the number of helicity couplings

A possible reduction of the helicity couplings can be achieved by relating them to the LS couplings ($B_{L,S}$) using Clebsch-Gordan coefficients

$$\mathcal{H}^{A\to BC}_{\lambda_B,\lambda_C} = \sum_L \sum_S \sqrt{\tfrac{2L+1}{2J_A+1}} B_{L,S} \left(\begin{array}{cc|c} J_B & J_C & S \\ \lambda_B & -\lambda_C & \lambda_B - \lambda_C \end{array} \right) \times \left(\begin{array}{cc|c} L & S & J_A \\ 0 & \lambda_B - \lambda_C & \lambda_B - \lambda_C \end{array} \right), \tag{61}$$

and then restricting the L values. Here L is the orbital angular momentum in the decay, and S is the total spin of the daughters, $\vec{S} = \vec{J}_B + \vec{J}_C$ ($|J_B - J_C| \leq S \leq J_B + J_C$). If the energy release in the decay, $Q = M_A - M_B - M_C$, is small, $Q/M_A \ll 1$, then higher values of L should be suppressed; this effect is usually called "the angular momentum barrier." Applying this approach to $\Lambda_b^0 \to \psi\Lambda_n^*$ decays, the lowest $L^{\Lambda_n^*}_{\Lambda_b^0}$ value ($L_{\min}$) corresponds to a single possible value of S, thus reducing the number of couplings to fit, from 4 ($J_{\Lambda_n^*} = \frac{1}{2}$) or 6 ($J_{\Lambda_n^*} \geq \frac{3}{2}$), to just one $B_{L,S}$ coupling per resonance. Accepting also $L_{\min}+1$ values, gives three $B_{L,S}$ couplings to fit per resonance.

In $\Lambda_b^0 \to P_{cj}K^-$ decays, $S = J_{P_{cj}}$ and $L^{P_{cj}}_{\Lambda_b^0} = J_{P_{cj}} \pm \frac{1}{2}$. Taking only the lower $L^{P_{cj}}_{\Lambda_b^0}$ value reduces the number of couplings from 2 to 1. Since its magnitude and phase convention can be absorbed into $\mathcal{H}^{P_{cj}\to\psi p}_{\lambda_\psi^{P_c},\lambda_p^{P_c}}$ (see the discussion in Sec. 5.3), one can simply set $B^{\Lambda_b^0\to P_{cj}K}_{J_{P_{cj}}-\frac{1}{2},J_{P_{cj}}} = (1,0)$ in this approach.

The reduction of couplings to fit for $P_{cj} \to \psi p$ decays depends on the spin and parity of the P_{cj} state. S can take values of $\frac{1}{2}$ and $\frac{3}{2}$. Values of $L_{P_{cj}}$ must be odd (even) for even (odd) $P_{P_{cj}}$. For a $J^P_{P_{cj}} = \frac{1}{2}^+$ state, only $L_{P_{cj}} = 1$ is allowed with the two possible values of S. Therefore, no reduction of couplings is possible. For a $J^P_{P_{cj}} = \frac{1}{2}^-$ state, $L_{P_{cj}} = 0, 2$ are allowed, each corresponding to one S value. Therefore, the number of couplings to fit can be reduced from 2 to 1 when taking $L_{P_{cj}} = 0$. Gains can be larger for $J_{P_{cj}} \geq \frac{3}{2}$ states.

Even if no reduction in parameters is achieved, expressing the helicity couplings via corresponding $B_{L,S}$ couplings using Eq. (61) is useful, since it automatically implements the parity constraints (Eq. (44)) by restricting possible L values. Since the overall mag-

nitude of the matrix element does not affect the normalized signal $\mathcal{PDF}$, and because its overall phase also drops out when taking its modulus, the magnitude and phase convention are fixed by setting $B_{0,\frac{1}{2}}^{\Lambda_b^0 \to \Lambda(1520) J/\psi} = (1, 0)$.

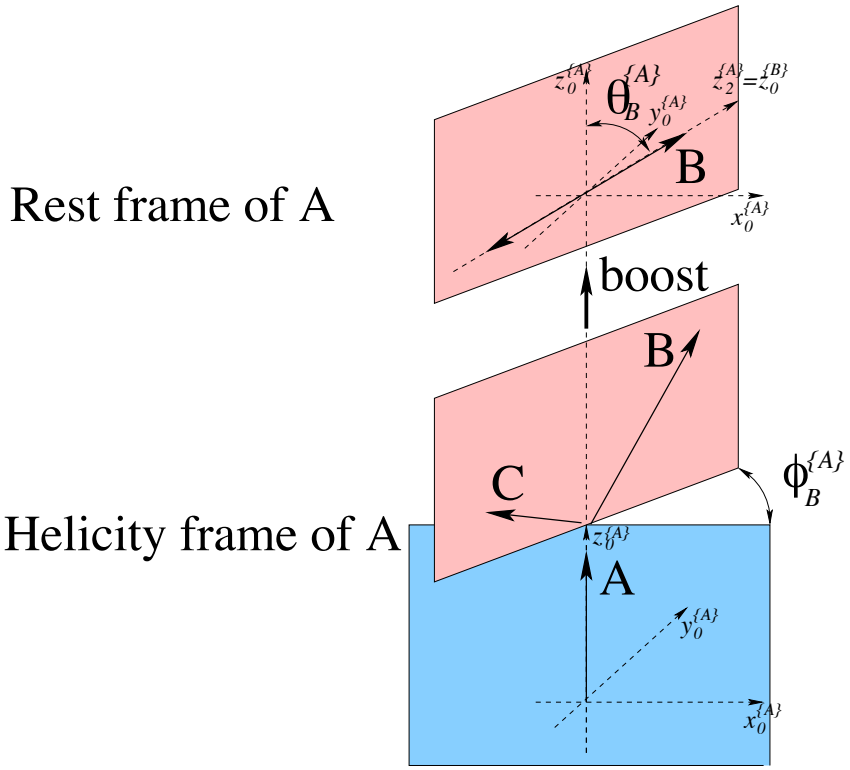

Figure 26: Coordinate axes for the spin quantization of particle A (bottom part), chosen to be the helicity frame of A ($\hat{z}_0 || \vec{p}_A$ in the rest frame of its mother particle or in the laboratory frame), together with the polar ($\theta_B^{\{A\}}$) and azimuthal ($\phi_B^{\{A\}}$) angles of the momentum of its daughter B in the A rest frame (top part). Notice that the directions of these coordinate axes, denoted as $\hat{x}_0^{\{A\}}$, $\hat{y}_0^{\{A\}}$, and $\hat{z}_0^{\{A\}}$, do not change when boosting from the helicity frame of A to its rest frame. After the Euler rotation $\mathcal{R}(\alpha = \phi_B^{\{A\}}, \beta = \theta_B^{\{A\}}, \gamma = 0)$ (see the text), the rotated z axis, $\hat{z}_2^{\{A\}}$, is aligned with the B momentum; thus the rotated coordinates become the helicity frame of B. If B has a sequential decay, then the same boost-rotation process is repeated to define the helicity frame for its daughters.

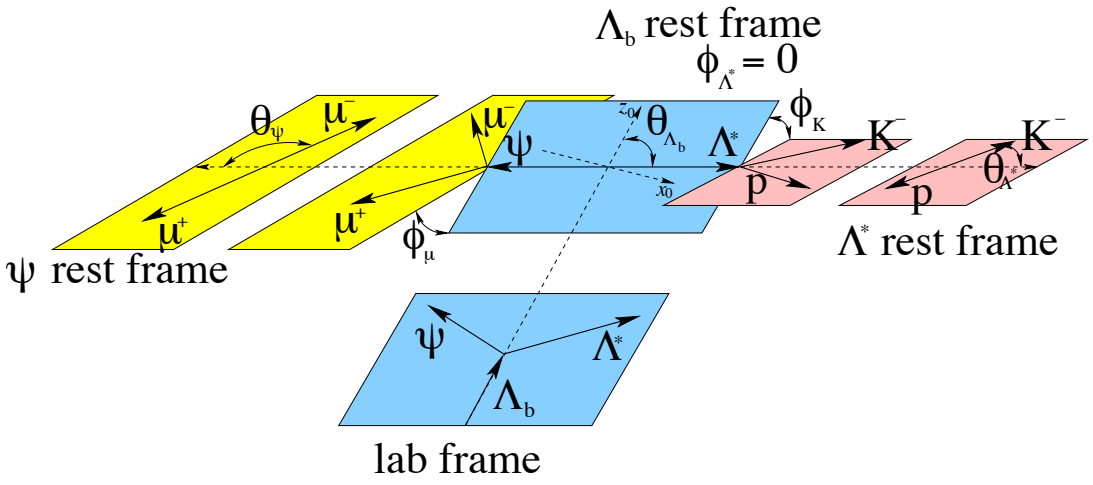

Figure 27: Definition of the decay angles in the Λ^* decay chain.

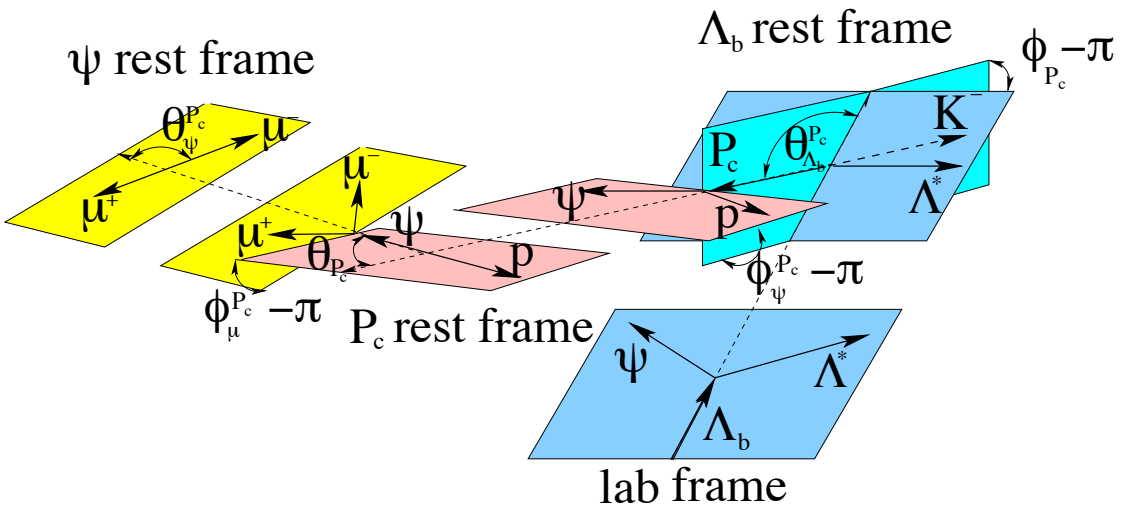

Figure 28: Definition of the decay angles in the P_c^+ decay chain.

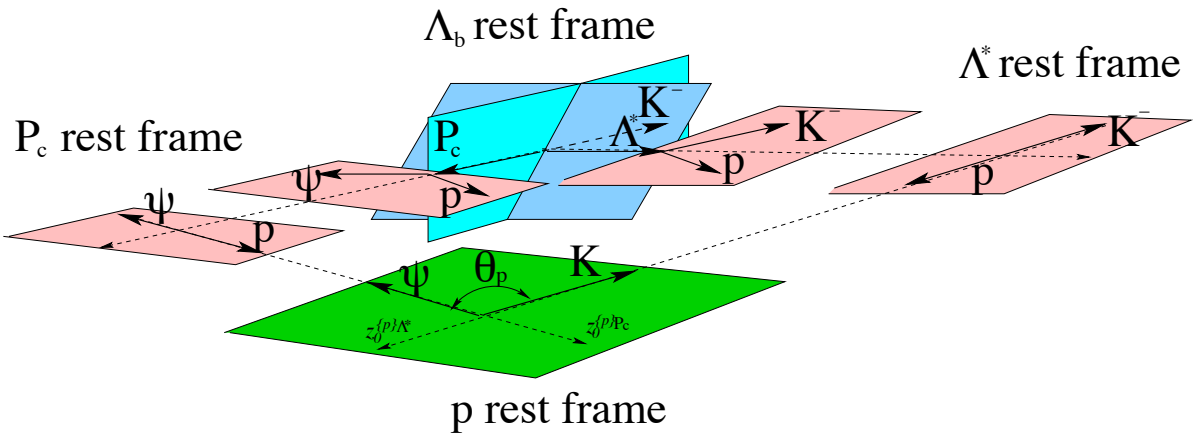

Figure 29: Definition of the θ_p angle.

6 Fitting techniques

In this section the formulation of the probability density function ($\mathcal{PDF}$) which is fit to the data is discussed. The $\mathcal{PDF}$, $\mathcal{P}$, is a function of the 6 independent variables which were introduced in the calculation of the matrix element: m_{Kp}, and the angular variables in the Λ^* decay chain $\cos\theta_{\Lambda_b^0}$, $\cos\theta_\Lambda$, $\cos\theta_{J/\psi}$, ϕ_K, and ϕ_μ. For brevity, the angular variables will be collectively denoted by Ω. Recall that the variables in the P_c decay chain are not independent, and can be calculated from the Λ^* decay chain. The $\mathcal{PDF}$ also depends on the fit parameters, $\overrightarrow{\omega}$, which generally include couplings and the masses and widths of resonances. An unbinned maximum likelihood fit of these parameters to the 6D data is performed by minimizing

$$-2\ln\mathcal{L}(\overrightarrow{\omega}) = -2\ln\sum_i \mathcal{P}(m_{Kp\ i}, \Omega_i|\overrightarrow{\omega}) \tag{62}$$

with respect to $\overrightarrow{\omega}$.

While the background contribution is quite small, it must still be accounted for in the minimization. There are two different methods for this which were implemented, and which lead to different definitions of $\mathcal{P}$ and $-2\ln\mathcal{L}(\overrightarrow{\omega})$. The first is *cFit*, which explicitly contains a background term in $\mathcal{P}$. The second is *sFit*, which uses event weights to statistically subtract the background from the likelihood calculation. These will be discussed in turn, after first discussing the signal $\mathcal{PDF}$. Two different procedures are used in order to provide a cross-check on the background subtraction method.

6.1 The signal $\mathcal{PDF}$

The signal $\mathcal{PDF}$ is the same in both the *cFit* and *sFit* method, and is written as

$$\mathcal{P}_{\rm sig}(m_{Kp}, \Omega|\overrightarrow{\omega}) \equiv \frac{1}{I(\overrightarrow{w})}\left|\mathcal{M}(m_{Kp}, \Omega|\overrightarrow{\omega})\right|^2 \Phi(m_{Kp})\epsilon(m_{Kp}, \Omega), \tag{63}$$

where $\mathcal{M}(m_{Kp}, \Omega|\overrightarrow{\omega})$ is the matrix element, $\Phi(m_{Kp}) = p\,q$ is the phase space function[11], $\epsilon(m_{Kp}, \Omega)$ is the efficiency, and $I(\overrightarrow{w})$ is the normalization integral. The $\Phi(m_{Kp})$ factor is included to account for working with the "rectangular Dalitz plane" variables $(m_{Kp}, \cos\theta_\Lambda)$, rather than the standard $(m^2_{Kp}, m^2_{J/\psi p})$. In particular, a weight of $\Phi(m_{Kp})$ will take a distribution which is uniform in $(m_{Kp}, \cos\theta_\Lambda)$ and make it uniform in $(m^2_{Kp}, m^2_{J/\psi p})$. The efficiency $\epsilon(m_{Kp\ i}, \Omega_i)$ includes all reconstruction and selection effects, and will be discussed later. The integral $I(\overrightarrow{\omega})$ is calculated via Monte Carlo integration, using the MC sample which was generated uniformly in phase space and then passed through the detector simulation and data selection. In particular, it is calculated as

$$I(\overrightarrow{\omega}) \equiv \int \mathcal{P}^u_{\rm sig}(m_{Kp}, \Omega)\, dm_{Kp}\, d\Omega \propto \frac{\Sigma_j w^{\rm MC}_j \left|\mathcal{M}(m_{Kp\ j}, \Omega_j|\overrightarrow{\omega})\right|^2}{\Sigma_j w^{\rm MC}_j}, \tag{64}$$

where $\mathcal{P}^u_{\rm sig}(m_{Kp}, \Omega|\overrightarrow{\omega}) = \left|\mathcal{M}(m_{Kp}, \Omega|\overrightarrow{\omega})\right|^2 \Phi(m_{Kp})\epsilon(m_{Kp}, \Omega)$, and $w^{\rm MC}_j$ are the correction weights described in Appendix B.

6.2 Description of *cFit* procedure

In the cFit method, only the $m_{J/\psi pK}$ region with a high density of signal events is fitted. This range is referred to as the **signal range**, and consists of the $N_{\rm signal-band} = 27469$ events lying within two units of the Λ^0_b signal peak mass resolution, *i.e.* $M_0 \pm 2\sigma$. The fit to $m_{J/\psi pK}$ is displayed again in Fig. 30 along with the signal range definition. The **sidebands** are also shown, and are defined as events lying 5σ away from the signal peak, and within the selected range of 4580 MeV to 5760 MeV. The 10259 events in the sideband are used to form a background $\mathcal{PDF}$, $\mathcal{P}_{\rm bkg}(m_{Kp\ i}, \Omega_i)$, which is combined with $\mathcal{P}_{\rm sig}(m_{Kp\ i}, \Omega_i|\overrightarrow{\omega})$ to form the total $\mathcal{PDF}$ as

$$\mathcal{P} = (1-\beta)\,\mathcal{P}_{\rm sig}(m_{Kp\ i}, \Omega_i|\overrightarrow{\omega}) + \beta\,\mathcal{P}_{\rm bkg}(m_{Kp\ i}, \Omega_i) \tag{65}$$

[11] As in Sec. 5, p is the momentum of the K^-p system (i.e. Λ^*) in the Λ^0_b rest frame, and q is the the momentum of K in the Λ^* rest frame.

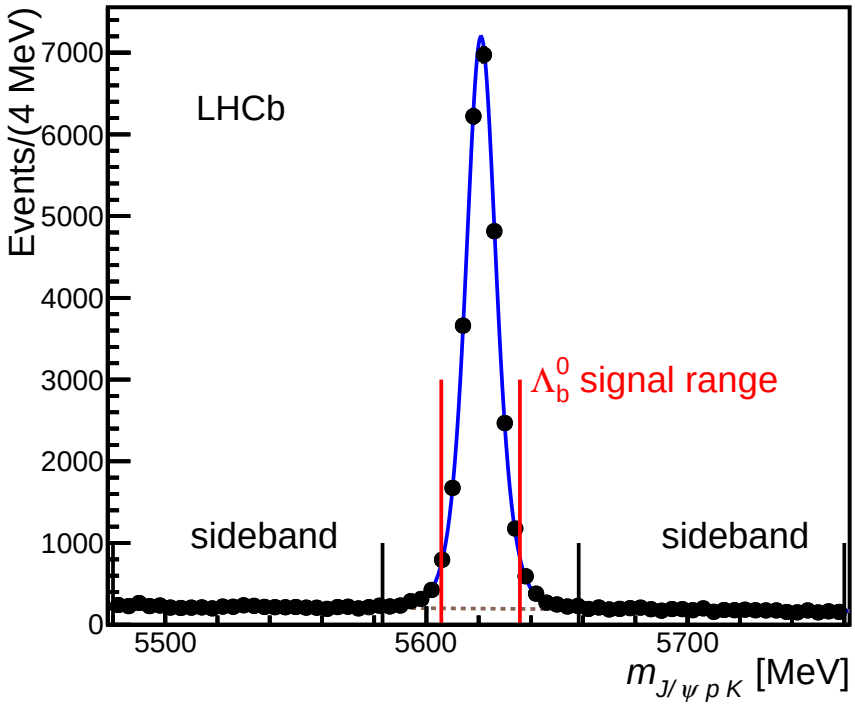

Figure 30: The invariant mass spectrum of $J/\psi pK^-$ combinations, shown with the signal range and sideband definitions.

with the integrated background probability set to $\beta = 5.4\%$, as determined from the fit to the $J/\psi K^- p$ mass distribution shown in Fig 30. Thus the log-likelihood which is minimized becomes

$$
\begin{aligned}
-\ln L(\overrightarrow{\omega}) &= -\Sigma_i \ln\left[(1-\beta)\,\mathcal{P}_{\rm sig}(m_{Kp\ i},\Omega_i|\overrightarrow{\omega}) + \beta\,\mathcal{P}_{\rm bkg}(m_{Kp\ i},\Omega_i)\right] \\
&= -\Sigma_i \ln\left[(1-\beta)\,\frac{|\mathcal{M}(m_{Kp\ i},\Omega_i|\overrightarrow{\omega})|^2\,\Phi(m_{Kp\ i})\epsilon(m_{Kp\ i},\Omega_i)}{I(\overrightarrow{\omega})} + \beta\,\frac{\mathcal{P}^u_{\rm bkg}(m_{Kp\ i},\Omega_i)}{I_{\rm bkg}}\right] \\
&= -\Sigma_i \ln\left\{\frac{(1-\beta)\,\Phi(m_{Kp\ i})\epsilon(m_{Kp\ i},\Omega_i)}{I(\overrightarrow{\omega})}\left[|\mathcal{M}(m_{Kp\ i},\Omega_i|\overrightarrow{\omega})|^2\right.\right. \\
&\qquad\left.\left. + \frac{\beta\,I(\overrightarrow{\omega})}{(1-\beta)\,I_{\rm bkg}}\,\frac{\mathcal{P}^u_{\rm bkg}(m_{Kp\ i},\Omega_i)}{\Phi(m_{Kp\ i})\epsilon(m_{Kp\ i},\Omega_i)}\right]\right\} \\
&= -\Sigma_i \ln\left[|\mathcal{M}(m_{Kp\ i},\Omega_i|\overrightarrow{\omega})|^2 + \frac{\beta\,I(\overrightarrow{\omega})}{(1-\beta)I_{\rm bkg}}\,\frac{\mathcal{P}^u_{\rm bkg}(m_{Kp\ i},\Omega_i)}{\Phi(m_{Kp\ i})\epsilon(m_{Kp\ i},\Omega_i)}\right] \\
&\qquad + N\ln I(\overrightarrow{\omega}) + \text{constant}, \qquad (66)
\end{aligned}
$$

where $\mathcal{P}^u_{\rm bkg}(m_{Kp},\Omega)$ is the unnormalized background density and $I_{\rm bkg}$ is its normalization integral. As the constant term does not affect the minimization, it can be dropped.

Thus, in formulating the log-likelihood in this way, the efficiency factor $\epsilon(m_{Kp\ i}, \Omega_i)$ only appears in the background term, which constitutes a small fraction of the overall $\mathcal{PDF}$. This is desirable, as it makes the minimization less prone to deficiencies in the efficiency parametrization. The same MC set used to evaluate $I(\overrightarrow{\omega})$ is also used to calculate $I_{\rm bkg}$ as [12]

$$I_{\rm bkg} \equiv \int \mathcal{P}^u_{\rm bkg}(m_{Kp})\, dm_{Kp}\, d\Omega \;\propto\; \Sigma_j w_j^{\rm MC} \frac{\mathcal{P}^u_{\rm bkg}(m_{Kp\ j}, \Omega_j)}{\Phi(m_{Kp\ i})\epsilon(m_{Kp\ j}, \Omega_j)} \,/\, \Sigma_j w_j^{\rm MC}. \qquad (67)$$

The construction of $\mathcal{P}^u_{\rm bkg}(m_{Kp\ i}, \Omega_i)$ closely follows that of the efficiency parametrization $\epsilon(m_{Kp\ i}, \Omega_i)$, which will be discussed now, followed by $\mathcal{P}^u_{\rm bkg}(m_{Kp\ i}, \Omega_i)$. It is assumed that $\epsilon(m_{Kp\ i}, \Omega_i)$ factorizes as

$$\epsilon(m_{Kp}, \Omega) = \epsilon_1(m_{Kp}, \cos\theta_\Lambda) \times \epsilon_2(\cos\theta_{\Lambda^0_b} | m_{Kp}) \times \epsilon_3(\cos\theta_{J/\psi} | m_{Kp}) \times \epsilon_4(\phi_K | m_{Kp}) \times \epsilon_5(\phi_\mu | m_{Kp}). \qquad (68)$$

The fully simulated MC sample, which has encoded in it the deviations from phase space caused by reconstruction and selection effects, is used to construct this parametrization. The $\epsilon_1(m_{Kp}, \cos\theta_\Lambda)$ term is obtained by binning a two-dimensional (2D) histogram of the simulated events. Each event is given a $1/\Phi(m_{Kp})$ weight, as they were originally generated uniformly in the $(m^2_{Kp}, m^2_{J/\psi p})$ plane. The $\epsilon_1(m_{Kp}, \cos\theta_\Lambda)$ efficiency and its visualization across the normal Dalitz plane are shown in Fig. 31. The other terms are again built from 2D histograms, but with each bin divided by the number of simulated events in the corresponding m_{Kp} slice, in order to remove the dependence on this mass. Each of the other terms are shown in Fig. 32. A bi-cubic interpolation is used to interpolate between bin centers in each 2D histogram.

The background $\mathcal{PDF}$, calculated for simplicity as $\mathcal{P}^u_{\rm bkg}(m_{Kp}, \Omega)/\Phi(m_{Kp})$, is built

[12] Notice that the distribution of MC events used to calculate this includes both the $\Phi(m_{Kp})$ and $\epsilon(m_{Kp}, \Omega)$ factors, thus it is necessary to divide by $\Phi(m_{Kp})\,\epsilon(m_{Kp}, \Omega)$.

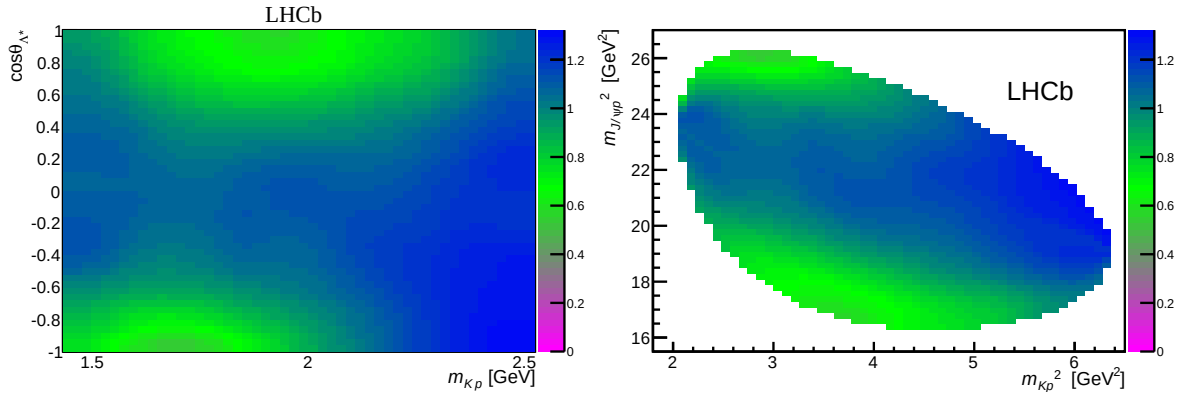

Figure 31: Parameterized dependence of the relative signal efficiency over the rectangular (left) and normal (right) Dalitz variables.

using the same approach. It is also assumed to factorize as

$$\frac{\mathcal{P}^{u}_{\rm bkg}(m_{Kp},\Omega)}{\Phi(m_{Kp})} = P_{\rm bkg_1}(m_{Kp},\cos\theta_\Lambda)\times P_{\rm bkg_2}(\cos\theta_{\Lambda^0_b}|m_{Kp})\times P_{\rm bkg_3}(\cos\theta_{J/\psi}|m_{Kp})\times$$
$$P_{\rm bkg_4}(\phi_K|m_{Kp})\times P_{\rm bkg_5}(\phi_\mu|m_{Kp}). \quad (69)$$

The 2D histograms are filled using the events from the sidebands, in the same manner as was used in the efficiency parametrization construction. Also, a bi-cubic interpolation is again used to interpolate between bin centers. The background function $P_{\rm bkg_1}(m_{Kp},\cos\theta_\Lambda)$ and its visualization across the normal Dalitz plane are shown in Fig. 33. The other terms are shown in Fig. 34.

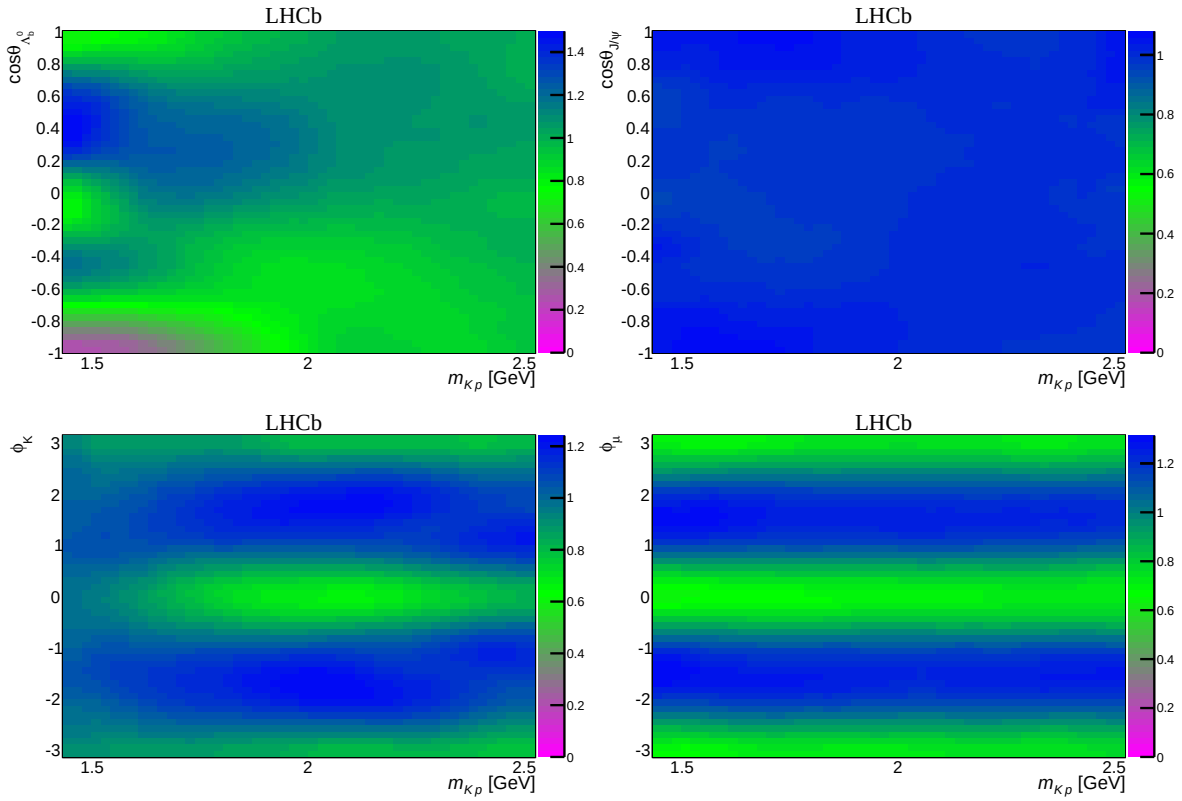

Figure 32: Parameterized dependence of the relative signal efficiency for the $\cos\theta_{\Lambda_b^0}$ (top left), $\cos\theta_{J/\psi}$ (top right), ϕ_K (bottom left), and ϕ_μ (bottom right) variables.

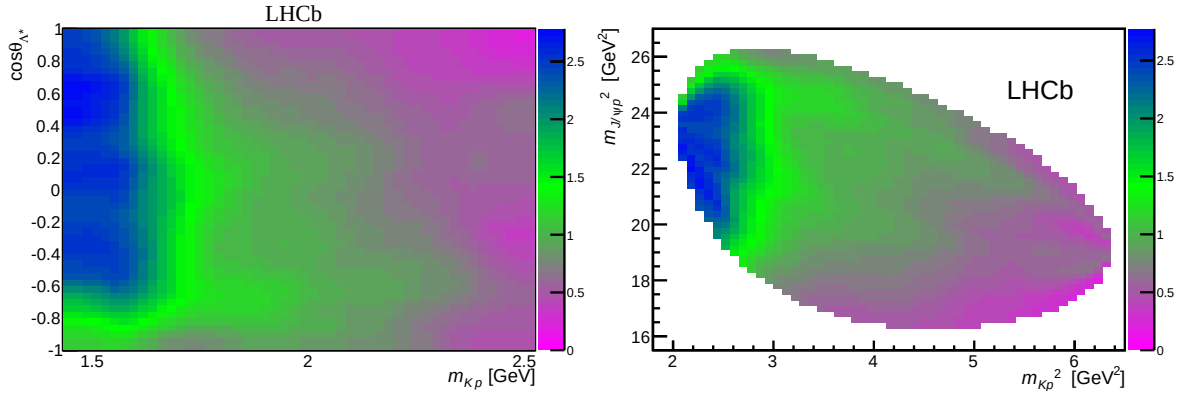

Figure 33: Parameterized dependence of the background density over the rectangular (left) and normal (right) Dalitz variables.

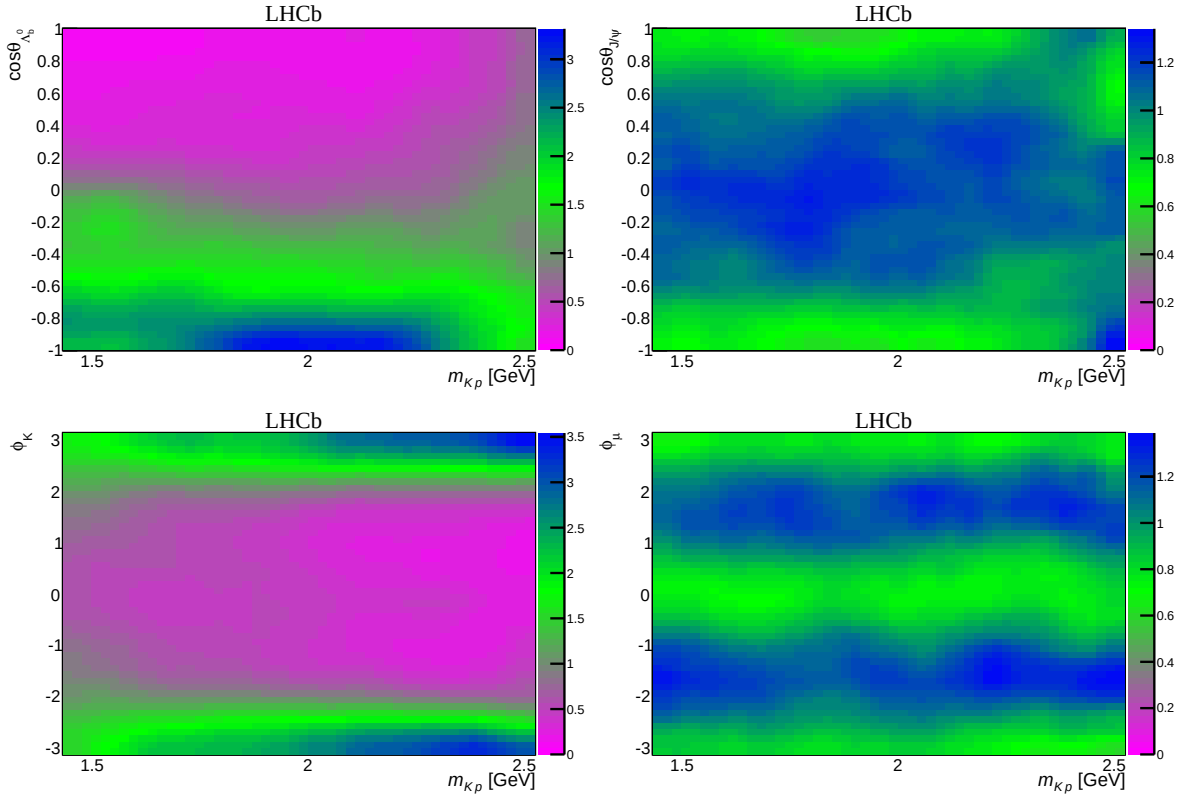

Figure 34: Parameterized dependence of the background density for the $\cos\theta_{\Lambda_b^0}$ (top left), $\cos\theta_{J/\psi}$ (top right), ϕ_K (bottom left), and ϕ_μ (bottom right) variables.

6.3 Description of sFit procedure

In the *sFit* method, the data in the entire $5480.0 - 5760.0$ MeV range is fitted. This procedure uses event weights obtained from the *sPlot* technique [47] to subtract the background from the log-likelihood sum as

$$-\ln L(\overrightarrow{w}) = -s_W \, \Sigma_i W_i \ln \mathcal{P}(m_{Kp\ i}, \Omega_i | \overrightarrow{\omega}). \tag{70}$$

Here W_i is the the "sWeight" and $s_W = \Sigma_i W_i / \Sigma_i W_i^2$ is a constant factor rescaling the log-likelihood function to take into account the statistical error due to the background subtraction. Note that since the events are weighted, strictly speaking this is not a maximum likelihood fit. The event weights are assigned via the fit to the $m_{J/\psi pK^-}$ distribution. Roughly stated, events will have weights dependent on the signal and background $\mathcal{PDF}$ values at the particular $m_{J/\psi pK}$ value. So events in the sideband region will have negative weights, which on average compensate for the background events present in the signal region, where events will have positive weights.

In this method, the total $\mathcal{PDF}$ consists of only the signal $\mathcal{PDF}$, $\mathcal{P}_{\rm sig}$. Thus the log-likelihood sum is

$$\begin{aligned} -2\ln \mathcal{L}(\overrightarrow{\omega}) =& -2s_W \sum_i W_i \ln \mathcal{P}_{\rm sig}(m_{Kp\ i}, \Omega_i | \overrightarrow{\omega}) \\ =& -2s_W \sum_i W_i \ln |\mathcal{M}(m_{Kp\ i}, \Omega_i | \overrightarrow{\omega})|^2 + 2s_W \ln I(\overrightarrow{\omega}) \sum_i W_i \\ & - \text{constant}, \end{aligned} \tag{71}$$

where the constant term can be dropped as it does not affect the minimization. As a result, the efficiency does not enter explicitly in the log-likelihood calculation. It is hidden in the normalization integral, but as that is calculated using Monte Carlo events which have the efficiency effects simulated, there is no need to use an efficiency parametrization in the *sFit* method.

A complication arises in the sWeight assignment, because the MC shows significant variations of the $m_{J/\psi pK}$ mass resolution as functions of two of the fitted variables: $\cos\theta_{\Lambda_b^0}$

and $\cos\theta_{J/\psi}$. This can be seen in Fig. 35, where $m_{J/\psi pK}$ is shown for different ranges of these angles. It can also be seen that no strong variations exist for the other angles. Thus, to more precisely determine the sWeights, the events are divided into 32 bins, corresponding to four equal divisions of $|\cos\theta_{J/\psi}|$ and eight equal divisions of $\cos\theta_{\Lambda_b^0}$. Note that as the $\cos\theta_{J/\psi}$ distributions are symmetric, the absolute value is used along with half the bins, allowing for better event statistics in each bin. The fit to the $m_{J/\psi pK}$ distribution is repeated for each bin, and the results are shown in Fig. 36. The *sPlot* procedure is then repeated for each bin in order to determine the sWeights.

6.4 Choice of Nominal Background-Handling Method

There is no clear choice of either *sFit* or *cFit* as a superior method. An advantage of *sFit* is that it does not require an efficiency or background parametrization. However, it operates under a pseudo-likelihood, as it is dealing with weighted events. The negative weights used in *sFit* can sometimes also lead to bad consequences, in which the events with negative weights can drive the likelihood. Meanwhile *cFit* operates under a true likelihood, but explicitly relies on 6D efficiency and background parametrizations.

Historically, the software for the *cFit* and *sFit* methods were developed independently of each other as a means for cross-checking the results. The motivation for the cross-checks were two-fold: to check for human error in developing these complicated fitters, and to compare the two background-handling methods. The *sFit* code was developed by Liming Zhang, and all studies which were performed with the *sFit* method were performed by him. Ultimately, the decision was made to use *cFit* for the central values of the results, and use *cFit*-*sFit* differences as a cross check.

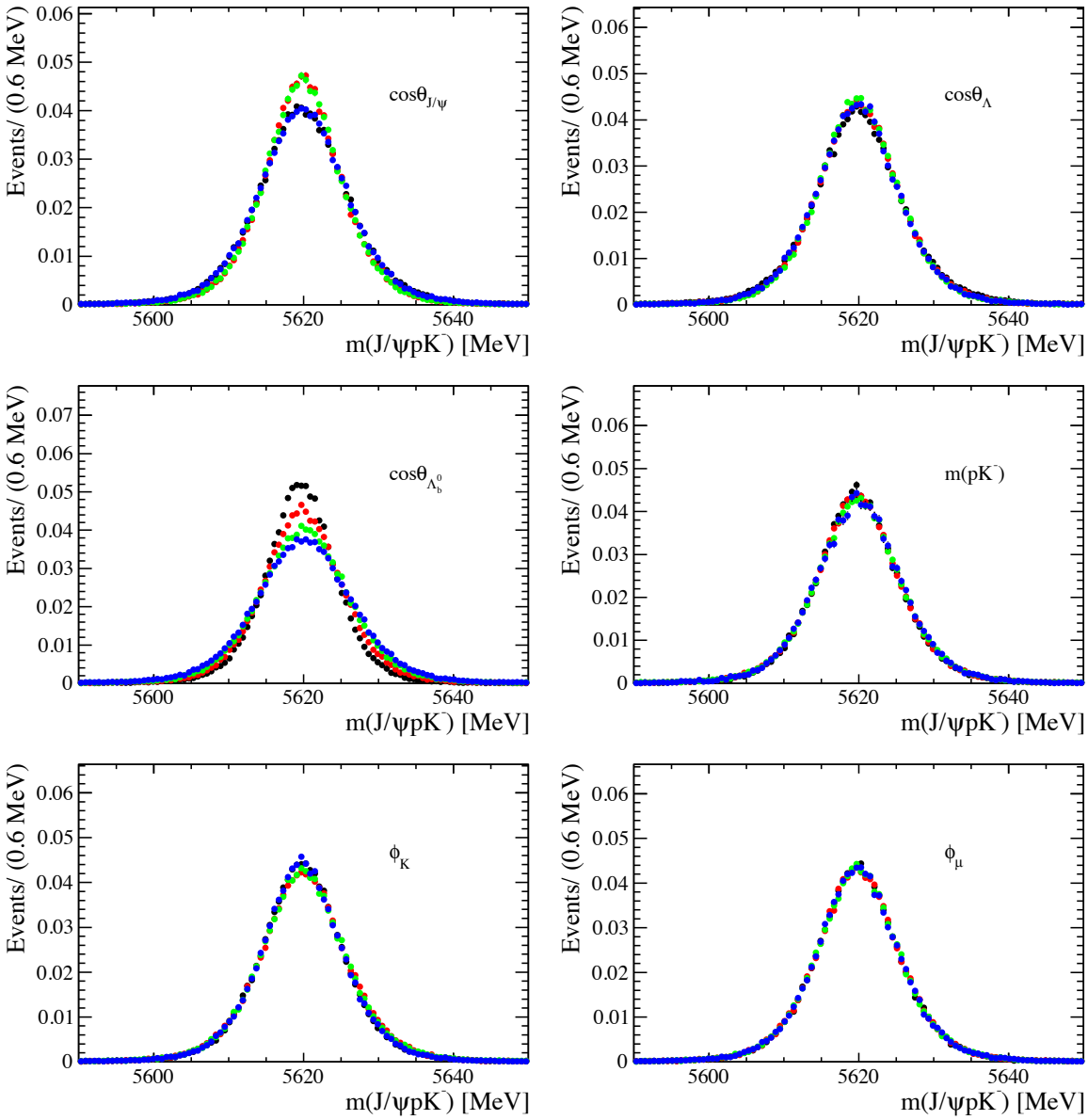

Figure 35: Simulated distributions of $m(J/\psi pK)$ for different ranges of the angular variables shown in different colors. The black, red, green and blue points correspond to the first, second, third, and fourth quarter of the range each variable covers, respectively. The distributions are normalized to unity.

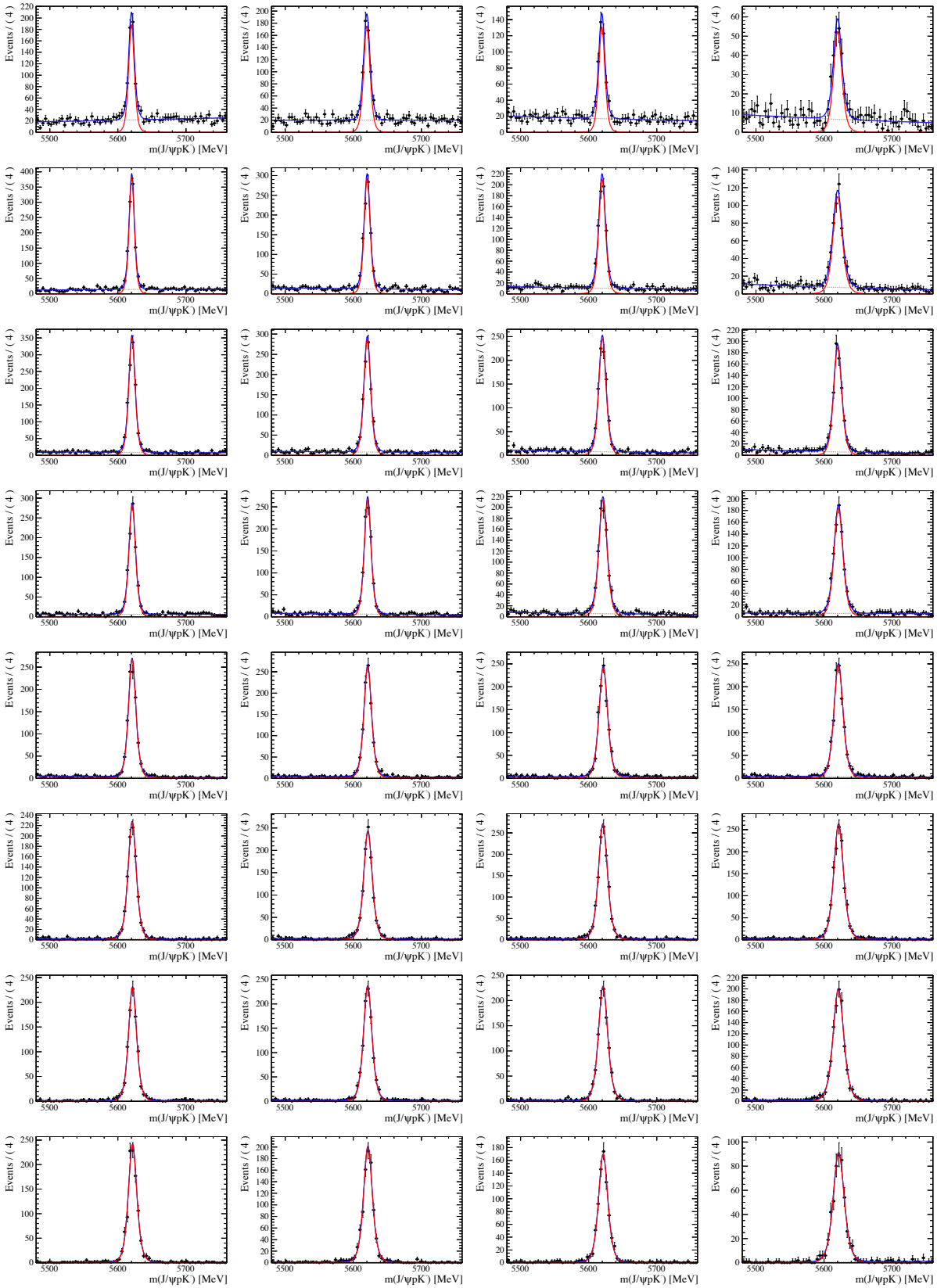

Figure 36: Fits to $m(J/\psi pK^-)$ distributions in 4 for $|\cos\theta_{J/\psi}| \times 8$ for $\cos\theta_{\Lambda_b^0}$ bins, where the blue curves show the total fits, the red solid line the signal and the brown dashed line the background. The columns from left to right correspond to 4 equal $|\cos\theta_{J/\psi}| \in [0,1]$ bins and the row from top to right correspond to 8 equal $\cos\theta_{\Lambda_b^0} \in [-1,1]$ bins.

7 Models of K^-p resonances

The m_{Kp} distribution shown in Fig. 23 shows several resonant structures. However, $\Lambda(1520)$ is the only prominent and immediately identifiable state; it is a non-trivial exercise to determine which resonances to include in the amplitude model. Thus far, only $\Lambda^* \to K^-p$ contributions have been spoken of, with no mention of $\Sigma^* \to K^-p$ contributions. Since the isospin of both the Λ_b^0 and the J/ψ are zero, it is expected that the dominant contributions in the K^-p system are from Λ^* states, which would proceed via a $\Delta I = 0$ process. It is also possible that Σ^* resonances contribute, but these would have $\Delta I = 1$. By analogy with kaon decays, the $\Delta I = 1$ process should be suppressed. [52]. The possibility of their presence is anyway revisited in Sec. 8.4. The list of Λ^* states as cataloged by the PDG [27] is shown in Table 5, along with their respective J^P quantum numbers, mass, width, and PDG class[13]. The J^P of $\Lambda(2585)$ is not known, and $5/2^-$ is assumed. Also listed in the table are the number of LS amplitudes allowed for two different models, which will be discussed now.

An attempt was first made to try and fit the data with only Λ^* resonances, in order to see if a good description of the mass and angular distributions can be obtained without including exotic pentaquark contributions. As part of the effort to do this, one should give the Λ^* model plenty of degrees of freedom with which to describe the data. However, including all resonances and all LS couplings can quickly lead to a large number of free parameters, as each additional resonance can contribute 8-12 new parameters if all couplings are allowed. It is likely that not all of these resonances are present in the data, for reasons which will be elaborated on shortly, and it is also likely that some of the higher L amplitudes are either heavily suppressed or non-existent. Still, the most general model includes all possible states and amplitudes. Thus the first model used is the "extended" model. It does not include * states, but includes all other states and allows all amplitudes, leading to a total of 146 free parameters. The masses and widths of the Λ^* states are fixed to their PDG values, as allowing them to float prevents the

[13] The PDG utilizes a classification scheme in which the class is given by one to four stars (*). The rankings range from very questionable (*) to well-estabilished states (****).

Table 5: Λ^* resonances listed by the PDG. The one star (*) states are not considered. The number of LS amplitudes is also listed for both the "reduced" and "extended" models. A zero entry means its not considered for the fits.

State	J^p	PDG class	Mass (MeV)	Γ (MeV)	# Default	# Extended
$\Lambda(1405)$	$1/2^-$	****	$1405.1^{+1.3}_{-1.0}$	50.5 ± 2.0	3	4
$\Lambda(1520)$	$3/2^-$	****	1519.5 ± 1.0	15.6 ± 1.0	5	6
$\Lambda(1600)$	$1/2^+$	***	1600	150	3	4
$\Lambda(1670)$	$1/2^-$	****	1670	35	3	4
$\Lambda(1690)$	$3/2^-$	****	1690	60	5	6
$\Lambda(1710)$	$1/2^+$	*	1713 ± 13	180 ± 40	0	0
$\Lambda(1800)$	$1/2^-$	***	1800	300	4	4
$\Lambda(1810)$	$1/2^+$	***	1810	150	3	4
$\Lambda(1820)$	$5/2^+$	****	1820	80	1	6
$\Lambda(1830)$	$5/2^-$	****	1830	95	1	6
$\Lambda(1890)$	$3/2^+$	****	1890	100	3	6
$\Lambda(2000)$	?	*	$\approx$2000	?	0	0
$\Lambda(2020)$	$7/2^+$	*	$\approx$2020	?	0	0
$\Lambda(2050)$	$3/2^-$	*	2056 ± 22	493 ± 60	0	0
$\Lambda(2100)$	$7/2^-$	****	2100	200	1	6
$\Lambda(2110)$	$5/2^+$	***	2110	200	1	6
$\Lambda(2325)$	$3/2^-$	*	$\approx$2325	?	0	0
$\Lambda(2350)$	$9/2^+$	***	2350	150	0	6
$\Lambda(2585)$	?	**	$\approx$2585	200	0	6

fit from converging. Variations in these parameters will be considered in the systematic uncertainties.

As will be shown, fits with K^-p resonances alone cannot adequately describe the data, and it is necessary to include exotic pentaquark contributions. This is despite the inclusion of free parameters describing resonances or amplitudes which likely do not contribute to the data. Due to the large number of free parameters, it is desirable to have an additional model with only more well-motivated parameters. This facilitates the process of carrying out the characterization of the P_c states, as well as the ensuing systematic studies. By removing the unlikely contributions, the very time-consuming fits can be performed quicker, and with less concern of converging to false minima. For these reasons, the "reduced" or "default" Λ^* model was created.

As the minimal $L^{\Lambda^*}_{\Lambda_b^0}$ for the spin 9/2 $\Lambda(2350)$ equals $J_{\Lambda^*} - J_{\Lambda_b^0} - J_{J/\psi} = 3$, it is extremely unlikely that this state can be produced while being so close to the phase-space limit ($Q = m_{\Lambda_b^0} - m_{J/\psi} \approx 160$ MeV). In fact $L = 3$ is the highest orbital angular

momentum observed, with a very small rate, in decays of B mesons [53] with much larger phase-space available (Q = 1780 MeV), and also without additional suppression from the spin counting factors present in the $\Lambda(2350)$ production (all three $\vec{J}_{\Lambda^*}$, $\vec{J}_{\Lambda_b^0}$ and $\vec{J}_{J/\psi}$ vectors have to line up in the same direction to produce the minimal $L_{\Lambda_b^0}^{\Lambda^*}$ value). Therefore, it is eliminated in the default Λ^* model. The $\Lambda(2585)$ is also eliminated, as it peaks beyond the kinematic limit and is not as well-established, with the J^P not even being known. Also, even for resonances which are present, some possible values of orbital angular momenta are not likely to contribute significantly due to high L values being suppressed. Thus some high $L_{\Lambda_b^0}^{\Lambda^*}$ amplitudes were removed. Only the lowest values were kept for the high mass resonances, and smaller reductions made for the lighter ones. The number of amplitudes used for each resonances is listed in Table 5. With this model the number of parameters used to describe the Λ^* decays was reduced from 146 to 64. The difference between the fit results obtained with the default and extended Λ^* models is included in the systematic uncertainties.

8 Fits with only K^-p contributions

In this section, fits to the data with an amplitude model consisting of only K^-p contributions are shown. When answering the question of whether or not conventional contributions can reproduce the data, it is important to give the model plenty of flexibility; thus, the extended model is used for all fits in this section. Results are first shown for the extended model by itself, and then with additions of further K^-p contributions.

8.1 Extended Model

The results of the fit with the extended Λ^* model without P_c^+ states are shown in this section. The amplitude model is compared to the data by projecting it onto the various kinematic variables. This is carried out by weighting the fully simulated MC sample with the matrix element squared calculated for each event. The projections onto the m_{Kp} and $m_{J/\psi p}$ variables are shown in Fig. 37. While m_{Kp} is reasonably well fit, the peaking structure in $m_{J/\psi p}$ is not reproduced. The angular distributions are also reasonably

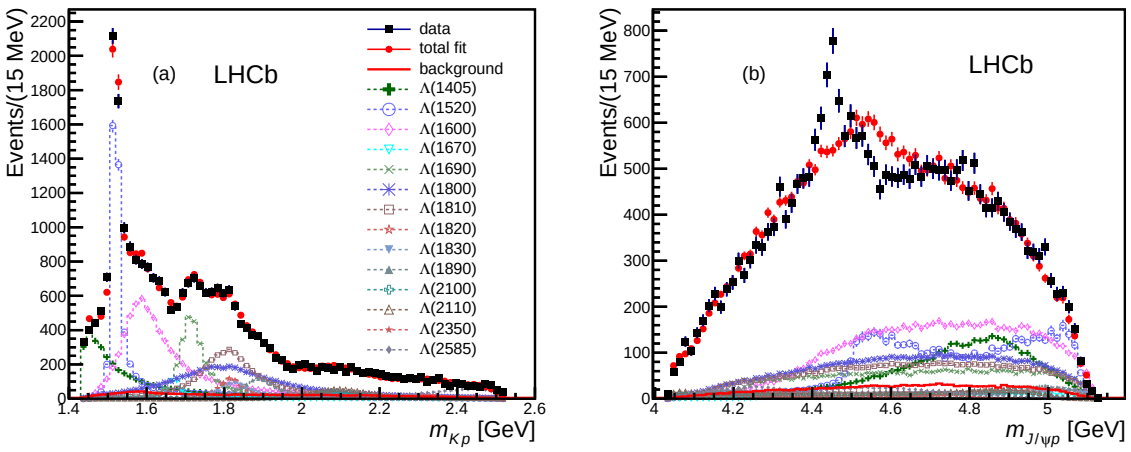

Figure 37: Results of the extended Λ^* model for (a) m_{Kp} and (b) $m_{J/\psi p}$. The data are shown as (black) squares with error bars, while the (red) circles show the projection of the fit. Each Λ^* component is also shown as specified in the legend. The error bars on the points showing the fit results are due to simulation statistics.

reproduced, as shown by the projections displayed in Fig. 38.

It is also instructive to look at the projections onto $m_{J/\psi p}$ in bins of m_{Kp}, as displayed in Fig. 39. Note that the peaking structures are outside of the allowed kinematic region in

the first bin. The inability of the model to reproduce the data is clearly seen throughout the remaining bins. It is apparent that the data can not be described by the extended Λ^* model.

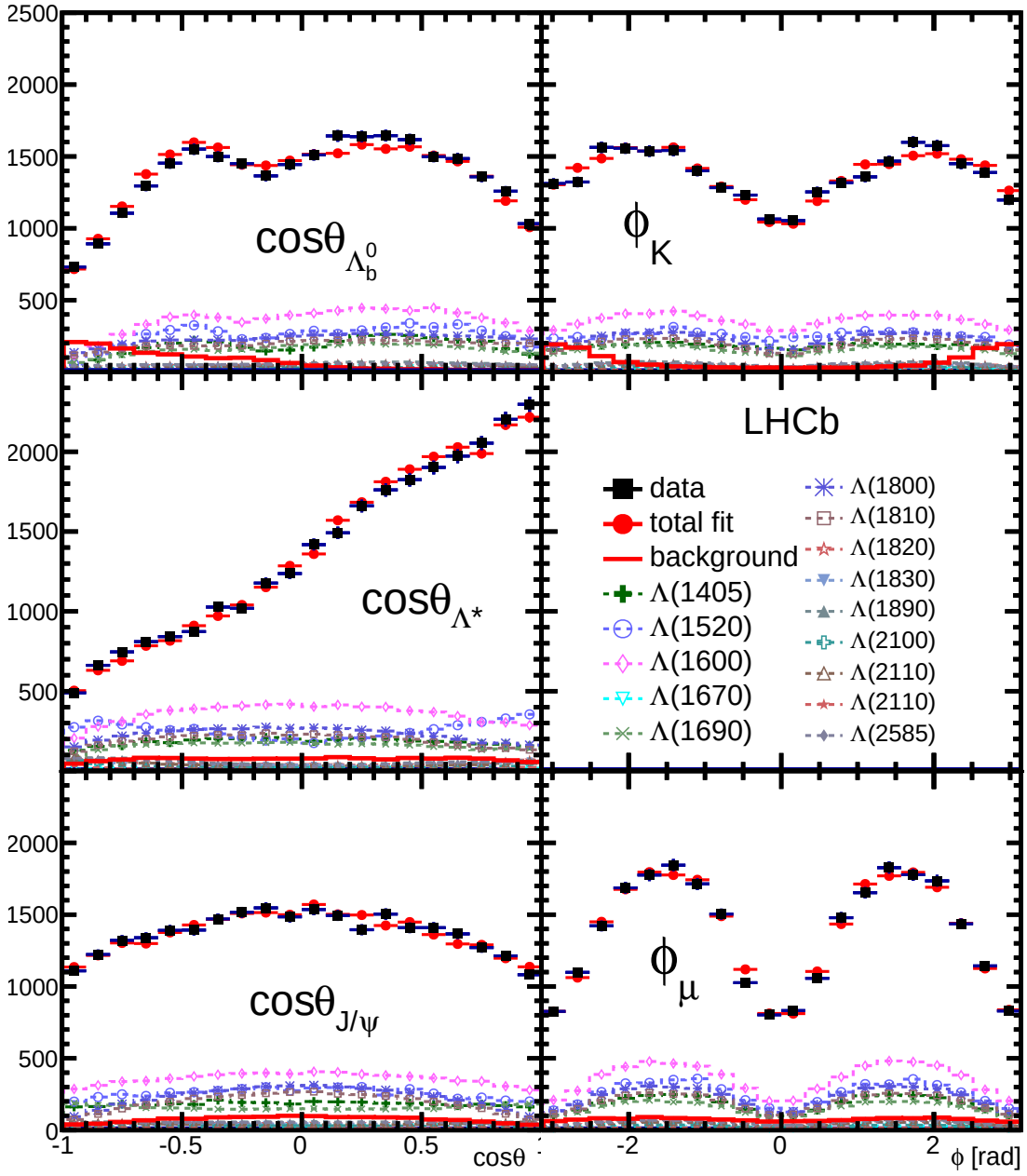

Figure 38: Results of the extended Λ^* model for the different decay angular distributions. The data are shown as (black) squares, while the (red) circles show the results of the fit. Each fit component is also shown. The angles are defined in Sec. 5.2.

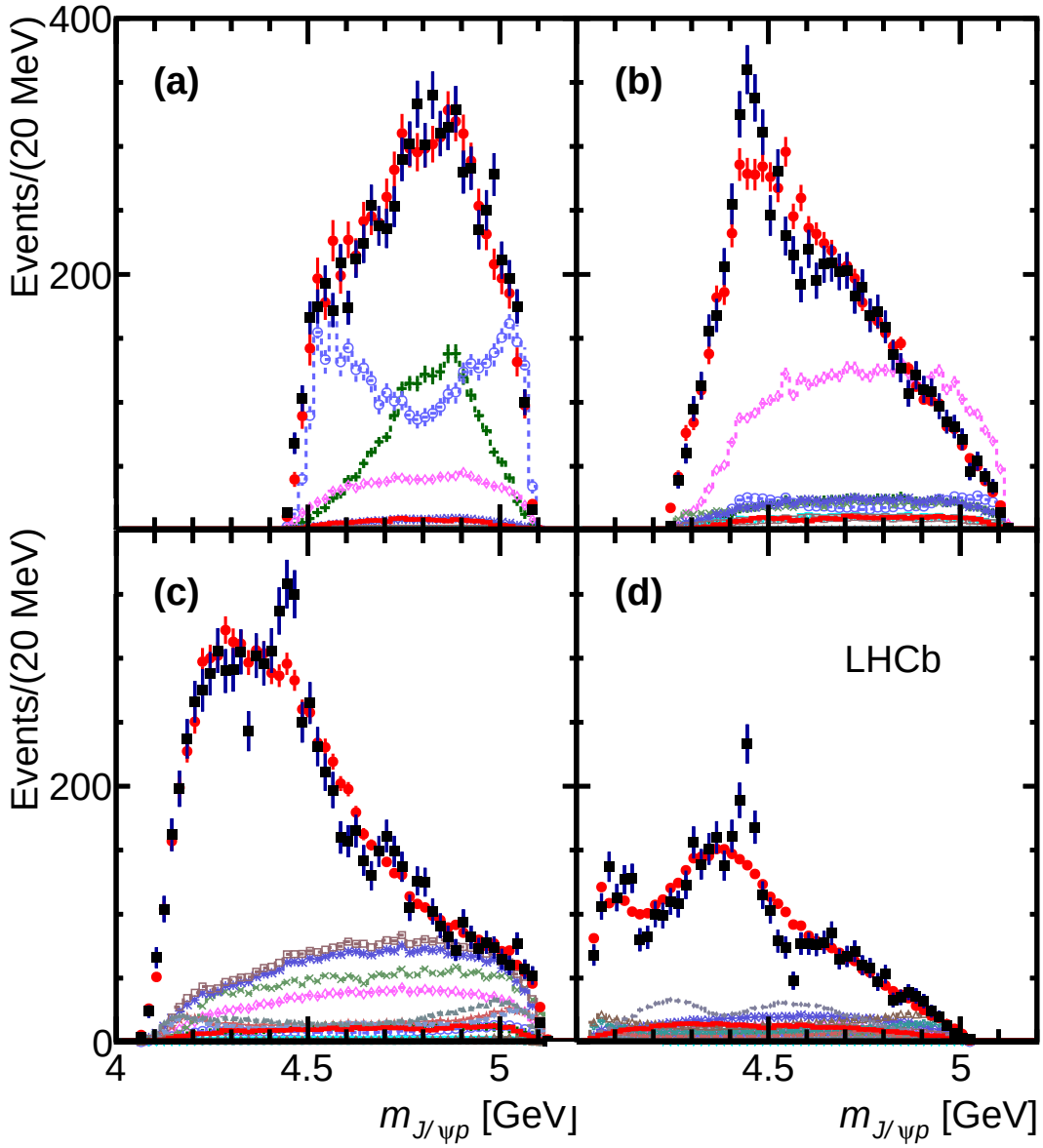

Figure 39: Results of the extended Λ^* for $m_{J/\psi p}$ in various intervals of m_{Kp}: (a) $m_{Kp} <$ 1.55 GeV, (b) 1.55 $< m_{Kp} <$ 1.70 GeV, (c) 1.70 $< m_{Kp} <$ 2.00 GeV, and (d) $m_{Kp} >$ 2.00 GeV. The data are shown as (black) squares with error bars, while the (red) circles show the results of the fit. Each fit component is also shown. See Fig. 38 for the legend.

8.2 Addition of two new Λ^* resonances

In addition to the resonances used in the extended model, two new Λ^* resonances were added to the amplitude model. All combinations of J^P for the two resonances were tested for spins up to 7/2. All LS couplings were allowed, and the masses and the widths of the added states were free in the fit. The largest improvement in $-2\ln\mathcal{L}$ came from adding a $\frac{1}{2}^-$ and $\frac{3}{2}^-$ state. The comparisons of this amplitude model to the data for m_{Kp} and $m_{J/\psi p}$ are shown in Fig. 40. Clearly, the addition of these states does not lead to a significantly improved ability to describe the peaking structure seen in $m_{J/\psi p}$.

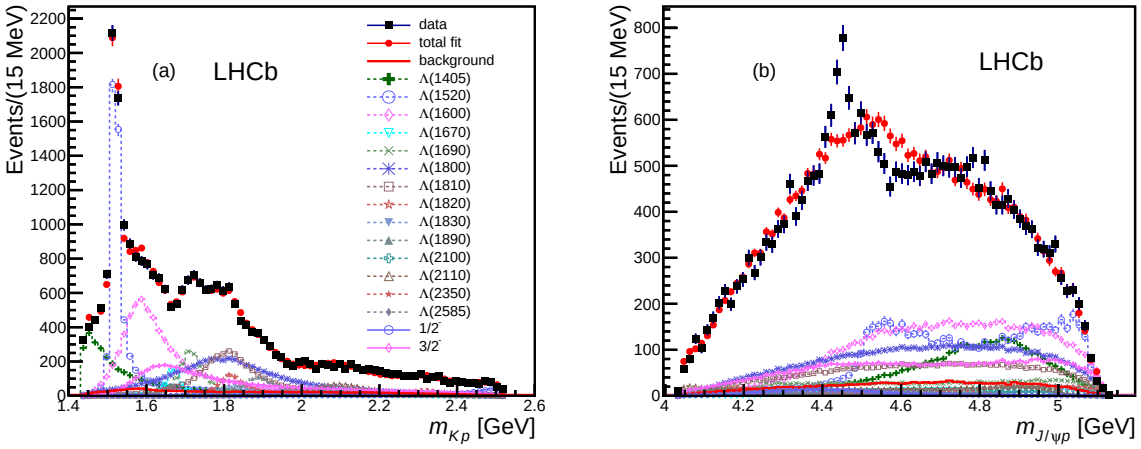

Figure 40: Results of the extended Λ^* model with an additional $\frac{1}{2}^-$ and $\frac{3}{2}^-$ state for (a) m_{Kp} and (b) $m_{J/\psi p}$. The data are shown as (black) squares with error bars, while the (red) circles show the projection of the fit. Each Λ^* component is also shown as specified in the legend. The error bars on the points showing the fit results are due to simulation statistics.

8.3 Addition of four nonresonant components

Four nonresonant components with J^P's of $1/2^+$, $1/2^-$, $3/2^+$, and $3/2^-$ were also added on top of the extended Λ^* model. All LS amplitudes of the nonresonant states were allowed to vary. The comparisons of this amplitude model to the data for the m_{Kp} and $m_{J/\psi p}$ variables are shown in Fig. 41. Even with the addition of these four new components, the amplitude model does not come close to being able to create the peaking structures seen in the data.

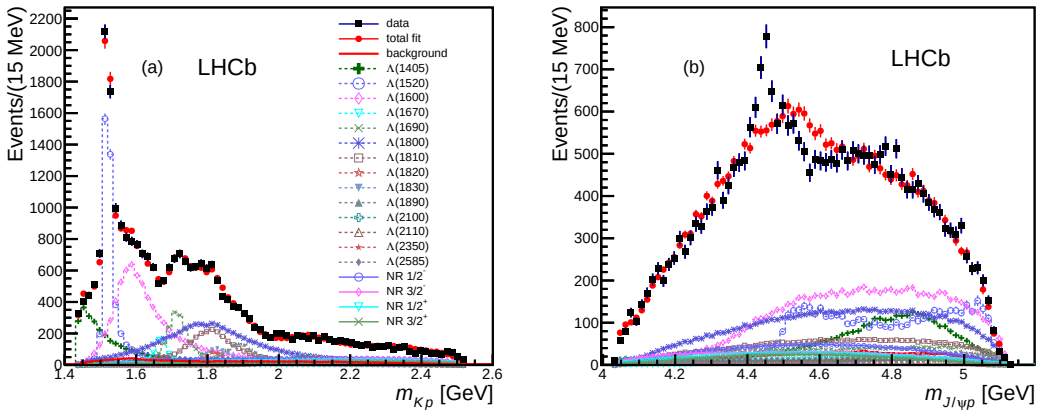

Figure 41: Results of the extended Λ^* model with $\frac{1}{2}^{\pm}$ and $\frac{3}{2}^{\pm}$ nonresonant contributions added on for (a) m_{Kp} and (b) $m_{J/\psi p}$. The data are shown as (black) squares with error bars, while the (red) circles show the projection of the fit. Each Λ^* component is also shown as specified in the legend. The error bars on the points showing the fit results are due to simulation statistics.

8.4 Addition of Σ^* states

As was stated earlier, significant contributions from $\Sigma^* \to K^- p$ are not expected due to the larger isospin change in $\Lambda_b^0 \to J/\psi \Sigma^*$ ($\Delta I = 1$) compared with $\Lambda_b^0 \to J/\psi \Lambda^*$ ($\Delta I = 0$). Nevertheless, the Σ^* states in the PDG with a *** or **** rating were added to the extended model. These newly included states are listed in Table 6 along with their properties. Here the $\Sigma(2250)$ state was picked arbitrarily to have $J^P = 3/2^+$. All LS amplitudes were allowed, resulting in a new total of 246 free parameters. The comparisons of this amplitude model to the data for the m_{Kp} and $m_{J/\psi p}$ variables are shown in Fig. 42. The results of the $m_{J/\psi p}$ projection are only marginally different from the extended model

fit without the Σ^* states, and no ability to produce the peaking structure is seen.

Table 6: List of added Σ^* states

State	J^P	PDG class	Mass (MeV)	Width (MeV)	# of LS amplitudes
$\Sigma(1385)$	$3/2^+$	****	1383.7 ± 1.0	36 ± 5	6
$\Sigma(1660)$	$1/2^+$	***	1660	100	4
$\Sigma(1670)$	$3/2^-$	****	1670	60	6
$\Sigma(1750)$	$1/2^-$	***	1750	90	4
$\Sigma(1775)$	$5/2^-$	****	1775	120	6
$\Sigma(1915)$	$5/2^+$	****	1915	120	6
$\Sigma(1940)$	$3/2^-$	***	1940	220	6
$\Sigma(2030)$	$7/2^+$	****	2030	180	6
$\Sigma(2250)$	??	****	2250	100	6

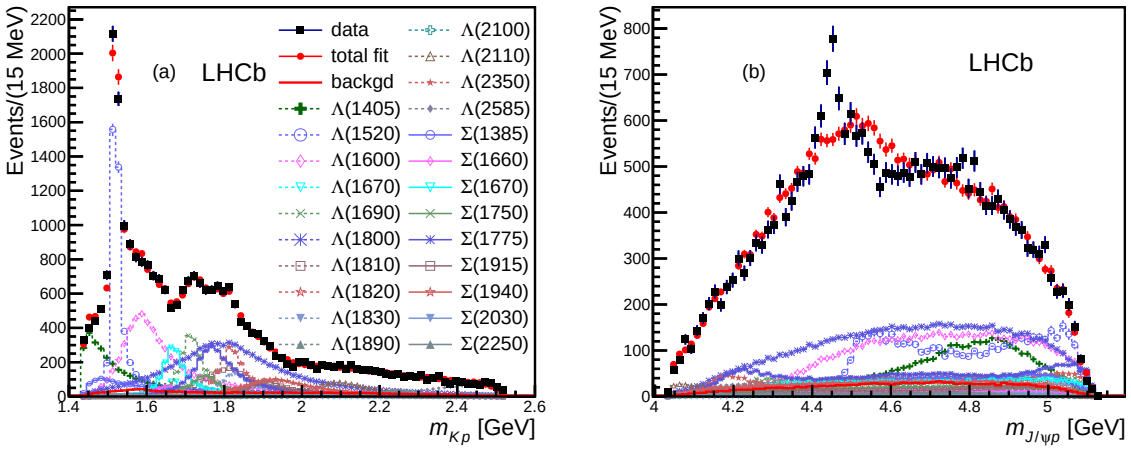

Figure 42: Results of the extended Λ^* model with Σ^* contributions added on for (a) m_{Kp} and (b) $m_{J/\psi p}$. The data are shown as (black) squares with error bars, while the (red) circles show the projection of the fit. Each Λ^* component is also shown as specified in the legend. The error bars on the points showing the fit results are due to simulation statistics.

9 Addition of a P_c resonance

The studies in the previous section have shown that the data clearly can not be described by only K^-p contributions. The well established Λ^* states failed to reproduce the peaking structures seen in the $m_{J/\psi p}$ distribution (Sec. 8.1), and the introduction of further states was seen to not help (Sec.8.2). Furthermore, the addition of four nonresonant (Sec. 8.3) or several Σ^* (Sec. 8.4) components to the amplitude model still lead to poor descriptions of the data.

As nothing in the K^-p system has shown any ability to produce the observed peaking structure, the next step is to add a resonance in the $J/\psi p$ system. Fits were performed with P_c states of varying quantum numbers: $J^P = 1/2^{\pm}$, $3/2^{\pm}$ and $5/2^{\pm}$. The mass and width of the P_c states were allowed to vary. The best fit to the data as determined from the $-2\ln\mathcal{L}$ was obtained with $J^P = 5/2^+$. However, this fails to give a good description of the data. Figure 43 compares the data to the projections of the amplitude model on the m_{Kp} and $m_{J/\psi p}$ variables. While the m_{Kp} projection is still well described, the model doesn't do a sufficient job of describing the peak in $m_{J/\psi p}$.

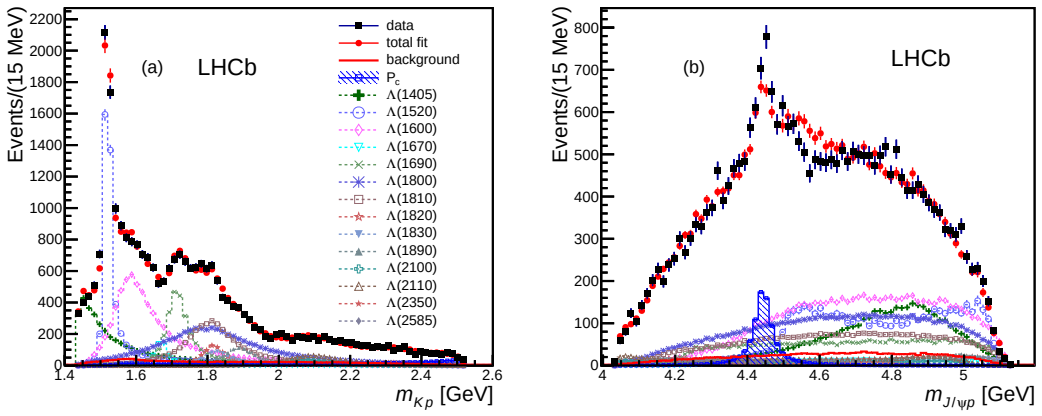

Figure 43: Results of the extended Λ^* model with a $\frac{5}{2}^+$ P_c state for (a) m_{Kp} and (b) $m_{J/\psi p}$. The data are shown as (black) squares with error bars, while the (red) circles show the projection of the fit. Each fit component is also shown as specified in the legend. The error bars on the points showing the fit results are due to simulation statistics.

The various angular distributions are shown in Fig. 44. The fit is again in good agreement with the data. The projection on to the $m_{J/\psi p}$ variable in various bins of m_{Kp} is shown in Fig. 45. Clearly, the discrepancy between the amplitude model and the

peaking structures in $m_{J/\psi p}$ is much less than in the fit without a P_c, but it still doesn't describe the data well, especially in the $1.55 < m_{Kp} < 1.70$ GeV interval.

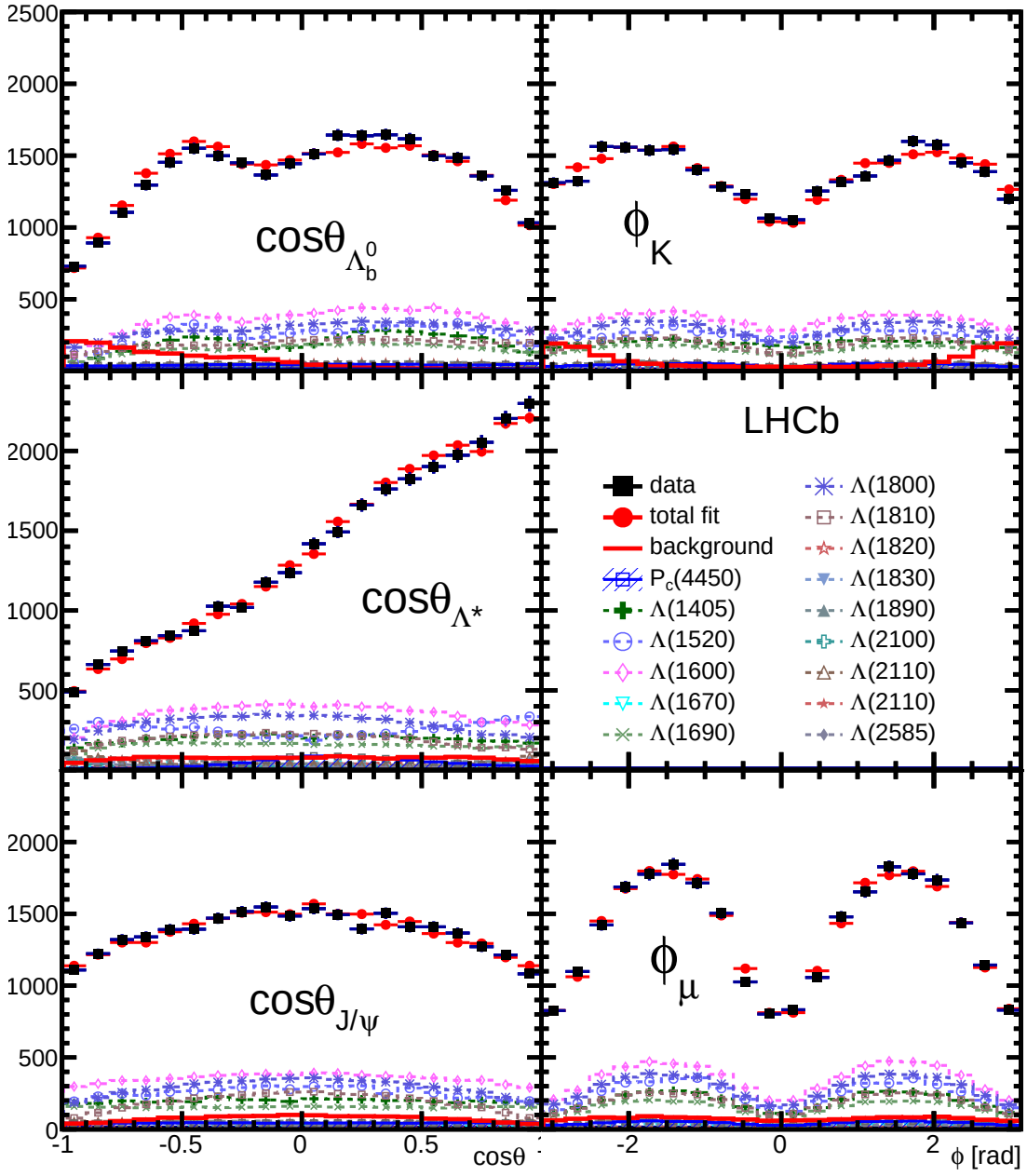

Figure 44: Results of the extended Λ^* model with a $\frac{5}{2}^+$ P_c state for various decay angular distributions. The data are shown as (black) squares, while the (red) circles show the results of the fit. Each fit component is also shown. The angles are defined in Sec. 5.2.

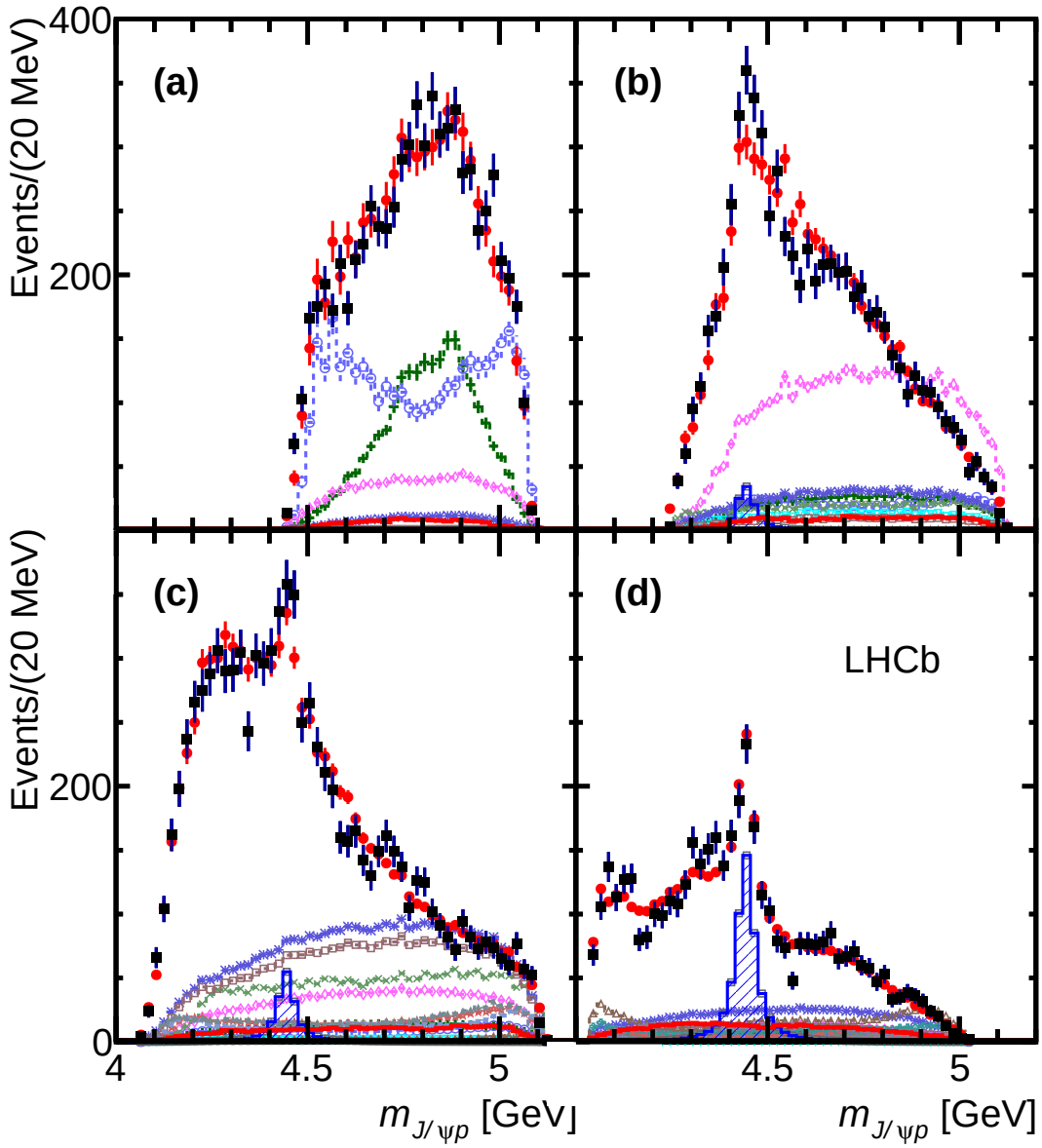

Figure 45: Results of the extended Λ^* with a $\frac{5}{2}^+$ for $m_{J/\psi p}$ in various intervals of m_{Kp}: (a) $m_{Kp} < 1.55$ GeV, (b) $1.55 < m_{Kp} < 1.70$ GeV, (c) $1.70 < m_{Kp} < 2.00$ GeV, and (d) $m_{Kp} > 2.00$ GeV. The data are shown as (black) squares with error bars, while the (red) circles show the results of the fit. Each fit component is also shown. See Fig. 44 for the legend.

10 Addition of a second P_c resonance

The purpose of the extended model was to give the conventional hadron model plenty of flexibility with which to describe the data before resorting to adding exotic hadron contributions. It was shown in Sec. 8 that such fits could not be obtained, and then in Sec. 9 it was shown that adequate descriptions of the data could not be obtained with just a single P_c resonance. As discussed in Sec. 7, it is desirable to work with a Λ^* model which has less free parameters[14]. This is achieved in the default model by removing the $\Lambda(2350)$ and $\Lambda(2585)$ as well as placing limits on the orbital angular momenta present in the $\Lambda_b^0 \to J/\psi\,\Lambda^*$ decays. For the comparison of the extended and default models, see Table 5. It is shown in this section that good descriptions of the data can be obtained with this "reduced" Λ^* model when two P_c resonances are included. Thus, this model is used for determining nominal values of the P_c resonances, while the extended Λ^* model will be used as part of the systematic studies.

10.1 Fit results for default amplitude model

Fits were performed with two P_c resonances for all combinations of J^P with spins up to $J = 7/2$, for a total of 64 different combinations. The improvement in fit quality from the default Λ^* model with no P_c resonances is quantified by the $-2\ln\mathcal{L}$. The best fit is obtained with a $3/2^-$ state having a mass of 4380 ± 8 MeV and a width of 205 ± 11 MeV, along with a $5/2^+$ state having a mass of 4449.8 ± 1.7 MeV and a width of 39 ± 5 MeV[15]. All uncertainties listed here are statistical; systematic uncertainties will be discussed later. These states were named using their respective masses as $P_c(4380)$ and $P_c(4450)$. In Fig. 46, the projections of the default amplitude model on m_{Kp} and $m_{J/\psi p}$ are shown along with the data. The m_{Kp} distribution is of course well-described, and it is now seen that $m_{J/\psi p}$ is well-described as well. Thus, it is seen that with two pentaquark resonances, a good description of the data can be obtained. To see the fit projections obtained with

[14] In fact it is necessary to do this, as the number of free parameters in the extended model prevents the determination of a positive-definite error matrix, and thus accurate statistical uncertainties.

[15] The mass resolution is 2.5 MeV at 4450 MeV, so these correspond to the natural widths of these states.

the extended Λ^* model and the two P_c states, see Appendix D.

Figure 47 shows that the angular distributions are also well-fit. The one difference is for the $\cos\theta_{\Lambda_b^0}$ distribution where the fit is higher than the data for $\cos\theta_{\Lambda_b^0} < 0$ and $\cos\theta_{\Lambda_b^0} > 0$. This can be due to a small mis-modeling of either the efficiency or the background. We will show in the systematic uncertainty section that this discrepancy has only a small effect on the final result. The $m_{J/\psi p}$ distribution in various intervals of m_{Kp} is shown in Fig. 48, where it is seen that a good description is obtained for $m_{J/\psi p}$ throughout the m_{Kp} range.

This amplitude model will henceforth be taken as the default, or nominal, amplitude model. An important point is that while the best fit is obtained with $J^P(P_c(4380), P_c(4450)) = (3/2^-,\ 5/2^+)$, the combinations $(3/2^+,\ 5/2^-)$ and $(\frac{5}{2}^+, \frac{3}{2}^-)$ are not far behind, with their $-2\ln\mathcal{L}$ values being only 0.9^2 and 2.3^2 worse, respectively. A full list of quantum number rankings is given in Sec. 13.

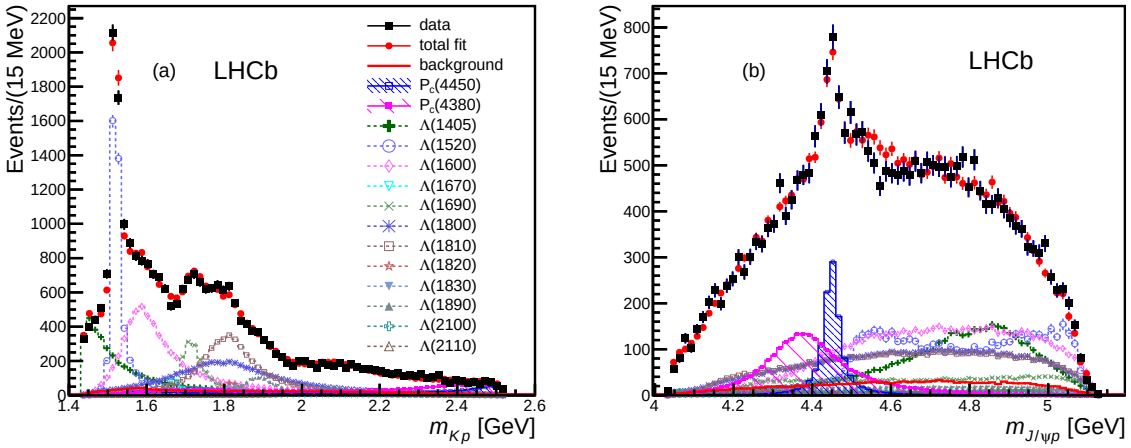

Figure 46: Fit projections of the default Λ^* model with two P_c^+ states onto the (a) m_{Kp} and (b) $m_{J/\psi p}$ distributions. The data are shown as solid (black) squares, while the solid (red) points show the results of the fit. The solid (red) histogram shows the background distribution. The (blue) open squares with the shaded histogram represent the $P_c(4450)^+$ state, and the shaded histogram topped with (purple) filled squares represents the $P_c(4380)^+$ state. Each Λ^* component is also shown. The error bars on the points showing the fit results are due to simulation statistics.

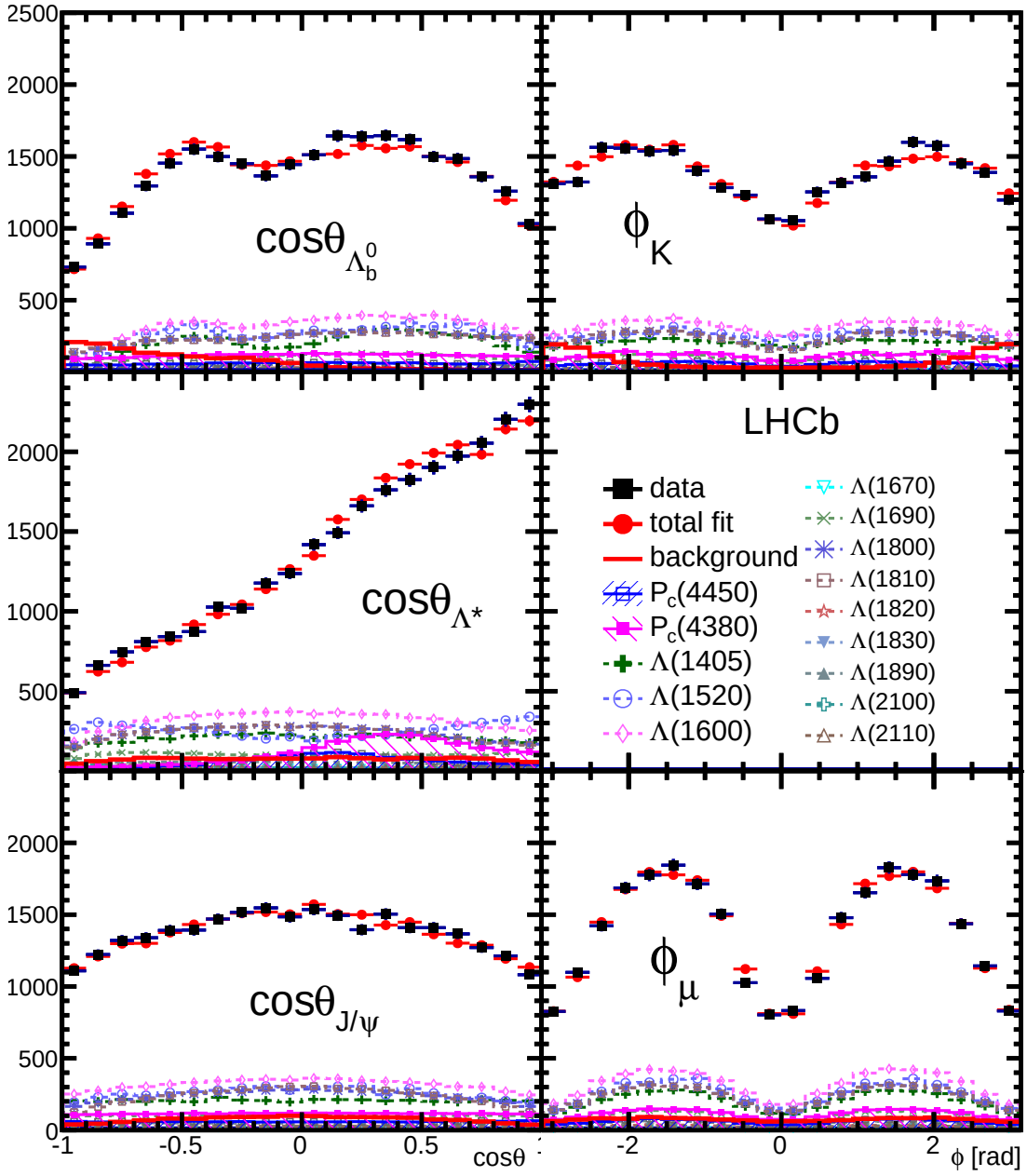

Figure 47: Fit projections of the default Λ^* model with two P_c^+ states onto the decay angular distributions. The data are shown as (black) squares, while the (red) circles show the results of the fit. Each fit component is also shown. The angles are defined in Sec. 5.2.

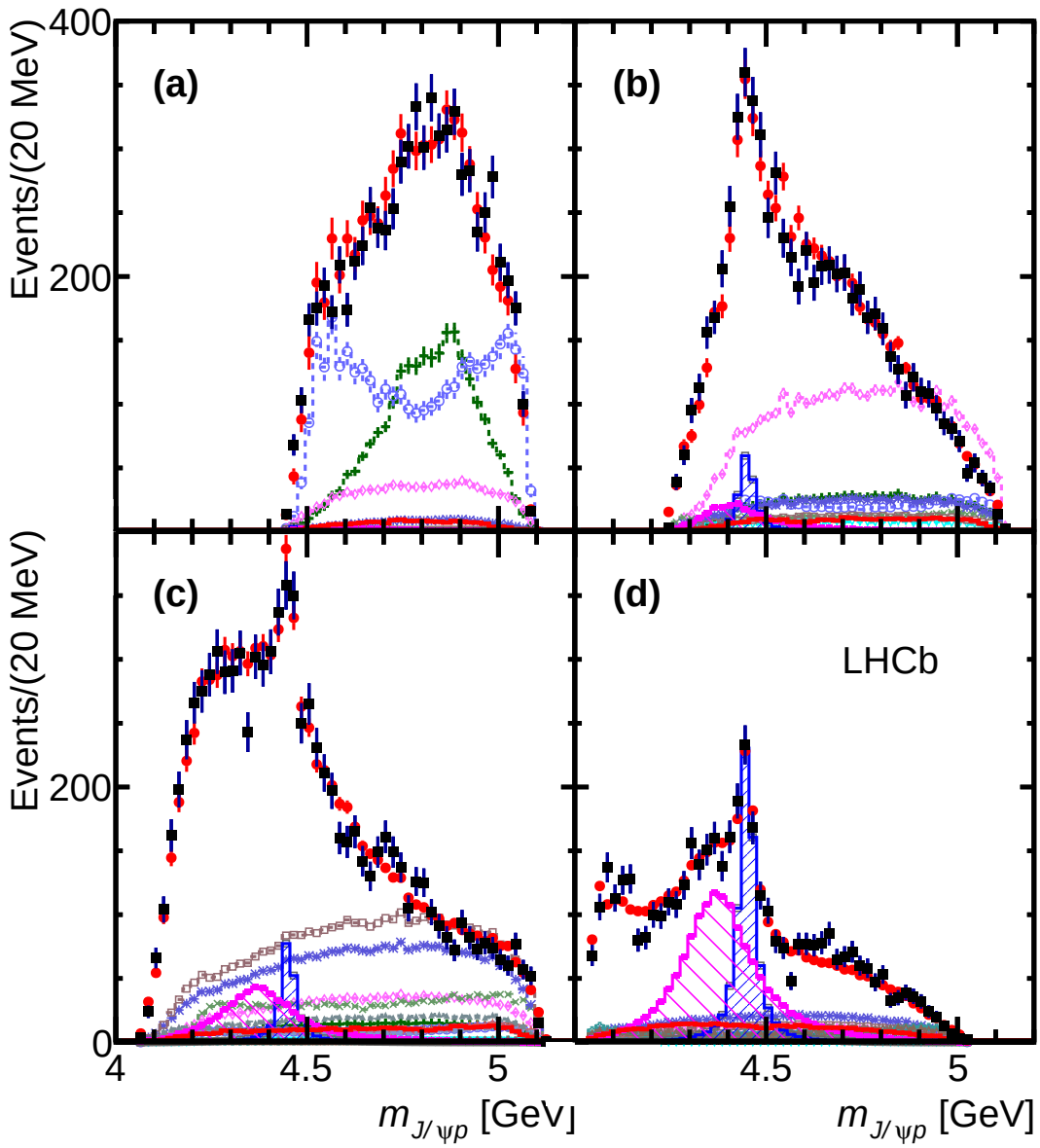

Figure 48: Fit projections of the default Λ^* model with two P_c^+ states onto $m_{J/\psi p}$ for various intervals of m_{Kp}: (a) $m_{Kp} < 1.55$ GeV, (b) $1.55 < m_{Kp} < 1.70$ GeV, (c) $1.70 < m_{Kp} < 2.00$ GeV, an d (d) $m_{Kp} > 2.00$ GeV. The data are shown as (black) squares with error bars, while the (red) circles show the results of the fit. The blue and purple histograms show the two P_c^+ states. See Fig. 47 for the legend.

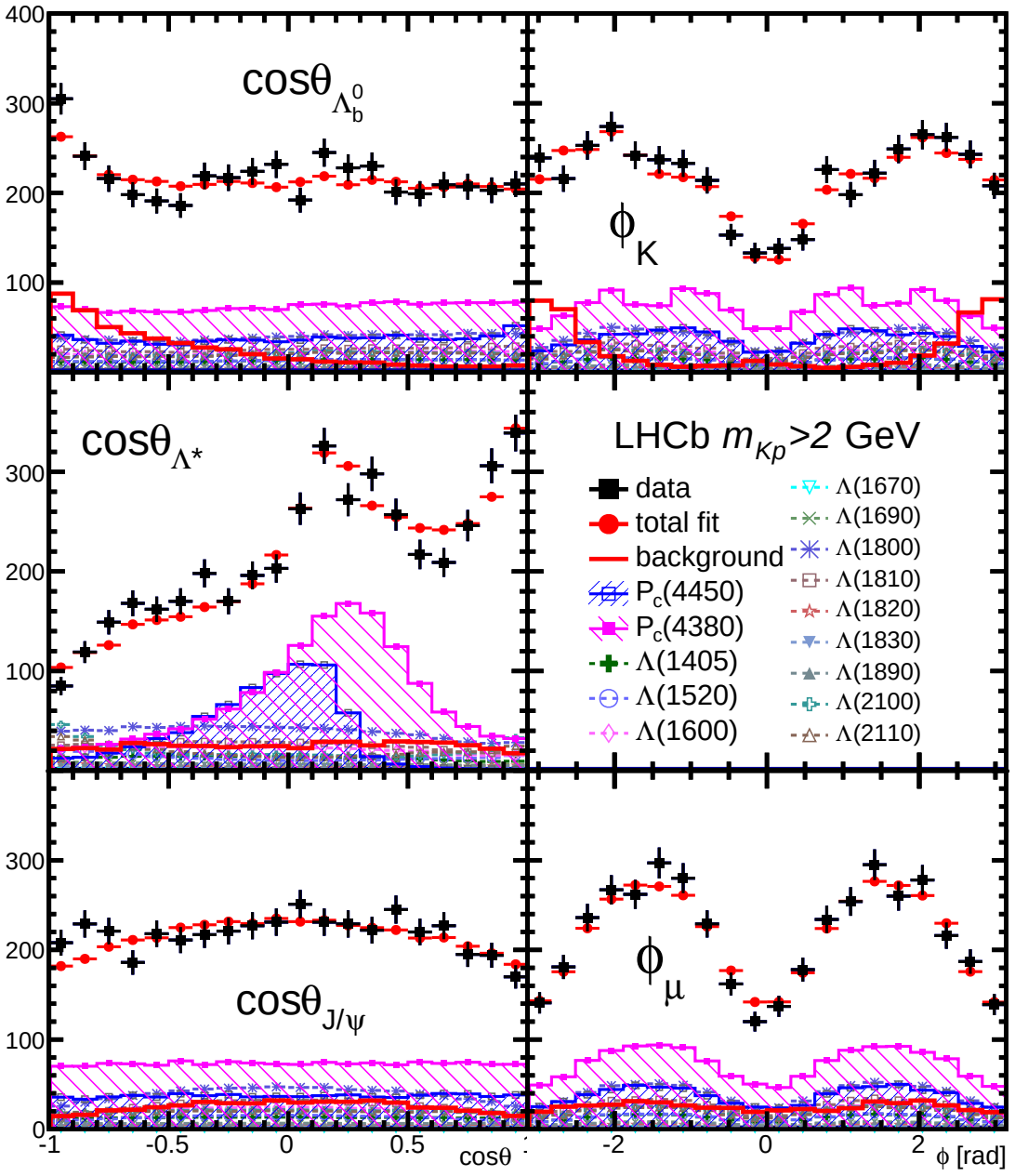

Figure 49: Fit projections of the default Λ^* model with two P_c^+ states onto the decay angular distributions $m_{Kp} > 2$ GeV. The data are shown as (black) squares, while the (red) circles show the results of the fit. Each fit component is also shown. The angles are defined in Sec. 5.2.

10.2 Fit fractions

The fit fraction for a given resonance is defined as the ratio of the phase space integral of the matrix element for the resonance taken by itself to the integral of the full matrix element.

$$\mathrm{FF}(\mathrm{res_i}) = \frac{\int dm_{Kp} d\Omega |M_{res_i}|^2}{\int dm_{Kp} d\Omega |M|^2} \tag{72}$$

Similarly, one can calculate the fit fraction of multiple resonances taken together. Note that interferences will allow for the sum of fit fractions for all the resonances in a model to be greater than unity. Using fit fractions, the interference can be quantified via the difference between the fit fraction of two resonances taken together and the fit fractions calculated for each resonance separately. The fit fractions are listed in Table 7. The $\Lambda_b^0 \to J/\psi\, \Lambda^*(1405)$ was recently predicted [54], and this measurement can be taken as a confirmation of this process. Systematic uncertainties of fit fractions for the P_c states and the well-separated $\Lambda^*(1405)$ and $\Lambda^*(1520)$ states are estimated in Sec. 15.

Table 7: Fit fractions of the different components for the default $3/2^-$, $5/2^+$ model.

Resonance	Fit fraction (%)
$P_c(4450)$	4.09 ± 0.48
$P_c(4380)$	8.42 ± 0.68
$\Lambda^*(1405)$	14.64 ± 0.72
$\Lambda^*(1520)$	18.93 ± 0.52
$\Lambda^*(1600)$	23.50 ± 1.48
$\Lambda^*(1670)$	1.47 ± 0.49
$\Lambda^*(1690)$	8.66 ± 0.90
$\Lambda^*(1800)$	18.21 ± 2.27
$\Lambda^*(1810)$	17.88 ± 2.11
$\Lambda^*(1820)$	2.32 ± 0.69
$\Lambda^*(1830)$	1.76 ± 0.58
$\Lambda^*(1890)$	3.96 ± 0.43
$\Lambda^*(2100)$	1.65 ± 0.29
$\Lambda^*(2110)$	1.62 ± 0.32

11 Necessity of two P_c states

From viewing the $m_{J/\psi p}$ distribution by itself, it isn't immediately clear why the addition of a single P_c state isn't better able to describe the data. This section examines why this is the case, and further demonstrates the importance of performing a full amplitude analysis which uses all kinematic variables and allows for the interference of the various contributions, rather than a naive 1D fit to the $m_{J/\psi p}$ distribution.

11.1 Studies of the P_c decay angular distribution

The reason why adding a single P_c state fails to describe the peaking structure can be found in the distribution of $\cos\theta_{P_c}$, the P_c helicity angle. It is plotted versus $m^2(J/\psi p)$ in Fig. 50. This corresponds to the rectangular Dalitz plane, using the variables of the P_c decay chain, and thus is a different representation of the usual Dalitz plot. The band indicative of contributions in the $J/\psi p$ system is clearly seen just below 20 GeV^2, and the presence of the lower mass Λ^* states can be clearly seen at larger values of $\cos\theta_{P_c}$, stretching across $m^2_{J/\psi p}$. It can be expected that the distribution of $\cos\theta_{P_c}$ resulting from

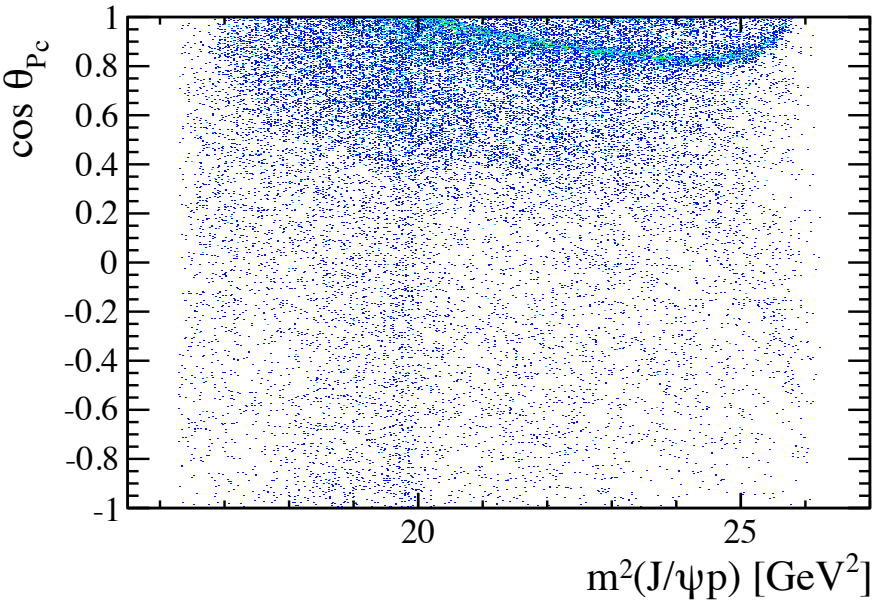

Figure 50: Distribution of $m^2_{J/\psi p}$ versus $\cos\theta_{P_c}$ for candidates within ±20 MeV of the Λ_b^0 mass.

a single P_c state should be symmetric about $\cos\theta_{P_c} = 0$, and this will be proven shortly.

However, if the $m_{J/\psi p}$ distribution of the data is split into two sets according to the sign of $\cos\theta_{P_c}$, there is a clear asymmetry in the size of the $m_{J/\psi p}$ peaking structure. This is shown in Fig. 51. To be clear, this is about the difference in the size of the peaking structure, and not about the difference in the total number of events. From viewing Fig. 50, it is clear that the total number of events would exhibit this feature. What is interesting is that the peak also shows this difference, which wouldn't be the case if only a single P_c state was present.

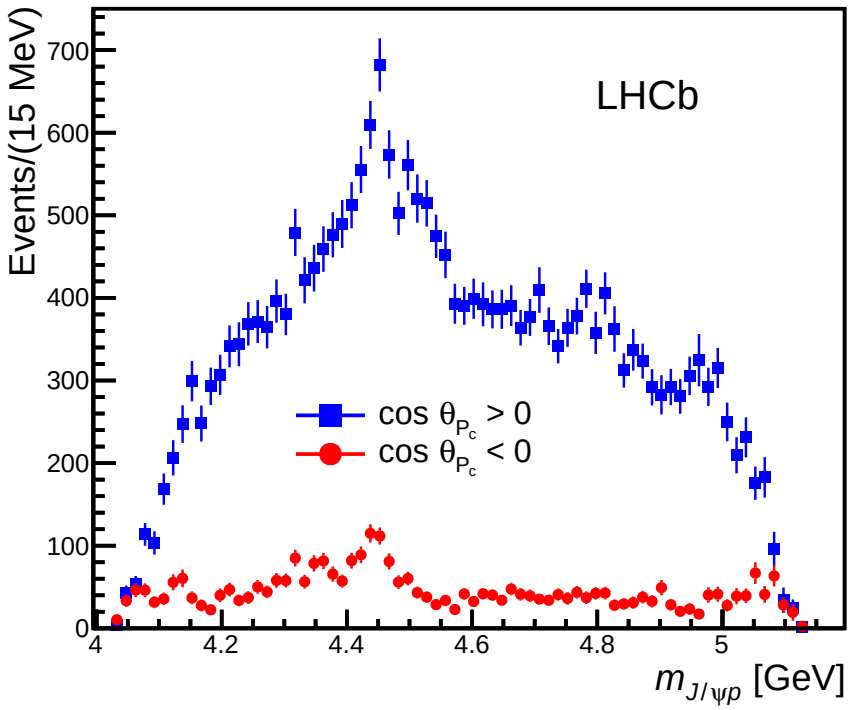

Figure 51: Distributions of $m_{J/\psi p}$ in the data for $\cos\theta_{P_c} > 0$ (solid black points) and $\cos\theta_{P_c} < 0$ (open red points). The background has been subtracted using sWeights.

The question then is how to get an asymmetric $\cos\theta_{P_c}$ distribution such as this from P_c contributions. In Fig. 52, the $\cos\theta_{P_c}$ distributions are shown for two combinations of possible quantum numbers: $J^P(P_c(4380), P_c(4450)) = (3/2^+, 5/2^+)$ and $J^P(P_c(4380), P_c(4450)) = (3/2^-, 5/2^+)$. Each figure shows the distributions resulting from their individual contributions, as well as their combined contribution, which includes their interference effects. Note that, for the case in which the two P_c states have matching parities, the combined distribution remains symmetric, while for the case in which they have opposite parities, the combined distribution is asymmetric. Indeed, the

combined distribution will in general be symmetric for the same-parity combinations, and asymmetric for the opposite-parity combinations. If it is accepted that only contributions from P_c states form the peaking structure, then the asymmetry shown in Fig. 51 can only be caused by the interference of P_c states which have opposite parities.

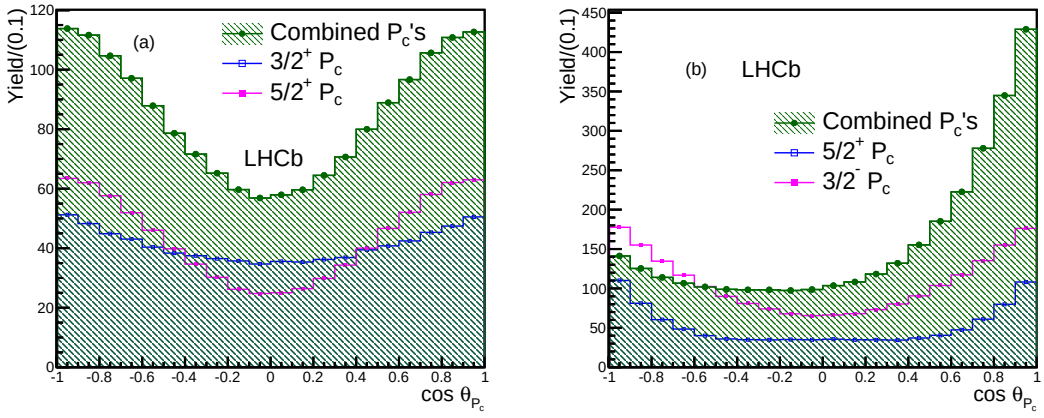

Figure 52: Distributions of $\cos\theta_{P_c}$ from individual and combined P_c contributions when the quantum numbers are taken as (a)$J^P(P_c(4380), P_c(4450)) = (3/2^+, 5/2^+)$ and (b) $J^P(P_c(4380), P_c(4450)) = (3/2^-, 5/2^+)$

To prove the statement that distributions resulting from a single P_c state will always be symmetric, the expression for the angular distribution of $\cos\theta_{P_c}$ is examined. In these considerations, the J/ψ is treated as a final state particle. Using the formalism and notation of Sec. 5, the distribution can be expressed as

$$I(\theta_{P_c}) = \sum_{\lambda_{P_c},\lambda_\psi^{P_c},\lambda_p^{P_c}} I^{\lambda_{P_c}}_{\lambda_\psi^{P_c},\lambda_p^{P_c}}(\theta_{P_c}), \tag{73}$$

with

$$I^{\lambda_{P_c}}_{\lambda_\psi^{P_c},\lambda_p^{P_c}}(\theta_{P_c}) = \left| \sum_j \mathcal{H}^{P_{cj}}_{\lambda_{P_c}} \mathcal{H}^{P_{cj}\to\psi p}_{\lambda_\psi^{P_c},\lambda_p^{P_c}} d^{J_{P_{cj}}}_{\lambda_{P_c},\lambda_\psi^{P_c}-\lambda_p^{P_c}}(\theta_{P_c}) \right|^2 . \tag{74}$$

A similar equation can be obtained from the full decay matrix of $\Lambda_b^0 \to P_c^+ K^-; P_c^+ \to \psi p; \psi \to \mu^+\mu^-$ decay chain, by integrating over all other variables. The λ_{P_c} index of the Wigner d-matrix can take values of $\pm\frac{1}{2}$, as determined by angular momentum conservation in the $\Lambda_b^0 \to P_c K^-$ decay, while the $\lambda_\psi^{P_c} - \lambda_p^{P_c}$ index takes the values $\pm\frac{3}{2}, \pm\frac{1}{2}$, as allowed in the $P_c \to \psi p$ decay. The P_c decays strongly, which means parity is conserved

and the $\mathcal{H}^{P_{cj}\to\psi p}_{\lambda_\psi^{P_c},\lambda_p^{P_c}}$ couplings must follow the relation

$$\mathcal{H}^{P_{cj}\to\psi p}_{-\lambda_\psi^{P_c},-\lambda_p^{P_c}} = P_{P_{cj}}(-1)^{\frac{1}{2}-J_{P_{cj}}}\mathcal{H}^{P_{cj}\to\psi p}_{\lambda_\psi^{P_c},\lambda_p^{P_c}}. \tag{75}$$

For only one P_c state ($j=1$), the sum of the terms with $(\lambda_\psi^{P_c},\lambda_p^{P_c})$ and $(-\lambda_\psi^{P_c},-\lambda_p^{P_c})$ for given any λ_{P_c} is

$$\begin{aligned} & I^{\lambda_{P_c}}_{\lambda_\psi^{P_c},\lambda_p^{P_c}}(\theta_{P_c}) + I^{\lambda_{P_c}}_{-\lambda_\psi^{P_c},-\lambda_p^{P_c}}(\theta_{P_c}) \\ = & \left|\mathcal{H}^{P_c}_{\lambda_{P_c}}\mathcal{H}^{P_c\to\psi p}_{\lambda_\psi^{P_c},\lambda_p^{P_c}}\right|^2\left(|d^{J_{P_c}}_{\lambda_{P_c},\lambda_\psi^{P_c}-\lambda_p^{P_c}}(\theta_{P_c})|^2 + |d^{J_{P_c}}_{\lambda_{P_c},-(\lambda_\psi^{P_c}-\lambda_p^{P_c})}(\theta_{P_c})|^2\right), \end{aligned} \tag{76}$$

where Eq. (75) is used. It is seen that the angular distribution is the sum of terms which are quadratic in Wigner small d-matrices. The Wigner d-matrices are always either odd or even functions. As both an odd function multiplying itself and an even function multiplying itself will always be even, and the addition of an even function with another even function is also even, the angular distribution will always be even. Thus, for a single P_c state, the $\cos\theta_{P_c}$ distribution will alawys be symmetric around 0.

Next the two P_c case is considered. The sum term is now given by

$$\begin{aligned} & I^{\lambda_{P_c}}_{\lambda_\psi^{P_c},\lambda_p^{P_c}}(\theta_{P_c}) + I^{\lambda_{P_c}}_{-\lambda_\psi^{P_c},-\lambda_p^{P_c}}(\theta_{P_c}) \\ & = \left|H_1 d^{J_{P_{c1}}}_{\lambda_{P_c},\lambda_\psi^{P_c}-\lambda_p^{P_c}}(\theta_{P_c}) + H_2 d^{J_{P_{c2}}}_{\lambda_{P_c},\lambda_\psi^{P_c}-\lambda_p^{P_c}}(\theta_{P_c})\right|^2 \\ & + \left|H_1 d^{J_{P_{c1}}}_{\lambda_{P_c},-(\lambda_\psi^{P_c}-\lambda_p^{P_c})}(\theta_{P_c}) + P_{P_{c1}}P_{P_{c2}}(-1)^{J_{P_{c1}}-J_{P_{c2}}}H_2 d^{J_{P_{c2}}}_{\lambda_{P_c},-(\lambda_\psi^{P_c}-\lambda_p^{P_c})}(\theta_{P_c})\right|^2, \end{aligned} \tag{77}$$

where $P_{P_{c1}}$ $P_{P_{c2}}$ are parities of the two P_c, and for short

$$H_j = \mathcal{H}^{P_{cj}}_{\lambda_{P_c}}\mathcal{H}^{P_{cj}}_{\lambda_\psi^{P_c},\lambda_p^{P_c}} \tag{78}$$

It is found by a Mathematica investigation that when the parities of the two P_c states are equal the $\cos\theta_{P_c}$ distribution will be symmetric, and when the parities are opposite the distribution will be asymmetric.

11.2 Comparison of the data and amplitude model $\cos\theta_{P_c}$ distributions

The asymmetric $\cos\theta_{P_c}$ distribution of the data and how it is accounted for in the default amplitude model is directly studied here. The distribution is examined in the range of $4.41 - 4.49$ GeV, in order to directly study the P_c region of interest and to reduce the Λ^* background. This corresponds to roughly $m_{P_c(4450)} \pm \Gamma_{P_c(4450)}$, and captures most of the $P_c(4450)$ rate and its interference with $P_c(4380)$. The data is efficiency-corrected and background-subtracted to remove distortions of the distribution from either of these sources. It is displayed along with the efficiency-corrected projections of the total amplitude model, total Λ^* and P_c contributions, and individual P_c constributions in the left plot of Fig. 53. The background component of the total amplitude model has also been removed. It is seen that there is a clear asymmetry in the excess of the data over the Λ^* contribution, indicating that the default Λ^* model is incapable of producing the asymmetry present in the P_c peak. Further, the combined P_c contribution matches this excess quite well. This can be more easily seen in the right plot of Fig. 53, in which the total Λ^* contribution has been subtracted from the data.

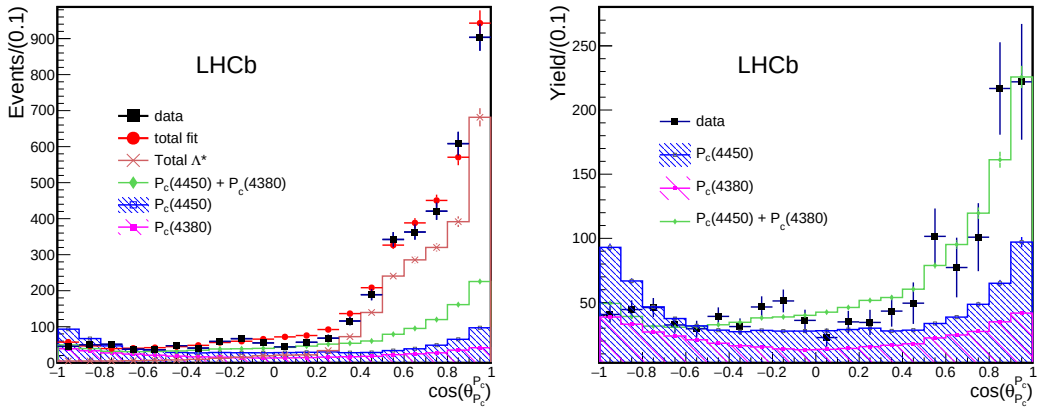

Figure 53: (left) Distribution of $\cos\theta_{P_c}$ from efficiency-corrected and background-subtracted data, along with the total fit, total Λ^* contribution, total P_c contribution, and individual P_c contributions. (right) The left plot with the total Λ^* contribution subtracted from the data.

For a direct demonstration that two same-parity P_c states will not be able to describe the data, see Appendix F, where the best fit obtained with same-parity states is shown.

The fit does a poor job of describing the $m_{J/\psi p}$ distribution, and has a $\Delta(-2\ln\mathcal{L})$ which is 5.1^2 worse than the default fit. Thus direct tests of the same-parity states are in agreement with the arguments presented in this section. It should be noted that low mass Λ^* states are also capable of generating an asymmetric $\cos\theta_{P_c}$ distibution which peaks towards $+1$. Thus the conclusion that two opposite-parity P_c states must be present in order to describe the data relies on the validity of the assumption that the asymmetry in the $m_{J/\psi p}$ peak is a result of activity in the $J/\psi p$ system, and not a byproduct of some unrepresented Λ^* components.

12 Significance of the P_c states

The significance of the P_c states is quantified via the hypothesis testing performed in this section. Three different hypotheses are considered: no P_c's are present in the data, a single P_c is present, and two P_c's are present. These are referred to as $H_{\text{no}\,P_c}$, $H_{1\,P_c}$, and $H_{2\,P_c}$. The goal is to calculate the probability that a "null hypothesis" is true against an "alternative hypothesis". This probability is the "$p-$value", which formally is the probability that, when the null hypothesis is true, the test variable returns a value equal to or more extreme than the measured value. The $p-$value is often expressed in terms of an equivalent number of Gaussian standard deviations, n_σ. They are related to each other as

$$p = 1 - \int_0^{n_\sigma} G(x)dx\,, \tag{79}$$

where $G(x)$ is the Gaussian distribution and one sided probability is used, as these are nested hypotheses. Thus n_σ can be calculated with the help of the inverse complementary error function:

$$n_\sigma(p) = \sqrt{2}\,\text{erfc}^{-1}(2p)\,. \tag{80}$$

Three types of hypothesis testing are performed

1. $H_{1\,P_c}$ **vs** $H_{\text{no}\,P_c}$: Null hypothesis $H_{\text{no}\,P_c}$ tested against alternative hypothesis $H_{1\,P_c}$. This can be thought of as the significance of $P_c(4450)$.

2. $H_{2\,P_c}$ **vs** $H_{1\,P_c}$: Null hypothesis $H_{1\,P_c}$ tested against alternative hypothesis $H_{2\,P_c}$. This can be thought of as the significance of $P_c(4380)$.

3. $H_{2\,P_c}$ **vs** $H_{\text{no}\,P_c}$: Null hypothesis $H_{\text{no}\,P_c}$ tested against alternative hypothesis $H_{2\,P_c}$. This can be thought of as the significance of both P_c's.

For each of these types of tests, the extended Λ^* model is used in order to be most conservative.

To calculate a $p-$value, the expected distribution of the $\Delta(-2\ln\mathcal{L})$ test variable must first be known, where the difference of the log-likelihoods is between the null and the alternative hypotheses. The hypothesis tests listed above are examples of nested hypotheses,

meaning the null hypothesis is a subset of the more general alternative hypothesis. For such cases, Wilks' Theorem says that in the asymptotic limit of infinite statistics, the $\Delta(-2\ln\mathcal{L})$ distribution will be distributed as a χ^2_k distribution with a number of degrees of freedom k which is equal to the difference in total free parameters between the alternative and null hypothesis. The $p-$value can then be calculated as

$$p = \int_{\Delta(-2\ln\mathcal{L})}^{\infty} \chi^2_k(x)\,dx. \tag{81}$$

An issue arises, though, in adding resonances with free mass and width, which are undefined under the null hypothesis. In such a scenario, the likelihood regularity is not satisfied, and Wilks' theorem no longer holds. This is a case of needing to take into account the "look elsewhere effect"; the null hypothesis isn't testing against a single alternative hypothesis, but a continuum of hypotheses with varying masses and widths. Statistical simulations under the null hypothesis must be performed in order to obtain an effective number of degrees of freedom ($\mathrm{ndf}_{\mathrm{eff}}$). This is done by generating pseudoexperiments under the null hypotheses, and calculating $\Delta(-2\ln\mathcal{L})$ for each pseudoexperiment. Enough of these are done to get a handle on the distribution of $\Delta(-2\ln\mathcal{L})$ under the null hypothesis. The distribution of $\Delta(-2\ln\mathcal{L})$ is then fit with a χ^2_k distribution in order to determine $k = \mathrm{ndf}_{\mathrm{eff}}$. This can then be used with the $\Delta(-2\ln\mathcal{L})$ to calculate the $p-$value using Eq. 81.

All parts of the fit are simulated in the pseudoexperiments. This includes simulating the event samples of the Λ_b^0 signal regions, the Λ_b^0 sidebands, and the fully simulated phase space MC, in statistics which match those used in the fit to the real data. The data sets are generated by throwing events uniformly in the 6D phase space, and then shaping them as described below. The events in the signal region are a mixture of the $\Lambda_b^0 \to J/\psi\, K^- p$ signal events and background events. Thus for the background fraction β (5.4%) and total number of events in the signal range $N_{\mathrm{signal-band}}$ (27469), a total of $\beta N_{\mathrm{signal-band}}$ background-type events are generated and $(1-\beta)N_{\mathrm{signal-band}}$ signal-type events are generated. The signal-type events are shaped according to the amplitude model corresponding to the null hypothesis being tested. Thus, for example, in the $H_{1\,P_c}$

vs $H_{\text{no}\,P_c}$ type of hypothesis test, the signal events are shaped according to the amplitude model obtained by fitting the extended Λ^* model to the data. The background-type events are shaped according to the parameterized background built from the Λ_b^0 sidebands of the real data (Eq. 69). The Λ_b^0 sidebands are also shaped according to the background parametrization. Note that this sideband pseudo-data set is then used for constructing the background parametrization used in the pseudoexperiment. Similarily the MC pseudo-data set is shaped using the efficiency parametrization built from the MC data set used in the fit to the real data, and is then used to construct the efficiency parametrization used in the pseudoexperiment. The fits are then performed the same way as to the real data sample, but using the pseudo-data sets.

Pseudoexperiments were performed for each of the types of hypothesis testing, and the distributions of the $\Delta(-2\ln\mathcal{L})$ test variable were accumulated. The fitted ndf_{eff} for each type can be seen in Table 8, where they can also be compared to the change in the number of parameters obtained when going from the nested null hypothesis to the more general alternative hypothesis. In the significance calculation of the $Z(4430)^+$ in the LHCb amplitude analysis, it was found that the simulated $\Delta(-2\ln\mathcal{L})$ distribution was well described by a χ^2 distribution with an ndf_{eff} value around twice the number of free parameters in the $Z(4430)^+$ term [19]. We see approximately the same behavior here. In order to be conservative, the statistical uncertainty for the fitted ndf_{eff} is added to it, and this value is then rounded up to the nearest integer before being used to calculate the $p-$value. For example, $k = 20$ is used in Eq. 81 along with $\Delta(-2\ln\mathcal{L}) = 14.7^2$ for the $H_{1\,P_c}$ vs $H_{\text{no}\,P_c}$ hypothesis test. Equation 80 is then used to convert the $p-$value to standard deviations. The resulting significances with which the null hypothesis can be rejected are also listed in Table 8. It is seen that the significance of $P_c(4450)$ can

Table 8: For each type of hypothesis testing performed: the difference in free parameters for the nested hypothesis, the ndf_{eff}, the $\Delta(-2\ln\mathcal{L})$, and the significance with which the null hypothesis can be rejected.

Test	Δ param	ndf_{eff}	$\Delta(-2\ln\mathcal{L})$	Significance (σ)
$H_{1\,P_c}$ vs $H_{\text{no}\,P_c}$	10	18.1 ± 1.0	14.7^2	12.2
$H_{2\,P_c}$ vs $H_{1\,P_c}$	10	13.6 ± 1.5	11.6^2	9.2
$H_{2\,P_c}$ vs $H_{\text{no}\,P_c}$	20	42.5 ± 2.4	18.7^2	14.6

be taken as approximately $12.2\,\sigma$, $P_c(4380)$ as approximately $9.2\,\sigma$, and their combined significance approximately $14.6\,\sigma$. These are about 20% lower than the naive estimates obtained using $\sqrt{(}\Delta(-2\ln\mathcal{L}))$. The word "approximately" needs to be noted here, as the number of pseudoexperiments necessary to calculate the significances to these precisions would be impractical. Each pseudoexperiment performed for this analysis takes about a day running on 12 CPU cores. Because of the limited availability of such hardware and the large CPU consumption, it is impossible to simulate such a large number of experiments. The conclusion that should be drawn is that the P_c states are overwhelmingly significant.

13 Quantum numbers of the P_c states

The studies done in this section detail the efforts to attempt a determination of the quantum numbers of the P_c states. For two models representing separate hypotheses, *e.g.* when discriminating between different J^P values assigned to a P_c state, the $\Delta(-2\ln\mathcal{L})$ can be assumed to be distributed under the disfavored J^P hypothesis as a χ^2 distribution with one degree of freedom (ndf = 1). This gives an upper limit on the $p-$value for the disfavored hypothesis [55], or equivalently a lower limit on the significance of its rejection. To accurately determine the significances, statistical simulations would be necessary in order to obtain the actual distribution of $\Delta(-2\ln\mathcal{L})$ under the disfavored hypothesis. These statistical simulations would require a large number of pseudoexperiments, and there are a large number of alternative quantum number hypotheses to test against (64 in total). While many of the hypotheses have such poor $\Delta(-2\ln\mathcal{L})$ values that they can be ruled out without statistical simulations, there is some dependence of the rankings on the Λ^* model used (see next subsection 13.1). For these reasons, and the fact that the pseudoexperiments are very computationally demanding, the lower limit of rejection for the disfavored hypotheses given by $\sqrt{\Delta(-2\ln\mathcal{L})}$ is used.

As was mentioned in Sec. 10.1, the fits to the data with the default Λ^* model and the two P_c states were performed with all possible combinations of the P_c quantum numbers for spins up to $J = 7/2$. The results for the J^P combinations with opposite parities are given in Table 9. They are ranked by $\Delta(-2\ln\mathcal{L})$, written as $(\sqrt{\Delta(-2\ln\mathcal{L})})^2$ so that the lower limit on the significance can easily be read off. Also given are the changes in mass and width for each P_c state, relative to the preferred hypothesis. While the $(3/2^-, 5/2^+)$ gives the best fit quality, $(3/2^+, 5/2^-)$ and $(5/2^+, 3/2^-)$ have comparable likelihoods. It was shown in Sec. 11 that the only way to obtain decent fits with this Λ^* model is for the P_c states to have opposite parities. Nevertheless, the results from the same parity combinations can be found in Appendix F, where it is shown that the same parity combinations are excluded at more than a 5σ level.

Table 9: Changes in fit quality ($(\sqrt{\Delta(-2\ln\mathcal{L})})^2$), masses, and widths of different J^P combinations with respect to the $(3/2^-, 5/2^+)$ fit.

		$P_c(4380)$		$P_c(4450)$	
$J^p(P_c(4380), P_c(4450))$	$(\sqrt{\Delta(-2\ln\mathcal{L})})^2$	M_0	Γ_0	M_0	Γ_0
Nominal Values					
$3/2^-, 5/2^+$	–	4380	205	4449.8	39
Δ from Nominal					
$3/2^+, 5/2^-$	0.9^2	-10	6	0.5	11
$5/2^+, 3/2^-$	2.3^2	-3	34	-1.3	6
$5/2^-, 3/2^+$	5.9^2	-30	-42	-4.1	17
$1/2^-, 3/2^+$	5.9^2	-10	47	-2.2	-2
$7/2^+, 5/2^-$	6.3^2	-4	48	-1.5	13
$3/2^-, 1/2^+$	6.3^2	-22	-19	-3.0	5
$3/2^+, 3/2^-$	6.4^2	-38	-64	-4.7	11
$5/2^-, 7/2^+$	6.8^2	6	47	-1.6	3
$7/2^-, 1/2^+$	6.8^2	-41	-69	-3.9	18
$7/2^+, 3/2^-$	7.2^2	-16	17	-3.9	13
$5/2^-, 5/2^+$	7.3^2	-27	-40	-3.8	5
$3/2^+, 1/2^-$	7.4^2	-38	-53	-3.1	11
$5/2^+, 1/2^-$	7.6^2	-38	-93	-4.0	15
$1/2^-, 1/2^+$	7.7^2	-22	-22	-4.4	7
$5/2^-, 1/2^+$	8.0^2	-15	21	-5.3	7
$3/2^-, 3/2^+$	8.3^2	-31	-55	-3.6	8
$7/2^+, 1/2^-$	8.5^2	-36	-57	-5.2	25
$7/2^+, 7/2^-$	8.6^2	27	174	-3.3	-0
$1/2^-, 5/2^+$	8.6^2	-9	-6	-2.2	-3
$7/2^-, 5/2^+$	8.9^2	-30	-63	-3.7	18
$1/2^+, 3/2^-$	8.9^2	-47	-87	-6.5	18
$7/2^-, 3/2^+$	8.9^2	-40	-67	-4.8	12
$1/2^+, 1/2^-$	9.0^2	-48	-71	-3.6	20
$1/2^-, 7/2^+$	9.4^2	-4	-1	-1.2	-5
$5/2^+, 7/2^-$	9.6^2	-16	-48	-0.3	9
$3/2^+, 7/2^-$	9.6^2	-13	-12	-2.9	-4
$5/2^+, 5/2^-$	9.9^2	-22	-4	-3.4	4
$3/2^-, 7/2^+$	9.9^2	2	17	-2.3	2
$7/2^-, 7/2^+$	10.5^2	-40	-91	-4.0	12
$1/2^+, 5/2^-$	10.9^2	-16	-37	-1.7	4
$1/2^+, 7/2^-$	11.6^2	-21	-33	-1.1	-1

13.1 Quantum Number Systematics

The preferred quantum numbers which were presented in the previous section are subject to potential biases from systematic effects. The most substantial effect arises from the model used to describe the Λ^* resonances, which dominate the $\Lambda_b^0 \to J/\psi K^- p$ decays. As a good description of the m_{Kp} distribution is already obtained with the default Λ^* model, deficiencies in the Λ^* model would show up in the description of angular distributions and their correlations. An imperfect description of these could then lead to the P_c contributions attempting to compensate for a lacking Λ^* model. In effect then, the quantum numbers would be tuned to the combined effects from the P_c contributions and the deficiencies in the Λ^* model, which could lead to departures from the true quantum numbers.

In order to study the systematic effect associated with the assumed Λ^* model, the quantum number study was repeated with the extended Λ^* model. As this includes more nuisance parameters for describing the Λ^* contributions, this allows for testing how much the preferred P_c quantum numbers are affected by possible deficiencies in the Λ^* model. These studies were only performed with the opposite-parity combinations of quantum numbers for spins up to 5/2, as it has been shown that an opposite parity is necessary and because spin 7/2 and higher are not plausible. The quantum number rankings obtained when using the extended Λ^* model are given in Table 10. It is seen that there is in fact some dependence on the Λ^* model, and the preferred set of quantum numbers changes. With the extended Λ^* model, the best fit occurs with the $5/2^+\,3/2^-$ set of quantum numbers. The $(3/2^-, 5/2^+)$ combination preferred with the default model is now ranked 3rd overall. Common between the default and extended Λ^* models, though, is that combinations with one P_c having spin 3/2 and the other having spin 5/2 are preferred. The conclusion from this study is that there are systematic effects associated with the Λ^* model. In-depth studies will have to be done in order to obtain a better Λ^* model, which will then hopefully lead to better determined quantum numbers for the P_c states.

Table 10: Results of the extended model quantum number preference study showing the changes in fit quality ($(\sqrt{\Delta(-2\ln\mathcal{L})})^2$), masses, and widths of different J^P combinations with respect to the $(3/2^-, 5/2^+)$ solution.

		$P_c(4380)$		$P_c(4450)$	
$J^p(4380, 4450)$	$(\sqrt{\Delta(-2\ln\mathcal{L})})^2$	M_0	Γ_0	M_0	Γ_0
	$(3/2-, 5/2^+)$ solution				
$3/2^-, 5/2^+$	$--$	4359	151	4450.1	49
	Δ from $(3/2-, 5/2^+)$ solution				
$5/2^+, 3/2^-$	-3.6^2	10	-7	-1.6	-6
$5/2^-, 3/2^+$	-2.7^2	-4	-9	-3.6	-2
$3/2^-, 5/2^+$	–	–	–	–	–
$3/2^+, 5/2^-$	$+3.5^2$	-3	-7	-1.9	-2
$5/2^-, 5/2^+$	$+3.6^2$	-26	-57	-4.8	-4
$5/2^+, 1/2^-$	$+4.2^2$	-19	-38	-4.4	-3
$3/2^-, 3/2^+$	$+5.1^2$	-27	-63	-5.1	-1
$3/2^+, 3/2^-$	$+5.7^2$	-23	-52	-5.2	-4
$3/2^+, 1/2^-$	$+5.9^2$	-8	-3	-2.6	-4
$1/2^+, 3/2^-$	$+6.7^2$	-11	-48	-4.1	-4
$5/2^-, 1/2^+$	$+7.0^2$	-17	-54	-4.8	-3
$5/2^+, 5/2^-$	$+7.2^2$	-14	-19	-2.5	-12
$3/2^-, 1/2^+$	$+7.3^2$	-10	-31	-2.8	-7
$1/2^-, 5/2^+$	$+7.5^2$	-15	-18	-4.4	-5
$1/2^-, 3/2^+$	$+7.7^2$	-17	-15	-2.0	-7
$1/2^-, 1/2^+$	$+8.2^2$	-8	-22	-2.8	-7
$1/2^+, 5/2^-$	$+8.4^2$	-41	-72	-5.8	-5
$1/2^+, 1/2^-$	$+8.5^2$	-36	-57	-3.8	-2

14 Further Cross checks

This section details various cross checks and studies which were performed. Some of these include comparisons of the fit results to the default fit, but are meant solely as consistency checks and do not warrant any systematic uncertainty to be associated with them. In addition to these studies, the fits to the data performed with the *sFit* method and using the default amplitude model can be found in Appendix E, along with fits peformed with the extended Λ^* model without P_c's, a single P_c, and two P_c's.

14.1 Examination of $m_{J/\psi K}$

When invoking pentaquark resonances to be able to reproduce the data, it is only natural to consider whether or not there are any Z tetraquark resonances present in the $J/\psi K^-$ system. This was discussed in Sec. 4.2, where the $(m^2_{Kp}, m^2_{J/\psi K})$ and $(m^2_{J/\psi p}, m^2_{J/\psi K})$ Dalitz planes, as well as the 1D $m_{J/\psi K}$ distribution, were shown. While there were apparent structures in the $m_{J/\psi K}$ distribution, studying the Dalitz planes indicated that any structures were reflections. Here, the ability of the default Λ^* model with the $P_c(4450)$ and $P_c(4380)$ states to reproduce the structures in $m_{J/\psi K}$ is studied. In Fig. 54 the $m_{J/\psi K}$ mass distribution of the data is shown along with the projection of the amplitude model. It is shown in the usual intervals of m_{Kp} mass, as well as for the full mass range. The amplitude model is seen to be able to reproduce the data, confirming that reflections are likely the cause of the structures seen.

14.2 Check on Λ_b^0 polarization

As a consequence of the parity conservation in the strong production mechanism, the Λ_b^0 polarization must be zero for the selected choice of its spin quantization axis. Therefore, measuring the longitudinal polarization by the fit to the data constitutes a good cross-check of the efficiency simulation. This is accomplished by introducing the polarization asymmetry, $a_{\rm pol} \equiv (P_{\lambda_{\Lambda_b^0}=+1/2} - P_{\lambda_{\Lambda_b^0}=-1/2})/(P_{\lambda_{\Lambda_b^0}=+1/2} + P_{\lambda_{\Lambda_b^0}=-1/2})$, as a free parameter in the fit by multiplying the $\lambda_{\Lambda_b^0} = +1/2$ term in Eq. (60) by $(1 + a_{\rm pol})/2$, and the $-1/2$

term by $(1 - a_{\rm pol})/2$ ($P_{\lambda_{\Lambda_b^0}}$ stands for the probability of helicity $\lambda_{\Lambda_b^0}$). This study was performed with the *sFit* technique. The fit with the default Λ^* and P_c model yields a polarization value consistent with zero, $(-2.0 \pm 2.3)\%$, as expected.

14.3 Subtraction of $\overline{B}{}^0_s \to J/\psi K^- K^+$ and $\overline{B}{}^0 \to J/\psi K^- \pi^+$ backgrounds in the fit

In the nominal method, reflections from $\overline{B}{}^0_s \to J/\psi K^- K^+$ and $\overline{B}{}^0 \to J/\psi K^- \pi^+$ are explicitly vetoed. The peaking structure is of course present before applying the veto. However as the veto does modify the efficiency across the Dalitz plane (see Fig. 103), it is worth examining the consistency of the results obtained when no such veto is applied. This test was done with the *sFit* method. Monte Carlo simulations of the $\overline{B}{}^0_s \to J/\psi K^- K^+$ and $\overline{B}{}^0 \to J/\psi K^- \pi^+$ decays were used to parametrize the $m_{J/\psi pK}$ distribution, as shown in Fig. 55. Using the usual shapes for the combinatoric background (exponential function) and signal peak (double-sided Hypatia function), the *sPlot* procedure is then performed with the four different event types. The sWeights are obtained only from the overall $m_{J/\psi K^- p}$ mass fit, because of the difficultly in obtaining an estimate of the reflection in each of the 4x8 bins nominally used for determining the sWeights.

The data with no vetos applied is compared to the projections of the amplitude model onto m_{Kp} and $m_{J/\psi p}$ in Fig. 56. The comparison of the angular variables is shown in Fig. 57, and $m_{J/\psi p}$ in different m_{Kp} mass intervals in Fig. 58. It is seen that good descriptions of the data without the veto are also obtained with the default amplitude model. The resulting changes in the P_c parameters from the nominal method are listed in Table 11. Overall, the results are consistent, and only modest changes are seen.

Table 11: Changes in mass, width, and fit fraction resulting from fitting the data without any vetoes applied.

State	ΔM_0 (MeV)	$\Delta\Gamma_0$ (MeV)	Δ FF (%)
$P_c(4380)$	-12	-19	-1.9
$P_c(4450)$	-1.9	-5.9	0.39

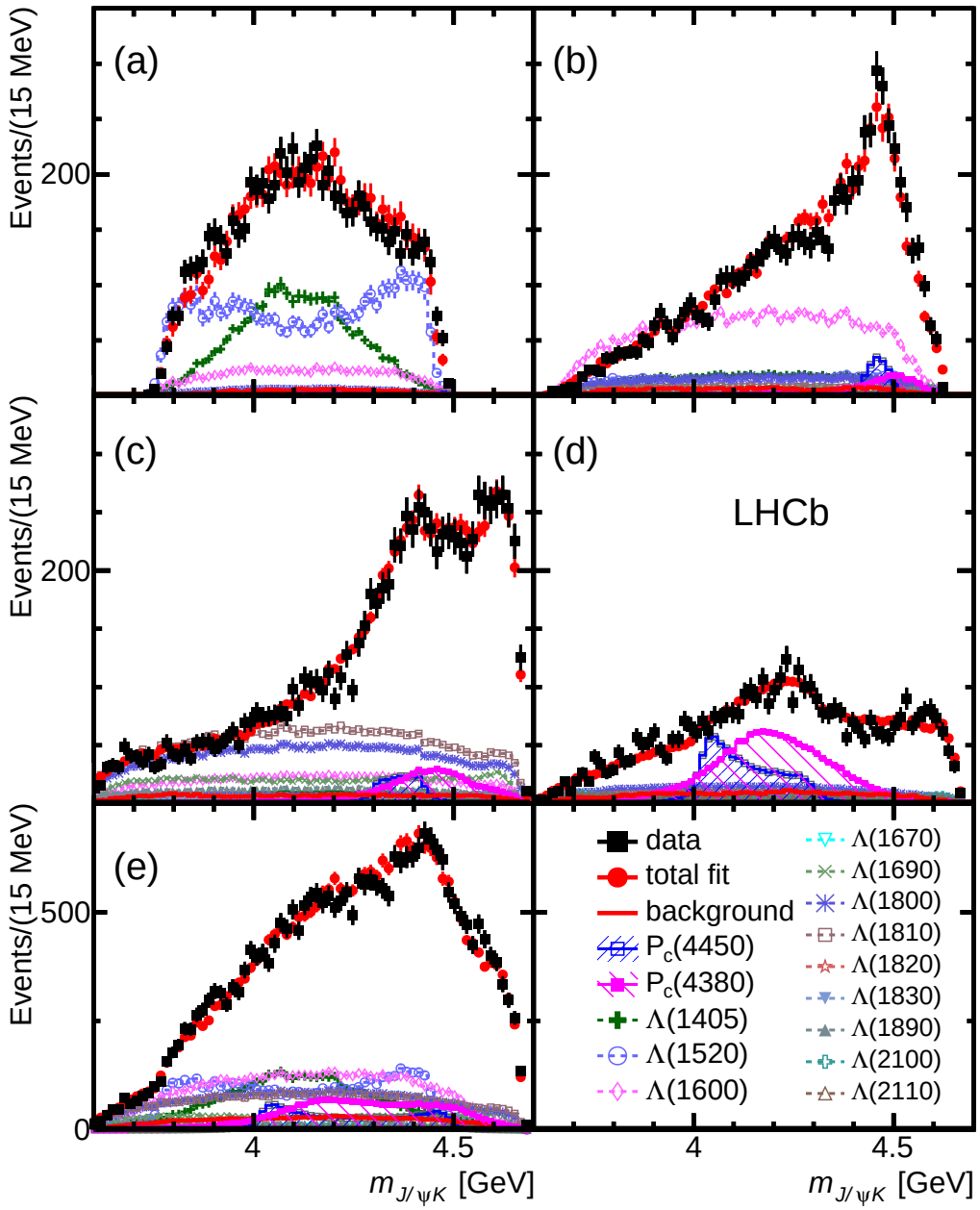

Figure 54: Fit projections of the default Λ^* model with two P_c^+ states onto $m_{J/\psi K}$ for various ranges of m_{Kp}: (a) $m_{Kp} < 1.55$ GeV, (b) $1.55 < m_{Kp} < 1.70$ GeV, (c) $1.70 < m_{Kp} < 2.00$ GeV, an d (d) $m_{Kp} > 2.00$ GeV. The data are shown as (black) squares with error bars, while the (red) circles show the results of the fit. The individual resonances are given in the legend.

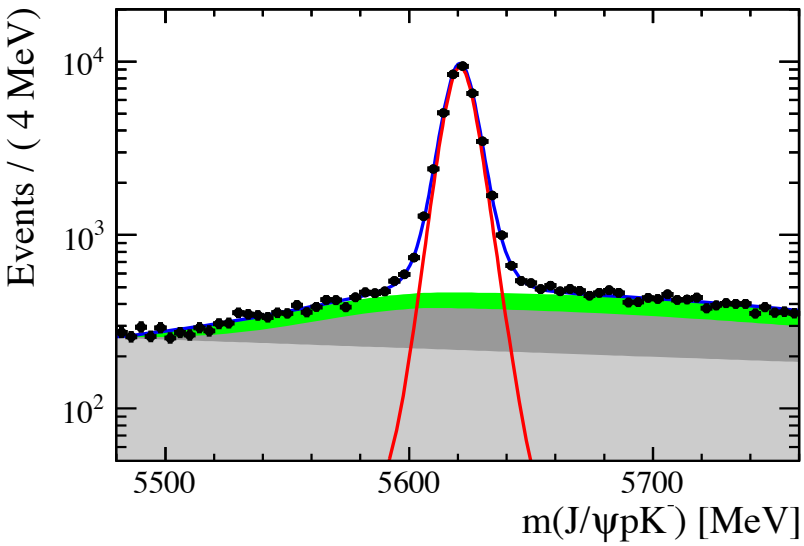

Figure 55: Fit to the $J/\psi K^-\pi^+$ mass spectrum where the $\overline{B}{}^0_s \to J/\psi K^-K^+$ and $\overline{B}{}^0 \to J/\psi K^-\pi^+$ reflections have been parameterized. The red solid line is the total fit, the blue solid line the signal shape, the light gray area the combinatoric background, the dark gray the contribution from $\overline{B}{}^0_s \to J/\psi K^-K^+$ and the green region the contribution from $\overline{B}{}^0 \to J/\psi K^-\pi^+$.

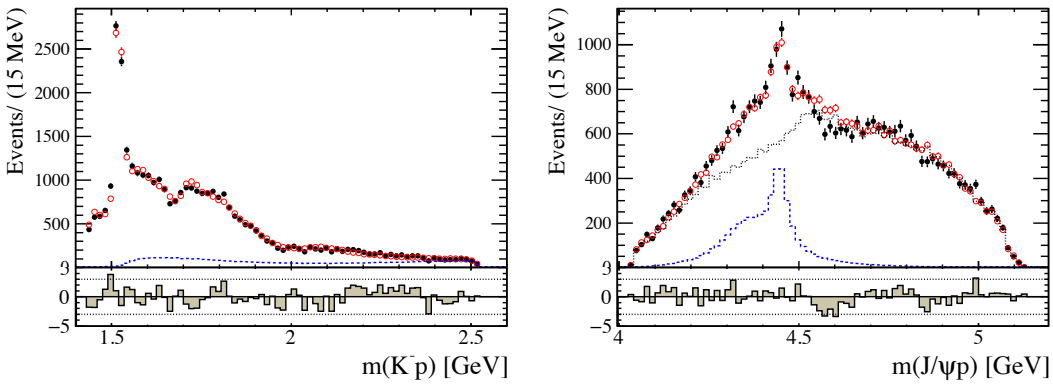

Figure 56: (*sFit*) Results of the study without any vetos and using the default amplitude model for (a) m_{Kp} and (b) $m_{J/\psi p}$. The data are shown as (black) squares with error bars, while the open (red) circles show the projection of the fit. The total Λ^* contribution is shown with the dashed grey line, and the total P_c contribution with the dashed blue line. The error bars on the points showing the fit results are due to simulation statistics.

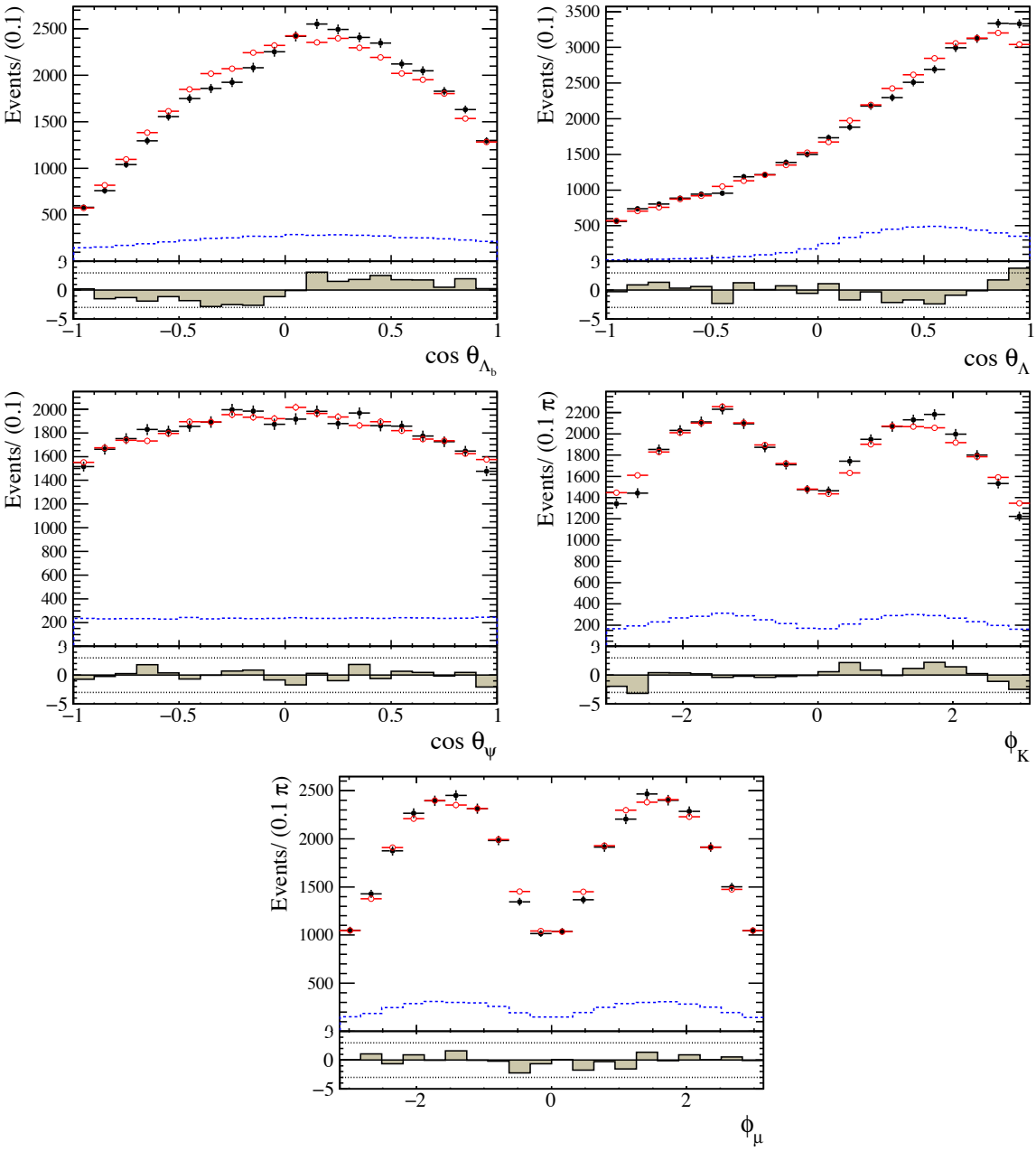

Figure 57: (*sFit*) Results of the study without any vetos and using the default amplitude model for the angular distributions. The data are shown as (black) squares with error bars, while the open (red) circles show the projection of the fit. The total Λ^* contribution is shown with the dashed grey line, and the total P_c contribution with the dashed blue line. The error bars on the points showing the fit results are due to simulation statistics.

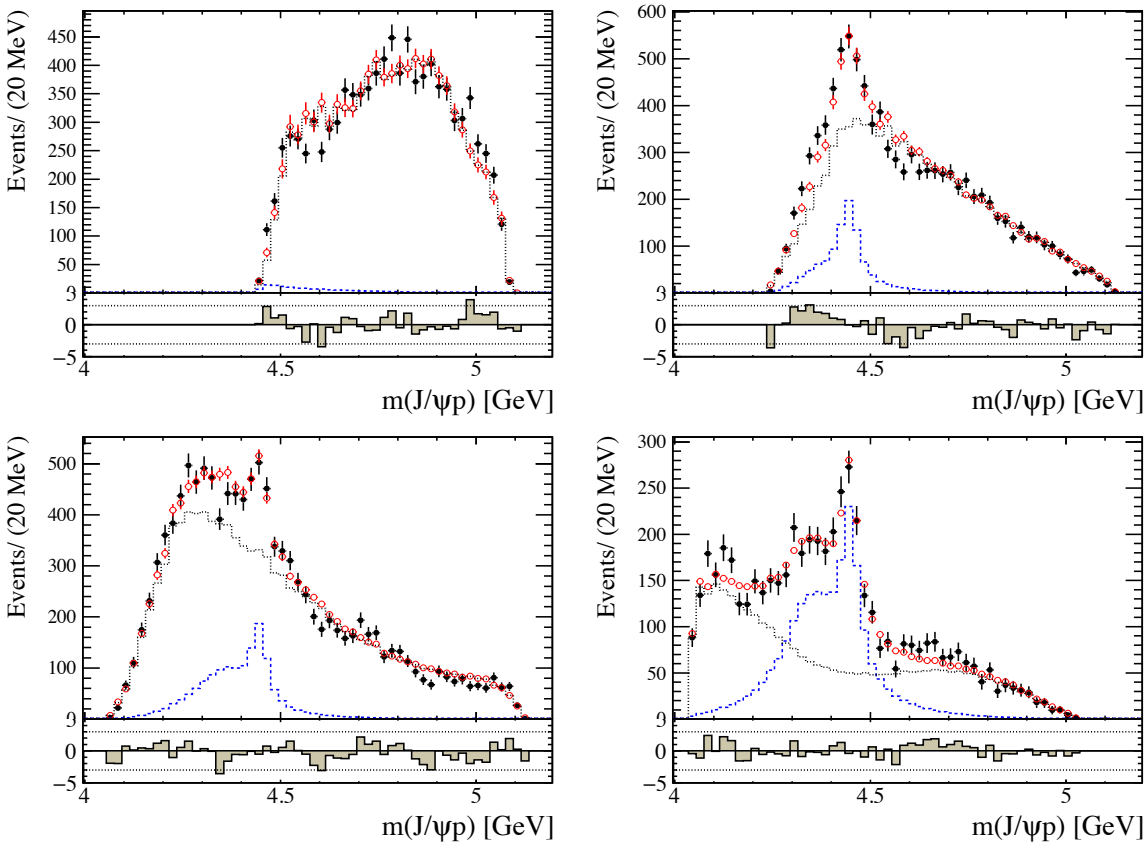

Figure 58: (*sFit*) Results of the study without any vetos and using the default amplitude model for for $m_{J/\psi p}$ in various intervals of m_{Kp}: (a) $m_{Kp} < 1.5$ GeV, (b) $1.55 < m_{Kp} < 1.70$ GeV, (c) $1.70 < m_{Kp} < 2.00$ GeV, and (d) $m_{Kp} > 2.0$ GeV. The data are shown as (black) squares with error bars, while the open (red) circles show the projection of the fit. The total Λ^* contribution is shown with the dashed grey line, and the total P_c contribution with the dashed blue line. The error bars on the points showing the fit results are due to simulation statistics.

14.4 Use of looser BDT cut

A fairly tight cut is used on the multivariate classifier (BDT) used for the final background suppression. For more details on this cut and to see various metrics that can be used for examining signal-to-background contributions, see Appendix C. In this section, a looser cut of BDT$>$ 0.5 is used. This doubles the background fraction (β), and increases the signal yield by 14%. The m_{Kp} and $m_{J/\psi p}$ mass distributions of the data with the looser BDT cut are shown along with the projections from the amplitude model in Fig. 59. The similar plots for the angular distributions are shown in Fig. 60, and the $m_{J/\psi p}$ distribution in intervals of m_{Kp} are shown in Fig. 61. The results are compared to the nominal values of the P_c parameters for consistency, and the changes reported as standard deviations are shown in Table 12. The results obtained with the looser BDT cut are in good agreement with the nominal results.

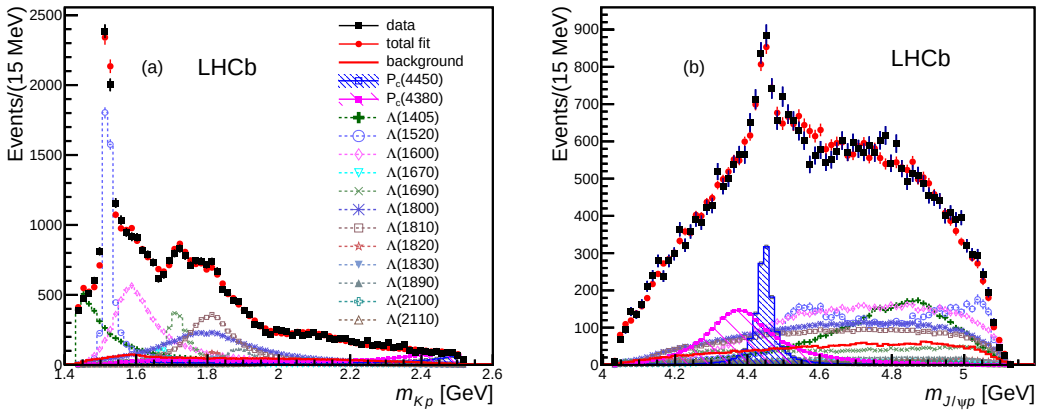

Figure 59: Results of the study using a looser BDT cut and using the default amplitude model for (a) m_{Kp} and (b) $m_{J/\psi p}$. The data are shown as solid (black) squares, while the solid (red) points show the results of the fit. The solid (red) histogram shows the background distribution. The (blue) open squares with the shaded histogram represent the $P_c(4450)^+$ state, and the shaded histogram topped with (purple) filled squares represents the $P_c(4380)^+$ state. Each Λ^* component is also shown. The error bars on the points showing the fit results are due to simulation statistics.

Table 12: Changes in mass, width, and fit fraction reported in standard deviations, resulting from fitting the data without any vetoes applied.

State	ΔM_0	$\Delta\Gamma_0$	Δ FF
$P_c(4380)$	0.0	0.1	-0.2
$P_c(4450)$	-0.7	0.2	0.2

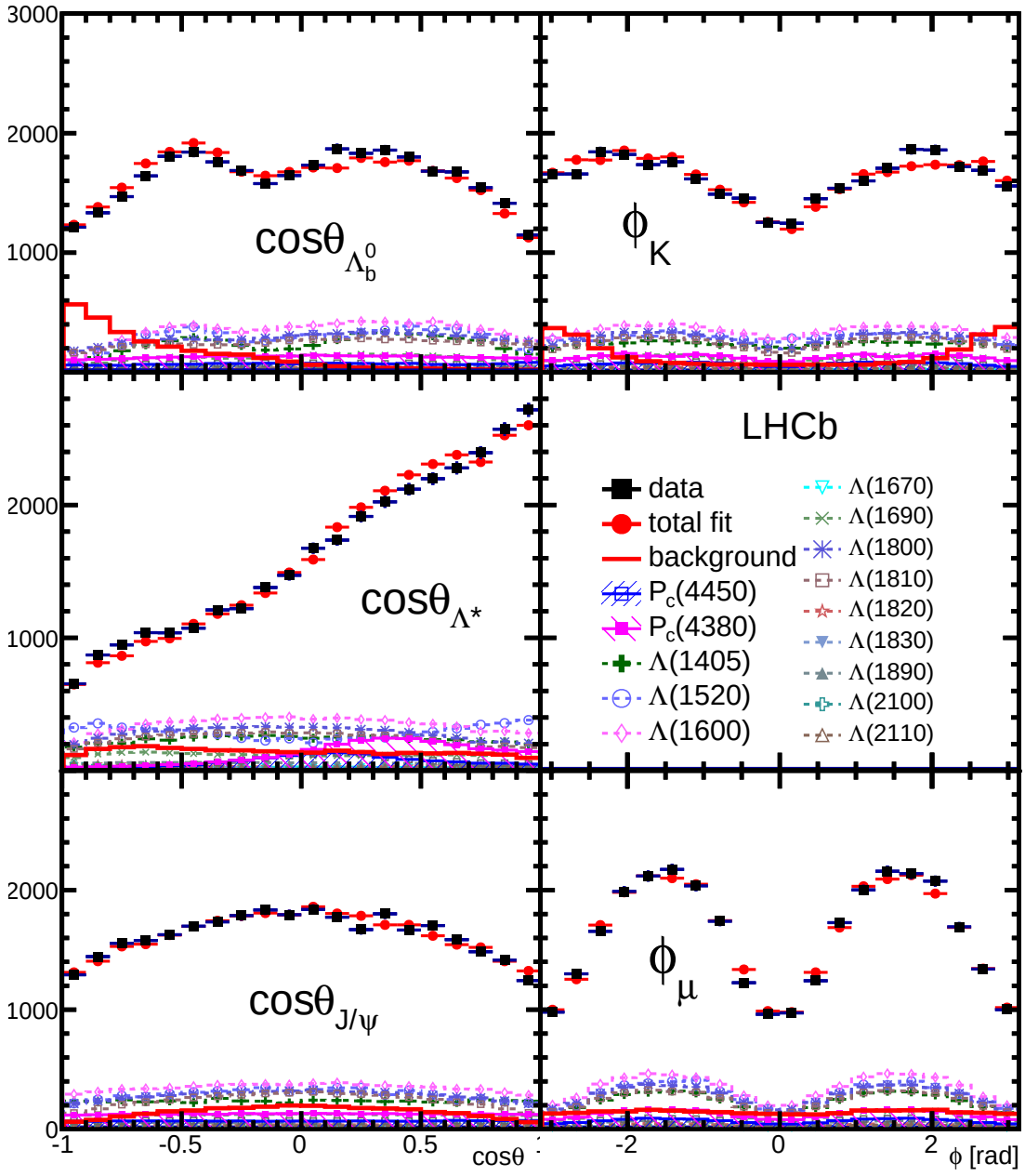

Figure 60: Results of the study using a looser BDT cut and using the default amplitude model for the angular distributions. The data are shown as (black) squares, while the (red) circles show the results of the fit. Each fit component is also shown. The angles are defined in Sec. 5.2.

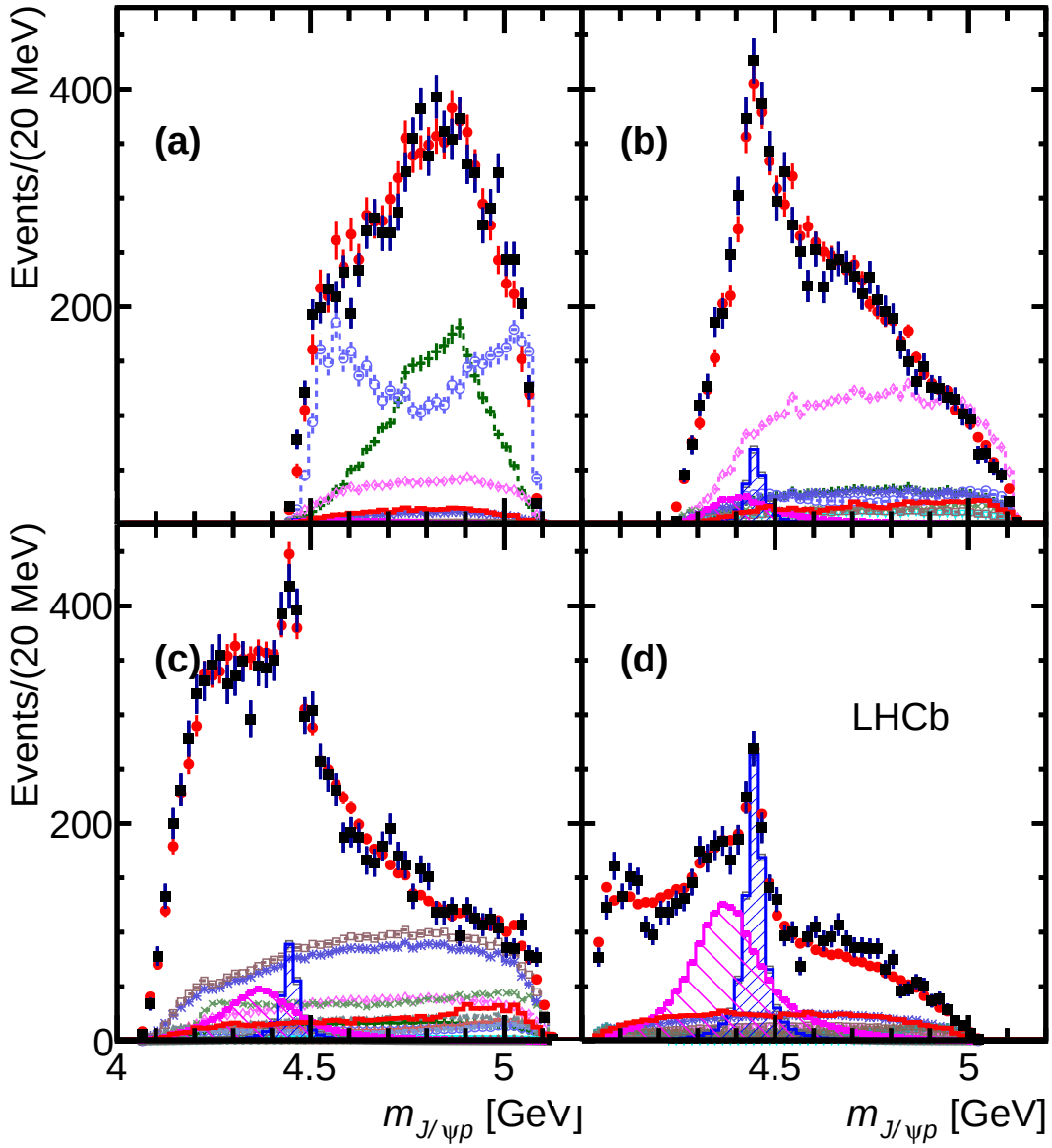

Figure 61: Results of the study using a looser BDT cut and using the default amplitude model for various intervals of m_{Kp}: (a) $m_{Kp} < 1.55$ GeV, (b) $1.55 < m_{Kp} < 1.70$ GeV, (c) $1.70 < m_{Kp} < 2.00$ GeV, an d (d) $m_{Kp} > 2.00$ GeV. The data are shown as (black) squares with error bars, while the (red) circles show the results of the fit. The blue and purple histograms show the two P_c^+ states. See Fig. 47 for the legend.

14.5 Separate Λ_b^0 p_{T} intervals

Here, the data is divided into two intervals corresponding to events in which the Λ_b^0 transverse momentum is above or below 6.5 GeV. The two data sets are then fit using the default amplitude model. This study was done with the *sFit* method, and the results are given in Table 13, where it is seen that the values obtained in the bins are all within two standard deviations of each other.

Table 13: Deviation in P_c fit parameters given in standard deviations, and obtained from data separated into two p_{T} intervals.

State	ΔM_0	$\Delta\Gamma_0$	Δ FF
$P_c(4380)$	1.2	0.2	0.9
$P_c(4450)$	1.1	2.0	1.1

14.6 Variations with HLT1 trigger line

In the nominal selection criteria, it is required that events pass at least one of three Hlt1 trigger lines. To examine any possible biases or differences in trigger lines, separate fits are performed to three data sets in which it is required that all events pass just one of the three trigger lines. This study was performed with the *sFit* method, and Table 14 shows the difference between the default fit and the fits using individual trigger lines.

Table 14: Changes in fit results from the nominal values for different HLT1 trigger lines: mass (M_0), width (Γ_0), and fit fractions (FF). Units of M_0 and Γ_0 are in MeV, while FF is in %.

		$P_c(4380)$			$P_c(4450)$			$\Lambda^*(1405)$	$\Lambda^*(1520)$
Hlt1 Line	f	M_0	Γ_0	FF	M_0	Γ_0	FF	FF	FF
DiMuonHighMass	0.82	+5	-5	-0.4	+0.3	+1	-0.5	+0.2	-0.4
TrackAllL0	0.75	+8	+25	-0.1	+0.3	-5	-0.5	-0.3	+0.1
TrackMuon	0.95	+1	+3	0.0	+0.7	-1	0.0	0.0	0.0

15 Systematic uncertainties

In this section, systematic uncertainties on the mass, width, and fit fraction of the P_c states are estimated. In addition, uncertainties on the fit fractions of the $\Lambda(1405)$ and $\Lambda(1520)$ states will be estimated, as they are well-separated from the other Λ^* resonances.

15.1 Variations in Λ^* masses and widths

In the nominal fits, the mass and width of the Λ^* states are fixed to the values reported by the PDG [27] and listed in Table 5. Thus, there is a systematic uncertainty associated with the masses and widths used. In order to assess this, fits were performed in which the masses and widths were allowed to vary within the uncertainties given in the PDG. This was done separately for each Λ^* state, and was performed with the *sFit* background subtraction method. The effects on the reported quantities are given in Table 15. The uncertainties associated with each resonance are added in quadrature, resulting in the values given at the bottom of the table.

Table 15: Variations in reported quantites when allowing the mass and width of each Λ^* resonance to vary in the fit. The last row gives the overall uncertainty.

Λ^* state	ΔM_0 (MeV)		$\Delta\Gamma_0$ (MeV)		FF (%)			
varied	$P_c(4380)$	$P_c(4450)$	$P_c(4380)$	$P_c(4450)$	$P_c(4380)$	$P_c(4450)$	$\Lambda(1405)$	$\Lambda(1520)$
1405	-1.0	0.00	1.1	-0.09	0.02	0.01	1.77	0.00
1520	-1.1	0.04	-1.1	0.44	-0.01	0.08	-0.20	1.02
1600	-0.3	-0.62	-9.6	3.69	-0.25	0.24	-1.70	-2.22
1670	0.8	-0.27	-4.0	-0.36	-0.15	-0.13	-0.11	-0.02
1690	-0.8	-0.03	1.2	-1.10	0.08	-0.06	-0.12	0.17
1800	-4.6	-0.20	4.7	1.40	0.21	0.13	-0.09	-0.06
1810	-2.6	0.01	3.2	0.45	0.14	0.13	-0.04	0.01
1820	-0.6	0.01	1.5	0.33	0.08	0.05	0.02	0.01
1830	-1.6	-0.12	2.4	0.14	0.08	0.02	0.15	0.00
1890	2.9	0.12	14.2	-1.19	0.37	-0.11	0.21	0.05
2100	0.3	0.03	-0.8	-0.10	-0.04	0.00	0.00	-0.02
2110	-1.3	-0.04	-5.1	0.25	-0.17	0.00	-0.12	0.00
Total	±6.6	±0.7	±19.5	±4.4	0.58	0.37	±2.49	±2.45

15.2 Orbital angular momentum in Λ^* parametrization

The resonance parametrization used for describing Λ^* resonances (Eq. 23) assumes the lowest possible value for $L^{\Lambda^*}_{\Lambda^0_b}$, the orbital angular momentum present in the $\Lambda^0_b \to J/\psi\,\Lambda^*$ decay. This is in accordance with the expectation that higher angular momenta values

are suppressed via angular momentum barriers. The value chosen enters explicitly in Eq. 23, and also enters via the Blatt-Weisskopf function, Eq. 24. Note that there are only two possible values of angular momentum in the $\Lambda^* \to K^- p$ decay, and the value used is fixed due to parity conversation. Thus there is no assumption which needs to be made regarding the orbital angular momentum in this decay. In order to estimate a systematic uncertainty associated with this choice of $L^{\Lambda^*}_{\Lambda_b^0}$, the value used is incremented for each of the Λ^* resonances. The fits are repeated for each possible value, such that it is consistent with the LS couplings allowed for the particular resonance. Thus, for example, there are no other values tested for $\Lambda(2100)$ and $\Lambda(2110)$, as only the LS amplitudes with the minimum $L^{\Lambda^*}_{\Lambda_b^0}$ are included in the default model. The resulting changes for each fit are listed in Table 16. The uncertainties are added in quadrature to determine a total systematic uncertainty from this source.

Table 16: Changes resulting from varying the $L^{\Lambda^*}_{\Lambda_b^0}$ value used in the resonance parametrization. The last row gives the overall uncertainty obtained from adding each row in quadrature.

	ΔM_0 (MeV)		$\Delta\Gamma_0$ (MeV)		FF (%)			
$L^{\Lambda^*}_{\Lambda_b^0}$ change	$P_c(4380)$	$P_c(4450)$	$P_c(4380)$	$P_c(4450)$	$P_c(4380)$	$P_c(4450)$	$\Lambda(1405)$	$\Lambda(1520)$
$L^{\Lambda(1405)}_{\Lambda_b^0}+1$	0.2	0.1	1.0	0.4	0.21	0.13	0.16	0.0
$L^{\Lambda(1520)}_{\Lambda_b^0}+1$	6.6	0.0	11.0	1.2	0.42	0.26	2.3	1.22
$L^{\Lambda(1520)}_{\Lambda_b^0}+2$	7.4	0.0	14.0	0.9	0.54	0.23	2.41	1.97
$L^{\Lambda(1600)}_{\Lambda_b^0}+1$	1.5	0.0	1.0	0.7	0.13	0.15	0.0	0.01
$L^{\Lambda(1670)}_{\Lambda_b^0}+1$	0.1	0.0	0.0	0.4	0.21	0.13	0.0	0.0
$L^{\Lambda(1690)}_{\Lambda_b^0}+1$	0.4	0.0	2.0	0.6	0.15	0.14	0.01	0.0
$L^{\Lambda(1690)}_{\Lambda_b^0}+2$	1.6	0.0	5.0	0.9	0.04	0.17	0.02	0.01
$L^{\Lambda(1800)}_{\Lambda_b^0}+1$	1.0	0.0	3.0	0.3	0.13	0.11	0.0	0.01
$L^{\Lambda(1800)}_{\Lambda_b^0}+2$	2.7	0.2	7.0	0.1	0.06	0.07	0.01	0.02
$L^{\Lambda(1810)}_{\Lambda_b^0}+1$	1.6	0.1	1.0	0.3	0.2	0.1	0.02	0.0
$L^{\Lambda(1890)}_{\Lambda_b^0}+1$	0.3	0.1	0.0	0.4	0.2	0.12	0.0	0.0
Uncertainty(MeV)	10.7	0.3	20.2	2.1	0.81	0.53	3.34	2.31

15.3 Orbital angular momentum in P_c parametrization

Similar to the previous section, the resonance parametrization used for describing P_c resonances (Eq. 45) assumes the lowest possible value for $L^{P_c}_{\Lambda_b^0}$, the angular momentum present in the decay $\Lambda_b^0 \to P_c K^-$. Again, this value enters both Eq. 45 and the Blatt-

Weisskopf function, Eq. 24. There are only two possible values for $L^{P_c}_{\Lambda_b^0}$, and fits are performed with the nominal value incremented by one in order to estimate the systematic uncertainty associated with the choice of the minimal value. Additionally, the lowest value is assumed for the orbital angular momentum in the decay $P_c \to J/\psi p$, L_{P_c}. This enters explicitly in Eq. 45, the Blatt-Weisskopf functions, and additionally the mass-dependent width (Eq. 26). The possible values for L_{P_c} are constrained by parity, and so they are incremented by two, for each of the P_c states, to the only other value allowed. The resulting changes of the reported values in each fit with respect to the nominal fit are listed in Table 17.

Table 17: Changes resulting from varying the $L^{P_c}_{\Lambda_b^0}$ or L_{P_c} value used in the resonance parametrization. The last row gives the overall uncertainty obtained from adding each row in quadrature.

	ΔM_0 (MeV)		Γ_0		Fit fractions (%)	
L changed	$P_c(4380)$	$P_c(4450)$	$P_c(4380)$	$P_c(4450)$	$P_c(4380)$	$P_c(4450)$
$L^{P_c}_{\Lambda_b^0}+1$ ($\Lambda_b^0 \to P_c(4380)K^-$)	+6	+0.1	+3	0.0	0.37	0.16
$L^{P_c}_{\Lambda_b^0}+1$ ($\Lambda_b^0 \to P_c(4450)K^-$)	0.0	+0.7	+4	0.0	0.09	0.14
Total	6	0.7	5	0	0.38	0.21
$L_{P_c}+2$ ($P_c(4380) \to J/\psi p$)	+1	-0.4	+31	0	0.61	0.09
$L_{P_c}+2$ ($P_c(4450) \to J/\psi p$)	+4	-0.1	-12	-2	0.63	0.37
Total	4	0.4	33	2	0.88	0.38

15.4 Background studies

The Λ_b^0 sidebands are used to model the background component which is present in the fitted signal range. The assumption is that the background events which comprise the sidebands will accurately represent the background events under the Λ_b^0 peak. As a way to probe for possible differences, the sidebands are split into the lower sideband and upper sideband, *i.e.* split by whether an event's $m_{J/\psi Kp}$ value is below or above the Λ_b^0 peak. The separate sideband background distributions in the m_{Kp} and $m_{J/\psi p}$ variables are shown in Fig. 62, while the distributions for the angular variables are shown in Fig. 63. The lower sideband contains 5661 events while the upper sideband contains 4598 events, and they are normalized to each other in the figures. The most prominent difference between the lower and upper sidebands is in the m_{Kp} distribution, as the upper sideband appears to have some partially reconstructed contributions present.

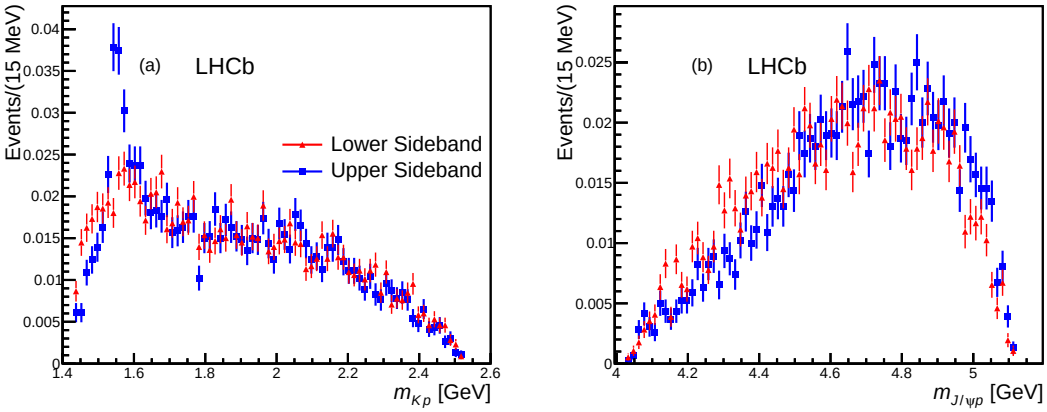

Figure 62: Distributions of the m_{Kp} (left) and $m_{J/\psi p}$ (right) variables in the lower (red triangles) and upper (blue squares) sidebands.

Ideally, the background composition in the signal range would be a mixture of the two sideband samples, and thus be accurately represented by their combination. Also recall that the background is only 5.4% of the signal sample size, which is quite a small component and not likely to cause large changes in the results. Still, to probe for the size of effects which might be caused by changing background compositions, fits are repeated in which either only the left or only the right sideband is used to construct the background parametrization. The largest deviations from the nominal values, caused by either using the lower or the upper sideband, are used to set the systematic uncertainties. The results are listed in the "Separate sidebands" entry of the summary Table 18. It is seen that the systematic uncertainties associated with this effect are small, as was predicted due to the low background fraction.

15.5 Efficiency mis-modeling

The weights $w_j^{\rm MC}$ are applied to the MC sample in order to correct for mismodeling in the simulation of $\Lambda_b^0 \to J/\psi K p$ events. For full details on how they are calculated, see Sec. B. These weights affect how the efficiencies are modeled in the 6D phase space, and so are part of the larger picture of how well the efficiency effects are represented in the MC sample. Of particular concern is that the $\cos\theta_{\Lambda_b^0}$ fit is consistently in excess over the data for $\cos\theta_{\Lambda_b^0} < 0$ and consistently below the data for $\cos\theta_{\Lambda_b^0} > 0$, regardless of

the amplitude model used. This suggests that there is efficiency mismodeling. In order to assess a possible systematic uncertainty associated with this, the MC set is further weighted to tune the projection of the default amplitude model onto $\cos\theta_{\Lambda_b^0}$, in order to better agree with the data. If it is assumed the amplitude model accurately represents the data, the changes caused by adjusting these weights then can give an idea of how large of an effect mismodeling the efficiency has. Three weights are used to help bring better agreement in this distribution: $w_p(p,\eta)$, $w_K(p,\eta)$, and $w_{\Lambda_b^0}(p,p_{\rm T})$ for the proton, kaon, and Λ_b^0, respectively. Using these new weights the data is then refit, and the fit was performed using the *sFit* method. The angular distributions for the fit projections using the new weights are shown in Fig. 64, where it is seen that the description of $\cos\theta_{\Lambda_b^0}$ is improved, without worsening the descriptions of the other fitted variables. The differences of the fit results with the nominal values are taken as an estimate of the systematic uncertainty due to possible efficiency mismodeling. The uncertainties are shown in the summary Table 18, in the "Efficiencies" row.

15.6 Additional systematic uncertainties

Various additional systematic uncertainties are listed here. The systematic uncertainty which comes from the assumed Λ^* model was estimated using the results obtained with the extended Λ^* model. For a full presentation of the results obtained with the extended Λ^* model, $P_c(4380)$, and $P_c(4450)$, see Appendix D. The uncertainties are shown in Table 18, in the "Λ^* model" row. This is a dominant source of systematic uncertainty for the P_c parameters.

The effect of adding a nonresonant K^-p component to the default model was also studied. A nonresonant component can usually be expected to show up most prominently in the quantum numbers which result in the lowest possible orbital angular momentum. In the $\Lambda_b^0 \to J/\psi\,\Lambda^*$ decay, $1/2^\pm$ and $3/2^\pm$ can all result in $L^{\Lambda^*}_{\Lambda_b^0} = 0$. In the $\Lambda^* \to K^-p$ decay, parity must be conserved, which gives the requirement $P_{\Lambda^*} = P_p P_{K^-}(-1)^{L_{\Lambda^*}}$. Thus in order to have $L_{\Lambda^*} = 0$ it is necessary to have $P_{\Lambda^*} = -$. The only remaining quantum number option with negative parity and capable of having $L_{\Lambda^*} = 0$ is $1/2^-$. Thus a

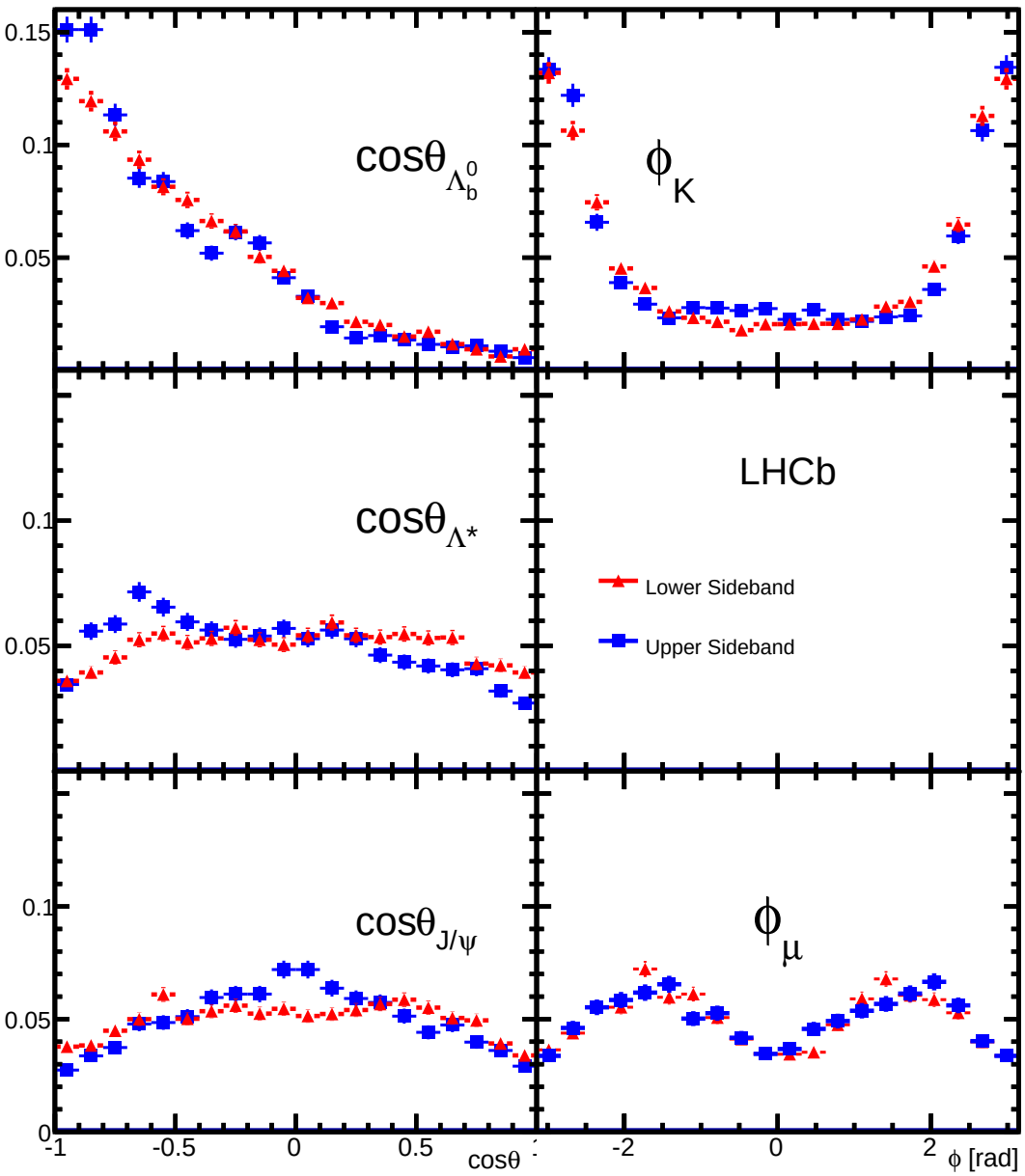

Figure 63: Distributions of the angular variables in the lower (red triangles) and upper (blue squares) sidebands.

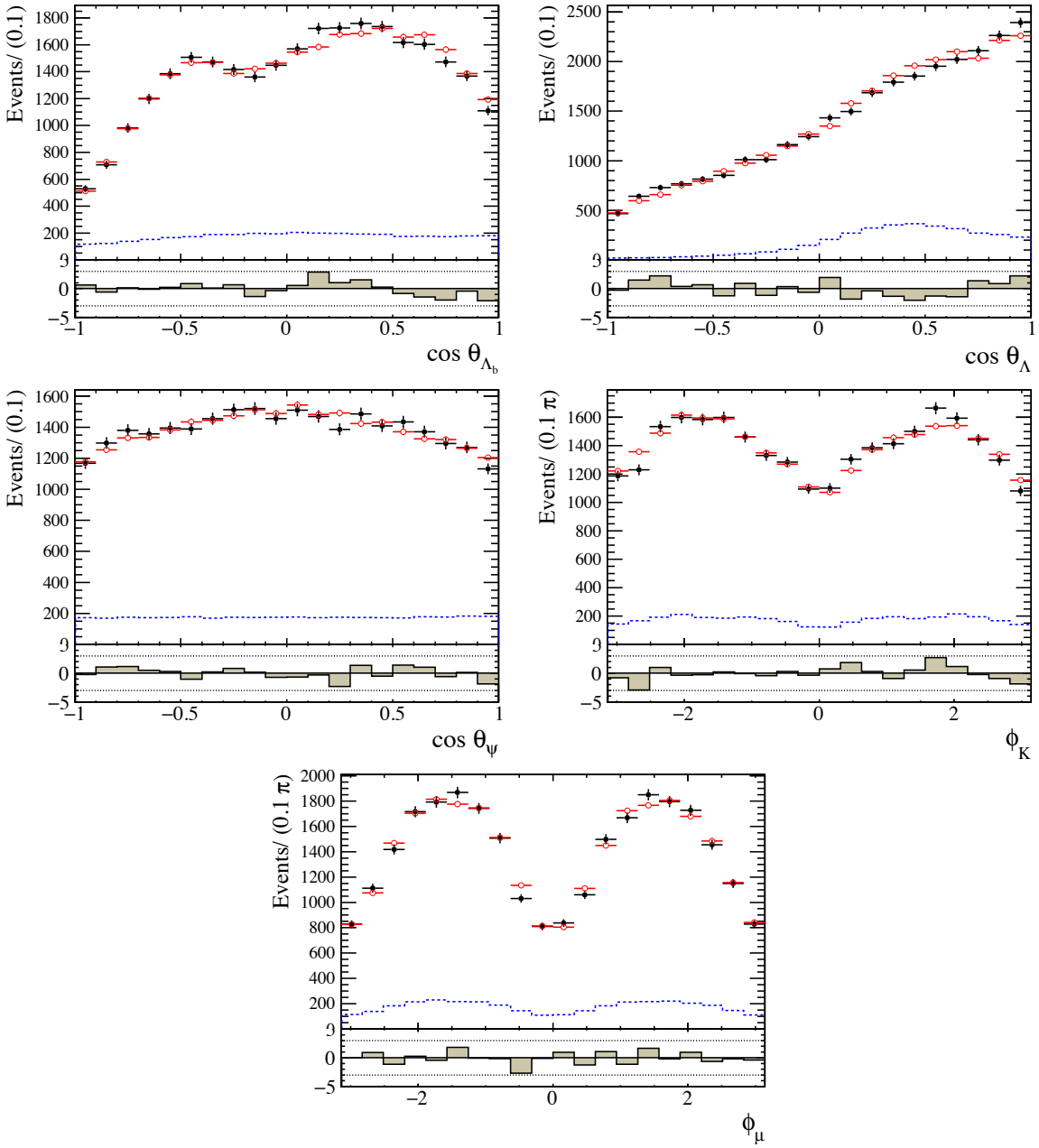

Figure 64: The fitted angular distributions with modified weights tuned to improve the description of the $\cos\theta_{\Lambda_b^0}$ distribution. The data (black squares), total amplitude model (open red circles), and P_c contribution (dashed blue line) are shown.

$1/2^-$ nonresonant component was added to model, and limited to only the complex amplitude with $L^{\Lambda^*}_{\Lambda^0_b} = 0$. Note that, while only this particular partial-wave was used for the estimation of systematic uncertainties associated with nonresonant components, a more aggressive study without P_c states was done in Sec. 8.3. The resulting uncertainties are shown in Table 18, in the "Nonresonant" row. The narrow P_c parameters are not observably changed, though there is a fairly large effect on the $P_c(4380)$ width and fit fraction, as well as the $\Lambda(1405)$ fit fraction. Including a nonresonant $J/\psi p$ component in the model was also tested, but had no observable effects.

As there is only a marginal preference for the $(3/2^-, 5/2^+)$ set of quantum numbers, and all other combinations can't be ruled out, there is a systematic uncertainty associated with the quantum number assignment. The changes in $\Delta(-2\ln\mathcal{L})$ and P_c parameters obtained with different quantum number assignments were given in Table 9. It was seen that the $(3/2+, 5/2^-)$ and $(5/2^+,\ 3/2^-)$ combinations also gave comparable fit qualities. The systematic uncertainty for each reported value is set by the largest deviation seen in either of these alternative fits. The obtained values are listed in the "J^P assignment" row of Table 18.

The Blatt-Weisskopf d parameter used in Eq. (24) was chosen as 3.0 GeV $^{-1}$ for the nominal value. The fits were repeated with $d = 1.5$ GeV^{-1} and $d = 4.5$ GeV^{-1}. The maximum change is taken as the uncertainty, which is listed in the "$d = 1.5 - 4.5$ GeV^{-1}" row of Table 18.

Two studies were performed which are related to the proton identification. To obtain a purer proton sample, the proton identification criteria was tightened by requiring $DLL(p-\pi) > 12$ and $DLL(p-K) > 5$, rather than the nominal cuts of 10 and 3, respectively. Separately, the default fit was redone after requiring the proton momentum p_p to the range above 10 GeV and below 100 GeV for all candidates. This range corresponds to where there is the most proton identification power, and thus will help ensure a more reliable identification. The study was performed with the *sFit* method, and the results are listed in Table 18 in the "Proton ID" and "$10 < p_p < 100$ GeV" rows, respectively.

There is also a systematic uncertainty associated with the Flatté couplings used for

the parametrization of $\Lambda(1405)$, as the coupling for the $\Lambda(1405) \to K^- p$ is not known. In the default model, it is set to the same value as the coupling to the dominant $\Lambda(1405) \to \Sigma^+\pi^-$ mode. To assess the systematic uncertainty associated with this, the $\Lambda(1405) \to K^- p$ is both doubled and halved. The maximum deviations are taken as the uncertainty, and are listed in the "$\Lambda(1405)$ coupling" row of Table 18.

15.7 Total systematic uncertainties

The uncertainties from the discussed sources are added in quadrature. The choice was made to take symmetric uncertainties from the deviations, as this is the more conservative choice, rather than quote positive and negative errors. The differences between *cFit* and *sFit* results are already covered in the other systematic uncertainties, and so their comparison is listed only as a cross-check and does not contribute to the total. For a detailed comparison between the *cFit* and *sFit* results, see Appendix E.3. In Table 18 the various sources of systematic uncertainties are listed along with the overall assessment.

Table 18: Summary of systematic uncertainties on P_c masses, widths and fit fractions, and Λ^* fit fractions. The sFit/cFit difference is listed as a cross-check and not included as a uncertainty.

Source	M_0 (MeV)		Γ_0 (MeV)		Fit fractions (%)			
	$P_c(4380)$	$P_c(4450)$	$P_c(4380)$	$P_c(4450)$	$P_c(4380)$	$P_c(4450)$	$\Lambda(1405)$	$\Lambda(1520)$
Λ^* model	21	0.3	54	10	3.14	0.32	1.37	0.15
Λ^* masses & widths	7	0.7	20	4	0.58	0.37	2.49	2.45
Proton ID	2	0.3	1	2	0.27	0.14	0.20	0.05
$10 < p_p < 100$ GeV	0	1.2	1	1	0.09	0.03	0.31	0.01
Nonresonant	3	0.3	34	2	2.35	0.13	3.28	0.39
Separate sidebands	0	0	5	0	0.24	0.14	0.02	0.03
J^P assignment	10	1.3	34	11	0.76	0.44		
$d = 1.5 - 4.5$ GeV^{-1}	9	0.6	19	3	0.29	0.42	0.36	1.91
$L^{P_c}_{\Lambda_b^0}$ $\Lambda_b^0 \to P_c K^-$	6	0.7	5	0	0.38	0.21		
L_{P_c} $P_c \to J/\psi p$	4	0.4	33	2	0.88	0.38		
$L^{\Lambda^*_n}_{\Lambda_b^0}$ $\Lambda_b^{0*} \to J/\psi \Lambda^*$	11	0.3	20	2	0.81	0.53	3.34	2.31
Efficiencies	1	0.4	4	0	0.13	0.02	0.26	0.23
$\Lambda(1405)$ coupling	0	0	0	0	0	0	1.90	0
Overall	29	2.2	87	16	4.26	1.07	5.82	3.89
sFit/cFit cross check	5	1.0	11	2	0.46	0.01	0.45	0.13

16 P_c Phase Motion Studies

16.1 Phase Motion Study Methodology

In this section, the resonant natures of the states are probed. This is done with the method pioneered in Ref. [19], in which the resonant nature of the tetraquark candidate $Z(4430)$ was studied. In a typical amplitude model, resonances are represented by a Breit-Wigner amplitude, multiplied by some factors to account for the difficulty in overcoming angular momentum barriers. The Breit-Wigner represents the expected behavior of a true resonance. In particular, there is a quick 180° change in phase of the complex amplitude as one moves across the pole mass. The complex amplitudes, if displayed in an Argand diagram, display a circular, counter-clockwise trajectory. These features are shown in Fig. 65, where the Breit-Wigner parameters are set to the values of the $P_c(4450)$ in the nominal amplitude fit: $M_0 = 4449.8\,\text{MeV}$ and $\Gamma_0 = 39\,\text{MeV}$. Note that trajectory on the Argand plane will intersect the (0,0) point, as the Breit-Wigner amplitude magnitude goes to zero far away from the resonance pole.

In order to test if the observed structures follow the expected phase motion of a resonance, the parametrization (Eq. 45) is replaced with six independent complex amplitudes, equally spaced in $m_{J/\psi p}$ in the range $M_0 \pm \Gamma_0$. The fit to the data then determines the real and imaginary part of the P_c amplitude in each $m_{J/\psi p}$ bin, and uses a cubic spline based on the closest 4 points to interpolate to masses between bin centers. The amplitude is set to zero outside this range. These fitted complex amplitudes for each $m_{J/\psi p}$ bin are displayed as in Fig. 65. In short, these amplitude points take over the role of the Breit-Wigner parametrization, and show changes in the magnitude and phase with $m_{J/\psi p}$. However, they are free to take whatever $m_{J/\psi p}$-dependence the data wants. Thus, if they still follow the form expected from a Breit-Wigner, it is indicative of a resonant nature.

In each bin the overall normalization and phase of the P_c amplitude is determined by floating its real and imaginary parts. As a technical point in performing the fit, this then requires fixing one of the LS amplitudes in the $P_c \to J/\psi p$ decay to (1,0). This

is necessary to avoid two free parameters directly multiplying each other, which would lead to convergence issues. Thus, the lowest LS coupling is set to (1,0), while the higher LS couplings are allowed to float and now have the meaning of the ratio with the lowest LS amplitude. The rest of the model reamins the same, and all of the other usual free parameters in the fit are still kept free. In general, this exercise is only carried out for one P_c resonance at a time, as there otherwise are convergence issues.

16.2 Phase motion of the $P_c(4450)^+$ state

The projection onto $m_{J/\psi p}$ for the default model in which the $P_c(4450)$ Breit-Wigner parametrization was replaced as specified above is shown in Fig. 66, where it is seen that the data are still well described. The six complex amplitudes representing the $P_c(4450)$ are displayed in an Argand diagram in Fig. 67. Note that because the magnitude and phase conventions are determined for all the terms in all the amplitude fits by setting the lowest LS amplitude of $\Lambda(1520)$ to (1,0), the orientation of the diagram in Fig. 67 gives the relative phase of the $P_c(4450)$ to the $\Lambda(1520)$. This is the reason it is rotated compared to Fig. 65. The red circle superimposed on the data points is the Breit-Wigner formula (i.e. Eq. (23)), covering the same $M_0 \pm \Gamma_0$ range, with the mass and width fixed to the default fit parameters: $M_0 = 4450$ MeV and $\Gamma_0 = 39$ MeV. The shape does not appear exactly as a circle because of the $p^L B'_L$ factors, however, their effect is very small. The phase and magnitude of the Breit-Wigner circle at the pole mass M_0 is set to the average values between the two points around M_0. It is seen that the six complex amplitudes follow the trajectory predicted by a Breit-Wigner lineshape quite well, indicating consistency of the $P_c(4450)$ structure with a true resonance.

The magnitude-squared and complex phase of the amplitudes are shown as a function of $m_{J/\psi p}$ in Fig. 68 and 69, respectively. Again, the red curves are the predictions from a Breit-Wigner lineshape with $M_0 = 4450$ MeV and $\Gamma_0 = 39$ MeV, scaled to the data as described above. The phase of the amplitudes undergo a rapid change when the magnitude peaks, as can also be concluded from the Argand diagram. Thus it is clearly seen that the data agree well with the Breit-Wigner expectations.

In order to test the sensitivity of the Argand diagram to the Λ^* model which is used, this exercise was repeated with the extended Λ^* model. Unfortunately, the fit did not converge, likely due to ambiguities caused by too many free parameters. Therefore, the test was done with an "intermediate" Λ^* model, which lies between the default and extended Λ^* models in terms of complexity. In this intermediate model, all possible LS couplings are allowed, but the poorly motivated $\Lambda(2350)$ and $\Lambda(2585)$ states are not included. The number of free parameters increases from 84 to 142, which constitutes a substantial change in the fit model. The resulting Argand diagram is shown in Fig. 70. The diagram is oriented somewhat differently, which must be due to the change of the average phase of the Λ^* contributions under the $P_c(4450)$ peak. The agreement between the complex amplitudes determined from the data and the Breit-Wigner expectation is even better than for the fit with the default Λ^* model.

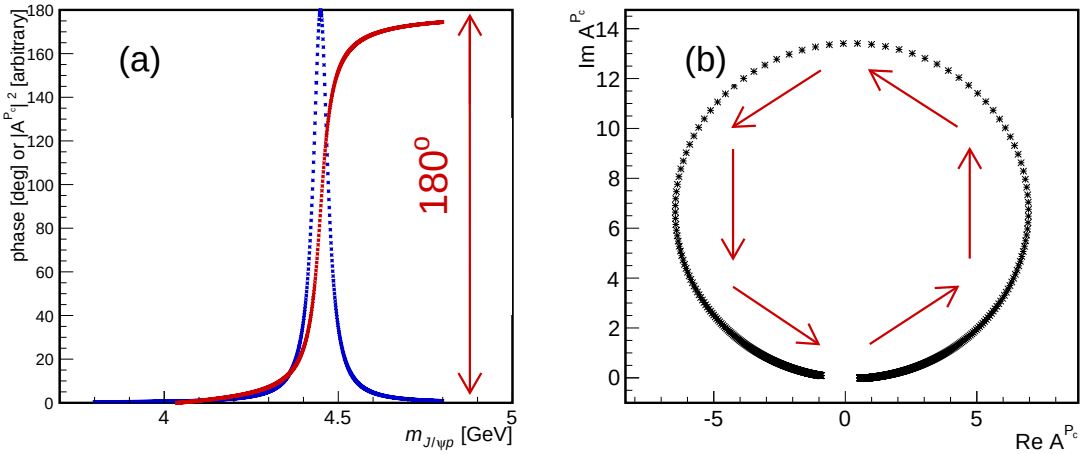

Figure 65: Demonstration of the expected phase motion of a resonance which follows a Breit-Wigner lineshape with the nominal P_c mass and width of $M_0 = 4449.8\,\text{MeV}$ and $\Gamma_0 = 39\,\text{MeV}$: (a) The magnitude of the complex amplitude is shown (blue) along with the phase (red) (b) the complex amplitude plotted in an Argand diagram.

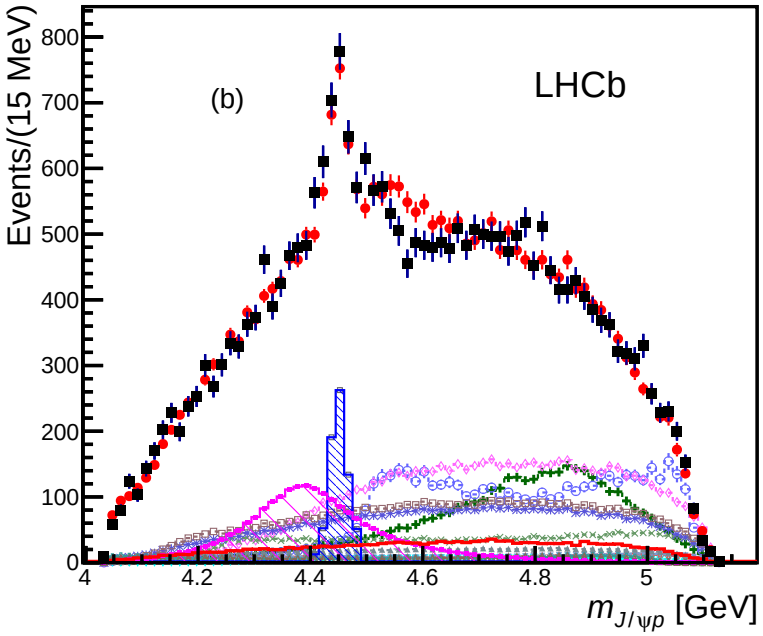

Figure 66: Results for $m_{J/\psi p}$ of the default amplitude model but with $P_c(4450)$ represented by six complex amplitudes, as described in the text. The data are shown as (black) squares with error bars, while the (red) circles show the projection of the fit. The other fit components are shown with the same style as usual (*e.g.* see Fig. 46). The fitted amplitude points are shown in the Argand diagram (Fig. 67).

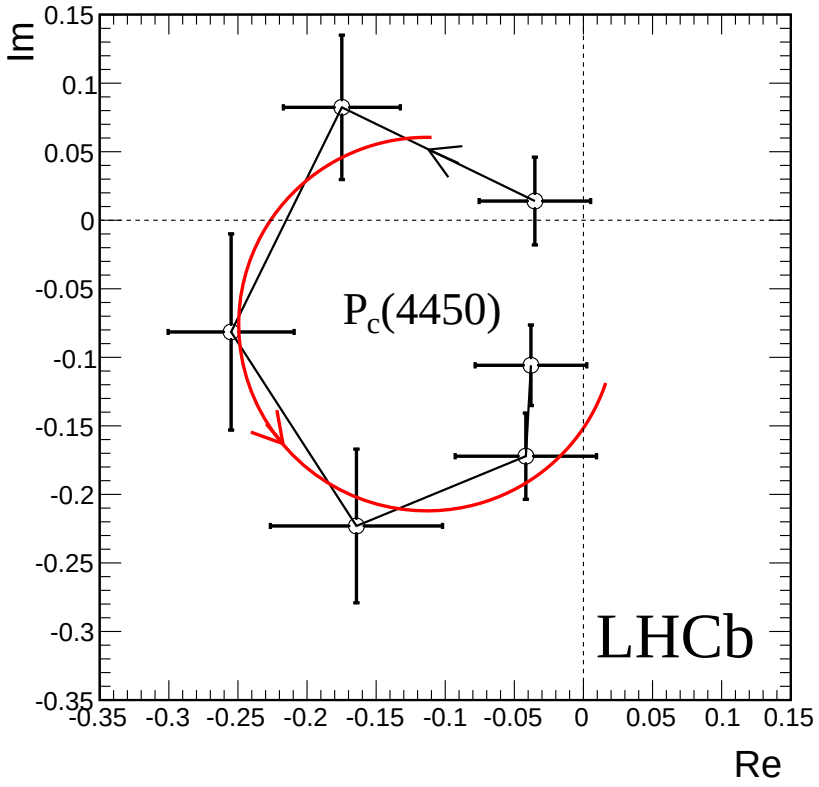

Figure 67: The real part versus imaginary part of the amplitudes used to represent $P_c(4450)$ (data points) for the fit shown in Fig 66. The (red) partial circle is the expectation for a Breit-Wigner amplitude. The arrows indicate the direction of the phase motion.

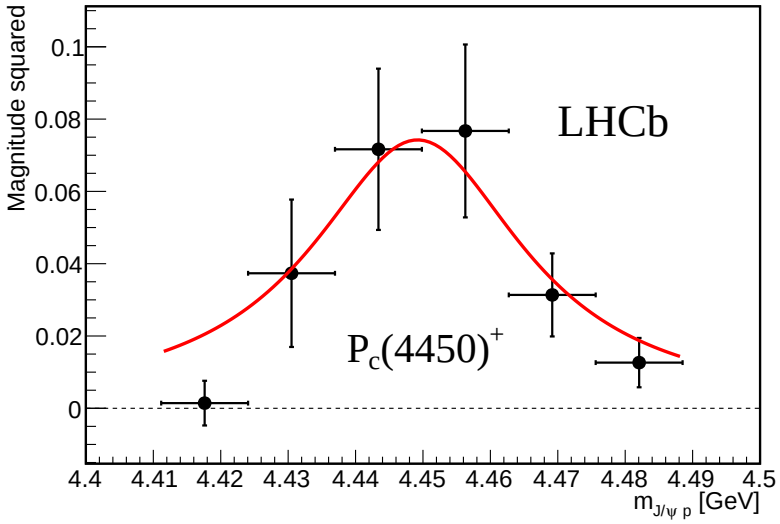

Figure 68: The measured magnitude-squared of the $P_c(4450)$ amplitude shown as (black) points with error bars. The (red) solid curve is the expectation from a Breit-Wigner lineshape.

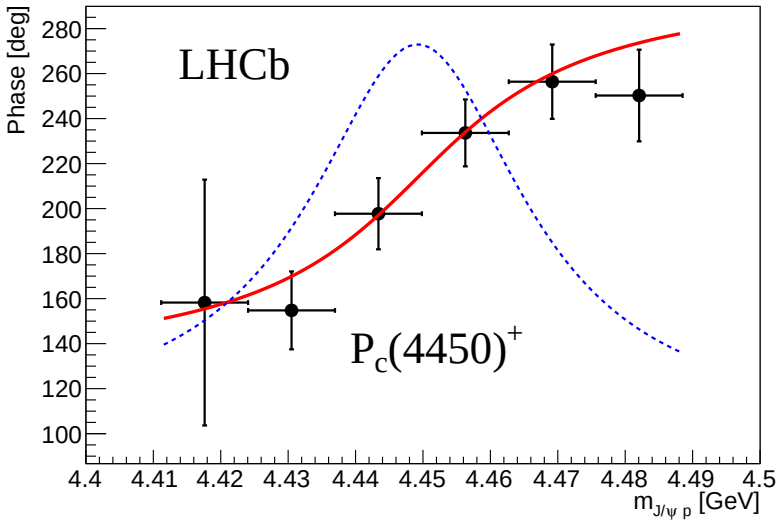

Figure 69: The measured phase of the $P_c(4450)$ amplitudes shown as (black) points with error bars. The (red) solid curve is the expectation from a Breit-Wigner lineshape, while the (blue) dashed line shows the magnitude-squared of the Breit-Wigner scaled arbitrarily to the range of this diagram.

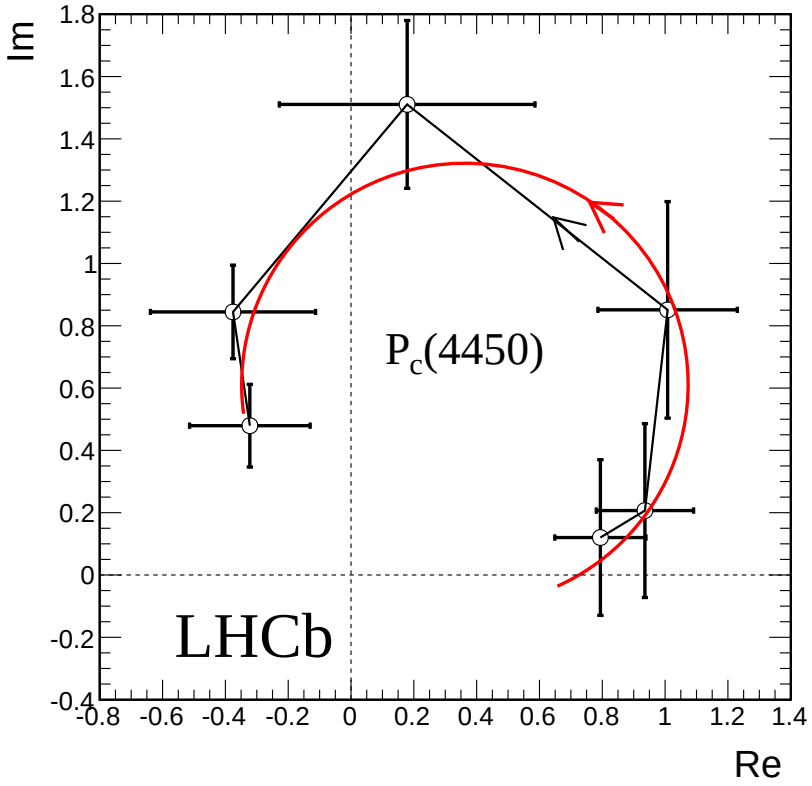

Figure 70: The real part versus imaginary part of the amplitudes used to represent $P_c(4450)$ (data points) for the fit performed with an intermediate Λ^* model instead of the default. The (red) partial circle is the expectation for a Breit-Wigner amplitude. The arrows indicate the direction of the phase motion.

16.3 The opposite parity $(3/2^+,\ 5/2^-)$ solution

In order to probe for a dependence on the assumed quantum numbers of the P_c states, the exercise was repeated using the alternate solution in which the quantum numbers of $P_c(4380)$ and $P_c(4450)$ are $3/2^+$ and $5/2^-$, respectively. The same procedure was followed, and the Argand plot obtained is shown in Fig. 71. This result also demonstrates a large phase change through the resonance peak, and follows the Breit-Wigner prediction well. A few points lie off the circle, but generally agree within uncertainties.

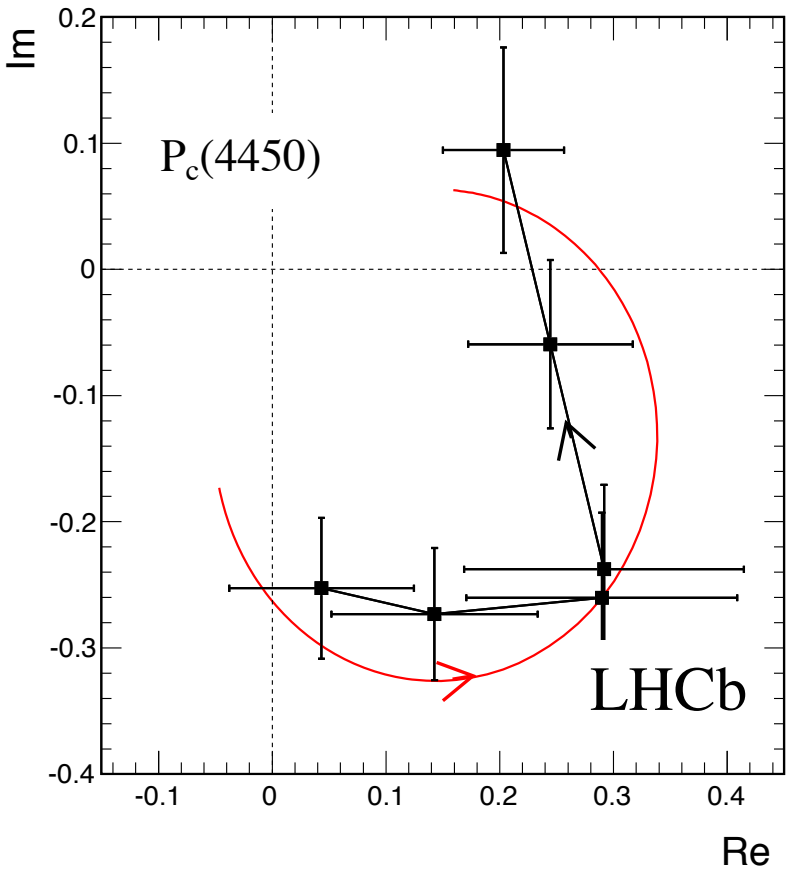

Figure 71: The real part versus imaginary part of the amplitudes used to represent $P_c(4450)$ (data points) for the fit performed with the $(3/2^+,\ 5/2^-)$ solution. The (red) partial circle is the expectation for a Breit-Wigner amplitude. The arrows indicate the direction of the phase motion.

16.4 Measuring the change in the amplitude phase of the $P_c(4380)^+$ state

The same studies were then performed with the $P_c(4380)$ state. Again, six complex amplitudes were used over the mass range of $M_0 \pm \Gamma_0$. The resulting Argand diagram is shown in Fig. 72, along with the expectations from a Breit-Wigner with parameters set to the nominal values of $M_0 = 4380$ MeV and $\Gamma_0 = 205$ MeV. Clearly, the results are not as aesthetically pleasing as those obtained for the $P_c(4450)$. Unfortunately, this state is much wider than the higher mass state, and is more sensitive to the underlying Λ^* model, as reflected in its mass and width dependence on the Λ^* model. It should be noted that there is evidence of a large change of phase, and it is mostly one point which lies off of the trajectory.

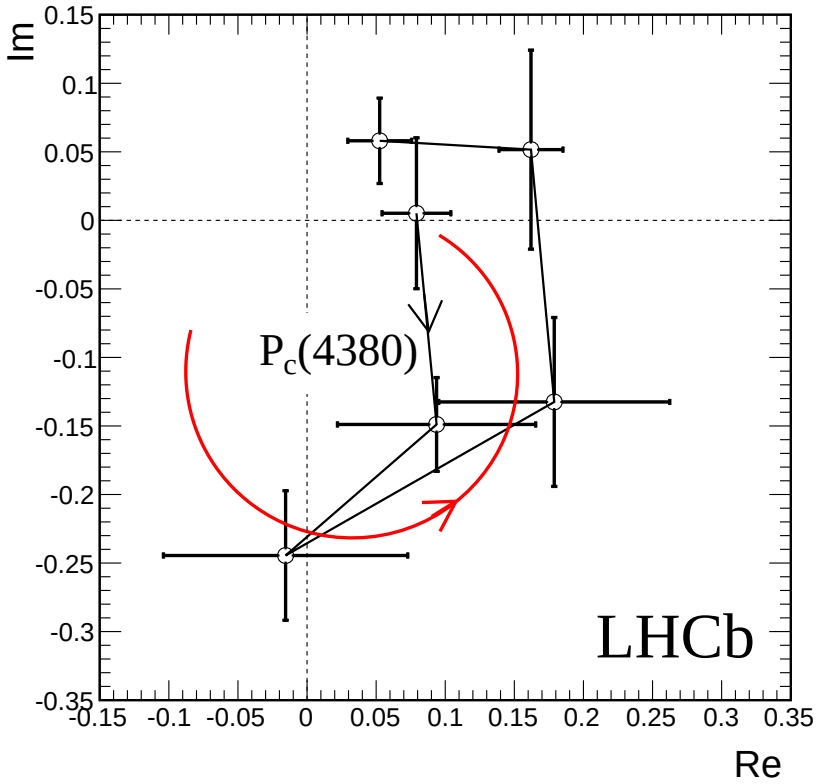

Figure 72: The real part versus imaginary part of the amplitude for the $P_c(4380)$ state (data points). The (red) partial circle is the expectation for a Breit-Wigner amplitude. The arrows indicate the direction of the phase motion.

The magnitude-squared and complex phase of the amplitudes are shown as a function of $m_{J/\psi p}$ in Fig. 73 and 74, respectively. Again, the red curves are the predictions from the

Breit-Wigner lineshape. While the magnitude-squared agrees well with the predictions, the phase does not exactly follow the expected behavior. There is clearly a large change of phase, though.

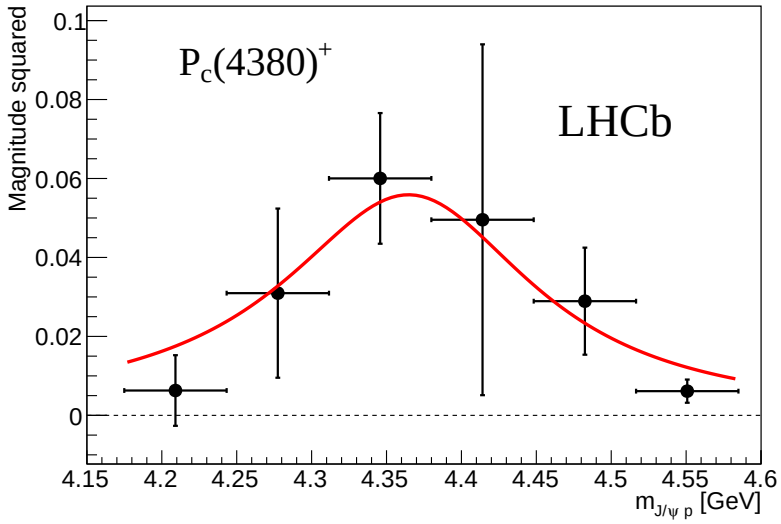

Figure 73: The measured magnitude-squared of the $P_c(4380)$ amplitude shown as (black) points with error bars. The (red) solid curve is the expectation from a Breit-Wigner phase.

As with the $P_c(4450)$ studies, the procedure was repeated with the intermediate Λ^* model in order to test the dependence on the Λ^* background. The results are shown in Fig. 75). Again, the two amplitudes corresponding to the lower $m_{J/\psi p}$ bins do not follow the circular trajectory well. It is not uncommon for a broad resonance not to follow the Breit-Wigner expectations exactly. Larger statistics and better understanding of Λ^* backgrounds will help to elucidate the nature of this state.

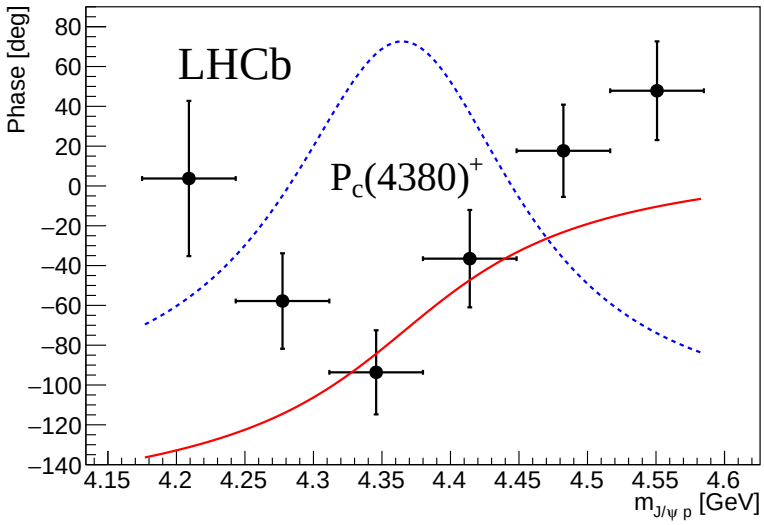

Figure 74: The measured phase of the $P_c(4380)$ amplitude shown as (black) points with error bars. The (red) solid curve is the expectation from a Breit-Wigner phase, while the (blue) dashed line shows the magnitude-squared of the Breit-Wigner scaled arbitrarily to the range of this diagram.

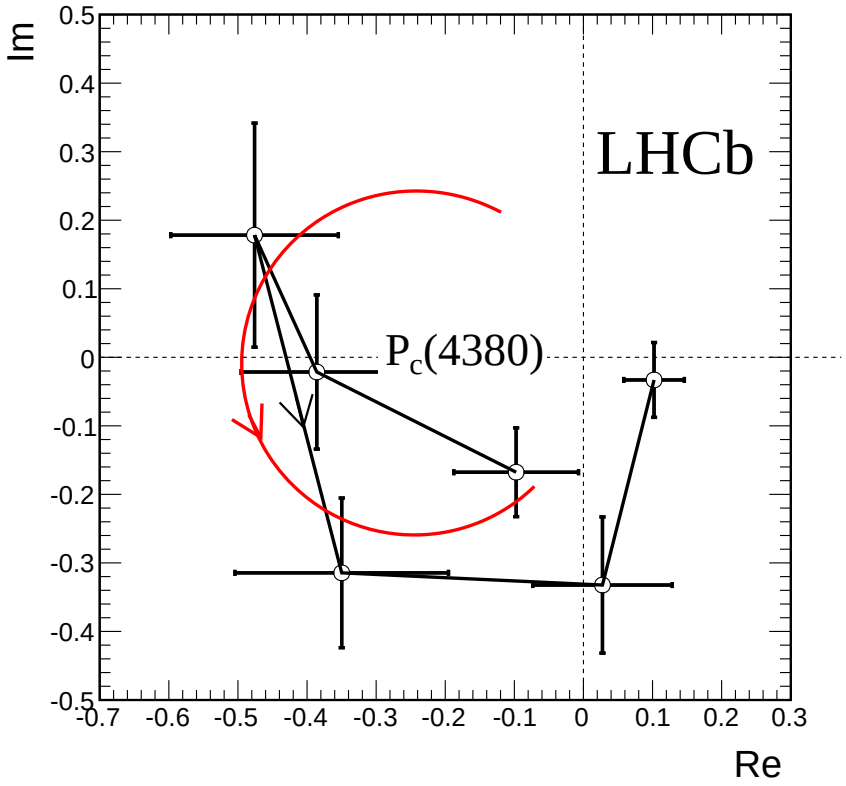

Figure 75: The real part versus imaginary part of the amplitude for the $P_c(4380)$ (data points) obtained with the intermediate Λ^* model. The (red) partial circle is the expectation for a Breit-Wigner amplitude with $M_0 = 4380$ MeV and $\Gamma_0 = 205$ MeV. The arrows indicate the direction of the phase motion.

16.5 Further phase studies

As the P_c^+ amplitudes stretch over a wide range of m_{Kp} masses, they cross many different Λ^* contributions (see Fig. 46). It is interesting to probe their magnitude and phase running at the different crossing points. Unfortunately, limited statistics makes it difficult to do this with the model independent parameterization, *i.e.* using the above method with different sets of amplitudes dependent on the m_{Kp} value as well. In a similar vein, an exercise is performed which assumes the Breit-Wigner amplitude, but allows M_0 and Γ_0 to vary independently in different slices of m_{Kp}. In this exercise, the Breit-Wigner amplitude is multipled by $1/\sqrt{\Gamma_0}$ to make the integral of its intensity (*i.e.* of the amplitude squared) over $m_{J/\psi p}$ be Γ_0–independent. In one variation of this type, the data was split at the midpoint of the m_{Kp} range (1978 MeV). The helicity couplings for a P_c^+ are shared between the two m_{Kp} slices, while the mass and width are allowed to be different. Specifically, if the m_{Kp} value of a data point is below the midpoint, the Breit-Wigner amplitude is calculated with one set of M_0 and Γ_0, and if it is above the midpoint it is calculated with another set. Both sets of parameters are simultaneously used as free parameters in the fit. The exercise is done using one P_c^+ state at a time, and the results are given in Table 19. The masses and widths determined in the two different m_{Kp} slices are very consistent for both states. In the second test of this type, the Breit-Wigner parameters were determined separately for an m_{Kp} band centered on the $\Lambda(1600)$ resonance, which has the largest fit fraction among all contributions. Thus the data was divided according to events lying within $1450 < m_{Kp} < 1750$ MeV ($M_0(\Lambda(1600)) \pm \Gamma_0(\Lambda(1600))$), and the rest of the m_{Kp} range. Note that the P_c^+ states will not contribute significantly to masses below this range. In particular, the $P_c(4450)^+$ state does not extend to the $\Lambda(1520)$ peak region at all. Thus the two ranges are still accurately described as "low" or "high" in Table 19. The results in different m_{Kp} slices are consistent again, with the largest deviation observed being 2.3σ for the $P_c(4380)$ width. From this exercise it is concluded that both the $P_c(4380)$ and $P_c(4450)$ resonances are consistently present in different parts of the Dalitz plot dominated by different Λ^* states.

Table 19: Mass and width of the P_c states fit in different slices of m_{Kp} mass. The combined probability for M_0 and Γ_0 being consistent in the low and high m_{Kp} slices is given in the row titled "CL".

state	$P_c(4450)$			$P_c(4380)$		
slice	low MeV	high MeV	diff.	low MeV	high MeV	diff.
Slice m_{Kp} in half						
M_0	4451.2 ± 2.5	4448.6 ± 2.5	$+0.73\sigma$	4399.0 ± 15.3	4375.6 ± 8.5	$+1.33\sigma$
Γ_0	38.7 ± 4.5	38.8 ± 4.4	-0.01σ	203.7 ± 20.6	202.2 ± 16.9	-0.05σ
CL			77%			41%
$\Lambda(1600)$ slice vs. the rest						
M_0	4451.1 ± 2.3	4449.6 ± 2.3	$+0.45\sigma$	4371.4 ± 12.1	4384.9 ± 8.9	-0.90σ
Γ_0	34.3 ± 4.4	39.8 ± 4.5	-0.9σ	164.2 ± 14.3	215.5 ± 16.7	-2.33σ
CL			62%			4.4%

17 Conclusions from amplitude analysis

A full amplitude analysis of $\Lambda_b^0 \to J/\psi K^- p$ decays in the LHCb Run I data set has been performed. The dominant contributions to this final state proceed via the expected $\Lambda_b^0 \to J/\psi \Lambda^*$, $\Lambda \to K^- p$ decays, for which a rich spectrum of known Λ^* states is observed. Unexpectedly, a prominent peak is also found in the $m_{J/\psi p}$ distribution. Many tests were performed to rule out the possibility this peak was artificially created, and to confirm that it must be due to physics processes in real $\Lambda_b^0 \to J/\psi K^- p$ decays. An amplitude analysis was performed to test if the peak could possibly be created via interferring Λ^* resonances reflecting into the $m_{J/\psi p}$ distribution. It was found that even if extra Λ^* resonances, four nonresonant contributions, or several Σ^* states were included, $K^- p$ contributions alone showed no ability to produce the peak. The addition of a single P_c state was also found to be inadequate, and in fact two P_c states were needed. Interpretted as resonant states, they must be composed of five quarks, $c\bar{c}uud$, and could therefore be called pentaquark states.

When using the default Λ^* model, the preferred quantum numbers for the states were found to be $(3/2^-, 5/2^+)$, though the $(3/2^+, 5/2^-)$ and $(5/2^+, 3/2^-)$ combinations are not much worse. The lighter state, $P_c(4380)$, has a mass of $4380 \pm 8 \pm 29$ MeV and a width of $205 \pm 18 \pm 87$ MeV, while the heavier state, $P_c(4450)$ has a mass of $4449.8 \pm 1.7 \pm 2.2$ MeV and a width of $39 \pm 5 \pm 16$ MeV. The fit fractions of $P_c(4380)$ and $P_c(4450)$ were found to be $(4.1 \pm 0.5 \pm 1.1)\%$ and $(8.4 \pm 0.7 \pm 4.3)\%$, respectively. The well separated $\Lambda(1405)$ and $\Lambda(1520)$ states were also reported as having fit fractions of $(15 \pm 1 \pm 6)\%$ and $(19 \pm 1 \pm 4)\%$, respectively. Phase motion studies were also performed on both of the P_c states. The $P_c(4450)$ phase motion appears to be in good agreement with the expectations of a resonance. The $P_c(4380)$ studies did demonstrate large changes in phase, but were in worse agreement.

As it stands, the default amplitude model constructed does have some shortcomings which merit discussion. The overall fit to $m_{J/\psi p}$ is reasonably good. Perfect amplitude fits are rarely achieved for high statistics samples like the one analyzed here. Still, there is a small discrepancy at masses slightly above the $P_c(4450)$ region. Furthermore, it was

found that performing the quantum number studies with the extended Λ^* model changed the ranking of preferred quantum numbers, *e.g.* making the $(5/2^-, 3/2^+)$ hypothesis more likely, while its statistical rejection was large with the default model. Thus, there should be a healthy dose of skepticism when making statements about the quantum numbers based on the default model only. It is possible that improvements in the Λ^* model could lead to an even better description of the $m_{J/\psi p}$ distribution, elucidation on the nature of $P_c(4380)$, and a unique determination of the quantum numbers of both P_c states. With larger data samples to be accumulated with the LHCb detector in the future, it will hopefully be possible to explore a wider range of extensions of the present Λ^* model than was documented in this work.

18 Model-Independent Confirmation

The amplitude analysis detailed in the first part of this thesis tested if interfering Λ^* states were capable of reproducing the peaking structures seen in the $m_{J/\psi p}$ distribution. It was shown that, with the known Λ^* resonances, this was not the case. Additional Λ^* states with varying quantum numbers, Σ^* states, and nonresonant contributions were also added. The resulting models still gave an inadequate description of the data. Thus it is unlikely that deficiencies in the conventional resonance model are likely to change the need to include exotic components in the amplitude model in order to reproduce the data. This is further supported by the interference patterns in the angular distributions, the overall improvement in fit quality upon addition of the P_c resonances, and the resonance phase motion studies. There is an abundance of evidence that the peaking structures are a result of activity in the $J/\psi p$ system.

Still, baryon spectroscopy is a complex problem from both experimental and theoretical points of view, and there are good reasons for believing that the Λ^* model used in the amplitude models has deficiencies. For instance, there are a large number of predicted resonances which have not been observed in the data, particularly at high masses, *i.e.* $m_{Kp} > 2\,\text{GeV}$. Various theoretical predictions are listed in Table 20, where it is shown that not only are there far more predicted states than listed in the PDG, but also there is not very good agreement between theoretical models. If the higher mass states exist, they may have evaded experimental detection for a variety of reasons. As evidenced by the m_{Kp} distribution (Fig 23), these states must have either a low production rate or a low rate to decay to K^-p. They may also be broad, making them difficult to identify as individual resonances in the presence of a high density of predicted excitations with identical quantum numbers. Further, the previous data from the scattering experiments do not cover the high mass region.

Even for the "well-established" states given by the PDG, there should be some degree of skepticism. These states usually come from simultaneous fits to partial wave analysis results, and have shown up in multiple different fits which are always somewhat model-dependent. Even for the lower mass regions, the interpretations of these data are

Table 20: Theoretical predictions for Λ^* resonance masses

J^P	State	Status	Mass	[56]	[57]	[58]	[59]	[60]	[61]
$\frac{1}{2}^+$	Λ	****	1115.683 ± 0.006	1115	1115	1108	1136	1116	1149 ± 18
	$\Lambda(1600)$	***	1560-1700	1615	1680	1677	1625	1518	1807 ± 94
	$\Lambda(1710)$	*	1713 ± 13						
	$\Lambda(1810)$	***	1750-1850	1901	1830	1747	1799	1666	2112 ± 54
				1972	1910	1898		1955	2137 ± 69
				1986	2010	2077		1960	
				2042	2105	2099			
				2099	2120	2132			
$\frac{3}{2}^+$	$\Lambda(1890)$	****	1850-1910	1854	1900	1823		1896	1991 ± 103
				1976	1960	1952			2058 ± 139
				2130	1995	2045			2481 ± 111
				2184	2050	2087			
				2202	2080	2133			
$\frac{5}{2}^+$	$\Lambda(1820)$	****	1815-1825	1825	1890	1834		1896	
	$\Lambda(2110)$	***	2090-2140	2098	2035	1999			
				2221	2115	2078			
				2255	2115	2127			
				2258	2180	2150			
$\frac{7}{2}^+$	$\Lambda(2020)$	*	1990-2130	2251	2120	2130			
				2471		2331			
$\frac{9}{2}^+$	$\Lambda(2350)$	***	2340-2370	2360		2340			
$\frac{1}{2}^-$	$\Lambda(1405)$	****	$1405.1^{+1.3}_{-1.0}$	1406	1550	1524	1556	1431	1416 ± 81
	$\Lambda(1670)$	****	1660-1680	1667	1615	1630	1682	1443	1546 ± 110
	$\Lambda(1800)$	***	1720-1850	1733	1675	1816	1778	1650	1713 ± 116
	$\Lambda(2000)$	*	1935-2040	1927	2015	2011		1732	2075 ± 249
				2197	2095	2076		1785	
				2218	2160	2117		1854	
$\frac{3}{2}^-$	$\Lambda(1520)$	****	1519.5 ± 1.0	1549	1545	1508	1556	1431	1751 ± 40
	$\Lambda(1690)$	****	1685-1695	1693	1645	1662	1682	1443	2203 ± 106
				1812	1770	1775		1650	2381 ± 87
	$\Lambda(2050)$	*	2056 ± 22	2035	2030	1987		1732	
				2319	2110	2090		1785	
	$\Lambda(2325)$	*	2300-2375	2322	2185	2147		1854	
				2392	2230	2259		1928	
				2454	2290	2275		1969	
				2468		2313			
$\frac{5}{2}^-$	$\Lambda(1830)$	****	1810-1830	1861	1775	1828	1778	1785	
				2136	2180	2080			
				2350	2250	2179			
$\frac{7}{2}^-$	$\Lambda(2100)$	****	2090-2110	2097	2150	2090			
				2583	2230	2227			
$\frac{9}{2}^-$				2665		2370			

ambiguous in places. This is well illustrated in the recently published fits in Ref [62], which are based on the coupled channel approach applied to all $\bar{K}N$ scattering data. There the *** $\Lambda(1800)$ state was not seen, while evidence for a few yet unidentified states was obtained. The PDG entries are compared to this result and other global fits in Table 21. In Ref. [62], fits to the scattering data also required significant non-resonant terms, whose magnitude and phase varied slowly with m_{Kp}. In the amplitude models used in this thesis, only constant non-resonant terms were tried.

Table 21: Quantum numbers, masses, and widths of Λ^* states found in $\bar{K}N$ scattering data

	PDG				[62]		[63]		[64]		[64]	
J^P	State	Status	Mass	Width	Mass	Width	Mass	Width	Mass	Width	Mass	Width
$\frac{1}{2}^+$	$\Lambda(1600)$	***	1560-1700	50-250	1568 ± 12	132 ± 22	1572	138	1544	112	1548	164
	$\Lambda(1710)$	*	1713 ± 13	180 ± 42	1685 ± 29	59 ± 34	1688	166				
					1835 ± 10	180 ± 22						
	$\Lambda(1810)$	***	1750-1850	50-250	1837.2 ± 3.4	58.7 ± 6.5	1780	64			1841	62
							2135	296	2097	116		
$\frac{3}{2}^+$					1690.3 ± 3.8	46.4 ± 11.0					1671	10
	$\Lambda(1890)$	****	1850-1910	60-200	$1846.36 \pm .81$	70.0 ± 6.0	1876	145	1859	112		
							2001	994				
$\frac{5}{2}^+$	$\Lambda(1820)$	****	1815-1825	70-90	1817 ± 57	85 ± 54	1814	85	1824	78	1821	64
	$\Lambda(2110)$	***	2090-2140	150-250	1931 ± 25	189 ± 36	1970	350				
$\frac{7}{2}^+$									1757	146		
	$\Lambda(2020)$	*	1990-2130	125-275	2012 ± 81	210 ± 120	1999	146			2041	238
$\frac{1}{2}^-$	$\Lambda(1405)$	****	$1405.1^{+1.3}_{-1.0}$	50.5 ± 2.0	1435.8 ± 5.9	279 ± 16	1402	49				
					1573	300					1512	370
	$\Lambda(1670)$	****	1660-1680	25-50	1636.0 ± 9.4	211 ± 35	1667	26	1669	18	1667	24
	$\Lambda(1800)$	***	1720-1850	200-400			1729	198				
	$\Lambda(2000)$	*	1935-2040	70-315	1983 ± 21	282 ± 22	1984	233				
					2043 ± 39	350 ± 29						
$\frac{3}{2}^-$	$\Lambda(1520)$	****	1519.5 ± 1.0	15.6 ± 1.0	1519.33 ± 0.34	17.8 ± 1.1	1518	16	1517	16	1517	16
	$\Lambda(1690)$	****	1685-1695	50-70	1687.40 ± 0.79	66.2 ± 2.3	1689	53	1697	66	1697	74
	$\Lambda(2050)$	*	2056 ± 22	493 ± 61	2051 ± 20	269 ± 35	1985	447				
	$\Lambda(2325)$	*	2300-2375	120-215	2133 ± 120	1110 ± 280						
$\frac{5}{2}^-$	$\Lambda(1830)$	****	1810-1830	60-110	1821.4 ± 4.3	102.3 ± 8.6	1809	109	1766	212		
							1970	350	1899	80	1924	90
					2199 ± 52	570 ± 180						
$\frac{7}{2}^-$	$\Lambda(2100)$	****	2090-2110	100-250	2079.9 ± 8.3	216.7 ± 6.8	2023	239				

Thus, in spite of a quality description of the m_{Kp} distribution by the amplitude models, it is very likely that the models missed or contained spurious K^-p components. Improvements to the Λ^* models could certainly be made, and doing so may even shed more light on the P_c states. However this is a difficult task which will take time and will necessarily remain a model-dependent interpretation of the data. Therefore, it is worth inspecting the data with an approach that is model-independent with respect to K^-p contributions. Such a method was used by the BaBar collaboration [65] and later improved upon by the LHCb collaboration [20]. In these studies, $B^0 \to \psi(2S)\pi^+K^-$ decays were inspected, which are dominated by kaon excitations decaying to $K^-\pi^+$. The goal was to understand whether the data also contain the tetraquark candidate $Z(4430)^+$ decaying to $\psi(2S)\pi^+$. In particular, the ability to describe the $\psi(2S)\pi^+$ mass distribu-

tion in terms of K^* resonances in the $K^-\pi^+$ system was examined. The method will be described in more detail in the following section, but in short it involves building a representation of the Dalitz plane which is taken directly from the data, and filtering out contributions (*i.e.* statistical fluctuations or exotic components) that couldn't plausibly come from K^* resonances. This representation is then projected onto the $\psi(2S)\pi^+$ variable and compared to the distribution observed in the data. Thus this probes how well the conventional resonances are able to describe the data, and if there is the need to include an exotic contribution. The method involves using only mild assumptions about the maximum spin of K^* resonances which are present in the data, and can be guided by the Quark Model as well as previous experimental results. However such an approach assumes nothing about the number of resonances, nor does it assume anything about their lineshapes, masses, widths, or possible interference patterns. It also does not require any assumptions about the presence of nonresonant contributions.

This approach can be used to show an inconsistency of the data with a hypothesis that only conventional resonances are present. Qualitatively, this approach can point to the location of an exotic structure which causes this inconsistency. However, it does not allow for the determination of any parameters of putative exotic resonances, since they can interfere with the conventional resonances, as well as feed into parts which can also be attributed to conventional resonances. This happens in an intractable way, and would necessarily require a model to predict. It also does not formally prove which channel the exotic contributions are in, *e.g.* in the $B^0 \to \psi(2S)\pi^+K^-$ study a tetraquark could be present in either the $\psi(2S)\pi^+$ or the $J/\psi K^-$ system. The sensitivity of such an approach is also dependent on a variety of factors. Most important are the fit fractions and spins of conventional hadrons which are present, and the fit fractions and decay widths of any exotic contributions which may be present. For these reasons, the sensitivity is a priori unknown without the use of an amplitude model. Therefore, this approach is only useful when it leads to a rejection of the hypothesis that only conventional resonances are present, and it produces only inconclusive results otherwise. It is also worth stressing that this approach cannot rule out contributions from rescattering mechanisms, which

can produce peaks that may fake the presence of exotic hadrons.

The model-independent nature of this method is certainly appealing and could serve to put to rest concerns about the modeling of conventional contributions to the data, but clearly this does come at the cost of less power. For this reason, this method and the amplitude analysis complement each other nicely. In the second part of this thesis, the method is used to test the hypothesis that the $\Lambda_b^0 \to J/\psi p K^-$ decays can be described with only conventional hadrons decaying to $K^- p$. Studies of the sensitivity of the method with amplitude models are also performed for the first time, and algorithmic improvements to the method are made.

19 The model-independent formalism

The aim of this analysis is to assess the level of consistency of the data with the hypothesis that all $\Lambda_b^0 \to J/\psi p K^-$ decays proceed via $\Lambda_b^0 \to J/\psi \Lambda^*$, $\Lambda^* \to pK^-$, while making only minimal assumptions about the spin of possible Λ^* contributions. This will be referred to as the H_0 (*i.e.* "null") hypothesis, and will be specified in more detail in this section. Here, the Λ^* denotes not only excitations of the Λ baryon, but also nonresonant K^-p contributions or excitations of the Σ baryon. As mentioned in the amplitude analysis sections, the latter contributions are expected to be small [52], but are still automatically covered by the analysis formalism. The method is two-dimensional and uses the information contained in the Dalitz variables, $(m^2_{Kp}, m^2_{J/\psi p})$, or equivalently in $(m_{Kp}, \cos\theta_{\Lambda^*})$. Equivalence between the two sets of variables can be seen from

$$m^2_{J/\psi p} = m^2_{J/\psi} + m^2_p + 2\left(E_{J/\psi}E_p - p_{J/\psi}p_p\cos\theta_{\Lambda^*}\right), \tag{82}$$

where the momenta

$$\begin{aligned} p^2_{J/\psi} &= E^2_{J/\psi} - m^2_{J/\psi}, \\ p^2_p &= E^2_p - m^2_p, \end{aligned}$$

and the energies

$$\begin{aligned} E_{J/\psi} &= (m^2_{\Lambda_b^0} - m^2_{J/\psi} - m^2_{Kp})/(2m_{Kp}), \\ E_p &= (m^2_{Kp} + m^2_p - m^2_K)/(2m_{Kp}) \end{aligned}$$

of J/ψ and p are expressed in the K^-p rest frame and $\cos\theta_{\Lambda^*} \equiv -\hat{p}_{J/\psi}\cdot\hat{p}_K = \hat{p}_{J/\psi}\cdot\hat{p}_p$ was used to arrive at Eq. 82. Thus, for a given value of m_{Kp}, there is a one-to-one correspondence between $m^2_{J/\psi p}$ and $\cos\theta_{\Lambda^*}$. The $(m_{Kp}, \cos\theta_{\Lambda^*})$ plane is particularly suitable for imposing constraints stemming from the H_0 hypothesis, as will be seen. All considerations in this section apply to data in which reconstruction and selection efficiency

effects have been corrected. To see the efficiency-corrected distribution of the data over the $(m_{Kp}, \cos\theta_{\Lambda^*})$ plane, along with simulations of expected Λ^* or P_c contributions, see Appendix. I.

The $\cos\theta_{\Lambda^*}$ dependence of the efficiency-corrected data is expanded in Legendre polynomials (P_l) as a function of m_{Kp}:

$$\frac{dN}{d\cos(\theta_{\Lambda^*})}(m_{Kp}) = \sum_{l=0}^{l_{\max}} \langle P_l^U \rangle (m_{Kp})\, P_l(\cos\theta_{\Lambda^*}). \tag{83}$$

where N is the efficiency corrected $\Lambda_b^0 \to J/\psi p K^-$ signal yield, and $\langle P_l^U \rangle (m_{Kp})$ are mass-dependent expansion coefficients ("moments") whose calculation will be detailed later. The specific choice of $l_{\max}$ will also soon be discussed. The Legendre polynomials are normalized and orthogonal:

$$\int_{-1}^{1} P_i(\cos\theta_{\Lambda^*}) P_j(\cos\theta_{\Lambda^*}) d\cos\theta_{\Lambda^*} = \delta_{ij}\,. \tag{84}$$

Using the orthogonality condition with Eq. (83), it is easy to show:

$$\langle P_l^U \rangle (m_{Kp}) = \int_{-1}^{1} P_l(\cos\theta_{\Lambda^*})\, \frac{dN}{d\cos\theta_{\Lambda^*}}\, d\cos\theta_{\Lambda^*}. \tag{85}$$

The m_{Kp}-dependence is accounted for by dividing the m_{Kp} dimension into bins, such that Eq. 83 is given for each bin as

$$\left.\frac{dN}{d\cos(\theta_{\Lambda^*})}\right|_k = \sum_{l=0}^{l_{\max}} \langle P_l^U \rangle_k\, P_l(\cos\theta_{\Lambda^*}). \tag{86}$$

The key to this analysis method is that, under the H_0 hypothesis, the expansion can be truncated at a reasonably small $l_{\max}$ value, after which higher order moments would only describe statistical fluctuations. Specifically, a Λ^* resonance with spin J_1 can only contribute to moments up to $l = 2J_1$, while interferences between two resonances with spin J_1 and J_2 can contribute up to moments $l = J_1 + J_2$. Thus, if the highest spin Λ^* resonance present in a particular m_{Kp} bin has spin $J_{\max}$, the expansion can be truncated

at order $l_{\max} = 2J_{\max}$.

A proof of the statement that $l_{\max}$ can be set to $2J_{\max}$ starts by examining the matrix element of the decay, which was been documented in the amplitude analysis (Sec. 5). As the analysis is working under the H_0 hypothesis, only the Λ^* part of the matrix element is considered. Furthermore, as this is a two-dimensional method concerned with only the Dalitz variables, the J/ψ is treated as a final state particle. Thus the sum over its helicities must be taken incoherently. The relevant matrix element is then

$$|\mathcal{M}|^2 = \sum_{\lambda_{\Lambda_b^0}} \sum_{\lambda_p} \sum_{\lambda_\psi} \Bigg| \sum_n R_n(m_{Kp})\, \mathcal{H}_{\lambda_p}^{\Lambda_n^* \to Kp} \times \sum_{\lambda_{\Lambda^*}} \mathcal{H}_{\lambda_{\Lambda^*},\,\lambda_\psi}^{\Lambda_b^0 \to \Lambda_n^* \psi}\; e^{i\,\lambda_{\Lambda^*}\phi_K}\; d^{\frac{1}{2}}_{\lambda_{\Lambda_b^0},\,\lambda_{\Lambda^*}-\lambda_\psi}(\theta_{\Lambda_b^0})\; d^{J_{\Lambda_n^*}}_{\lambda_{\Lambda^*},\,\lambda_p}(\theta_{\Lambda^*}) \Bigg|^2 , \tag{87}$$

where the $\mathcal{H}$ are the constant helicity couplings, λ_X is a projection of the spin of particle X onto its momentum direction ("helicity"), $R_n(m_{Kp})$ represents the mass dependence of the decay amplitude for the given $\Lambda^*{}_n$ resonance (which could also be a non-resonant contribution or $\Sigma^* \to pK^-$ resonance), $d^J_{m'\,m}(\theta)$ are the small Wigner functions, the θ are the helicity angles, and ϕ_K is the angle between the decay planes of Λ_b and Λ^* (see Sec. 5 for a more detailed explanation). Expanding this equation in order to integrate over the extraneous angles results in

$$\begin{aligned} |\mathcal{M}|^2 = \sum_{\substack{\lambda_{\Lambda_b^0}\,\lambda_p\,\lambda_\psi \\ n\,n'\,\lambda_{\Lambda^*}\,\lambda_{\Lambda^{*\prime}}}} & R_n(M_{Kp})(R_{n'}(M_{Kp}))^*\, \mathcal{H}_{\lambda_p}^{\Lambda_n^* \to Kp} (\mathcal{H}_{\lambda_p}^{\Lambda_n^{*\prime} \to Kp})^* \times \\ & \mathcal{H}_{\lambda_{\Lambda^*},\,\lambda_\psi}^{\Lambda_b^0 \to \Lambda_n^* \psi}\; (\mathcal{H}_{\lambda_{\Lambda^{*\prime}},\,\lambda_\psi}^{\Lambda_b^0 \to \Lambda_n^{*\prime} \psi})^*\; e^{i(\lambda_{\Lambda^*}\phi_K - \lambda_{\Lambda^{*\prime}}\phi_K)} \\ & d^{\frac{1}{2}}_{\lambda_{\Lambda_b^0},\,\lambda_{\Lambda^{*\prime}}-\lambda_\psi}(\theta_{\Lambda_b^0})\; d^{\frac{1}{2}}_{\lambda_{\Lambda_b^0},\,\lambda_{\Lambda^*}-\lambda_\psi}(\theta_{\Lambda_b^0})\; d^{J_{\Lambda_n^*}}_{\lambda_{\Lambda^*},\,\lambda_p}(\theta_{\Lambda^*})\; d^{J_{\Lambda_n^{*\prime}}}_{\lambda_{\Lambda^{*\prime}},\,\lambda_p}(\theta_{\Lambda^*}) \end{aligned} \tag{88}$$

Next, integration over ϕ_K will yield the factor $\int_{-\pi}^{\pi} e^{i(\lambda_\Lambda - \lambda'_\Lambda)\phi_K} d\phi_K = 2\pi\delta_{\lambda_\Lambda\,\lambda'_\Lambda}$. Finally

integration over $\theta_{\Lambda_b^0}$ is performed to give

$$|\mathcal{M}|^2 \propto \sum_{\substack{\lambda_{\Lambda_b^0}\lambda_p\lambda_\psi \\ nn'\lambda_{\Lambda^*}}} R_n(M_{Kp})(R_{n'}(M_{Kp}))^* \, \mathcal{H}_{\lambda_p}^{\Lambda_n^* \to Kp} (\mathcal{H}_{\lambda_p}^{\Lambda_n^{*\prime} \to Kp})^* \times \\ \mathcal{H}_{\lambda_{\Lambda^*},\lambda_\psi}^{\Lambda_b^0 \to \Lambda_n^* \psi} \, (\mathcal{H}_{\lambda_{\Lambda^*},\lambda_\psi}^{\Lambda_b^0 \to \Lambda_n^{*\prime} \psi})^* \, d^{J_{\Lambda_n^*}}_{\lambda_{\Lambda^*},\lambda_p}(\theta_{\Lambda^*}) \, d^{J_{\Lambda_n^{*\prime}}}_{\lambda_{\Lambda^*},\lambda_p}(\theta_{\Lambda^*}) \tag{89}$$

Thus the end result is the matrix element is proportional to various amplitudes multiplying two d-matrices. Note that while the quantum number J can differ between the two d-matrices, the helicity projections must be the same. It is not immediately obvious how many moments are necessary to include in a Legendre polynomial expansion of the products of these d-matrices. To make this clearer, examine the general formula for the d-matrix:

$$\begin{aligned} d^J_{m'm}(\theta) = {} & [(J+m')!(J-m')!(J+m)!(J-m)!]^{1/2} \\ & \times \sum_s \frac{(-1)^{m'-m+s}}{(J+m-s)!s!(m'-m+s)!(J-m'-s)!} \\ & \times \left(\cos\frac{\theta}{2}\right)^{2J+m-m'-2s} \times \left(\sin\frac{\theta}{2}\right)^{m'-m+2s}, \end{aligned} \tag{90}$$

where the the sum over s is over all values such that the factorials are nonnegative. Multiplying two of these expressions with identical values of m and m', one obtains (with the labeling of the unimportant constant factors with K):

$$\begin{aligned} d^{J_1}_{m'm}(\theta)\, d^{J_2}_{m'm}(\theta) &\propto \sum_{s_1\, s_2} K^{J_1}_{m'ms_1} K^{J_2}_{m'ms_2} \times \left(\cos\frac{\theta}{2}\right)^{2J_1+2J_2+2m-2m'-2s_1-2s_2} \\ &\quad \times \left(\sin\frac{\theta}{2}\right)^{2m'-2m+2s_1+2s_2} \\ &\propto \sum_{s_1\, s_2} K^{J_1}_{m'ms_1} K^{J_2}_{m'ms_2} \times \left(\frac{1}{2}(1+\cos\theta)\right)^{J_1+J_2+m-m'-s_1-s_2} \\ &\quad \times \left(\frac{1}{2}(1-\cos\theta)\right)^{m'-m+s_1+s_2}. \end{aligned} \tag{91}$$

Thus the product of two d-matrices with the same m, m' values can be expressed as a summation over powers in $\cos\theta$. The absence of terms such as $\sin\theta$ and $\cos\theta/2$ then

means that this can be expressed in terms of Legendre polynomials with a clean cut-off at some order $l_{\max}$. From examining the powers in Eq (91), the highest order term in $\cos\theta$ is $J_1 + J_2$, which corresponds to a highest order Legendre polynomial of $l_{\max} = J_1 + J_2$. Thus the result has been proven, and Eq (83) is a useful means for examining how well Λ^* resonances can describe the data.

An appropriate cut-off for $l_{\max}$ needs to be decided upon, which is the key concept of this analysis approach. The PDG and theoretical predictions are in agreement that the highest spin state present in the data should correspond to $J = 9/2$, which in turn corresponds to expecting Λ^* contributions to Legendre moments up to order $l_{\max} = 9$. However, high spin states are not present at low m_{Kp} masses. Thus using $l_{\max} = 9$ at low m_{Kp} does not make sense, and a mass-dependent $l_{\max}$ is used instead. In particular, if the lowest lying known resonance with spin J has mass M_0 and width Γ_0, moments up to order $2J$ are allowed for masses above $m_0 - 2\Gamma_0$. As the $J = 1/2$ $\Lambda(1405)$ occurs below threshold, $l = 1$ is allowed throughout the whole mass range. And as the $J = 3/2$ $\Lambda(1520)$ is sufficiently close to the threshold, $l = 3$ is also allowed over the whole mass range. The rest of the dependence is taken as

$$l_{\max}(m_{Kp}) = \begin{cases} 3 & \text{if } m_{Kp} < 1.64\,\text{GeV} \\ 5 & \text{if } 1.64 \leq m_{Kp} < 1.7\,\text{GeV} \\ 7 & \text{if } 1.7 \leq m_{Kp} < 2.050\,\text{GeV} \\ 9 & \text{if } m_{Kp} \geq 2.050\,\text{GeV}. \end{cases} \tag{92}$$

This dependence is shown in Fig. 76, along with the experimental results listed in the PDG and the predictions from Ref. [58].

As a cross-check of the theorem derived above, the Legendre moments of the $\cos\theta_{\Lambda^*}$ distribution as a function of m_{Kp} are shown in Fig. 77 for a very large statistics sample (10^7 events) of decays generated according to the extended Λ^* amplitude model (no P_c contributions) with its parameters set by the fit to the data (Sec. 8.1). The displays for each order Legendre moment are shown with the same scale in order to show their

relative importance, but Fig 78 shows the results zoomed in to see more detail. As a reminder, the model contains 14 Λ^* resonances with spins up to 9/2, as listed in Table 5. Following expectations, the moments with l above the maximal $2J_{\Lambda^*}$ value present at a given m_{Kp} value are all consistent with zero.

In contrast, $\Lambda_b^0 \to P_c^+ K^-$, $P_c^+ \to J/\psi p$ contributions can induce non-zero values of even very high l moments through a wide range of m_{Kp} masses. This important point, which allows this method to work, is illustrated in Fig. 79, where a high statistics sample was generated with an amplitude model containing only the $P_c(4380)$ and $P_c(4450)$ contributions. The parameters of these components were set from the fit of the default amplitude model to the data (see Sec. 10.1). In a similar exercise, high statistics samples were generated with amplitude models containing only the individual $P_c(4380)^+$ and $P_c(4450)^+$ contributions, with all parameters again taken from the default fit to the data (Sec. 10.1). The resulting Legendre moments for both are shown in Fig. 80. One notes that the narrower $P_c(4450)$ contributes much more in the higher moments than the broad $P_c(4380)$. This reflects the important point that the narrower an exotic resonance, the more it will reflect into higher order Legendre moments of the conventional hadron helicity angles. This in turn has important implications on the expected levels of sensitivity to exotic contributions.

By taking the observed m_{Kp} distribution of the data, and expanding the $\cos\theta_{\Lambda^*}$ distribution in bins of m_{Kp} with Legendre polynomials truncated at $l_{\rm max}$, a representation of the Dalitz plane under the H_0 hypothesis can be constructed. Thus if the H_0 hypothesis is true, the projection of the representation onto $m_{J/\psi p}$ should be consistent with the observed distribution in the data, up to statistical fluctuations that get smoothed out by not including higher order moments. The consistency of the H_0 hypothesis with the data can thus be probed. In the next section, the details of this procedure are laid out.

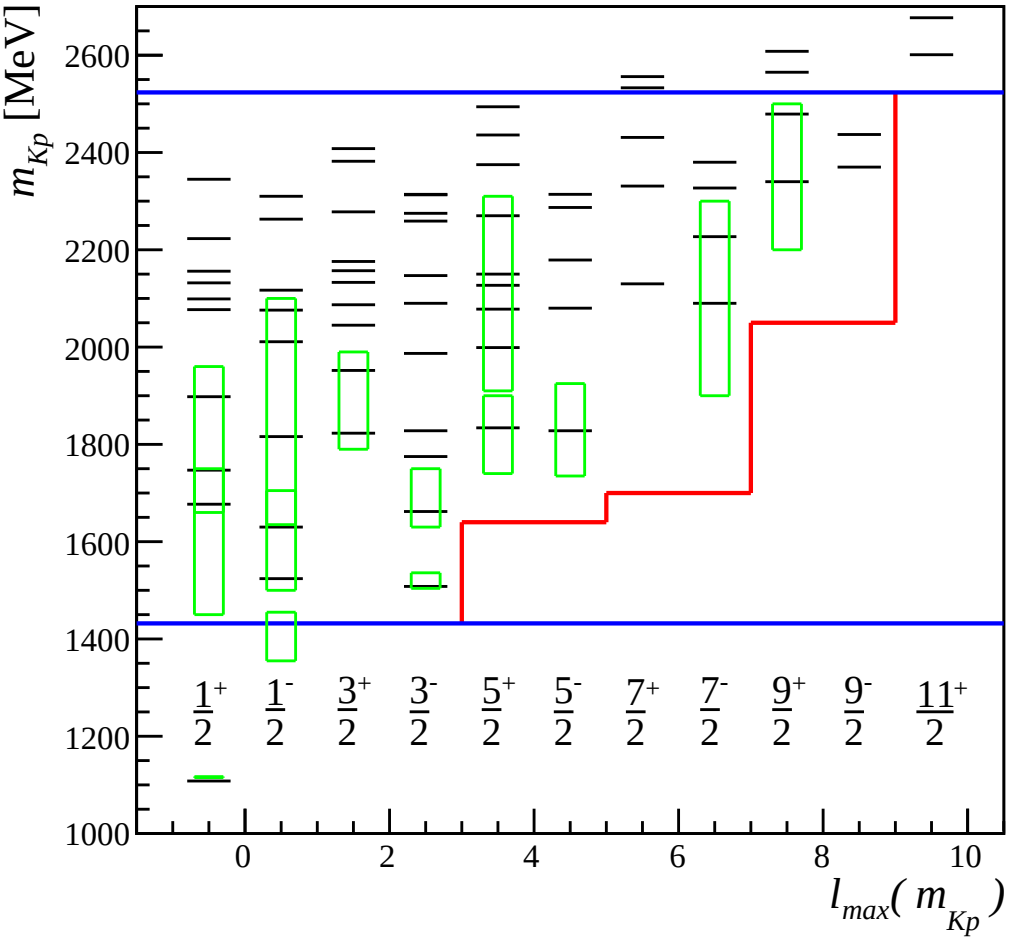

Figure 76: Excitations of the Λ baryon. States predicted in Ref. [58] are shown as short horizontal bars (black) and experimentally well-established Λ^* states are shown as green boxes covering the mass ranges from $M_0 - \Gamma_0$ to $M_0 + \Gamma_0$. The m_{Kp} mass range probed in $\Lambda_b^0 \to J/\psi p K^-$ decays is shown by long horizontal lines (blue). The $l_{\max}(m_{Kp})$ filter is shown as a stepped line (red). All contributions from Λ^* states with J^P values to the left of the red line are accepted by the filter. The filter works well also for the excitations of the Σ baryon [27, 58] (not shown).

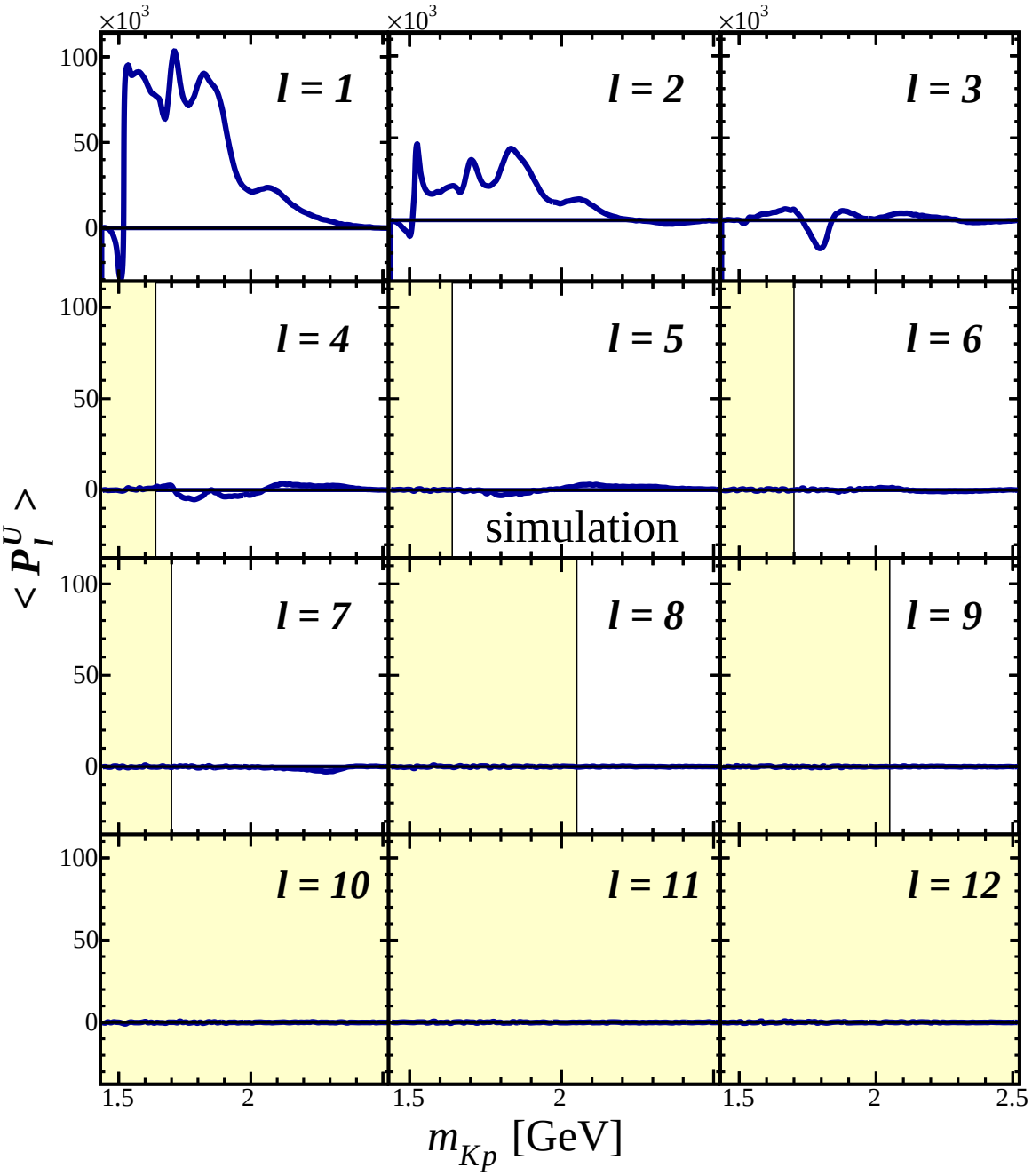

Figure 77: Legendre moments of $\cos\theta_{\Lambda^*}$ as a function of m_{Kp} for simulated data from an amplitude model with only Λ^* resonances (see the text for more details). The regions excluded by the $l \leq l_{\max}(m_{Kp})$ filter are shaded. The displayed range of values of Legendre moments (the vertical axis) is kept the same between various ℓ to illustrate their relative importance. See Fig. 78 for the same plots displayed with an ℓ-dependent display range, which makes the variations more visible.

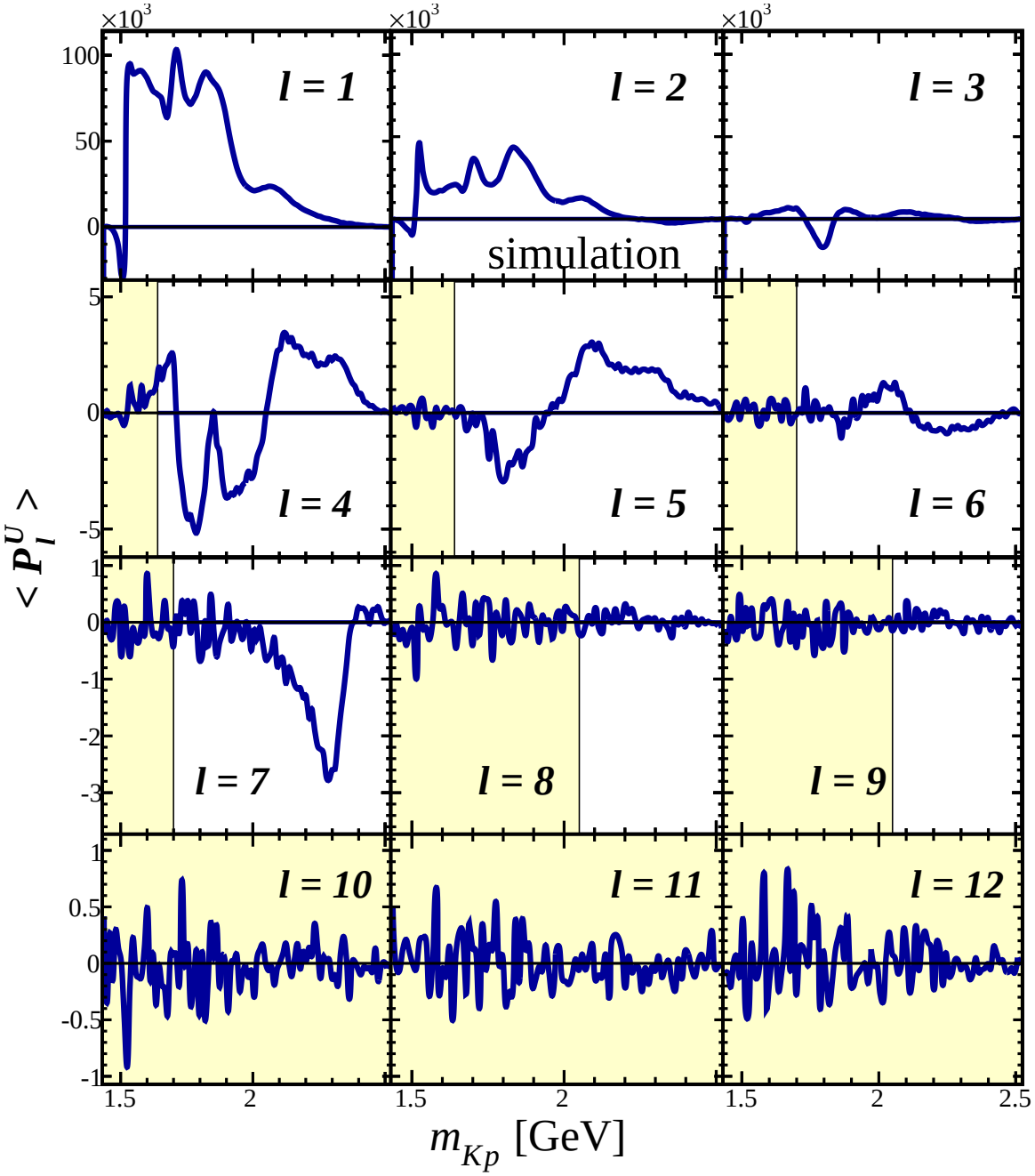

Figure 78: Legendre moments of $\cos\theta_{\Lambda^*}$ as a function of m_{Kp} for simulated data from an amplitude model with only Λ^* resonances (see the text for more details). The regions excluded by the $l \leq l_{\max}(m_{Kp})$ filter are shaded. These are the same plots as already shown in Fig. 77, but displayed here with an $\ell-$dependent range in order to make higher order moments more visible.

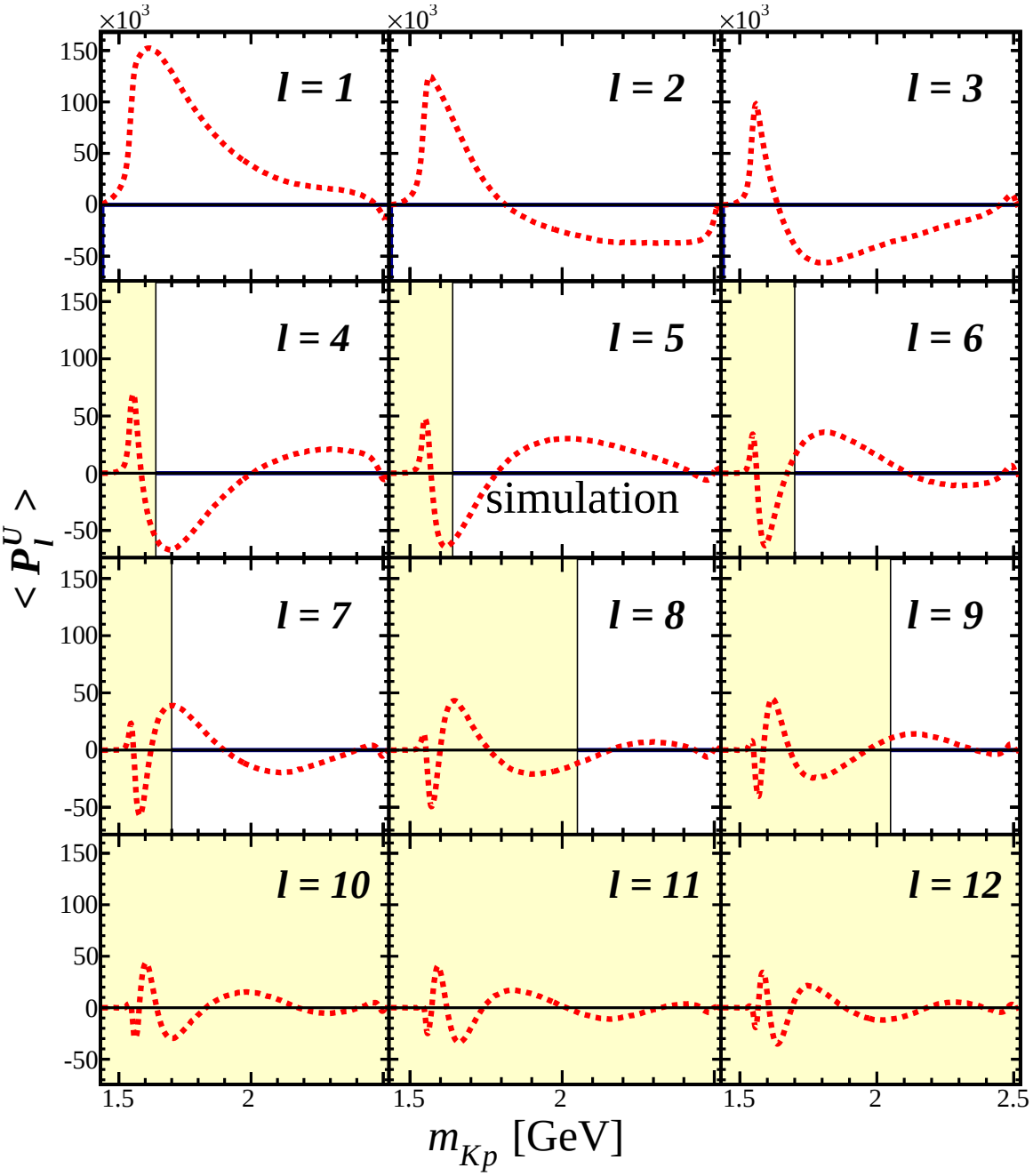

Figure 79: Legendre moments of $\cos\theta_{\Lambda^*}$ as a function of m_{Kp} for simulated data from an amplitude model with only the $P_c(4380)$ and $P_c(4450)$ resonances (see the text for more details). The regions excluded by the $l \leq l_{\max}(m_{Kp})$ filter are shaded.

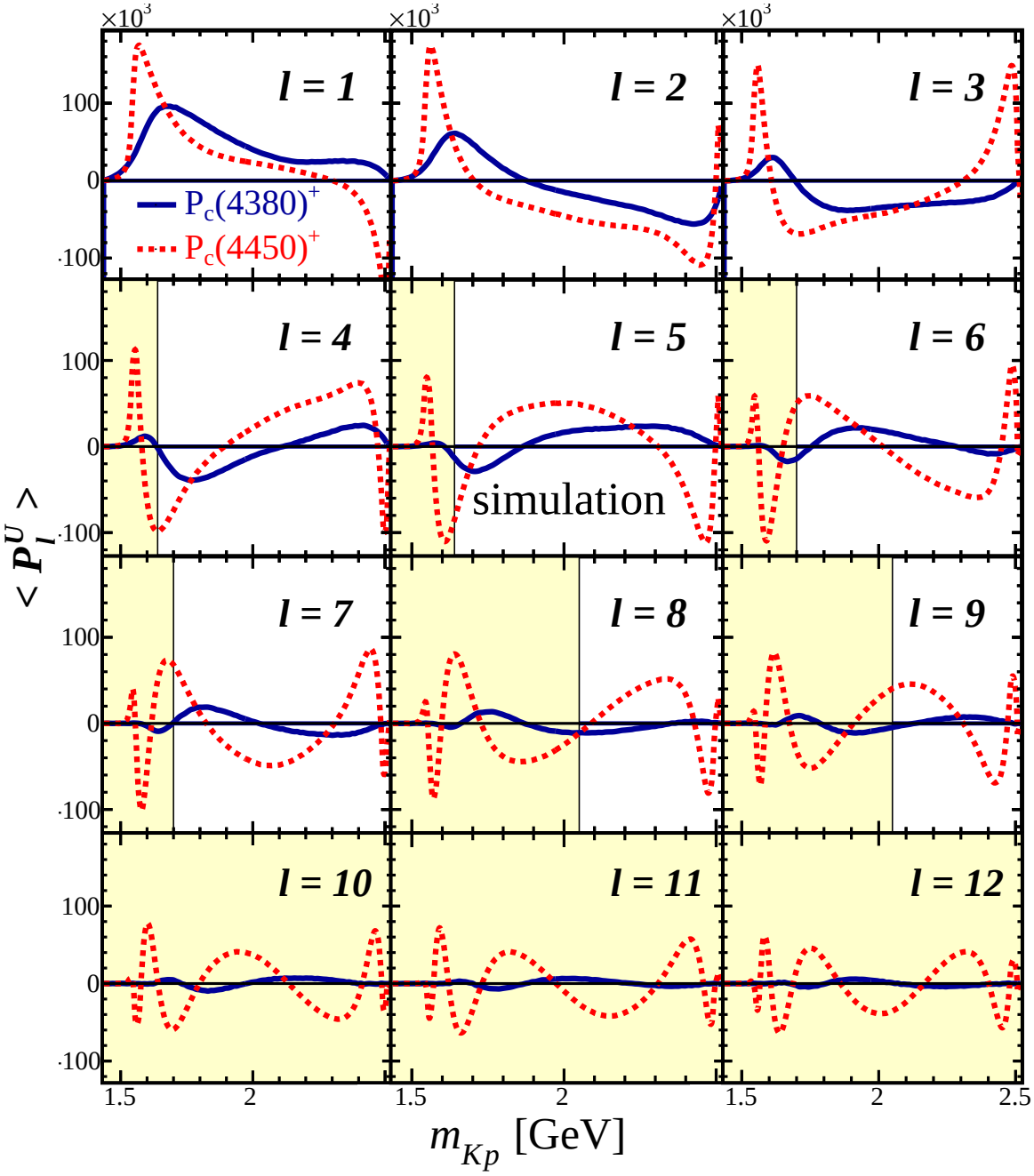

Figure 80: Legendre moments of $\cos\theta_{\Lambda^*}$ as a function of m_{Kp} for simulated data from amplitude models with either only the $P_c(4380)$ (solid blue) or $P_c(4450)$ (dashed red) resonance (see the text for more details). The regions excluded by the $l \leq l_{\max}(m_{Kp})$ filter are shaded.

20 Procedure

The general strategy of the analysis is outlined in the following steps, for which more details will be given in the rest of this section:

1. Form efficiency-corrected and background-subtracted binned m_{Kp} and $m_{J/\psi p}$ distributions. Use also efficiency corrections and background-subtraction in the calculation of Legendre moments of $\cos\theta_{\Lambda^*}$ in each bin of m_{Kp} ($\langle P_l^U \rangle_k$).

2. Use the m_{Kp} distribution and Legendre moments obtained in (1), along with the $l_{\max}$ filter of the H_0 hypothesis, to form a two-dimensional $\mathcal{PDF}$: $\mathcal{F}(m_{Kp}, \cos\theta_{\Lambda^*}|H_0)$.

3. Project $\mathcal{F}(m_{Kp}, \cos\theta_{\Lambda^*}|H_0)$ onto $m_{J/\psi p}$ by using the $m_{J/\psi p} \leftrightarrow \cos\theta_{\Lambda^*}$ correspondence (Eq. 82), and integrating over m_{Kp}. Such projection allows to construct tests of H_0 which take into account that exotic hadron contributions peak in certain $m_{J/\psi p}$ range. As their reflections create complicated bands in the $(m_{Kp}, \cos\theta_{\Lambda^*})$ plane (see *e.g.* the right plot of Fig. 129), which cannot be built into 2D test variables in a model independent way, tests constructed directly in this plane have very poor sensitivity to exotic hadrons.

4. Probe the compatibility of $\mathcal{F}(m_{J/\psi p}|H_0)$ with the $m_{J/\psi p}$ distribution obtained in (1) via a hypothesis test variable t (to be made more specific later).

5. As there are many parameters in $\mathcal{F}(m_{J/\psi p}|H_0)$, which are correlated in a complicated way, run pseudoexperiments to get the distribution of t under the H_0 hypothesis: $\mathcal{F}(t|H_0)$.

6. With $\mathcal{F}(t|H_0)$, and the value of t obtained on the data, calculate a p-value for H_0. If the p-value is sufficiently low[16] the H_0 hypothesis can be rejected. Otherwise, the data are not inconsistent with the presence of only $l \leq l_{\max}$ moments. Such a statement does not rule out the presence of exotic hadron contributions.

[16] A p-value is the probability that H_0 is rejected even though it is true, thus frequency of such undesired "type I error" can be directly dialed by a choice of a cut-off value.

Similar to the *cFit* method which was used in the amplitude analysis, events are selected from the signal range, while the sidebands are used for subtraction of the background (see Fig 30). Details will now be given for the general procedure, and the construction of the $\mathcal{PDF}$'s will be outlined.

20.1 Efficiency correction and background subtraction

Efficiency effects lead to distortions in the distributions of the data, and thus need to be corrected for in order for the considerations in Sec. 19 to hold. For example, in addition to the directly used m_{Kp} and $m_{J/\psi p}$ distributions, efficiency effects would also lead to modifications of the Legendre moments, and invalidate the conclusion that $l_{\max} = 2J_{\max}$ is the highest rank of Legendre polynomial needed to fully describe the $\cos\theta_{\Lambda^*}$ distribution. Thus efficiency corrections must be applied, and this requires an efficiency parameterization. Unless the efficiency is completely uniform in the other decay angles (which is not the case here), the parameterization should still take them into account. Thus the efficiency correction is applied to all six dimensions which describe the decay. The parametrization used is the same as in the amplitude analysis (Sec. 6.2). In particular, the efficiency is assumed to factorize as

$$\begin{aligned}\epsilon(m_{Kp}, \cos\theta_{\Lambda^*}, \Omega_a) = \epsilon_1(m_{Kp}, \cos\theta_{\Lambda^*}) \times \epsilon_2(\cos\theta_{\Lambda_b^0}|m_{Kp}) \times \epsilon_3(\cos\theta_{J/\psi}|m_{Kp}) \times \\ \epsilon_4(\phi_K|m_{Kp}) \times \epsilon_5(\phi_\mu|m_{Kp}).\end{aligned} \tag{93}$$

The notation is slightly different in order to separate the Dalitz variables from the other decay angles Ω_a, but the parametrization is exactly the same as Eq. 68. This is used to calculate the efficiency on an event-by-event basis, and its inverse is used as an event weight when making histograms of efficiency-corrected yields as well as when calculating the Legenedre moments.

The background subtraction is done using the events from the Λ_b^0 sidebands, which are the same as defined in Sec 6.2. A scaling factor, $\alpha \equiv \beta N_{\text{signal-band}}/N_{\text{sideband}}$, corrects for different background yields in the signal-band and in the sidebands. Here $N_{\text{signal-band}}$

is the number of selected events in the signal region, N_{sideband} is the number of selected events in the Λ_b^0 sidebands, and β is the background fraction in the signal region (5.4%), also defined in Sec 6.2. When calculating the signal yields or Legendre moments, all events in the signal-band and sidebands are summed over, with each event having a background subtraction weight w assigned. This weight is set to one for events in the signal region and to $-\alpha$ for events in the sidebands. In a variation of this default method, the *sPlot* technique is used to set w to sWeights which are determined by the fits to $m_{J/\psi pK}$ (Fig. 20).

20.2 Construction of $\mathcal{PDF}$'s

The full $\mathcal{PDF}$ representing the H_0 hypothesis is factored as

$$\mathcal{F}(m_{Kp}, \cos\theta_{\Lambda^*}|H_0) = \mathcal{F}(m_{Kp}|H_0)\,\mathcal{F}(\cos\theta_{\Lambda^*}|H_0, m_{Kp}), \tag{94}$$

where $\mathcal{F}(m_{Kp}|H_0)$ gives a dependence on m_{Kp}, and $\mathcal{F}(\cos\theta_{\Lambda^*}|H_0, m_{Kp})$ gives the dependence on $\cos\theta_{\Lambda^*}$ at a given m_{Kp}. The construction of both, and the determination of their numerical parameters will now be shown.

In order to make the analysis as model-independent as possible, no interpretations are imposed on the m_{Kp} mass distribution. Instead, the observed efficiency-corrected and background-subtracted histogram of m_{Kp} is simply incorporated as a part of the numerical representation of the H_0 hypothesis. These parameters are denoted as

$$\{\Delta N^k/\Delta m_{Kp}, k = 1, \ldots, n_{\text{bin}}^{Kp}\}, \tag{95}$$

where k denotes the bin index, $\Delta N^k/\Delta m_{Kp}$ is the bin yield, and $n_{\text{bin}}^{Kp} = 100$ is the number of bins used. The bins are divided evenly in the kinematically allowed range: $(m_K + m_p, m_{\Lambda_b^0} - m_{J/\psi})$. The yields in each bin are determined from the data as

$$\Delta N^k/\Delta m_{Kp} = \sum_{i=1}^{n_{\text{cand}}{}^k} w_i/\epsilon_i. \tag{96}$$

Here the i index iterates over selected $J/\psi pK^-$ candidates in the signal and sideband regions for the k^{th} bin of m_{Kp} (${n_{\rm cand}}^k$ is their total number), $\epsilon_i = \epsilon({m_{Kp}}^i, \cos{\theta_{\Lambda^*}}^i, {\Omega_a}^i)$ is the efficiency correction, and w_i is the background subtraction weight. To obtain a continuous probability density function, $\mathcal{F}(m_{Kp}|H_0)$, a quadratic interpolation between nearby $\Delta N^k/\Delta m_{Kp}$ values is used. The m_{Kp} distribution of the data and $\mathcal{F}(m_{Kp}|H_0)$ are shown in Fig 81.

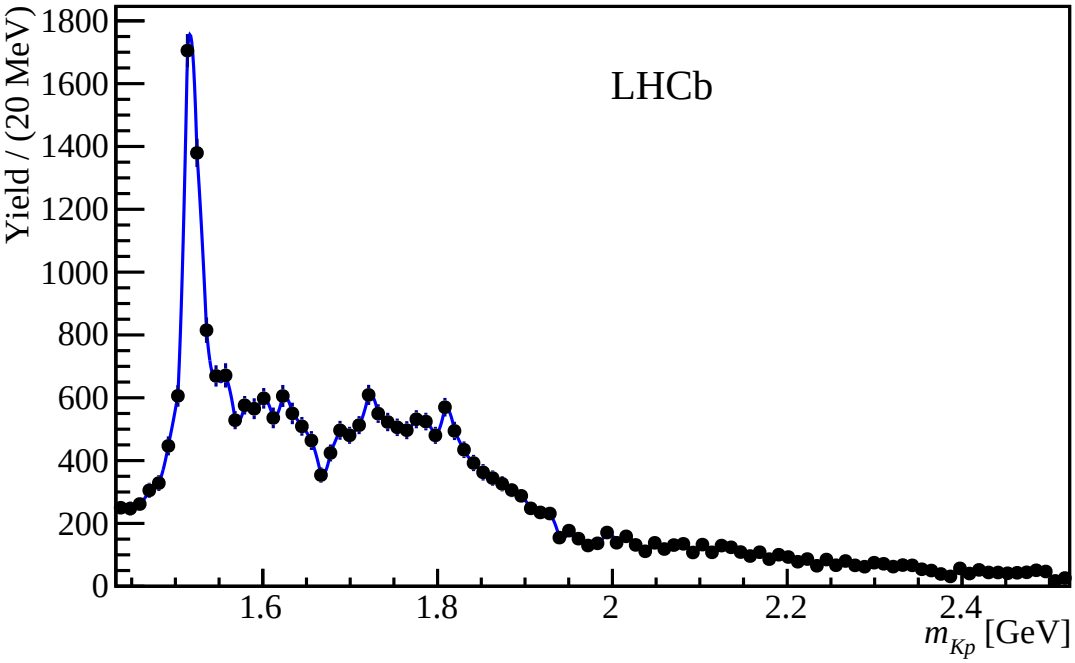

Figure 81: Efficiency-corrected and background-subtracted m_{Kp} distribution of the data (black points with error bars), with $\mathcal{P}(m_{Kp}|H_0)$ superimposed (solid blue line). $\mathcal{P}(m_{Kp}|H_0)$ fits the data by construction.

To construct $\mathcal{F}(\cos\theta_{\Lambda^*}|H_0, {m_{Kp}}^k)$, the Legendre polynomial expansion of $\cos\theta_{\Lambda^*}$ is used. The Legendre moments are determined from the data as

$$\langle P_l^U \rangle^k = \sum_{i=1}^{{n_{\rm cand}}^k} (w_i/\epsilon_i) P_l(\cos\theta^i_{\Lambda^*}), \tag{97}$$

where the same binning as Eq. 96 is used. The values of $\langle P_l^U \rangle^k$ are shown in Fig. 82, and again in Fig. 83 with only 25 bins so that the structures are more clearly seen. Note that the lower order moments dominate, consistent with expectations of greater contributions coming from resonances with relatively low spins. However, there is substantial activity in the higher moments as well. It is important to also note the presence of structures

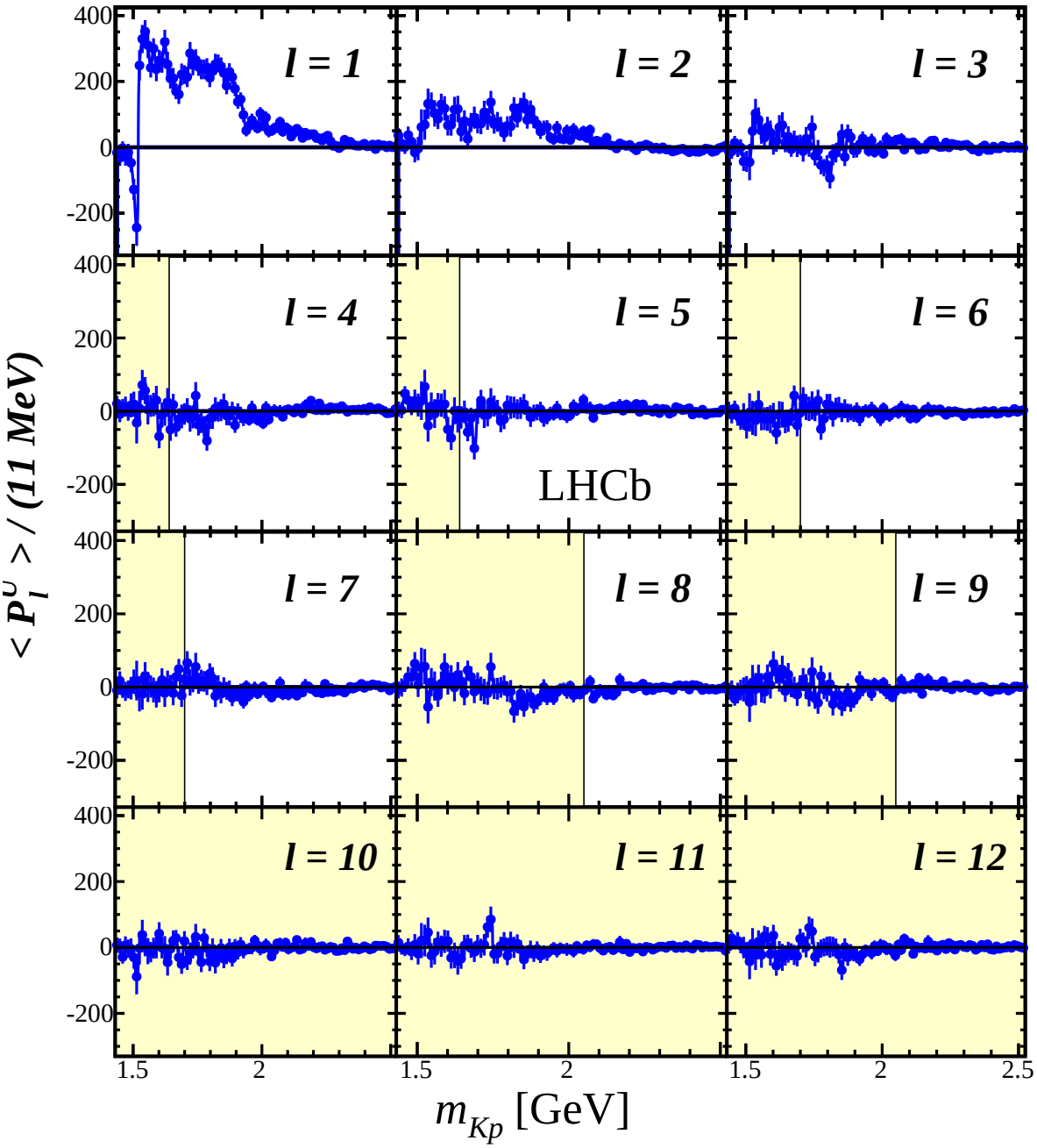

Figure 82: Legendre moments of $\cos\theta_{\Lambda^*}$ as a function of m_{Kp} in the data. Regions excluded by the $l \leq l_{\max}(m_{Kp})$ filter are shaded. For coarser binning, see Fig. 83.

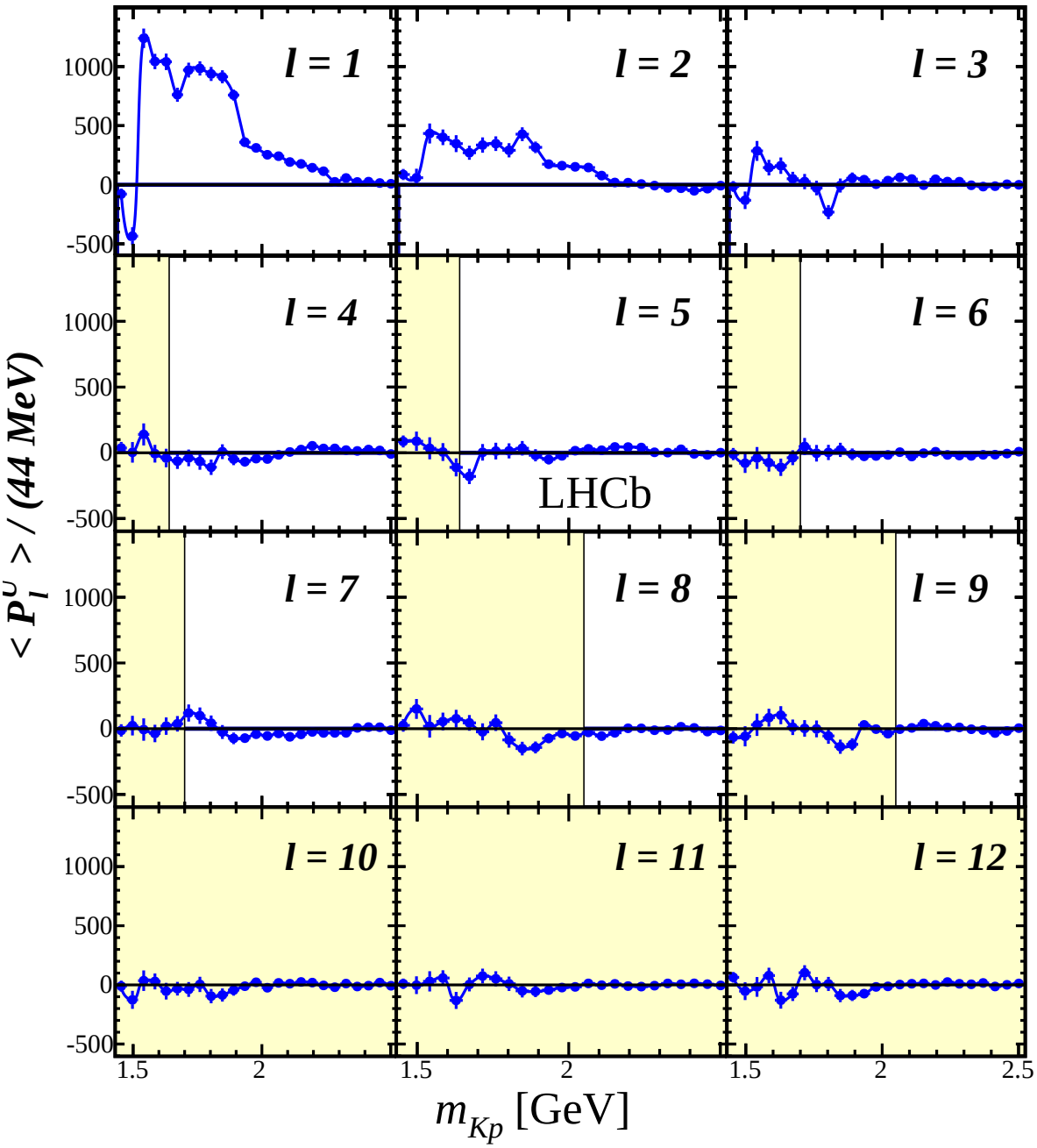

Figure 83: Legendre moments of $\cos\theta_{\Lambda^*}$ as a function of m_{Kp} in the data, shown with just 25 bins. Regions excluded by the $l \leq l_{\max}(m_{Kp})$ filter are shaded.

in regions which are excluded by the $l_{\max}(m_{Kp})$ filter. The deviations from the expected behavior of K^-p contributions can by itself be taken as indications of exotic contributions. Still, as the fit fractions of the $P_c(4380)$ and $P_c(4450)$ in the amplitude model are only 8.4% and 4.1%, respectively, it is important to probe the presence of moments induced via exotic contributions in a way which aggregates the entire data set. Towards obtaining a continuous $\mathcal{PDF}$, linear interpolation between neighboring m_{Kp} bins is used for each l-th moment. The moments are then used to construct $\mathcal{F}(\cos\theta_{\Lambda^*}|H_0, {m_{Kp}}^k)$ as

$$\mathcal{F}(\cos\theta_{\Lambda^*}|H_0, {m_{Kp}}^k) = \sum_{l=0}^{l_{\max}({m_{Kp}}^k)} \langle P_l^N \rangle^k P_l(\cos\theta_{\Lambda^*}).$$

Here the Legendre moments are normalized,

$$\langle P_l^N \rangle^k = \langle P_l^U \rangle^k \, 2/(\Delta N^k/\Delta m_{Kp}),$$

since the overall normalization of $\mathcal{F}(\cos\theta_{\Lambda^*}|H_0, m_{Kp})$ to the data is already contained in the $\mathcal{F}(m_{Kp}|H_0)$ definition. With this, the construction of the full $\mathcal{F}(m_{Kp}, \cos\theta_{\Lambda^*}|H_0)$ has been specified. A complete list of its parameters, and a full numerical representation of the H_0 hypothesis, is given by

$$\{\Delta N^k/\Delta m_{Kp}, [\langle P_l^U \rangle^k, l = 1, \ldots, l_{\max}({m_{Kp}}^k)], k = 1, \ldots, n_{\text{bin}}^{Kp}\}. \tag{98}$$

20.3 Projection onto $m_{J/\psi p}$

In order to probe the consistency of H_0 with the data, $\mathcal{F}(m_{Kp}, \cos\theta_{\Lambda^*}|H_0)$ is projected onto $m_{J/\psi p}$. This is done using the $m_{J/\psi p} \leftrightarrow \cos\theta_{\Lambda^*}$ correspondence (Eq. 82), and integrating over m_{Kp}. In practice, this is done via Monte Carlo techniques. A total of 10^7 events are generated uniformly over the $(m_{Kp}, \cos\theta_{\Lambda^*})$ plane. Each event is then weighted by its value of $\mathcal{F}(m_{Kp}, \cos\theta_{\Lambda^*}|H_0)$. Each event's value of $m_{J/\psi p}$ is then calculated, and a histogram of $m_{J/\psi p}$ filled with each event's weight. To achieve a continuous $\mathcal{F}(m_{J/\psi p}|H_0)$, quadratic splines are used to interpolate between nearby $m_{J/\psi p}$ bins of the histogram.

Shown in Fig. 84 is the efficiency-corrected and background-subtracted $m_{J/\psi p}$ distribution of the data, along with $\mathcal{F}(m_{J/\psi p}|H_0)$. The distribution of the data has been obtained just as the m_{Kp} distribution, with histogram bins determined as

$$\Delta N^k/\Delta m_{J/\psi p} = \sum_{i=1}^{n_{\rm cand}{}^k} w_i/\epsilon_i. \tag{99}$$

Clearly, there is an excess of the data over $\mathcal{F}(m_{J/\psi p}|H_0)$ in the $P_c(4450)$ region. Because of

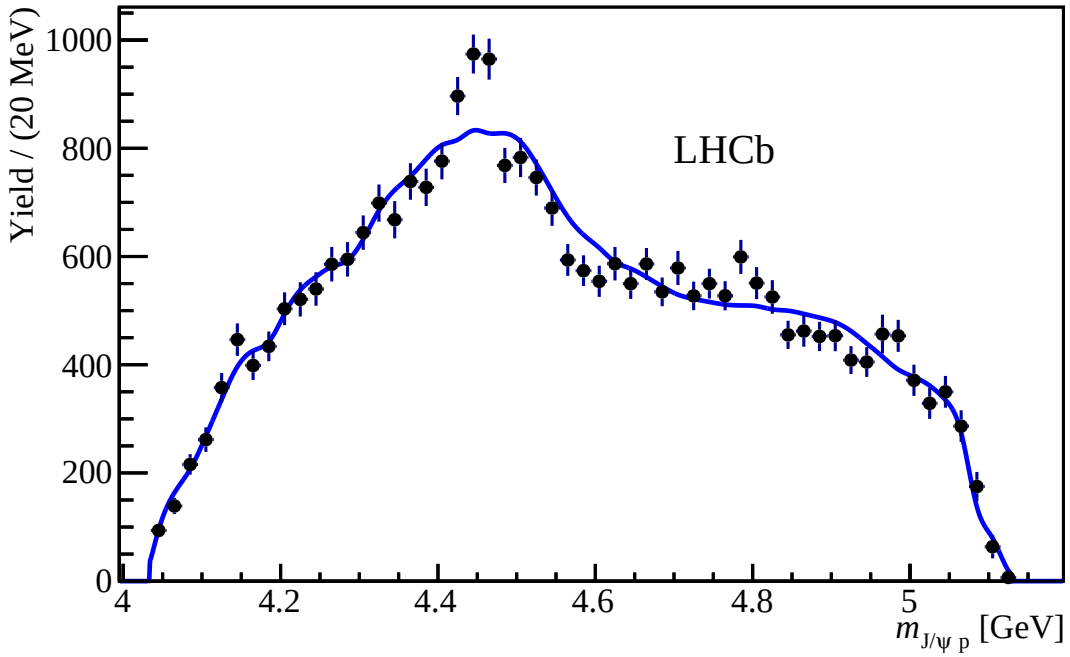

Figure 84: Efficiency-corrected and background-subtracted $m_{J/\psi p}$ distribution of the data (black points with error bars), with $\mathcal{F}(m_{J/\psi p}|H_0)$ (solid blue line) superimposed.

the statistical correlations between the data and $\mathcal{F}(m_{J/\psi p}|H_0)$, no quantitative statements can immediately be made on the size of the disagreement between them. The quantitative tests used, and the statistical simulations necessary to turn the results into a p-value, are discussed in the following sections.

20.4 Hypothesis Testing

The hypothesis testing is performed with test variables, generically denoted as t, which probe the compatibility of H_0 with the data. A natural test variable is a χ^2 variable:

$$
\begin{aligned}
t_{\chi^2} &= \sum_{k=1}^{n_{\text{bins}}} \left(\frac{c_k - \mathcal{F}({m_{J/\psi p}}^k | H_0)}{\sigma(c_k)} \right)^2 , \\
c_k &= \Delta N^k / \Delta m_{J/\psi p} = \sum_{i}^{{n_{\text{cand}}}^k} w_i / \epsilon_i , \\
\sigma(c_k) &= \sqrt{\sum_{i}^{{n_{\text{cand}}}^k} (w_i/\epsilon_i)^2}
\end{aligned}
\tag{100}
$$

where c_k is the k^{th} bin content of the directly obtained efficiency-corrected and background-subtracted $m_{J/\psi p}$ distribution, ${m_{J/\psi p}}^k$ is the bin center, ${n_{\text{cand}}}^k$ is the number of events contributing to this bin, and n_{bins} is the number of bins. Since c_k and the values of $\mathcal{F}({m_{J/\psi p}}^k | H_0)$ are strongly correlated[17], the average t_{χ^2} value is expected to be smaller than $n_{\text{bins}} - 1 = 54$, which is the number of degrees of freedom (ndf) for a χ^2 calculated between uncorrelated histograms normalized to the same area. The $\mathcal{F}(m_{J/\psi p}|H_0)$ function can roughly be thought of as a display of the fit of $\mathcal{F}(m_{Kp}, \cos\theta_{\Lambda^*}|H_0)$ to the 2D distribution $(m_{Kp}, \cos\theta_{\Lambda^*})$, projected onto the $m_{J/\psi p}$ axis. However as the parameters of the model, $\{\Delta N^k/\Delta m_{Kp},\ [\langle P_l^U \rangle^k,\ l = 1, \ldots, l_{\max}({m_{Kp}}^k)],\ k = 1, \ldots, n_{\text{bin}}^{Kp}\}$, are not actually fit to the $m_{J/\psi p}$ distribution, the reduction of ndf of the t_{χ^2} variable cannot be predicted without statistical simulations. These will be discussed in Sec. 20.4.

The appeal of any χ^2 test is the simplicity of its formulation, as it tests a given hypothesis, H_0, against any alternative hypothesis, H_1, which is simply defined as *not* H_0. However, its power against any more specific H_1 hypothesis may be poor. The sensitivity of the above described χ^2 test, t_{χ^2}, can also suffer from the use of overestimated errors in its definition, which do not correct for the statistical correlations between c_k and $\mathcal{F}({m_{J/\psi p}}^k|H_0)$. For a more specific H_1 hypothesis, which can predict $\mathcal{F}(m_{J/\psi p}|H_1)$,[18] the

[17] In fact, for $l_{\max} \to \infty$ the two values must be exactly equal, resulting in $t_{\chi^2} = 0$.
[18] $H_1 = .not.H_0$ cannot predict it!

most sensitive choice of a test variable often is:

$$t_{\rm DLL} = -2\sum_i \log\left(\frac{\mathcal{P}(x_i|H_0)}{\mathcal{P}(x_i|H_1)}\right), \tag{101}$$

where the sum is over all events in the data sample. Such a likelihood-ratio test is guaranteed to be the most powerful test between H_0 and H_1 if the hypotheses are simple *i.e.* contain no free parameters. In the present case, H_0 contains a large number of parameters which are determined from the data. Nevertheless, the likelihood-ratio test can be useful if H_1 is made more specific than $.not.H_0$.

Thus, as was done in the analysis of $B^0 \to \psi(2S)\pi^+K^-$ decays [20], the alternative hypothesis is taken as including moments up to $l \leq l_{\rm large}$, where $l_{\rm large}$ is some value which is sufficiently large to describe exotic hadron contributions. The precise meaning of such a constructed likelihood-ratio test, is to test the significance of the $l_{\rm max}(m_{Kp}) \leq l \leq l_{\rm large}$ moments of the $\cos\theta_{\Lambda^*}$ distributions in the data; these are the moments which cannot be plausibly induced via $\Lambda_b^0 \to J/\psi\,\Lambda^*$, $\Lambda^* \to K^-p$ decays. It is important to choose the value of $l_{\rm large}$ independently of the actual data set, otherwise the choice of $l_{\rm large}$ value must be subject to statistical simulations with pseudoexperiments. This can be cumbersome, especially without a well defined numerical algorithm. In Ref [20], a value of $l_{\rm large} = 30$ was used, and so a similar choice of $l_{\rm large} = 31$ was decided upon. Note that the value is incremented by one, because in the present case baryons are being studied, which have fractional spin. Thus, a complete list of parameters which specify the H_1 hypothesis is

$$\{\Delta N^k/\Delta m_{Kp}, [\langle P_l^U\rangle^k, l = 1, \ldots, l_{\rm large} = 31], k = 1, \ldots, n_{\rm bin}^{Kp}\}. \tag{102}$$

A $\mathcal{PDF}$ describing this hypothesis, $\mathcal{F}(m_{Kp}, \cos\theta_{\Lambda^*}|H_1)$, is then built and projected onto $m_{J/\psi p}$ to get $\mathcal{F}(m_{J/\psi p}|H_1)$ in the same manner as was done for H_0. It can be seen in Fig. 85 that this choice of $l_{\rm large}$ is capable of capturing the observed $m_{J/\psi p}$ structures rather well, including the narrow peak associated with the $P_c(4450)$ state.

It is worth emphasizing that a choice of $l_{\rm large}$ cannot be "wrong", as it is ultimately just a test variable, whose distribution under the H_0 hypothesis can be simulated. Thus,

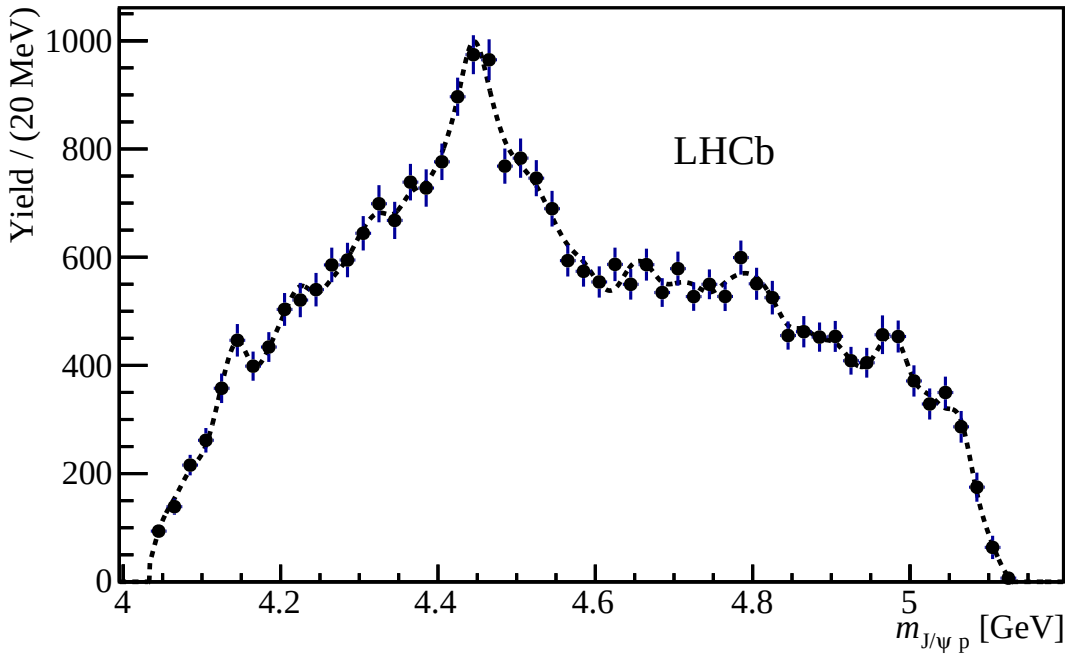

Figure 85: Efficiency-corrected and background-subtracted $m_{J/\psi p}$ distribution of the data (black points with error bars), with $\mathcal{P}(m_{J/\psi p}|H_1)$ (dashed black line).

a choice of l_{large} can only be questionable due to sub-optimal discriminating power. At first, it might seem that l_{large} should be taken as large as is practically possible. However, after a certain point, increasing it even further only serves to better describe statistical fluctuations. This doesn't capture any physics, and only weakens its discriminating power. In Appendix M, the full analysis is repeated with a range of l_{large} values.

The data contains an admixture of background events and signal events. Instead of incorporating the background $\mathcal{PDF}$ into $\mathcal{P}(m_{J/\psi p\ i}|H_{0,1})$ in Eq. (101), an approach is used which was motivated by the *sFit* method: the background contribution is subtracted from the log-likelihood value on a statistical basis by using the sidebands and event weights (w_i):

$$t_{\text{DLL}} = -2 \sum_{i}^{n_{\text{cand}}^{\text{sig}}+n_{\text{cand}}^{\text{side}}} w_i \left(\frac{\mathcal{P}(m_{J/\psi p\ i}|H_0)}{\mathcal{P}(m_{J/\psi p\ i}|H_1)} \right). \tag{103}$$

These weights are the same as the simple sideband-subtraction weights which were discussed already in Sec. 20.1. In a systematic check, the sWeights determined by the fit to $m_{J/\psi Kp}$ are used instead.

In Ref. [20], the log-likelihood ratio was efficiency-corrected, by using a $1/\epsilon_i$ weight

for each event, such that the total weight was w_i/e_i. It was decided not to follow this approach here, as the weights do not seem well justified from likelihood theory. Further, it makes the test variable more dependent on the efficiency. Instead, the $\mathcal{PDF}$ for each hypothesis has the efficiency factored in:

$$\mathcal{P}(m_{J/\psi p\ i}|H_{0,1}) = \mathcal{F}(m_{J/\psi p\ i}|H_{0,1})\,\epsilon_i/I_{H_{0,1}}, \tag{104}$$

where $I_{H_{0,1}}$ is the normalization. The event efficiencies ϵ_i then cancel in the calculation of the likelihood ratio $\mathcal{P}(m_{J/\psi p\ i}|H_0)/\mathcal{P}(m_{J/\psi p\ i}|H_1)$. While they still affect the normalization, this definition of log-likelihood ratio is less dependent on the efficiency. The normalization integral is performed via Monte Carlo integration with an $n_{\mathrm{MC}} = 10^7$ event sample generated uniformly in phase space:

$$I_{H_{0,1,}} \propto \sum_{k}^{n_{\mathrm{MC}}} \mathcal{P}(m_{J/\psi p\ k}|H_{0,1})\,\epsilon_k. \tag{105}$$

Putting things together, a pseudo[19] log-likelihood ratio test variable is defined as

$$t_{\mathrm{DLL}} = \Delta(-2\log\mathcal{L}) = -2 \sum_{i}^{n^{\mathrm{sig}}_{\mathrm{cand}}+n^{\mathrm{side}}_{\mathrm{cand}}} w_i \log\left(\frac{\mathcal{F}(m_{J/\psi p\ i}|H_0)/I_{H_0}}{\mathcal{F}(m_{J/\psi p\ i}|H_1)/I_{H_1}}\right). \tag{106}$$

Both test variables are studied in this analysis. However, it can be expected, and is in fact seen, that the log-likelihood ratio proves to be the more powerful discriminator.

20.5 Pseudoexperiments

In order to turn the values of the test variables obtained from the data, $t^{\mathrm{data}}_{\chi^2}$ and $t^{\mathrm{data}}_{\mathrm{DLL}}$ into a p-value for the H_0 hypothesis, the distributions of t_{χ^2} and t_{DLL} under the H_0 hypothesis, $\mathcal{F}_t(\chi^2|H_0)$ and $\mathcal{F}_t(\Delta(-2\ln\mathcal{L})|H_0)$, must first be known. In order to obtain these, a large number of pseudoexperiments are generated according to the H_0 hypothesis, and the test variables are calculated and accumulated until a good handle on the $\mathcal{F}_t(t|H_0)$ distributions are obtained. In the pseudoexperiments, all parts of the analysis are simulated in order

[19] "pseudo" since the event weighting is involved.

to capture all contributions of statistical fluctuations. Thus, three different types of toy data sets are produced in each pseudoexperiment, which are analyzed in the same exact way as the real data. They are:

- Λ_b^0 **signal region** pseudo-events, corresponding to real data taken from $\pm 2\sigma$ of the Λ_b^0 mass peak. This sample is a mixture of signal events corresponding to true $\Lambda_b^0 \to J/\psi\, pK^-$ events in the data as well as background events.

- Λ_b^0 **sideband region** pseudo-events, corresponding to data taken from the sidebands of the Λ_b^0 mass peak. This sample contains only background events, which are used for the statistical subtraction of the background in the Λ_b^0 signal region.

- **Efficiency MC** pseudo-events, corresponding to the fully simulated, phase space MC data set used to construct the efficiency parameterization. The parametrization is used for the efficiency correction when making displays of the data and when calculating the Legendre moments of $\cos\theta_{\Lambda^*}$.

The toy data sets are generated with statistics exactly matching that used in the analysis of the actual data. The generation procedure consists of generating events uniformly, and then shaping them based off specific procedures dependent on the event type. In general, there may be multiple effects shaping a data sample, such as efficiency and decay dynamics. Each of these effects has a weight w^j associated with it, such that there is a total weight

$$w = \prod_{j=1} w^j \tag{107}$$

As the data set used in the actual analysis was unweighted, it was decided to perform the generation with an accept/reject algorithm, rather than handle weighted data events. For an event i, the ratio $w_i/w_{\max}$ is formed, where w_i is the total weight for that particular event and $w_{\max}$ is the maximum possible weight. A random number x in the interval of $(0, 1)$ is then thrown, and if $x < w_i/w_{\max}$ the event is accepted; otherwise it is rejected. This procedure results in the data set being shaped by all relevent effects.

The MC pseudo-data set, used in the efficiency correction procedure, is generated uniformly in phase space and then shaped with the efficiency parameterization used

when correcting the real data. The Λ_b^0 sideband events are also generated uniformly, and then shaped using a background parametrization. The background parametrization is the same as was used in the amplitude analysis (Sec.6.2). It is built the same way as the efficiency parametrization, but using the sideband events. The Λ_b^0 signal region pseudo-events are simulated by combining signal and background pseudo-events, which contribute $n_{\rm cand}^{\rm sig}(1-\beta)$ and $n_{\rm cand}^{\rm sig}\beta$ events, respectively. The background pseudo-events are necessary to include in order to simulate the background subtraction. They are generated in the same way as the sideband events. The signal events are generated uniformly on the $(m_{Kp}, \cos\theta_{\Lambda^*})$ plane, and in all other decay angles as well. These events are shaped by $\mathcal{F}(m_{Kp}, \cos\theta_{\Lambda^*}|H_0)$ and the efficiency parametrization. The $\mathcal{F}(m_{Kp}, \cos\theta_{\Lambda^*}|H_0)$ weight by itself would result in the pseudo-signal data matching the efficiency-corrected and background-subtracted m_{Kp} distributions of the real data, as well as its angular structure expanded in Legendre moments of $\cos\theta_{\Lambda^*}$ filtered through the $l \leq l_{\rm max}(m_{Kp})$ requirement. Therefore, they represent data constructed under the H_0 hypothesis. There is a subtle effect which results from the fact that the other decay angles, $\Omega_a = (\cos\theta_{\Lambda_b^0}, \cos\theta_{J/\psi}, \phi_K, \phi_\mu)$ are only shaped by the efficiency parametrization, whereas in the real data they are shaped by decay dynamics as well as efficiency effects. These angles enter the analysis only via the efficiency correcion, and so their particular distributions would only affect the size of fluctuations due to regions of phase space not being sampled in the same way as the data. As the pseudoexperiments are concerned with measuring the size of fluctuations, and there is no way to shape the angles without assuming a model, it is a systematic effect which is studied in Sec. 24.2.

The pseudoexperiments used for quoting actual p-values for the H_0 hypothesis are generated independently of amplitude models in order to make the model-independent approach self-contained. Such pseudoexperiments are referred to as H_0 pseudoexperiments. However, in validation, sensitivity, and systematic studies the pseudoexperiments may be shaped with an amplitude model. In these cases, the signal events are generated uniformly in phase space, and shaped with the efficiency parametrization and the modulus-squared of the matrix element of the corresponding amplitude model. In such

cases, the effect discussed above with regards to the shaping of the Ω_a angles is not present.

21 Validation and Sensitivity

While this analysis method is model-independent, amplitude models can provide a means to perform validation and sensitivity studies. Since what is present in the amplitude model during the pseudo-data generation is controlled, "the truth" is known and the response of the analysis method to this truth can be tested. This allows for testing whether or not the H_0 hypothesis will be accepted for data sets which contain only the well-motivated Λ^* states. Further, it allows for testing the sensitivity to data sets with both P_c states built into them by construction, and whether or not the H_0 hypothesis would be rejected.

It is also important to study the expected sensitivity as a function of the width of prospective exotic contributions. Exotic, but broad, peaking structures in $m_{J/\psi p}$ will contribute mostly to lower order moments, as was shown in Fig 80. If the exotic contribution contributes mostly to $l \leq l_{\max}(m_{Kp})$, then it is possible that the H_0 hypothesis will be accepted, though it shouldn't be. Within the terminology of hypothesis testing, this is referred to as a "Type II error". This "self-subtraction" is unavoidable, as even narrow exotic contributions will feed down into the numerical representation of H_0 to some extent. The degree to which this is done cannot be a priori known without the usage of some particular amplitude model, with already well determined parameters of all contributions. Due to this effect, if H_0 is accepted, no firm conclusion can be drawn. It is only when H_0 can be rejected that the results become interesting. For these reasons it is useful to probe the expected sensitivity of the method before applying it to the data.

21.1 Validation on extended Λ^* model and sensitivity to default amplitude model

The extended Λ^* amplitude model without any P_c contributions is used to perform pseudoexperiments to check that the model-independent method can reproduce the pseudo-data, i.e. that the H_0 hypothesis would be accepted on data sets with only the conventional resonances. This model contains 14 Λ^* states which span all expected spin values.

The parameters of the amplitude model are taken from the fit to the data (Sec. 8.1). The efficiency-corrected and background-subtracted distribution of $m_{J/\psi p}$ for one pseudoexperiment is compared to $\mathcal{F}(m_{J/\psi p}|H_0)$ obtained from the pseudo-data set in Fig. 86. Also shown is $\mathcal{F}(m_{J/\psi p}|H_1)$, which is used in the likelihood ratio test. The distributions appear compatible with each other, and indicate that the H_0 hypothesis would be accepted. Note that they are not expected to look identical, since the $\mathcal{F}(m_{Kp}, \cos\theta_{\Lambda^*}|H_0)$ construction is equivalent to a complicated smoothing algorithm of the directly obtained distribution, and thus leaves out statistical fluctuations.

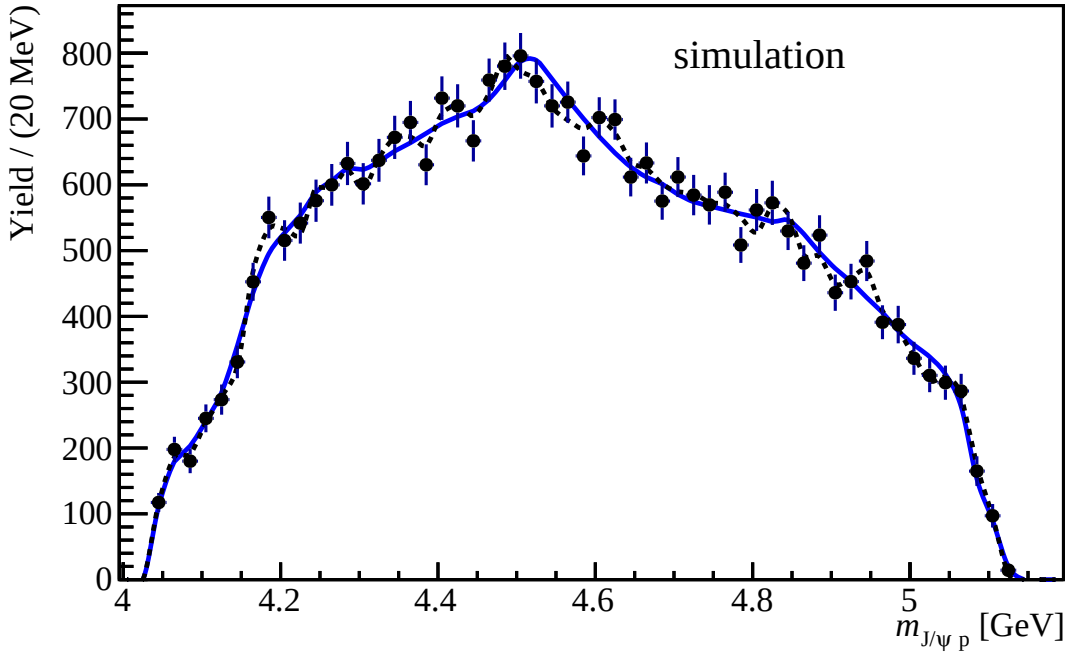

Figure 86: The efficiency-corrected and background-subtracted distribution of $m_{J/\psi p}$ for the pseudo-data-set (black points with error bars) generated according to the extended Λ^* amplitude model without any P_c^+ states, compared to $\mathcal{P}(m_{J/\psi p}|H_0)$ (solid blue line) and $\mathcal{P}(m_{J/\psi p}|H_1)$ (dashed black line).

To test the sensitivity of the method to data sets with $P_c(4450)$ and $P_c(4380)$ built into them, pseudo-data sets are constructed using the default (*i.e.* "reduced") Λ^* amplitude model with both P_c^+ states. Shown in Fig. 87 is the efficiency-corrected and background-subtracted distribution of $m_{J/\psi p}$ in the pseudo-data set together with $\mathcal{F}(m_{J/\psi p}|H_0)$ and $\mathcal{F}(m_{J/\psi p}|H_1)$. The directly obtained distribution has a clear excess over $\mathcal{F}(m_{J/\psi p}|H_0)$ in the region of $P_c(4450)$, and appears very similar to the result shown on the data in

Fig. 84. Meanwhile, $\mathcal{F}(m_{J/\psi p}|H_1)$ reproduces the distribution of the data quite well.

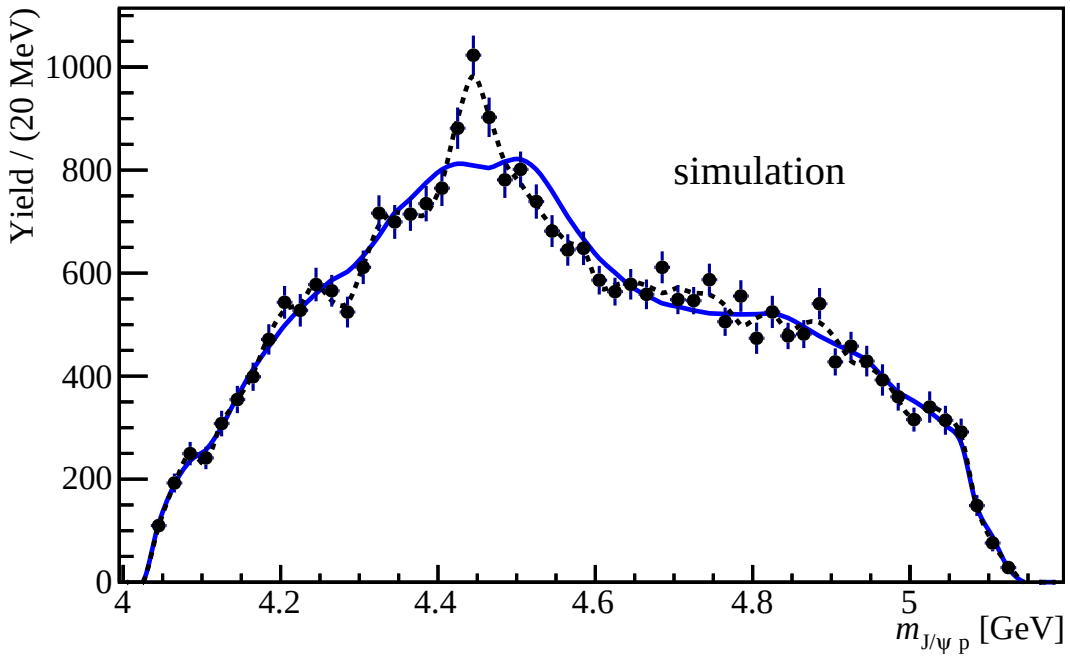

Figure 87: The efficiency-corrected and background-subtracted distribution of $m_{J/\psi p}$ for the pseudo-data-set (black points with error bars) generated according to the default Λ^* amplitude model with both $P_c(4380)$ and $P_c(4450)$ included, compared to $\mathcal{P}(m_{J/\psi p}|H_0)$ (solid blue line) and $\mathcal{P}(m_{J/\psi p}|H_1)$ (dashed black line).

Many pseudoexperiments were performed to get the distribution of the test variables for pseudo-data sets generated from the Λ^*-only amplitude model. This is then compared to the distribution of the test variables for the H_0 pseudoexperiments, as a means of validation. The comparisons for t_{χ^2} and t_{DLL} are shown in Fig. 88 on the left and right, respectively. The distribution of the black Λ^*-only histogram is nearly identical to that of the red-dashed H_0 histogram. This indicates that the Λ^*-only pseudoexperiments would all be assigned high p-values, and therefore the H_0 hypothesis would have always been accepted, thus validating the test. Many pseudoexperiments were also ran for the default amplitude model with both P_c states. These are shown as the blue histograms in Fig. 88 for both test variables. From the separation of the blue and red histograms, it is clear that most of the time a low p-value would have been assigned to the H_0 hypothesis, and thus H_0 would have been rejected. Thus, if the amplitude model with the $P_c(4380)$ and $P_c(4450)$ accurately represents the data, it can be expected that the H_0 hypothesis can

be rejected with a good level of confidence. It is also clear from the sensitivity studies that the t_{DLL} test variable is going to be the more powerful variable, as predicted.

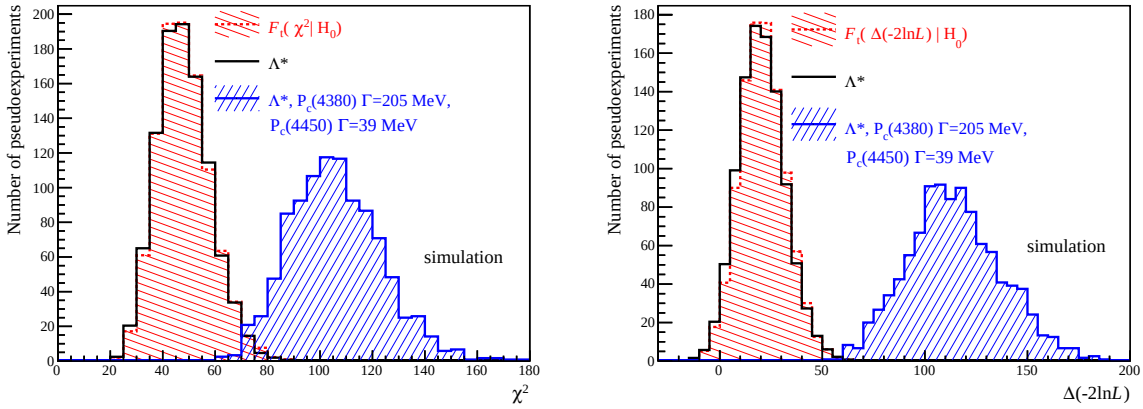

Figure 88: Distribution of t_{χ^2} (left) and t_{DLL} (right) in the H_0 pseudoexperiments (red falling hatched), compared to the distributions obtained from the Λ^*-only amplitude pseudo-experiments (black) and the pseudo-experiments generated from the default amplitude model, *i.e.* with the $P_c(4380)$ and $P_c(4450)$ included (blue rising hatched).

21.2 Dependence of sensitivity on width

To study the dependence of the sensitivity on the width of exotic contributions, pseudoexperiments were generated with amplitude models containing only a single P_c resonance. In particular, the default amplitude model with the $P_c(4450)$ and $P_c(4380)$ was used, but with the $P_c(4450)$ contribution removed. Thus the model contains only the Λ^* and $P_c(4380)$ contributions. Versions of the pseudoexperiments were generated which differ only by the width of the $P_c(4380)$ resonance. Starting with the nominal value, the width was reduced by half in the subsequent sets of pseudo-experiments. The resulting distributions from many pseudo-experiments are shown in Fig. 89 for the t_{χ^2} and t_{DLL} test variables. The set in which the nominal $P_c(4380)$ width (205 MeV) was used gives a distribution (blue histogram) which is essentially indistinguishable from the distribution of the H_0 pseudoexperiments (red falling hatched histogram). This indicates that the H_0 hypotheses is expected to be accepted, even though this is not the desired outcome and illustrates an insensitivity of the model-independent approach to broad resonances. When the width is cut in half (102.5 MeV; magenta histogram), the distribution of the

pseudo-experiments starts separating from the H_0 hypothesis, but there is still substantial overlap. Thus the H_0 hypothesis would only be rejected occasionally. When the width is reduced by another factor of two (51.2 MeV; green histogram) a full separation develops. Thus, in this cases the H_0 hypothesis can always be expected to be rejected. A comparison of these figures with those shown in Fig. 88 reflects the unsurprising dependence of the sensitivity of the method to the production rate of the resonance. Despite the $P_c(4450)$ state having a width of 39 MeV, the separation from H_0 of the amplitude model with both $P_c(4380)$ and $P_c(4450)$ included is worse than the separation obtained when just the $P_c(4380)$ state is included with a width of ~ 50 MeV. This is because the fit fraction for $P_c(4450)$ is less than half of that for $P_c(4380)$.

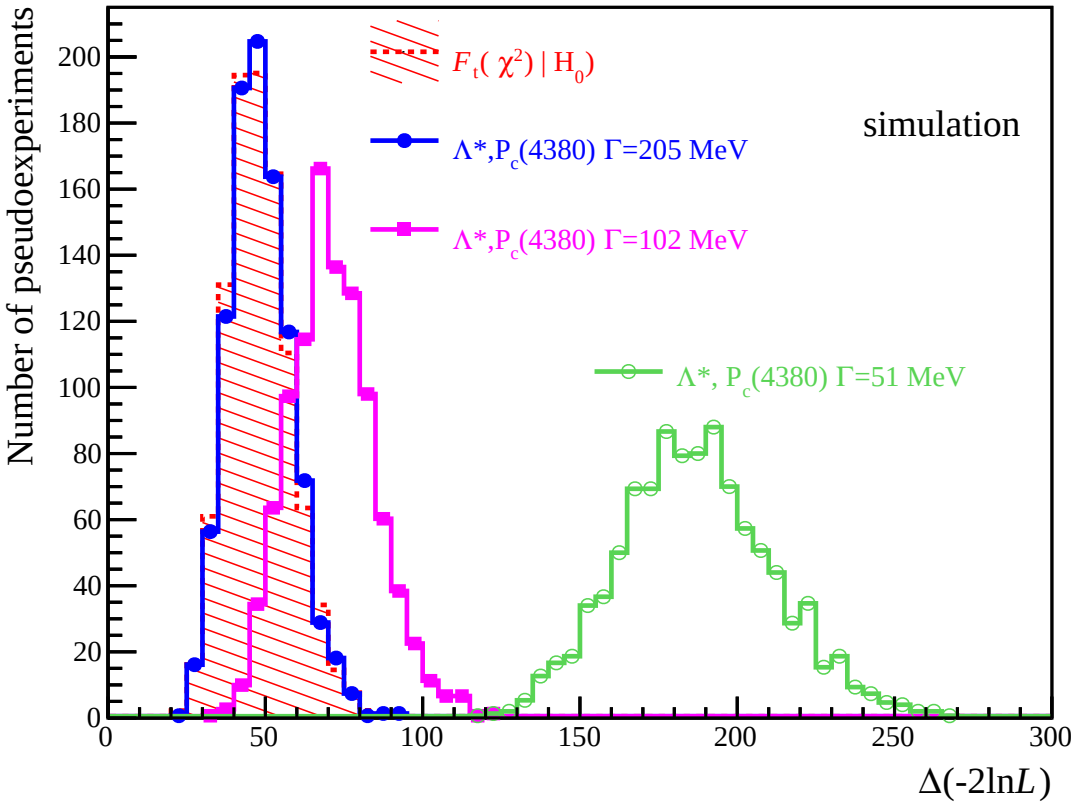

Figure 89: Distribution of t_{χ^2} (left) and $t_{\rm DLL}$ (right) in pseudoexperiments generated from an amplitude model with only the $P_c(4380)$ (no $P_c(4450)^+$) included, and taking widths of the nominal 205 MeV (blue solid histogram), 102.5 MeV (magenta solid histogram), and 51.2 MeV (green solid histogram). Also shown are the distributions from the H_0 pseudoexperiments (red falling hatched).

The fact that the method is not at all sensitive to the nominal $P_c(4380)$ state is

an interesting one. It was already expected from visualizing the Legendre moments of the individual P_c states (Fig. 80) that there would be little sensitivity to the broader state. The reason for this effect comes from the one-to-one correspondence between $m_{J/\psi p}$ and $\cos\theta_{\Lambda^*}$ values, which exists for a given m_{Kp} (Eq.82). From this it is seen that a peak in the $m_{J/\psi p}$ mass distribution generates a peak in the cosine of the Λ^* helicity angle. The narrower the $m_{J/\psi p}$ peak, the sharper the peak in the $\cos\theta_{\Lambda^*}$ distribution. Quickly changing structures in $\cos\theta_{\Lambda^*}$ then will result in larger contributions to higher order Legendre moments. To summarize, broader resonances result in broader structures in the $\cos\theta_{\Lambda^*}$ distribution, which leads to larger contributions to lower order Legendre moments, which then get attributed to Λ^* resonances.

In fact, it was already known from the amplitude model fits to the data without both P_c states that the broad peaking attributed to $P_c(4380)$ can also be approximately described with Λ^* resonances. This can be seen in the projections of the amplitude model on $m_{J/\psi p}$ for events lying in the high m_{Kp} mass interval: $m_{Kp} > 2$ GeV. In Fig. 90, these projections are shown for the extended Λ^* model with no P_c states, a single P_c state, and both $P_c(4380)$ and $P_c(4450)$. Even in the fits without the $P_c(4380)$ state, the broad structure is roughly reproduced. Of course, the significance of the $P_c(4380)$ contribution in the amplitude analysis is only partially related to this m_{Kp}-slice of the $m_{J/\psi p}$ distribution. Much of it comes from the asymmetry in the $\cos\theta_{P_c}$ distribution produced in the mass region of the $P_c(4450)$ state through their interference, which shows up through the whole m_{Kp} range. Indeed in the other m_{Kp} slices, the Λ^* resonances fail to describe the $m_{J/\psi p}$ distribution. The 2D model-independent approach is completely oblivious to such interference effects. It would be naive to expect the 2D method, which allows for the self-subtraction of exotic hadron components and also does not benefit from functional forms imposed on resonant amplitudes, to be as sensitive as the 6D amplitude fits. As noted already, the model independence comes at the expense of lower sensitivity.

The ability of $\mathcal{F}(m_{J/\psi p}|H_0)$ to reproduce the $P_c(4380)$ structure can be seen by viewing the $m_{J/\psi p}$ distribution in slices of m_{Kp}. This is shown in Fig. 91, where the data are compared to $\mathcal{F}(m_{J/\psi p}|H_0)$ using the same intervals of m_{Kp} as were often used in the

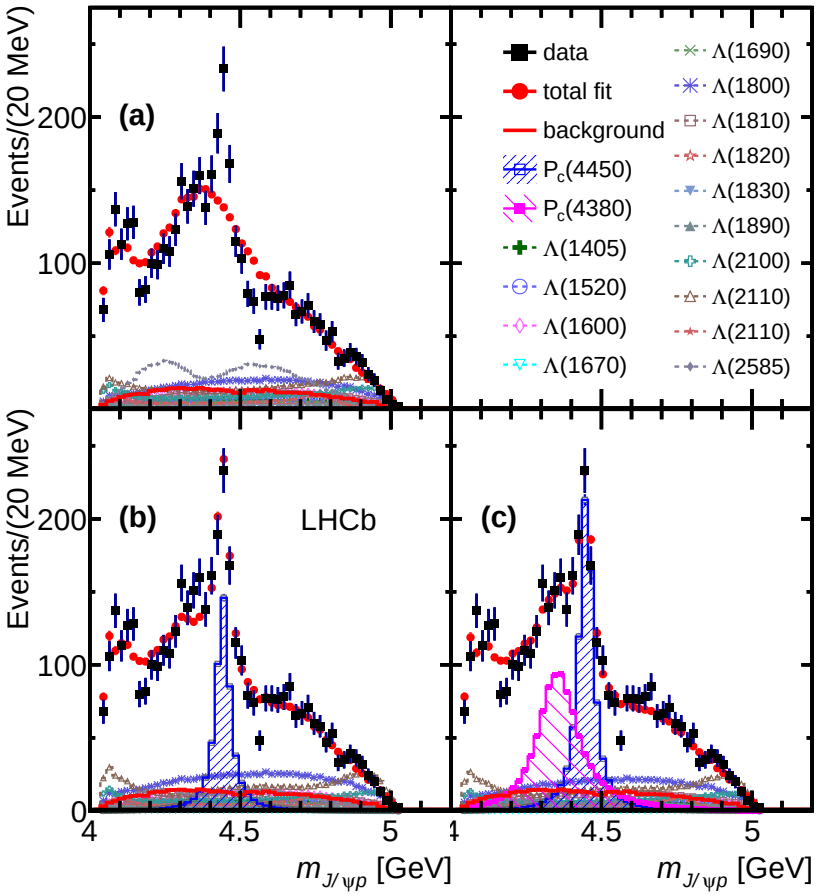

Figure 90: The distribution of $m_{J/\psi p}$ (no efficiency-corrections or background-subtraction) for the real data (black points with error bars) satisfying $m_{Kp} > 2.0$ GeV, and various amplitude fit results superimposed. The results shown are: (a) the extended Λ^* model and no P_c^+ states, (b) only one P_c^+ state, and (c) two P_c^+ states (bottom). The total fits are shown (red dots), as well as $P_c(4450)$ (blue hatched) and $P_c(4380)$ (magenta hatched) when present Individual Λ^* resonances are also shown.

amplitude analysis. Also shown is $\mathcal{F}(m_{J/\psi p}|H_1)$. Again, the interesting slice is for $m_{Kp} > 2$ GeV, where the best P_c to Λ^* yield ratio is found, and the $P_c(4380)$ state structure is seen most visibly. However, while there is a clear excess of the data in the $P_c(4450)$ region, it is seen that $\mathcal{F}(m_{J/\psi p}|H_0)$ describes the $P_c(4380)$ region well. One can check that this is the expected behavior, even when the $P_c(4380)$ is guaranteed to be present in the data, by showing the displays for a pseudoexperiment in which the pseudo-data has been generated according to the default Λ^* model with both the $P_c(4380)$ and $P_c(4450)$. This is shown in Fig. 92, where again it is seen that $\mathcal{F}(m_{J/\psi p}|H_0)$ reproduces the $P_c(4380)$ region.

It is of course tempting to compare what has been shown here to the previous application of this method, in which it was used to probe for the presence of the $Z(4430)^+$ in $B^0 \to \psi(2S)\pi^+K^-$ decays. In the LHCb publication [20] in particular, evidence was found for the presence of the $Z(4430)^+$. As its width has been determined to be $172 \pm 13\,^{+37}_{-34}$ MeV, this may at first seem to be at odds with the conclusion that there is no sensitivity to $P_c(4380)$, despite its comparable width. The conventional hadron "background" is much different in $B^0 \to \psi(2S)\pi^+K^-$ decays, however. As a result the $l_{\rm max}(m_{K\pi})$ filter was a factor of two tighter than the $l_{\rm max}(m_{Kp})$ filter which could be deployed in this analysis. This point is illustrated in Table 22. Unfortunately, the looser filter is unavoidable in the present use-case. This is partly due to the fact that the kinematic threshold for the K^-p decays studied here is 316 MeV above the Λ mass *i.e.* the ground state of the Λ^* system. This is significantly higher than for the $K^-\pi^+$ decays studied in the $Z(4430)^+$ analysis, where the threshold was only 139 MeV above the kaon mass. Therefore, higher Λ excitations, which have higher spins, cover a larger fraction of the available phase-space. Furthermore, because of the third quark in the baryon, which contributes its spin to possible J values, higher J values are reached at lower excitation energies. As a result of all of this, the $B^0 \to \psi(2S)\pi^+K^-$ was able to be sensitive to broader resonances.

To conclude this section, sensitivity studies of this model-independent method have been performed for the first time. There are three effects which determine the overall

Table 22: Comparison of $l_{\max}(m)$ filters used in the model independent analysis of $B^0 \to \psi(2S)K^-\pi^+$ and this analysis of $\Lambda_b^0 \to J/\psi\, K^- p$. The bottom row shows $l_{\max}$ values averaged over the entire m range, using mass range fraction as a weight. On average, the $\Lambda_b^0 \to J/\psi\, K^- p$ is a factor of 2 looser than the $B^0 \to \psi(2S)K^-\pi^+$ filter.

$B^0 \to \psi(2S)K^-\pi^+$			$\Lambda_b^0 \to J/\psi\, K^- p$		
m range	$l_{\max}$ value	range fraction	m range	$l_{\max}$ value	range fraction
633- 836 MeV	2	21.1%	1432-1640	3	19.0%
836-1000 MeV	3	17.1%	1640-1700	5	5.5%
			1700-2050	7	32.0%
1000-1593 MeV	4	61.8%	2050-2524	9	43.4%
average $l_{\max}$	3.4		average $l_{\max}$	7.0	

sensitivity. One very important effect, for which the main study was done, is the width of the exotic resonance. It was demonstrated here that there is no sensitivity to the $P_c(4380)$, with its particular parameters determined from the amplitude analysis. Also important is the overall rate which the exotic contribution contributes, as was evidenced by the difference in separation between the pseudoexperiments based on the default amplitude model, and the pseudoexperiments in which the $P_c(4380)$ was given a width comparable to the $P_c(4450)$. It is of course not surprising that larger decay rates lead to better sensitivity. Finally, the comparison to the previous application, in which $B^0 \to \psi(2S)\pi^+K^-$ decays were studied, highlighted the importance of the spin-mass relation for conventional hadrons present in the data.

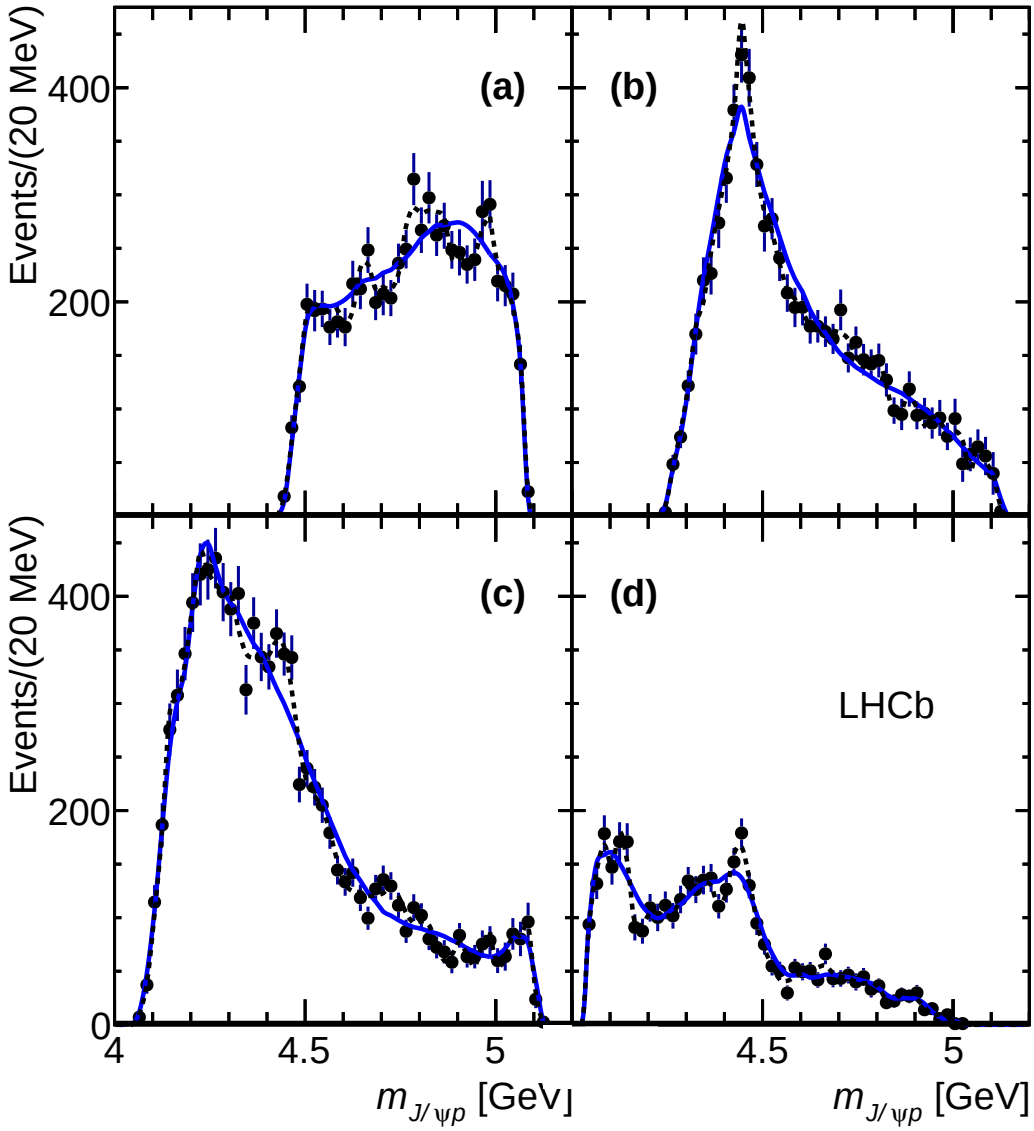

Figure 91: Efficiency-corrected and background-subtracted $m_{J/\psi p}$ distribution of the data (black points with error bars), with $\mathcal{F}(m_{J/\psi p}|H_0)$ (solid blue line) and $\mathcal{P}(m_{J/\psi p}|H_1)$ (dashed black line) superimposed, shown for different ranges of m_{Kp}: (a) $m_{Kp} < 1.55$ GeV, (b) $1.55 < m_{Kp} < 1.70$ GeV, (c) $1.70 < m_{Kp} < 2.00$ GeV, and (d) $m_{Kp} > 2.0$ GeV.

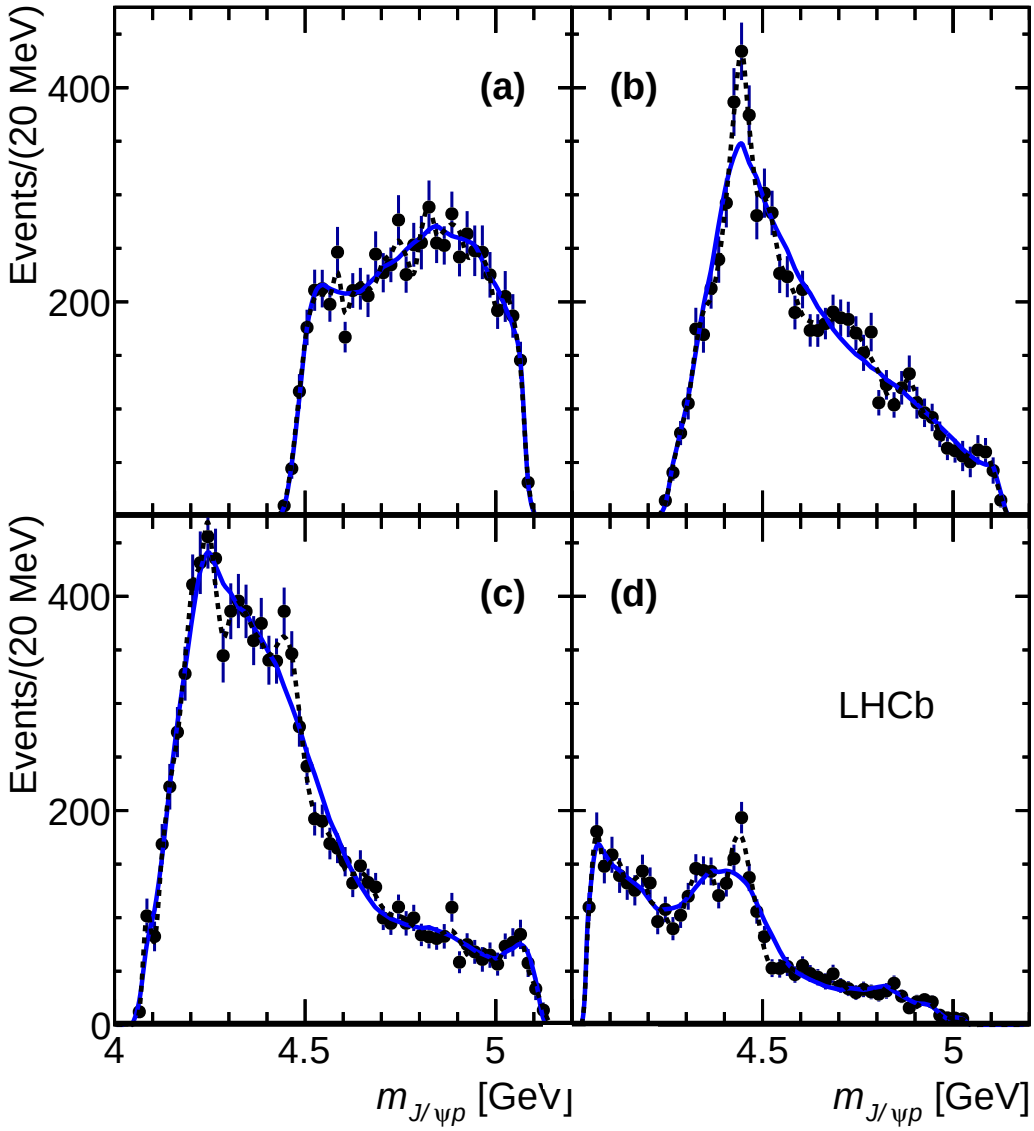

Figure 92: Efficiency-corrected and background-subtracted $m_{J/\psi p}$ distribution of the pseudo-data set (black points with error bars), generated according to the default amplitude model, with $\mathcal{F}(m_{J/\psi p}|H_0)$ (solid blue line) and $\mathcal{P}(m_{J/\psi p}|H_1)$ (dashed black line) superimposed, shown for different ranges of m_{Kp}: (a) $m_{Kp} < 1.55$ GeV, (b) $1.55 < m_{Kp} < 1.70$ GeV, (c) $1.70 < m_{Kp} < 2.00$ GeV, and (d) $m_{Kp} > 2.0$ GeV.

22 Compatibility of H_0 with the data

In this section, the values of the test variables obtained from the data, $t_{\chi^2}^{\rm data}$ and $t_{\rm DLL}^{\rm data}$, are turned into p-values for the H_0 hypothesis. The histogram of the t_{χ^2} values for many pseudoexperiments generated under the H_0 hypothesis is shown again in Fig. 93, for both log and linear scale, where it is compared to the value obtained on the data, $t_{\chi^2}^{\rm data} = 120.5$. For a true χ^2 distribution, one expects RMS $= \sqrt{2 < \chi^2 >}$. The t_{χ^2} value averaged over all pseudo-experiments is $< t_{\chi^2} >= 48.2 \pm 0.1$. The RMS of the distribution is 10.1 ± 0.1, which agrees well with $\sqrt{2 < t_{\chi^2} >} = 9.8$. In fact, the simulated t_{χ^2} distribution is well described with a nominal χ^2 distribution having ndf $= 48.1 \pm 0.1$, as determined by the fit shown with the solid red line. As a measure of fit quality, the χ^2/ndf of the fit is 82.1/73, corresponding to a $p-$value for the fit of 21.7%. To determine a $p-$value of the H_0 hypothesis, the fitted ndf was rounded up (to be conservative), and the nominal $\mathcal{P}(\chi^2|{\rm ndf} = 49)$ distribution was taken as an approximation of $\mathcal{F}_t(t_{\chi^2}|H_0)$. Using the measured $t_{\chi^2}^{\rm data}$ value, this yields $p_{\rm data} = 5.8 \cdot 10^{-8}$. The equivalent standard deviation in the Gaussian distribution is calculated via[20]

$$n_\sigma(p_{\rm data}) = \sqrt{2}\,{\rm erfc}^{-1}(2p_{\rm data})\,. \tag{108}$$

as 5.3σ. Thus, using the t_{χ^2} test variable, the H_0 hypothesis can be rejected at 5.3 standard deviations.

The histogram of the $t_{\rm DLL}$ values obtained over many pseudoexperiments generated under the H_0 hypothesis is shown in log and linear scale in Fig. 94. The value obtained on the real data, $t_{\rm DLL}^{\rm data} = 144.7$, is marked by the vertical black line. Originally a Gaussian function was used to fit to the distribution, for use as an approximation for $\mathcal{F}(t_{\rm DLL}|H_0)$. However, an increasingly high number of pseudoexperiments performed allowed for the

[20]This is using the convention in which $p_{\rm data} = 0.5$ corresponds to 0σ and is valid for $p_{\rm data} < 0.5$. For $p_{\rm data} > 0.5$, $n_\sigma(p_{\rm data}) = \sqrt{2}\,{\rm erfc}^{-1}(2 \times (1 - p_{\rm data}))$ would need to be used. This is a more conservative definition of $n_\sigma(p_{\rm data})$ than was used in the amplitude analysis (Sec. 12), where 0σ was defined to correspond to $p_{\rm data} = 1.0$. The difference in the conventions was motivated by the fact that in the amplitude fits the null hypothesis was exactly nested in the alternative hypothesis, as reflected by the $\Delta(-2\ln\mathcal{L}) \geq 0$ constraint. Meanwhile here H_0 and H_1 are only approximately nested, as evidenced by the possibility of $t_{\rm DLL}$ reaching negative values (this is because the free parameters of these hypotheses are not obtained by minimizing the corresponding negative log-likelihoods).

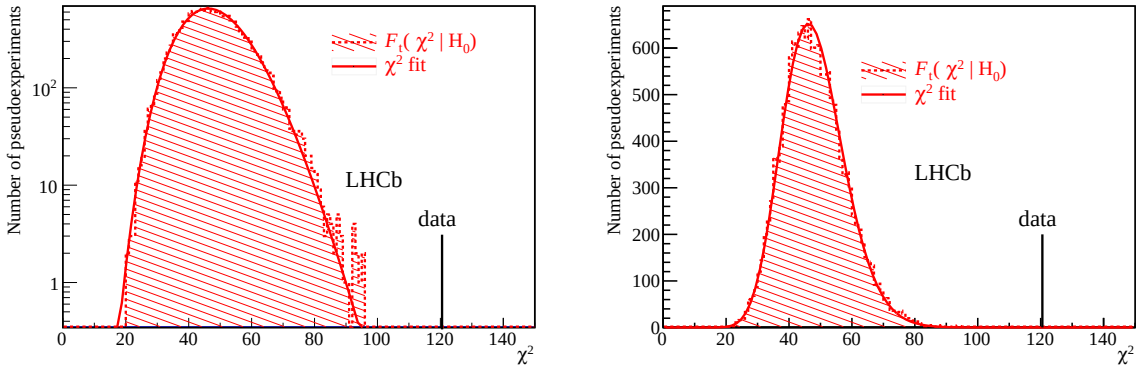

Figure 93: Distribution of t_{χ^2} in the H_0 pseudoexperiments (red histogram) in log (left) and linear (right) scale compared to the value obtained in the data (vertical black bar). The distribution is fitted with and well described by a χ^2 distribution (solid red line).

development of a slightly observable asymmetry in the distribution. As a result, it is not described well in the higher end by a Gaussian function. Thus the distribution is instead fit with a bifurcated Gaussian distribution,

$$\mathcal{P}(t_{\mathrm{DLL}}|\sigma_l,\sigma_r,t_{\mathrm{DLL}_0}) = \frac{2}{\sqrt{2\pi}(\sigma_l+\sigma_r)} \times e^{-\frac{(t_{\mathrm{DLL}}-t_{\mathrm{DLL}_0})^2}{2\sigma_i^2}} \quad , \quad \sigma_i = \begin{cases} \sigma_l & t_{\mathrm{DLL}} \leq t_{\mathrm{DLL}_0} \\ \sigma_r & t_{\mathrm{DLL}} > t_{\mathrm{DLL}_0}. \end{cases} \tag{109}$$

The fit is also shown in Fig. 94 by the solid red line. The distribution is well-described by the bifurcated Gaussian, and the fit has a χ^2/ndf of 87.1/82, corresponding to a $p-$value for the fit of 33.0%. The obtained bifurcated Gaussian parameters are $t_{\mathrm{DLL}_0} = 18.9 \pm 0.2$, a left width of $\sigma_l = 9.6 \pm 0.1$, and a right width of $\sigma_r = 12.4 \pm 0.2$. The $p-$value for the data is determined through integration of $\mathcal{F}(t_{\mathrm{DLL}}|\sigma_l,\sigma_r,t_{\mathrm{DLL}_0})$ in the region beyond $t_{\mathrm{DLL}}^{\mathrm{data}}$. This integral from $t_{\mathrm{DLL}}^{\mathrm{data}}$ to ∞ can be calculated with the help of the complementary error function as

$$I(t_{\mathrm{DLL}}^{\mathrm{data}}) = \frac{\sigma_r}{\sigma_l+\sigma_r}\mathrm{erfc}\left(\frac{t_{\mathrm{DLL}}^{\mathrm{data}}}{\sigma_r\sqrt{2}}\right) \tag{110}$$

The $p-$value is found to be $p_{\mathrm{data}} = 2.3 \cdot 10^{-24}$. The equivalent standard deviation in the normal Gaussian distribution is 10.1σ. This value is not much lower than the 11.3σ one would obtain using the normal Gaussian distribution to fit the pseudoexperiment distribution. To estimate the importance of the statistical uncertainty of the fit parameters in calculating the significance, t_{DLL_0} and σ_r were shifted up by one unit of its statistical error,

while σ_l was shifted down by one unit of its statistical error. The resulting significance is 10.0σ, indicating the effect from the statistical uncertainty of the fit parameters is very small. The significances obtained with the $t_{\rm DLL}$ test variable can formally be interpreted as the significance of the higher order ($l_{\rm max}(m_{Kp}) \leq l \leq 31$) moments of the Λ^* helicity angle distributions. As these are beyond what can be generated via $\Lambda_b^0 \to J/\psi\,\Lambda^*$ decays, the hypothesis that the data can be described with the $\Lambda_b^0 \to J/\psi\,\Lambda^*$ decays alone is ruled out at 10.1σ level.

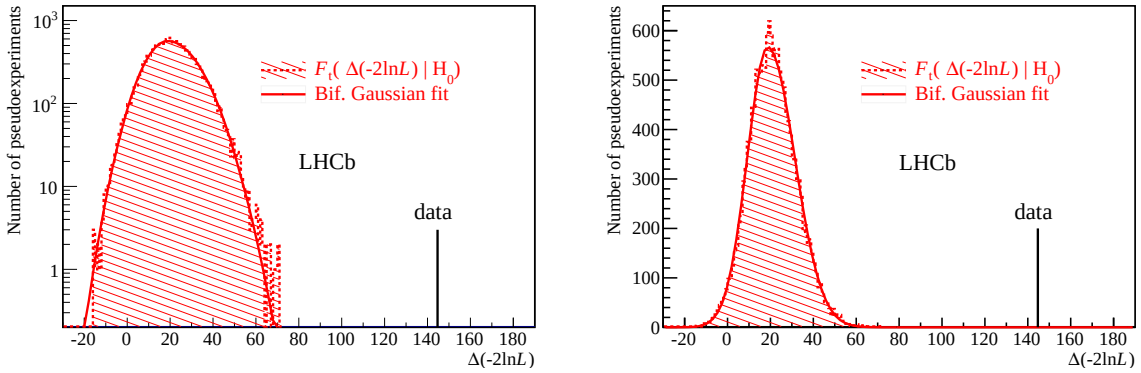

Figure 94: Distribution of $t_{\rm DLL}$ in the H_0 pseudoexperiments (red histogram) in log (left) and linear (right) scale compared to the value obtained in the data (vertical black bar). The distribution is fitted with and well described by a bifurcated Gaussian distribution (solid red line).

The data represents one instance of an "experiment". Thus, one can ask how likely it was to be able to reject the H_0 hypothesis. For example, one can calculate the values of $t^{\rm data}$ that would be necessary to achieve $3\,\sigma$ and $5\,\sigma$ levels of rejection by using the fits to the H_0 distributions shown in this section. If the default amplitude model with both P_c states is assumed to be an accurate representation of the data, the distributions shown in Sec. 21.1, can then be used to estimate the probability of obtaining a value of $t^{\rm data}$ that is at least as large as the values necessary for $3\,\sigma$ and $5\,\sigma$ significances. When using the t_{χ^2} variable, rejections of at least 3σ (5σ) are expected for 91.3% (28.2%) of the pseudoexperiments generated from this amplitude model. For the $t_{\rm DLL}$ variable, rejections of at least 3σ (5σ) are expected for 99.9% (93.0%) of the pseudoexperiments. While it is known that the amplitude model doesn't provide a perfect description of the data, it is still reasonably good. Thus, this study shows it is not surprising that the H_0

hypothesis was rejected with both test variables.

It is also reasonable to ask why the t_{DLL} variable has significantly better discriminating power than the t_{χ^2} variable. One possibility is that there is an over-estimation of errors used in calculating the t_{χ^2}. However the dominant factor likely lies in the nature of the more specific H_1 hypothesis that H_0 is tested against. In particular, the construction of $\mathcal{F}(m_{Kp}, \cos\theta_{\Lambda^*}|H)$ is essentially a complicated smoothing procedure. Thus $\mathcal{F}(m_{Kp}, \cos\theta_{\Lambda^*}|H_1)$ captures the essential physics, while removing noise from statistical fluctuations. In fact, it can been seen in Appendix M that increasing l_{large} to higher values results in diminished discriminatory power, presumably from inserting more statistical noise into the test.

23 Hypothesis testing with $m_{J/\psi K}$

The evidence points towards the source of incompatibility with H_0 coming from activity in the $J/\psi p$ system. For instance, the Dalitz planes shown in Sec. 4.2 indicated that structures seen in the $J/\psi K^-$ system were reflections from the $J/\psi p$ system. This was also supported by the amplitude analysis, in which the default amplitude model was seen to reproduce the $m_{J/\psi K}$ distribution reasonably well (Fig. 54). Nevertheless, it is worth repeating the model-independent analysis with the $m_{J/\psi K}$ distribution in order to compare the results to those obtained with the $m_{J/\psi p}$ distribution.

The procedure is carried out just as in the nominal analysis. The same $\mathcal{F}(m_{Kp}, \cos\theta_{\Lambda^*}|H_0)$ function is used, except it is projected on $m_{J/\psi K}$. The $m_{J/\psi K} \leftrightarrow \cos\theta_{\Lambda^*}$ correspondence for a given m_{Kp} can be seen with the $J/\psi K^-$ version of Eq. 82:

$$m^2_{J/\psi K} = m^2_{J/\psi} + m^2_K + 2\left(E_{J/\psi}E_K + p_{J/\psi}p_K\cos\theta_{\Lambda^*}\right), \tag{111}$$

where the momenta

$$\begin{aligned} p^2_{J/\psi} &= E^2_{J/\psi} - m^2_{J/\psi}, \\ p^2_K &= E^2_K - m^2_K, \end{aligned}$$

and the energies

$$\begin{aligned} E_{J/\psi} &= (m^2_{\Lambda^0_b} - m^2_{J/\psi} - m^2_{Kp})/(2m_{Kp}), \\ E_K &= (m^2_{Kp} + m^2_K - m^2_p)/(2m_{Kp}) \end{aligned}$$

of J/ψ and K^- are expressed in the K^-p rest frame and $\cos\theta_{\Lambda^*} \equiv -\hat{p}_{J/\psi}\cdot\hat{p}_K$ was used. With this, the projection of $\mathcal{F}(m_{Kp}, \cos\theta_{\Lambda^*}|H_0)$ onto $m_{J/\psi K}$ can proceed in the usual manner. A total of 10^7 events are generated uniformly over the $(m_{Kp}, \cos\theta_{\Lambda^*})$ plane, and their corresponding value of $m_{J/\psi K}$ is calculated. Each event then fills a histogram of $m_{J/\psi K}$ with $\mathcal{F}(m_{Kp}, \cos\theta_{\Lambda^*}|H_0)$ as its weight. To achieve continuous $\mathcal{F}(m_{J/\psi K}|H_0)$

distributions, quadratic splines are used to interpolate between nearby $m_{J/\psi K}$ bins of the histogram. The efficiency-corrected and background-subtracted $m_{J/\psi K}$ distribution of the data is shown along with $\mathcal{F}(m_{J/\psi K}|H_0)$ (and $\mathcal{F}(m_{J/\psi K}|H_1)$) in Fig. 95.

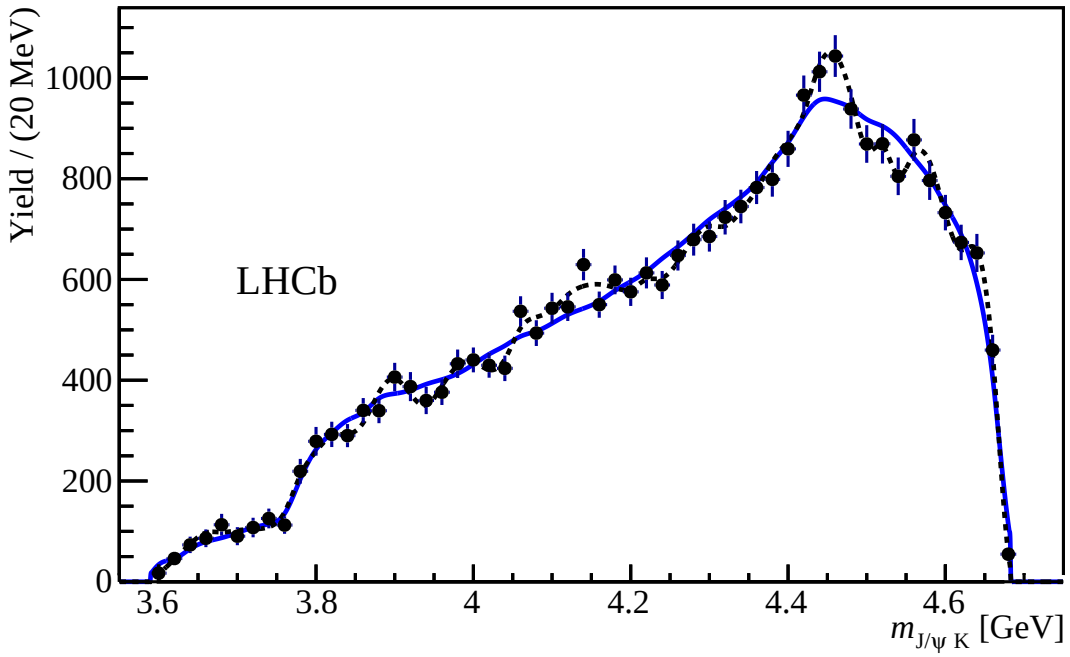

Figure 95: Efficiency-corrected and background-subtracted $m_{J/\psi K}$ distribution of the data (black points with error bars), with $\mathcal{F}(m_{J/\psi K}|H_0)$ (solid blue line) and $\mathcal{F}(m_{J/\psi K}|H_1)$ (dashed black line) superimposed.

The data shows a clear disagreement with $\mathcal{F}(m_{J/\psi K}|H_0)$ in the higher $m_{J/\psi K}$ regions. This is expected, because P_c resonances will reflect into this distribution, as previously mentioned. However reflections will be more smeared out, and less localized than in the system in which they peak. Thus a discrepancy is expected, though it should be weaker than in the system the suspected reflections are coming from. In order to quantify the level of discrepancy, pseudoexperiments are again necessary. The hypothesis testing procedure

is thus repeated for these displays, with the analogously defined test variables.

$$
\begin{aligned}
t_{\chi^2} &= \sum_{k=1}^{n_{\text{bins}}} \left(\frac{c_k - \mathcal{F}(m_{J/\psi K}{}^k | H_0)}{\sigma(c_k)} \right)^2, \\
c_k &= \Delta N^k / \Delta m_{J/\psi K} = \sum_i^{n_{\text{cand}}{}^k} w_i/\epsilon_i, \\
\sigma(c_k) &= \sqrt{\sum_i^{n_{\text{cand}}{}^k} (w_i/\epsilon_i)^2}
\end{aligned}
\tag{112}
$$

where c_k is the k^{th} bin content of the directly obtained efficiency-corrected and background-subtracted $m_{J/\psi K}$ distribution, $m_{J/\psi K}{}^k$ is the bin center, $n_{\text{cand}}{}^k$ is the number of events contributing to this bin, and n_{bins} is the number of bins. And t_{DLL} becomes

$$
t_{\text{DLL}} = \Delta(-2\log\mathcal{L}) = -2 \sum_i^{n_{\text{cand}}^{\text{sig}} + n_{\text{cand}}^{\text{side}}} w_i \log \left(\frac{\mathcal{F}(m_{J/\psi K\ i} | H_0)/I_{H_0}}{\mathcal{F}(m_{J/\psi K\ i} | H_1)/I_{H_1}} \right). \tag{113}
$$

The pseudoexperiments are also simulated just as before. The histogram of the t_{χ^2} values obtained from the pseudoexperiments are shown in Fig. 96 along with the result from the data, $t_{\chi^2}^{\text{data}} = 98.6$. The fit of the histogram with a χ^2 distribution returns ndf $= 49.1 \pm 0.1$. Rounding up, the nominal $\mathcal{P}(\chi^2|\text{ndf} = 50)$ distribution is used to calculate a $p-$value. The corresponding result in Gaussian standard deviations is a 3.9σ rejection of the H_0 hypothesis. The distribution of t_{DLL} values obtained from the pseudoexperiments is shown in the histogram in Fig. 97 along with the result from the data, $t_{\text{DLL}}^{\text{data}} = 90.1$. The fit with a bifurcated Gaussian gives $t_{\text{DLL}_0} = 17.8 \pm 0.3$, a left width of $\sigma_l = 10.3 \pm 0.1$, and a right width of $\sigma_r = 13.5 \pm 0.2$. The bifurcated Gaussian is then used to approximate $\mathcal{F}(t_{\text{DLL}}|H_0)$, and the p-value calculated. The result in Gaussian standard deviations is a 5.3σ rejection of the H_0 hypothesis.

Thus in both tests fairly significant rejections of the H_0 hypothesis are obtained. However, they are substantially weaker than the rejections obtained when using the $m_{J/\psi p}$ distributions to perform the hypothesis testing. Again, this is in accordance with expectations of the discrepancies between $\mathcal{F}(m_{J/\psi K}|H_0)$ and the data being a result of activity in the $J/\psi p$ system. This adds to the model-dependent evidence obtained from

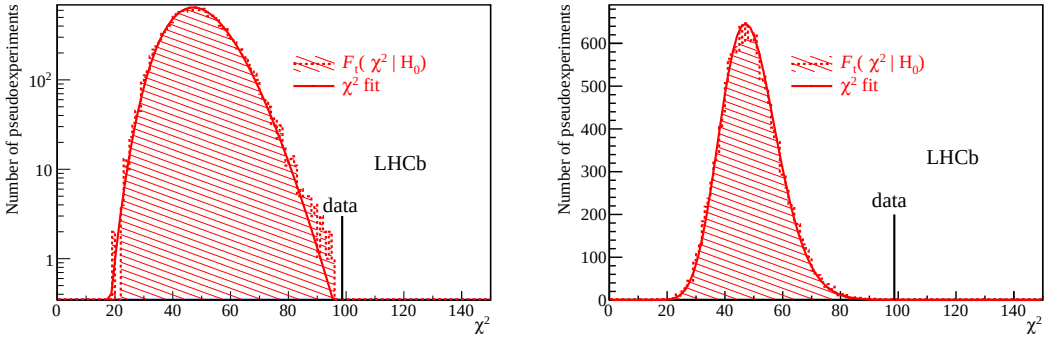

Figure 96: Distribution of t_{χ^2} calculated on the $m_{J/\psi K}$ distribution in the H_0 pseudo-experiments (red histogram) in log (left) and linear (right) scale compared to the value obtained in the data (vertical black bar). The distribution is fitted with and well described by a χ^2 distribution (solid red line).

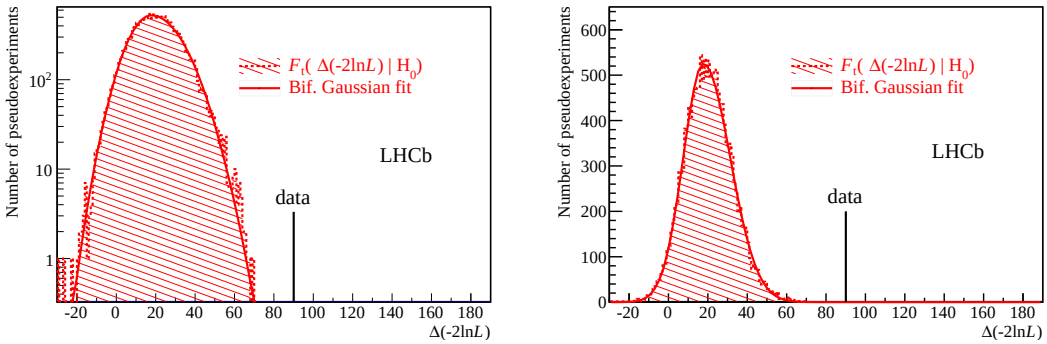

Figure 97: Distribution of $t_{\rm DLL}$ calculated on the $m_{J/\psi K}$ distribution in the H_0 pseudo-experiments (red histogram) in log (left) and linear (right) scale compared to the value obtained in the data (vertical black bar). The distribution is fitted with and well described by a bifurcated Gaussian distribution (solid red line).

the amplitude analysis that discrepancies from a Λ^* only model come from activity in the $J/\psi p$ system.

24 Systematic checks

In this section, variations on the nominal method are performed in order to probe for the size of possible systematic effects. For many of these, identical results to the nominal method are not necessarily expected. Rather, the variations are performed in order to check for consistency with expectations and to set possible lower bounds on the significance of the rejection of the H_0 hypothesis.

24.1 Background subtraction

Here systematic effects associated with the background subtraction are studied. The background is subtracted in three variables throughout the analysis procedure: $m_{Kp}, \cos\theta_{\Lambda^*}$, and $m_{J/\psi p}$. This subtraction is nominally performed using the Λ_b^0 sidebands. This assumes that the backgrounds in the signal region can be accurately represented by the events in the sidebands. The efficiency-corrected distributions of the three variables are checked for consistency between the left and right sidebands in Fig. 98. The left sideband contains 5661 events while the right side band contains 4598, and they are normalized to each other in the figure. There is a fair amount of disagreement between them, and the χ^2/ndf values are are $68.4/(40-1), 135.5/(100-1)$, and $99.9/(54-1)$ for the $m_{Kp}, \cos\theta_{\Lambda^*}$,and $m_{J/\psi p}$ distributions, respectively.

Ideally, the background in the signal region can accurately be represented by a mixture of the left and right sidebands, and is well described by their combined distribution. However, to probe for systematic uncertainties associated with this, the data are reanalyzed with the background subtraction being performed using either only the left or the right sideband. The efficiency-corrected and background-subtracted $m_{J/\psi p}$ distributions of the data obtained from using the individual sidebands for the background subtraction are shown in Fig. 99 along with the obtained $\mathcal{F}(m_{J/\psi p}|H_{0,1})$ $\mathcal{PDF}$'s. Note that the $\mathcal{PDF}$'s probe the background subtraction in m_{Kp} and $\cos\theta_{\Lambda^*}$. There are no significant visual differences between the $m_{J/\psi p}$ distributions obtained from the data, or $\mathcal{F}(m_{J/\psi p}|H_{0,1})$. These distributions can be also compared to the nominal display in Fig. 84, where both

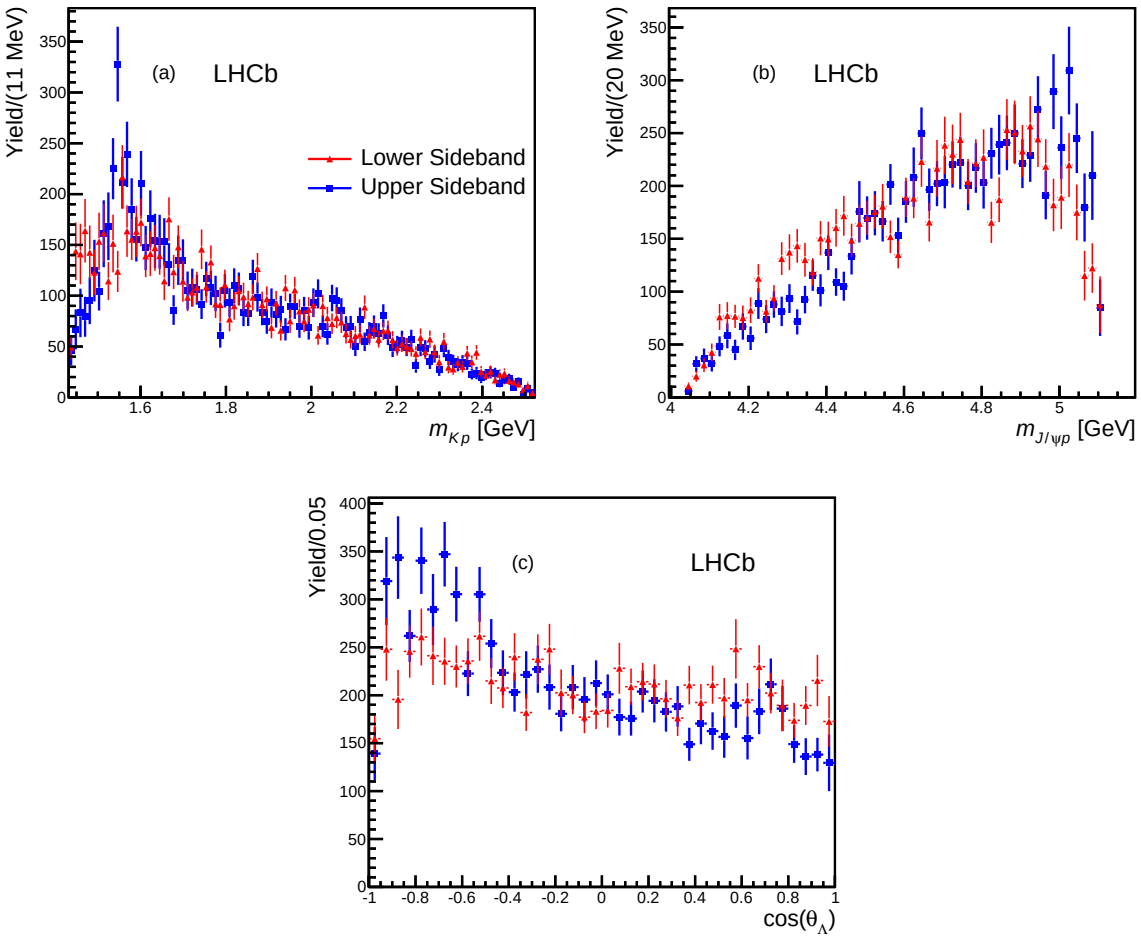

Figure 98: The efficiency-corrected distributions of the variables $m_{Kp}, \cos\theta_{\Lambda^*}, m_{J/\psi p}$ in the left (red) and right (blue) sidebands separately. The distributions are normalized to each other.

sidebands are used, and no significant differences are seen.

The hypothesis testing is also repeated, for cases in which the backgrounds are modeled using either the left or the right sideband. Pseudoexperiments are performed in the same manner as the nominal method, but with background events shaped according to the background parametrization built from either the left or the right sideband. The results of the significances obtained with both test variables are listed in Table 23. From these tests it is concluded that the background subtraction systematics are small, which is not surprising given that the background fraction in the signal region is only $\beta = 5.4\%$.

As an additional cross-check, the analysis is repeated using the *sPlot* technique to subtract the background. In this method, the full $m_{J/\psi pK}$ distribution is passed through the analysis chain, rather than just the signal range (see Fig 30). The events are weighted, as

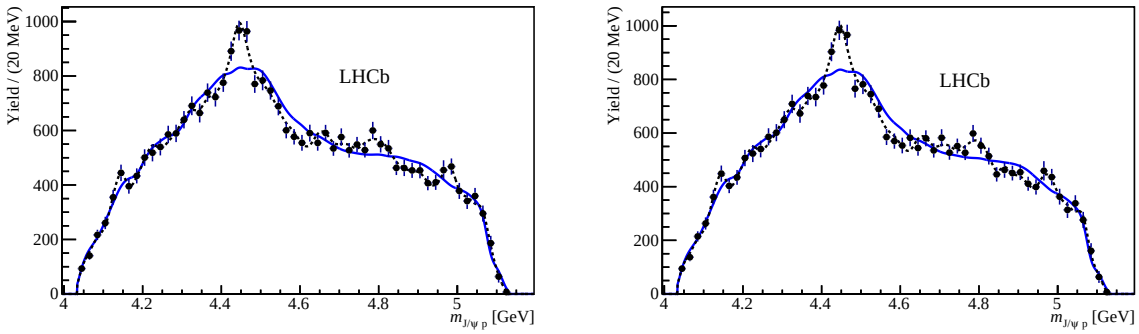

Figure 99: Results for when only the lower (left) or upper (right) mass sidebands of the Λ_b^0 peak are used for the background-subtraction. The efficiency-corrected and background-subtracted distribution of $m_{J/\psi p}$ for the data (black points with error bars), compared with $\mathcal{P}(m_{J/\psi p}|H_0)$ (solid blue line) and $\mathcal{P}(m_{J/\psi p}|H_1)$ (dashed black line). These should be compared to each other and to the nominal distribution obtained using both sidebands together, shown in Fig. 84.

Table 23: Significances obtained in Gaussian standard deviations when only lower or upper Λ_b^0 mass sidebands are used to model the backgrounds.

Sideband	t_{χ^2}	t_{DLL}
Lower	5.2	9.8
Upper	5.3	10.5

in Sec. 6.3. The weights then are used as the w_i weights used for background-subtraction in making the m_{Kp} (Eq. 96) and $m_{J/\psi p}$ (Eq. 99) histograms, determining the Legendre moments (Eq. 97), and in the calculation of the t_{χ^2} (Eq. 100) and t_{DLL} (Eq. 106) test variables. Shown in Fig. 100 is the $m_{J/\psi p}$ distribution of the data, along with the $\mathcal{F}(m_{J/\psi p}|H_{0,1})$ distributions. Again, there are no large changes observed as compared to the nominal result Fig. 84.

The hypothesis testing was repeated using the *sPlot* background subtraction technique. The *sPlot* procedure used in the amplitude analysis is quite intricate (Sec. 6.3), and performing statistical simulations for it would be overly complicated to implement. As an alternative, a simple *sPlot* procedure is used for the statistical simulations, in which the overall weights are assigned from a single global fit to the $m_{J/\psi pK}$ distribution. This then neglects any dependence of the $m_{J/\psi pK}$ mass resolution on $\cos\theta_{\Lambda_b^0}$ and $\cos\theta_{J/\psi}$, which anyway only enter the analysis through the efficiency correction. The signal events are generated as described previously for the nominal procedure, and the background events are also generated as in the nominal procedure, *i.e.* with the background parametrization

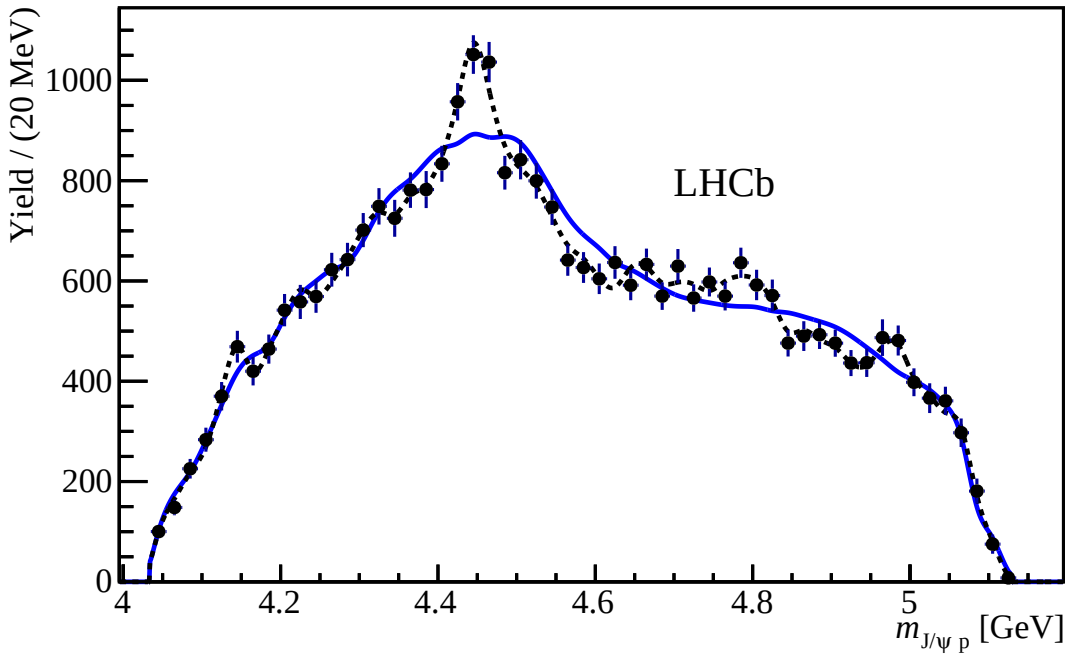

Figure 100: Results when the *sPlot* technique is used for background subtraction. The efficiency-corrected and background-subtracted distribution of $m_{J/\psi p}$ for the data (black points with error bars), compared with $\mathcal{P}(m_{J/\psi p}|H_0)$ (solid blue line) and $\mathcal{P}(m_{J/\psi p}|H_1)$ (dashed black line). The figure should be compared to the nominal distribution obtained using sideband subtraction, shown in Fig. 84.

built from the sidebands. The *sPlot* procedure also requires that a value of $m_{J/\psi pK}$ is also generated. This is done according to the one-dimensional signal and background $\mathcal{PDF}$'s obtained from the fit to the $m_{J/\psi pK}$ distribution of the data, as was described in Sec. 4.2. The simulated $m_{J/\psi pK}$ distribution is then fit in the same way, and the fit results are used to set the sWeights for the given pseudoexperiment.

As usual, many pseudoexperiments were then ran in order to get a handle on the distributions of the test variables under the H_0 hypothesis. The t_{χ^2} test variable yields a $5.7\,\sigma$ rejection of the H_0 hypothesis, in comparison to the $5.3\,\sigma$ obtained using the nominal procedure The t_{DLL} test variable yields a a $10.4\,\sigma$ rejection, as compared to the nominal value of $10.1\,\sigma$. Thus performing the background subtraction with the *sPlot* technique gives slightly stronger rejections than are obtained with the nominal method. A larger rejection is at least partially due to the increased size of the event sample passed through the analysis chain (*i.e.* events in between the sidebands and the signal regions are now included). There are also increased statistics of background events used, which

would lead to less fluctuations in the background subtraction.

24.2 Simulations of efficiency corrections

As noted in Sec. 20.5, there is also a systematic uncertainty associated with how the other decay angles $\Omega_a = (\cos\theta_{\Lambda_b^0}, \cos\theta_{J/\psi}, \phi_K, \phi_\mu)$, which only enter the analysis via the efficiency correction, are generated in the pseudoexperiments. In particular, in the pseudoexperiments they are only shaped by the efficiency parametrization, whereas in the real data they are shaped by both the decay dynamics and efficiency effects. While the dominant factor in their shaping is the efficiency, different shapes or correlations in these variables between the real signal data and signal data in the pseudo-experiments could result in different statistical sampling of the 6D phase space. When averaged over many pseudoexperiments, this does not affect the average values of the quantities used in the hypothesis testing: the bin contents in the histograms of m_{Kp} and $m_{J/\psi p}$, and the Legendre moments. However, the size of fluctuations in these quantities in each pseudoexperiment are affected. The size of statistical fluctuations is what finding the distribution of the test variables over many pseudoexperiments is concerned with. Thus, there is a potential bias induced in these distributions, which in turn affects the $p-$value of the test variables obtained for the H_0 hypothesis. It should be stressed that just ignoring the efficiency dependence on these angles and parameterizing the efficiency on the Dalitz plane only makes the systematics worse, as in that case not only the fluctuations are mismodeled, but also the average values of simulated histogram contents and Legendre moments.

It is worth noting that this effect can already be seen to be small, due to the similarity of the test variable distributions of H_0 pseudoexperiments and pseudoexperiments generated with the extended Λ^* amplitude model, which was shown in Sec.21. In the latter pseudoexperiments, the Ω_a variables were shaped by the decay dynamics, and no substantial difference was seen from the H_0 pseudoexperiments. However, in order to more directly estimate the size of such systematic effects, pseudoexperiments are performed in which the Ω_a variables of the signal events are shaped by an amplitude model. In particular, the full events are generated according to the extended Λ^* model. No P_c contributions were included, in order to keep with the philosophy of this analysis, *i.e.* that

only Λ^* resonances are present in the data. This more realistically shapes the non-Dalitz angular variables, including correlations among them. As the $(m_{Kp}, \cos\theta_{\Lambda^*})$ plane is to be shaped by $\mathcal{F}(m_{Kp}, \cos\theta_{\Lambda^*}|H_0)$, it first needs the shaping from the amplitude model to be undone. This is done by forming a 2D, binned representation of the distribution of the extended Λ^* model over the $(m_{Kp}, \cos\theta_{\Lambda^*})$ plane. With this, event weights determined by the $(m_{Kp}, \cos\theta_{\Lambda^*})$ value can be applied such that the 2D distribution is flattened. The shaping from $\mathcal{F}(m_{Kp}, \cos\theta_{\Lambda^*}|H_0)$ weights can then be carried out in the usual way. The flattening and re-shaping procedure results in the correlations between the $(m_{Kp}, \cos\theta_{\Lambda^*})$ plane and the Ω_a variables being lost. However this procedure still results in a better representation of the 1D distributions of Ω_a, as well as their correlations with each other.

The pseudoexperiments were performed to obtain the distributions of $\mathcal{F}_t(t_{\chi^2}|H_0)$ and $\mathcal{F}_t(t_{\rm DLL}|H_0)$. Using the values obtained on the data, rejections of the H_0 hypothesis are obtained with the t_{χ^2} and $t_{\rm DLL}$ variables at $5.3\,\sigma$ and 9.9σ, respectively. Thus there was no change for t_{χ^2}, and the results change for $t_{\rm DLL}$ only modestly ($\sim 2\%$). In the Appendix K, results are also shown in which the distributions of test variables are obtained with the extended Λ^* model. This test against only one specific Λ^* model, but does take all correlations between kinematic variables into account. The conclusions obtained are the same, *i.e.* this systematic effect is very small. While the studies presented in this section and in Appendix K do result in pseudoexperiments with angular distributions more representative of what is actually in the data, it would not be appropriate to make either a default approach. Doing so would result in an explicit dependence of the results on a model-dependent amplitude analysis, which is completely against the goal of this analysis method. Thus these studies are only used to assess a systematic uncertainty from this effect.

24.3 Looser BDT cut

In this section the analysis is performed with the data set obtained from the looser BDT cut which was used as a cross-check in the amplitude analysis (Sec. 14.4). In particular, the nominal BDT cut is loosened from > 0.9, to > 0.5. For more details on the BDT variable and training, see Appendix C. This increases the background fraction (β) by a factor of 2, while increasing the signal yield by 14%. Thus this test probes both the efficiency parametrization and background subtraction. Since the background remains relatively small ($\sim 10\%$), a slightly improved statistical sensitivity is expected. Shown in Fig. 101 is the efficiency-corrected and background-subtracted $m_{J/\psi p}$ distribution of the data obtained with this cut, along with the obtained $\mathcal{F}(m_{J/\psi p}|H_{0,1})$ distributions. Clearly, there is still a large excess of the data over the $\mathcal{F}(m_{J/\psi p}|H_0)$ distribution in the P_c region.

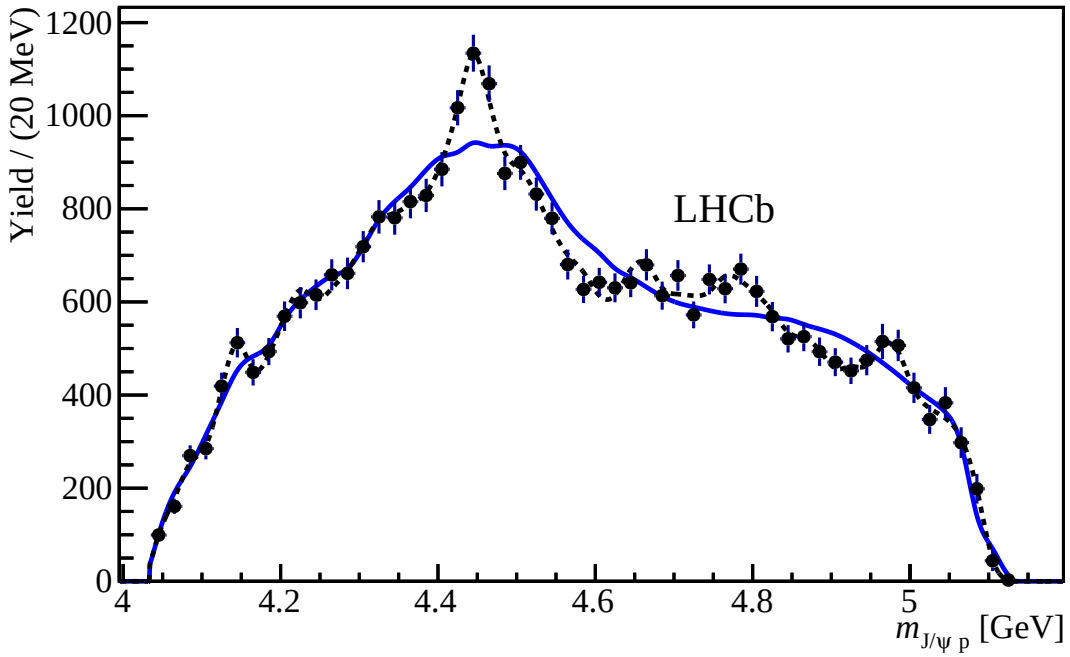

Figure 101: Results when a looser BDT cut is used. The efficiency-corrected and background-subtracted distribution of $m_{J/\psi p}$ for the data (black points with error bars), compared with $\mathcal{P}(m_{J/\psi p}|H_0)$ (solid blue line) and $\mathcal{P}(m_{J/\psi p}|H_1)$ (dashed black line).

Statistical simulations are performed in order to quantify the H_0 rejection levels in the same way as described for the nominal results. The t_{χ^2} test variable results in a

6.7σ rejection of H_0 (vs. 5.3σ in the nominal cut). The t_{DLL} test variable gives an 11.1σ rejection of H_0 (vs. 10.1σ in the nominal cut). Both test variables give a larger significance than those obtained with the default BDT cut, which is consistent with the expectations of higher sensitivity.

24.4 Summary of Systematic Effects

The significances for each of the studies performed in this section are shown for both test variables in Table 24. For the sideband test, the weaker significance obtained from using the lower sideband is listed. All systematic variations result in large significances for the rejection of the H_0 hypothesis, and are generally in line with what was expected.

Table 24: Significances obtained in Gaussian standard deviations for the various systematic studies performed.

Test	t_{χ^2}	t_{DLL}
Nominal	5.3	10.1
Sideband	5.2	9.8
sPlot	5.7	10.4
Simulations of efficiency corrections	5.3	9.9
Loose BDT	6.7	11.1

25 Conclusions from model-independent study

Previously, it had been shown via an amplitude analysis that K^-p contributions could not produce the peaking structures found in the $m_{J/\psi p}$ distribution of $\Lambda_b^0 \to J/\psi K^- p$ decays. This model-dependent study provided an abundance of evidence this was the case, but still required making several assumptions about the Λ^* "background". In particular, assumptions were made regarding the number of states and their quantum numbers, lineshapes, masses, widths and interference patterns. As the spectroscopy of these K^-p resonances is poorly understood, the amplitude analysis was open to some criticism. This model-independent analysis aimed to alleviate any worries about mismodeling of K^-p contributions, and what it could mean for the conclusion that they are unable to describe the data by themselves.

The hypothesis that only $\Lambda_b^0 \to J/\psi \Lambda^*$, $\Lambda^* \to Kp$ decays (Λ^* could also be Σ^* or nonresonant components) contribute to the $J/\psi K^- p$ final state was tested. This was referred to as the H_0 hypothesis, and it contained only mild model assumptions pertaining to the masses at which certain spins appear. It was found that the H_0 hypothesis was not compatible with the observed $m_{J/\psi p}$ distribution of the data. After systematic uncertainty studies, it is reported that the H_0 hypothesis can be rejected at $> 9\,\sigma$ from a log likelihood ratio test, and $> 5\,\sigma$ from a simple χ^2 test. Repeating the analysis, but probing compatibility with the $m_{J/\psi K}$ distribution of the data, lower rejections levels were obtained. This gives a model-independent hint from the data that $J/\psi p$ contributions are more significant than $J/\psi K^-$ contributions (if any). Tests studying the sensitivity of this method on the narrowness of exotic resonances were also performed for the first time.

It should be stressed, that the values quoted here are not to be thought of as the significances of any particular pentaquark candidate, as the hypotheses tested in the model-independent approach make no assumptions about any exotic states decaying to $J/\psi p$ (or $J/\psi K^-$). Evidence that the failure of the Λ^* resonances to describe the data has something to do with a P_c contributions is based on a qualitative inspection of Fig. 84. To turn such an inspection into a probabilistic statement for a given mass

range, a deterministic peak-search algorithm would need to be developed with its own discrimination variable, which would then need to be statistically simulated. This is impossible to implement rigorously as the shape of any exotic state can be affected by interferences with other components, and thus is not universal. Still, to conclude, it has been shown via model-independent methods that the hypothesis that the data contains only K^-p contributions can be rejected with high significance. The analysis requires only minimal assumptions on the mass and spin of the K^-p contributions; no assumptions on their number, their resonant or nonresonant nature, or their lineshapes have been made. Non-K^-p contributions, which must be present in the data, can be either of the exotic hadron type, or due to rescattering effects among ordinary hadrons. This result supports the amplitude model-dependent observation of the $J/\psi\, p$ resonances presented in the first part of this thesis.

26 Discussion

The observation of the $P_c(4380)$ and $P_c(4450)$ pentaquark candidates presented in this thesis has revitalized interest in pentaquarks. There has been much discussion in the theoretical community about the nature of these states and possible methods for internal binding of the five quarks. It is beyond the scope of this dissertation to give a full summary of the large number of publications which have already been released on this topic. Instead a brief overview of the more popular interpretations of the candidates will be given. For more detailed reviews of the models and interpretations, see Refs. [66, 67]. Each of these models has difficulties, and so this section will be concluded with a discussion of the outlook on what to look forward to in order to elucidate the nature of these states. Note that, while the preferred quantum numbers of the default Λ^* model will be taken as being correct in this discussion, they may change as better representations of the Λ^* component are found.

26.1 Theoretical Models

A leading interpretation of the $P_c(4380)$ and $P_c(4450)$ pentaquark candidates is that they are baryon-meson molecules, loosely bound by pseudoscalar meson exchange [68–77]. Molecular models have already been employed to describe exotic meson candidates, and appear to be reasonable explanations for several of them. See Ref. [68] for a discussion of the application of the molecular model to several tetraquark candidates. Inspiration for these interpretations generally comes from the proposed exotic hadron lying right at the threshold of the two hadrons comprising the molecule. The binding energy is not expected to be large, and so the mass of the molecule is expected to be close to the threshold. Due to this, it is expected that these bound states occur only for a ground state *i.e.* are in an S-wave configuration (no orbital angular momentum between the two hadrons) and with no radial excitation. Radial or orbital excitations would push the energy of the constituent hadrons above the shallow potential well between them. Nearby thresholds for each of the P_c states are listed in Table 25. The possible quantum numbers for each

of these molecular hypotheses are set, due to the assumption that the constituents are combined in an S-wave. These are also listed in Table 25. It should be noted, however, that depending on the exact model of inter-hadron forces, not all of these combination are expected to create a bound state. For example, constituent hadrons must have a non-zero isospin to couple via pion exchange, which excludes molecules with charmonium as a constituent. For $P_c(4380)$, a $\Sigma_c(2520)^+\bar{D}^0$ molecule appears to be a viable candidate; however the molecular model has difficulty accounting for its rather large width, as will be explained later. For $P_c(4450)$, which is suitably narrow for molecular interpretations, none of the possible combinations have spin $J = 5/2$. Indeed, to create an S-wave molecule with spin $J = 5/2$, the mass would likely be well over that of $P_c(4450)$. The most reasonable quantum numbers that the molecular model is able to provide for $P_c(4450)$ are $3/2^-$ and $3/2^+$, from $\Sigma_c(2455)^+\bar{D}^{*0}$ [68] and $\chi_{c1}p$ molecules, respectively. The only opposite parity combination then is ($3/2^-$,$3/2^+$), which did not fare well using either the default Λ^* model or the extended Λ^* model. Thus it does not appear that **both** P_c states can fit into the molecular model, with $P_c(4380)$ appearing to be the weaker molecular candidate of the two of them.

Table 25: P_c states and nearby baron-meson thresholds.

Measured	$P_c(4380)$	$P_c(4450)$	
Mass	$4380 \pm 8 \pm 29$ MeV	$4449.8 \pm 1.7 \pm 2.2$ MeV	
Width	$205 \pm 18 \pm 87$ MeV	$39 \pm 5 \pm 16$ MeV	
Nearby Threshold	$P_c(4380)$	$P_c(4450)$	S-wave J^P
$\Sigma_c(2520)^+\bar{D}^0$	4382.3 ± 2.4		$3/2^-$
$\chi_{c1}p$		4448.93 ± 0.07	$1/2^+$, $3/2^+$
$\Lambda_c(2595)\bar{D}^0$		4457.09 ± 0.35	$1/2^+$
$\Sigma_c(2455)^+\bar{D}^{*0}$		4459.9 ± 0.5	$1/2^-$, $3/2^-$
$\Sigma_c(2455)^+\bar{D}^0\pi^0$		4452.7 ± 0.5	$1/2^+$

Another popular interpretion employs other colored objects to construct the pentaquark candidates, *e.g.* antiquark-diquark-diquark [78–83] and diquark-triquark configurations [84, 85]. The former are constructed as the $\bar{c}$ antiquark grouped with (cu) and (ud) diquarks, and the latter as a (cu) diquark paired with a $\bar{c}(ud)$ triquark. Such colored objects represent spatial correlations between groups of the constituent quarks of hadrons, and have been employed in the past as part of models for conventional baryons

as well as tetraquark candidates. Each of these colored objects would be in the same color confinement volume and feel the color force of the others. Since the confinement volume cannot be much larger than about 1 fm, pentaquarks constructed with this picture are generally tightly bound resonances, though Ref. [84] offers a picture in which a diquark and triquark are rapidly separating. Pentaquark candidates of various J^P quantum numbers can be obtained by realignments of the constituent spins or increasing their orbital angular momentum. The mass can also be easily shifted up by allowing radial excitations. Thus there is more flexibility in predicting whether tightly bound pentaquark resonances with certain quantum numbers might be present at the P_c masses, and this typically involves some sort of phenomonological model of color forces at confining distances. In particular, a pair of $(3/2, 5/2)$ states of opposite parity can be accommodated by changing orbital angular momentum between quarks by one unit. Such models consider the proximity of the P_c states to the baryon-meson thresholds as coincidence. These models have difficulty explaining the narrow width of the $P_c(4450)$, as discussed next.

An important feature of $P_c(4450)$ to consider is its small width of 39 MeV, despite lying several hundred MeV above the $J/\psi p$ threshold. The width of a state depends on the product of the matrix element for the decay and the amount of phase space available. This seems to indicate that $P_c(4450)$ has an internal structure which works to suppresses the matrix element for a rearrangment of quarks into J/ψ plus p configuration. Molecular models, in which c and $\overline{c}$ are separated into two constituent hadrons (*i.e.* into a charm baryon and a charm meson) provide a natural mechanism for such a suppression; the average distance between the hadrons can be larger than the color confinement volume, and thus much larger than the J/ψ size. The separation between the c and $\overline{c}$ inside a tightly bound pentaquark is necessarily much smaller, making their recombination into J/ψ more likely. On the other hand, this would make the large $P_c(4380)$ width difficult to accommodate in the molecular model, and the tightly bound models would be more suitable interpretations if it is a true resonance. It should also be noted that the explanation of the pentaquarks in terms of a confined, yet rapidly separating, uc diquark and $\overline{c}(ud)$ pair does not have this difficulty [84]. In this model, the energy release in the

production ($\Lambda_b^0 \to P_c K$) is hypothesized to lead to the rapid separation. Such a picture offers a suggestion on how the rearrangement of quarks into $J/\psi p$ could be suppressed.

Another group of interpretations attribute the structures as not being due to bound states, but scattering effects between virtual hadrons [86–89]. Like the molecular picture, these are inspired by the nearness of the structures to meson-baryon thresholds. The proposed effects are a result of the rescattering of conventional hadrons causing singularities in the S-matrix, which manifest themselves as mass peaks in the system produced via quark rearrangement in the hadron rescattering. Such models have also been proposed in the past to account for other exotic hadron candidates. These models face a similar difficulty as the molecular models in that they have troubles accomodating one of the proposed P_c states having an effective $J = 5/2$, since only S-wave rescattering can be significant. Nevertheless, P-wave couplings have still been assumed in two possible scenarios: the decay $\Lambda_b^0 \to \chi_{c1} K^- p$ with the rescattering of $\chi_{c1} p \to J/\psi p$ can lead to a two-point singularity, and $\Lambda_b^0 \to \chi_{c1}\Lambda(1890)$, $\Lambda(1890) \to K^- p$ with the rescattering of $\chi_{c1} p \to J/\psi p$ can lead to a triangle singularity [86]. A similar picture was also used in Ref. [87]. Ref. [89] proposes the structure is a result of $\Lambda_b^0 \to \Sigma_c^+ D_s^{*-}$, $D_s^{*-} \to \bar{D}^{*0} K^-$ followed by $\Sigma_c \bar{D}^{*0} \to J/\psi p$. Ref. [88] employ a variety of rescatterings which result in two-point or triangle singularities. The observability of these singularities has been in discussion for a long time [90, 91], and thus if this hypothesis is true for one or both of the observed structures, this would also be an interesting outcome [92].

26.2 Outlook

As discussed, each of the models presented has difficulties in describing both states. A number of possible explanations exist. One is that the interpretation of the data is not correct. It is certainly possible, for instance, that the most preferred quantum numbers are incorrect. The results are already ambiguous in the default amplitude model, and the fact that the preferences have significant changes when using the extended Λ^* model casts more uncertainty on the quantum number assignments. Another realistic scenario is that the two states have different natures and internal bindings. There is no good reason,

other than simplicity, why different interpretations can't be given for the two candidates.

Towards the goal of understanding the nature of the results presented in this dissertation, there are a number of directions to look towards. It will be important to see confirmation of these states in other experiments. Of particular interest would be seeing them in different production methods. It has been suggested that they could be seen in photoproduction [93–96]. If they were seen in this production mechanism, it would rule out any interpretations in terms of rescaterring effects. Direct production in pp collisions is another possibility, but backgrounds are large.

Further studies in the $\Lambda_b^0 \to J/\psi K^- p$ decay mode will also be useful. Resolving ambiguities in the quantum numbers would greatly help in narrowing down possible models. Hopefully this will be possible with increased statistics and a more sophisticated handling of the Λ^* model (*e.g.* going beyond the limitations of the Isobar approximation). One could also look forward to more conclusive studies of the phase motion of the $P_c(4380)$ state. Many of the different proposed models predict other states which should be visible in this channel. Better statistics and improved amplitude models would help in terms of giving better sensitivity to these searches.

These states should also be looked for in other Λ_b^0 decays. Recently, evidence of exotic contributions in $\Lambda_b^0 \to J/\psi \pi^- p$ decays was published by LHCb [97]. If the $P_c(4380)$ and $P_c(4450)$ are true resonant states, they should also be present in this decay channel. As this decay is Cabibbo suppressed, the statistics are significantly less than in the $\Lambda_b^0 \to J/\psi p^- K$ mode, and the backgrounds are also higher. With the present statistics it was not possible to decisively determine if the exotic contributions were from $P_c \to J/\psi p$ contributions or from $Z_c \to J/\psi \pi$ contributions. Such a Z_c state was reported by Belle in $\bar{B}^0 \to J/\psi K^- \pi^+$ decays [98]. It will be interesting to see what conclusions are reached with more data. It should also be noted, however, that there has already been discussion of a triangle singularity appearing in this channel near the $P_c(4450)$ mass as well [92]. Also interesting would be to see $P_c(4450)$ in other decays *e.g.* in $\Lambda_b^0 \to \chi_{c1} K^- p$, as this would rule out some rescattering models [86], while observing a deficit at the $P_c(4450)$ mass in $m_{\chi_{c1}p}$ would confirm them. The observation of the P_c states decaying to open

charm pairs would be interesting. Searches for such decays would be useful in terms of narrowing down models (see Table 3 of Ref [66]). Such decays have more tracks in the final-state, though, and thus are much more difficult as they will suffer from lower efficiency and higher backgrounds.

Finally, searches for other charmonium-pentaquarks, as well as bottomonium-pentaquarks or $\bar{b}c$-pentaquarks, will be avenues to watch. This is not to say that pentaquarks with only light-flavored quarks should be ruled out. However, due to the history with tetraquark searches, along with recent theoretical studies suggesting heavy quarks are important in forming exotic hadrons [32–34], these certainly seem like the most promising searches.

27 Conclusions

The observation of structures consistent with charmonium-pentaquark states decaying to $J/\psi\, p$ in $\Lambda_b^0 \to J/\psi\, K^- p$ decays has been presented. A 6D amplitude analysis demonstrated that good descriptions of the data can't be achieved with only the known $K^- p$ resonances in the amplitude model. For good fits of the data, it is necessary to have two $J/\psi\, p$ resonances in the amplitude model. These new pentaquark candidates, $P_c(4450)$ and $P_c(4380)$, each have significances of over 9 standard deviations. The mass and width of $P_c(4450)$ were found to be $4449.8 \pm 1.7 \pm 2.2$ MeV and $39 \pm 5 \pm 16$ MeV, respectively, while the mass and width of $P_c(4380)$ were found to be $4380 \pm 8 \pm 29$ MeV and $205 \pm 18 \pm 87$ MeV, respectively. The J^P assignments could not be uniquely determined, though there is a preference for opposite parity states with spin 3/2 and spin 5/2. A model-independent analysis confirmed that the data could not be described with only $K^- p$ contributions at over 9 standard deviations, and that $J/\psi\, p$ contributions play a dominant role in this incompatibility. This was done while making only minimal assumptions on the mass and spin of the $K^- p$ contributions, and without making any assumptions on their number, their resonant or nonresonant nature, their lineshapes, or interference patterns. Non-$K^- p$ contributions, which must be present in the data, can be either of the exotic hadron type, or due to rescattering effects among ordinary hadrons.

The studies in this dissertation have revitalized experimental and theoretical interest in pentaquark resonances. There has already been a large amount of theoretical activity attempting to explain these states, and it is going to take a large amount of experimental effort to sort out the situation. The field of exotic hadrons is going to be quite exciting in the coming years, and much will be learned about how quarks bind together. In the meantime, these results have already provided much input towards understanding QCD, and could also help with other strongly coupled theories.

Appendices

A Effects of $\overline{B}{}^0_s$ and $\overline{B}{}^0$ vetos

To check for contributions from $\overline{B}{}^0_s \to J/\psi K^- K^+$ and $\overline{B}{}^0 \to J/\psi K^- \pi^+$ decays, the proton track is reassigned as either a kaon or a pion, and then either the $m_{J/\psi K^- K^+}$ or $m_{J/\psi K^- pi^+}$ invariant mass is calculated. Both of these are shown for the data which has passed the selection criteria in Fig. 102.

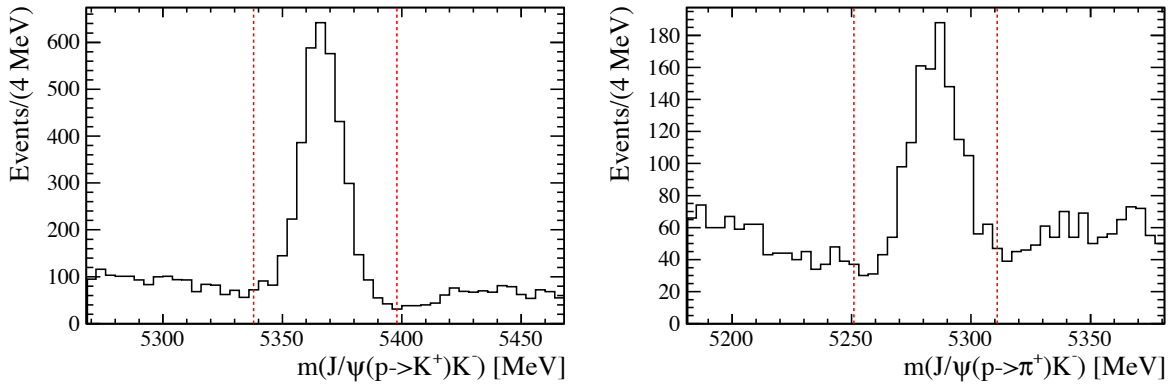

Figure 102: (a) Invariant mass of $J/\psi K^+ K^-$ combinations from $\Lambda^0_b \to J/\psi K^- p$ candidates where the p is interpreted as a K^+. (b) Invariant mass of $J/\psi \pi^+ K^-$ combinations from $\Lambda^0_b \to J/\psi K^- p$ candidates where the p is interpreted as a π^+. The vertical dashed (red) lines indicates the vetoed events.

Clearly, there are substantial contributions from both sources. The decision was made to remove the $\overline{B}{}^0_s$ and $\overline{B}{}^0$ backgrounds, rather than attempt to parametrize them somehow. This was done by vetoing the candidates which fall between the vertical red dashed lines, effectively eliminating the pollution from these backgrounds. Naturally, this procedure modifies the detection efficiencies. In Fig. 103 the effects of the vetos on the efficiency across the Dalitz plane is shown. The scale is such that a value of unity means that the vetos had no effect on the bin. One can see the vetos cause only fairly smooth modifications to the Dalitz plane. There is also a small background from real $\Lambda^0_b \to J/\psi K^- p$ events where both the K^- and p are misidentified. Using sidebands and simulation this contribution is estimated to amount to be only 0.4% of all combinations, and the decision was made to neglect this background.

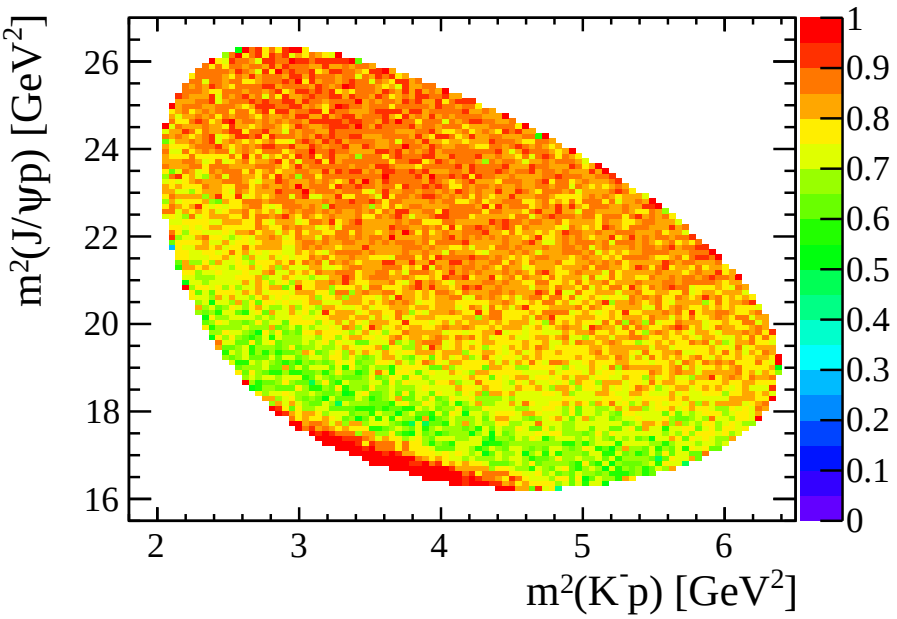

Figure 103: The reduction of efficiency across the Dalitz plane from the vetos, where unity indicates no effect.

B Monte Carlo weights

The weights which are given to MC events in order to more accurately represent the behavior of the data are discussed in this section. These weights then affect the efficiency parametrization and the integration of $\mathcal{PDF}$'s defined in Sec. 6. The overall weight applied to each MC event is defined as

$$w^{\mathrm{MC}} = \varepsilon_p(p, \eta, \mathrm{nTracks})\, \varepsilon_K(p, \eta, \mathrm{nTracks})\, w(\mathrm{nTracks})\, w_{\Lambda_b^0}(p, p_{\mathrm{T}})\, w_K(p)\, w_p(p). \quad (114)$$

Each term in the equation is obtained in sequence from left to right, in order to account for correlations. The above is somewhat of a simplification, as portions of the procedure are applied in an iterative manner, as described below.

In the first step, the first four terms are determined. The first term is to correct for well-known deficiencies in the simulation's modeling of particle identification efficiencies. Thus, rather than just applying a selection cut and discarding events which do not pass the criteria, it is common practice to instead use event weights obtained with data-driven methods to replicate the action of performing such cuts. Thus, no explicit particle identification cuts were applied to the p and K candidates when selecting the Monte Carlo events. Instead, the ε_p and ε_K weights are used, which are obtained from high statistics and high purity calibration samples of $\Lambda^0 \to p\pi^+$ and $D^0 \to K^-\pi^+$, respectively. The efficiencies from these samples for the particular PID cuts used are parametrized in terms of the proton's or kaon's momentum p, pseudorapidity η, or total number of long tracks (nTracks) in the event. The weight $w(\mathrm{nTracks})$ corrects for the remaining differences between the data and MC for the dependence of the overall signal efficiency on nTracks. It is obtained from the distribution of nTracks in the background-subtracted data divided by that in the simulation. The term $w_{\Lambda_b^0}(p, p_{\mathrm{T}})$ is due to an imperfect description of the Λ_b^0 production kinematics in the simulation. It is obtained as the ratio of two-dimensional $(p, p_{\mathrm{T}})_{\Lambda_b^0}$ distributions between the data and simulation. To obtain the distribution, the phase space signal sample must be modified to account for the decay kinematics in data. Here the background-subtracted two-dimensional Dalitz-plot distribution from data is

used.

The above terms are used for the initial weights. They are applied to the MC, and an amplitude fit is then performed. The matrix element from the fitted amplitude model is then applied as a weight to the MC set. Then the p_K, p_p and $(p, pt)_{\Lambda_b^0}$ distributions from the weighted MC set are compared to the corresponding distributions in the data. The p_K and p_p distributions for both the MC and data are shown in Fig. 104, where the ratios between them are seen to be relatively uniform and have values near unity over a large momentum range. In the regions below 10 GeV and above 100 GeV, where particle identification is less reliable, the ratios are closer to 0.5. The ratios between the data and the simulation for p_K and p_p are taken as $w_K(p_K)$ and $w_p(p_p)$.

It is somewhat surprising that the ratio of $(p, pt)_{\Lambda_b^0}$ between the data and MC varies from 0.95 to 1.25, as shown in Fig. 105. In principle, it should be close to unity, as the initial $w_{\Lambda_b^0}(p, pt)$ weight has already applied. The reason it changes is that the initial weight was obtained using the data's two-dimensional Dalitz-plot distribution as an "amplitude model", while here the six-dimensional amplitude model has been used as a weight. Therefore, $w_{\Lambda_b^0}(p, pt)$ is updated using this newer model. After applying this new weight, the data and fit agreement on $\cos\theta_{\Lambda_b^0}$ is largely improved as the $\cos\theta_{\Lambda_b^0}$ distribution strongly depends on the distribution of $(p, pt)_{\Lambda_b^0}$ at production.

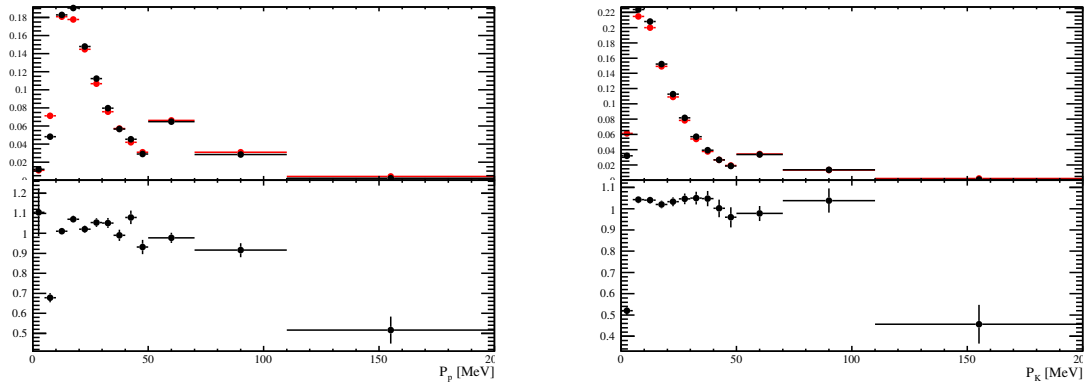

Figure 104: Distribution of proton (left) and kaon (right) momentum (top) for the $\Lambda_b \to J/\psi pK$ candidates in the data (black points) and in the simulations (red points). The ratio of these distributions (bottom) defines the $w_p(p)$ and $w_K(p)$ terms in the MC weight. The background in the data is subtracted using sWeights.

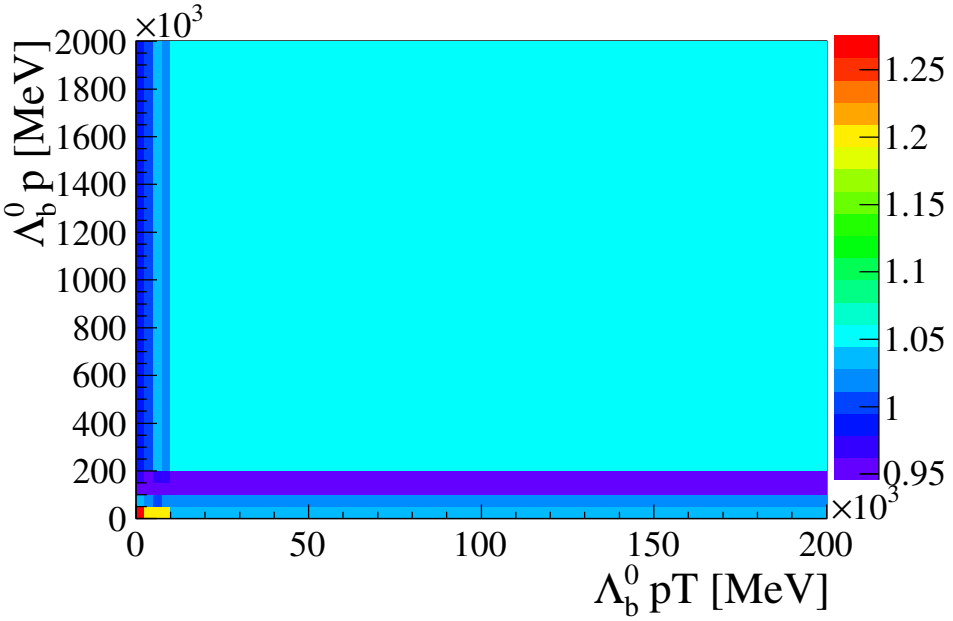

Figure 105: Dependence of the $w_{\Lambda_b^0}(p, p_{\mathrm{T}})$ weight on Λ_b momentum and its transverse component.

C BDT training

A Boosted Decision Tree (BDT) is used as a multivariate analyzer, taking input from multiple variables and using them to attempt to classify an event as either signal or background. It was constructed using the Toolkit for Multivariate Data Analysis (TMVA) package [99], using the gradient boosting method. Hereafter it is referred to as BDTG, to reflect the use of gradient boosting. The BDTG is "trained" to distinguish between the signal and background events. The fully simulated MC data sample is used to model the $\Lambda_b^0 \to J/\psi K^- p$ signal events. To model the background, events with invariant mass $m_{J/\psi Kp}$ lying in the interval of 150 to 250 MeV from the Λ_b^0 mass peak are used. The samples for both the signal and background event types which remain after the selection criteria are divided into two nearly equal parts. Half of the sample is used for the BDTG training, and the other half is used to test the BDTG performance.

The variables used as input to the BDTG are listed below, with a brief explanation and the name with which they are labeled Fig. 106, which shows their distribution in both the signal and background sample.

- The minimum $DLL_\pi(\mu)$ of the μ^+ and μ^- (mmPIDmu).
- The minimum $\chi^2_{\rm IP}$ of either the K^- or the p. The natural logarithm is taken in order to reduce the range the variable takes [log(pmipCHI2)].
- The cosine of the angle between the Λ_b^0 momentum and the direction between its PV and decay vertex [dira].
- $\chi^2_{\rm IP}(\Lambda_b^0)$ [log(BCHI2)].
- Flight distance of the Λ_b^0 [FD].
- $p_{\rm T}$ of the Λ_b^0 [BPT].
- $\chi^2_{\rm vtx}(\Lambda_b^0)$ [LogBIPCHI2].
- $p_{\rm T}$ sum of the K^- and p [SumPT].

Note that there is discrimination power between signal and background in all of these variables, though several of them would be very weak if they were to be used by themselves. The distributions of the BDTG classifier response to the signal and background performance test samples are shown in Fig. 107. Clearly, there is good separation between the signal and background test samples, and the BDTG is much more powerful than any of the individual variables.

In order to choose an optimal selection criteria for the BDTG output, different metrics are often used which depend on the number of signal (S) and background (B) events. Examples are $S/\sqrt{S+B}$, $S/(S+B)$, and $S^2/(S+B)^{1.5}$. Figure 108 shows these different metrics, where the numbers of signal and background events were determined by fitting the $m_{J/\psi Kp}$ distribution in the data for different values of the BDTG cut. Ultimately, a cut of BDTG > 0.9 was used. This is a fairly agressive choice, but experience with the multivariable fits in this analysis led to the conclusion that a better optimization was found by rejecting more background. Less background will obviously lead to less concerns about how it is modeled, and a large signal sample still remains after the tigher cut. In order to estimate systematic effects which come with this cut, some studies are also performed with a cut of BDTG > 0.5. Decreasing the BDTG requirement to be greater than 0.5 increases the number of signal events by 13% and the number of background events by 93%.

Note that the output of the BDTG can never be wrong, in the sense that it is ultimately just a variable that uses information from multiple inputs to try to classify an event as either signal or background. However the performance of the BDTG can certainly be poor if the distributions of the variables used in the training samples do not correctly represent what is in the actual data. In Fig. 109, comparisons of the variables used in the BDTG are shown between the background-subtracted data and the simulated signal sample used to train the BDTG. The events in the simulation sample are weighted using the modulus-squared of the matrix element from the default amplitude model, in order to reflect the dynamics which are present in the data. It is seen that there is good agreement between the training sample and the data.

In the amplitude analysis, all independent kinematic variables in the decay are fitted. (The fitting variables are all defined in Sec. 5.) While any significant correlation of these variables with the variables used in the BDTG is not inherently a problem, if the BDTG significantly modifies one of these distributions it makes the analysis more susceptible to mismodeling issues. The correlation of the BDTG variables with the fitted variables are given in Table 26. Here the correlation coefficient is defined as

$$\rho_{X,Y} = \frac{\mathrm{cov(X,Y)}}{\sigma_X \sigma_Y,} \tag{115}$$

with cov(X,Y) being the covariance, and σ_i the standard deviation. The correlations are small except for those of SumPT and LogmIPCHI2 with $\cos\theta_{\Lambda_b^0}$. The 2D histograms of these combinations are shown in Fig. 110. The distributions are smooth and the correlations are not a problem. Furthermore, one notes that the correlations of the fitted variables with the BDTG output are all small.

Table 26: Correlations of the variables used in the BTDG and the BDTG output with the six fitted variables.

	m_{Kp}	$m_{J/\psi p}$	$\cos\theta_{\Lambda_b^0}$	$\cos\theta_{J/\psi}$	ϕ_K	ϕ_μ
mmPIDmu	-0.0102	0.0144	0.0410	-0.0063	0.0026	-0.0010
LogmIPCHI2	0.0300	-0.0034	-0.1567	-0.0017	0.0003	0.0008
DIRA	-0.0181	-0.0079	0.0195	0.0038	-0.0023	0.0030
LogBCHI2	-0.0042	0.0030	0.0041	-0.0023	0.0026	-0.0006
FD	-0.0203	-0.0206	-0.0064	0.0005	-0.0038	0.0013
BPT	-0.0266	-0.0224	-0.0219	-0.0039	-0.0015	0.0013
LogBIPCHI2	0.0018	0.0025	0.0036	-0.0033	-0.0025	-0.0017
SumPT	0.037	-0.0243	0.3480	-0.0031	-0.0011	0.0003
BDTG	0.0346	-0.0212	0.0647	0.0009	-0.0046	0.0013

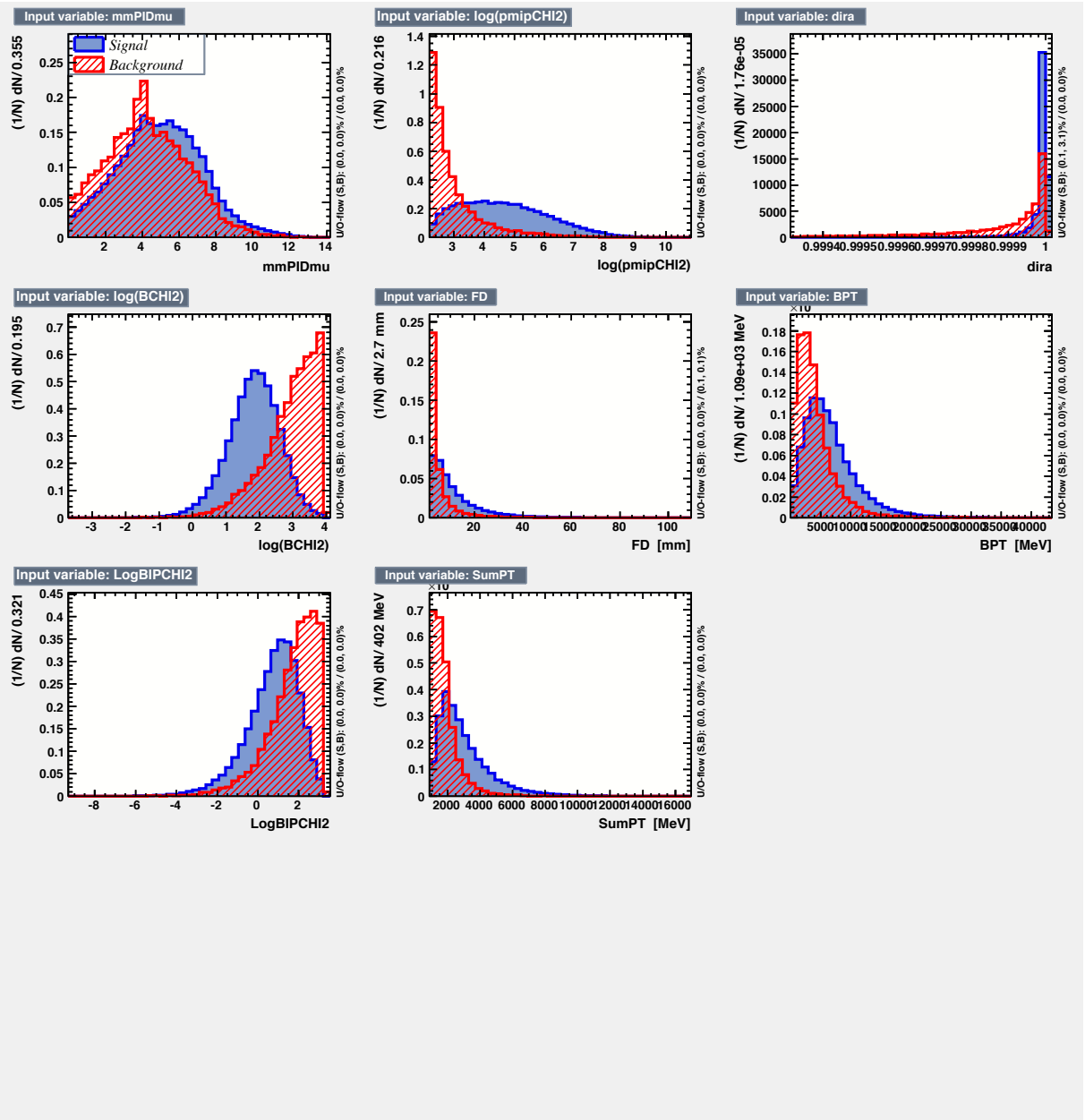

Figure 106: Signal and background distributions of variables used in BDTG.

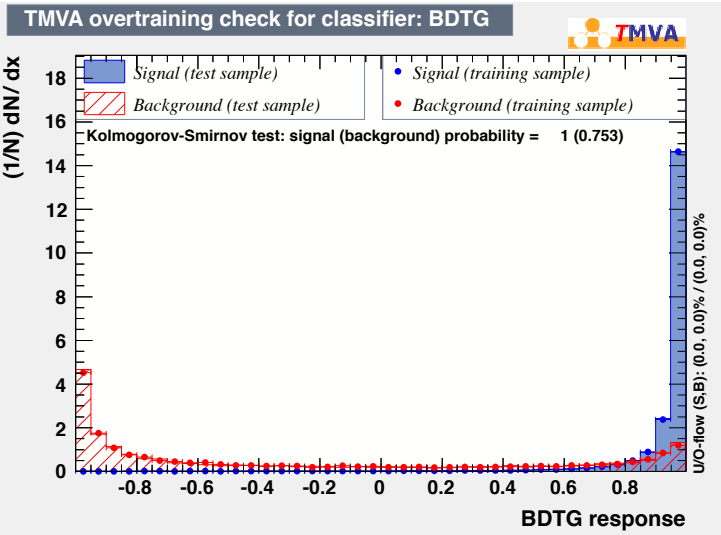

Figure 107: BDTG distributions for the signal and background.

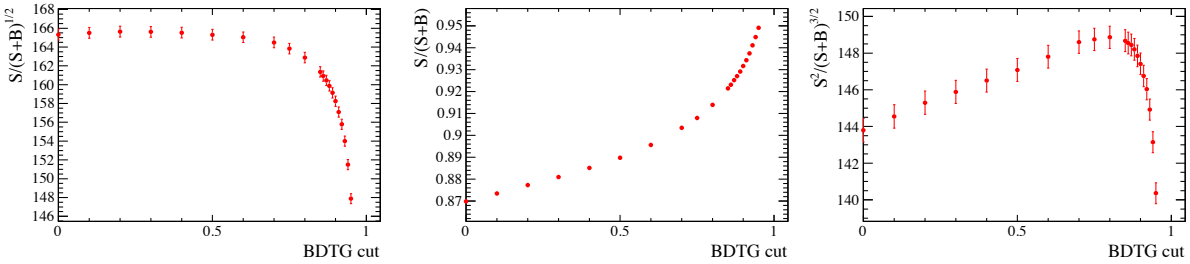

Figure 108: Different metrics that can be used for the BDTG cut choice in terms of the number of signal (S) and background (B) events. Note the severely suppressed zero in the vertical axes.

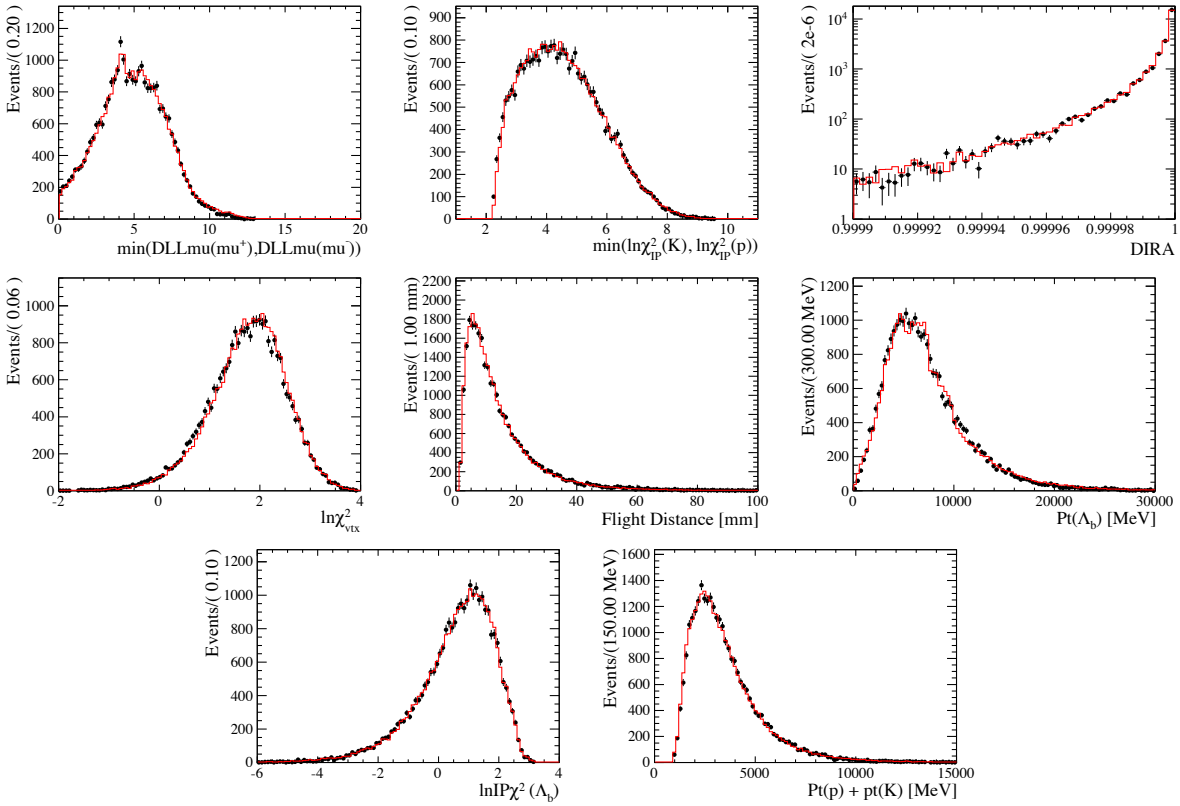

Figure 109: Comparisons of the BDT variables in data and the training sample.

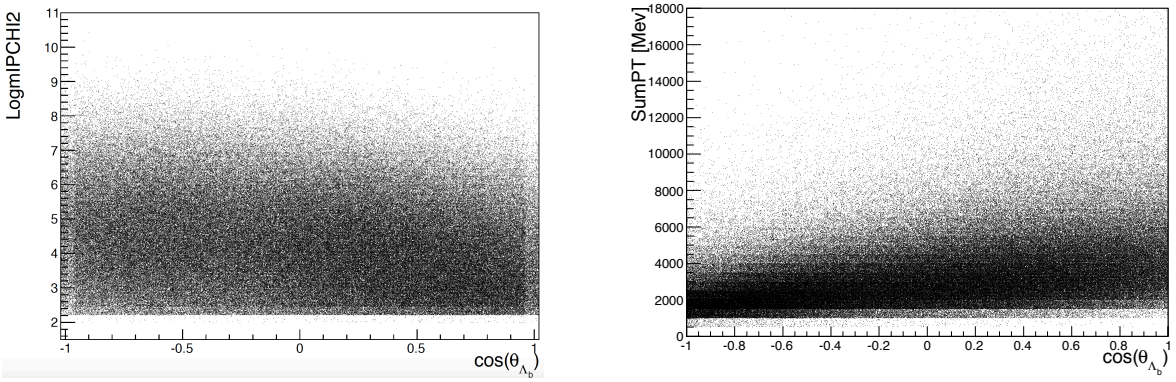

Figure 110: Correlations of $\cos\theta_{\Lambda_b^0}$ with (a) LogmIPCHI2 and (b) SumPT.

D Results for extended model with both P_c states

It was shown in Sec. 10.1 that good descriptions of the data can be obtained with the default (or "reduced") Λ^* model and the two P_c states: $P_c(4380)$ and $P_c(4450)$. The preferred quantum numbers with the default Λ^* model are $J^P(P_c(4380), P_c(4450)) = (3/2^-, 5/2^+)$. The results for the fit performed with the extended Λ^* model and two P_c's of the same quantum numbers are shown in this section. The mass, width, and fit fraction of $P_c(4380)$ with the extended Λ^* model were found to be 4359 MeV, 151 MeV, and 5.28, respectively, while the mass, width, and fit fraction of $P_c(4450)$ were found to be 4450.1 MeV, 49 MeV, and 4.41, respectively[21]. In Fig. 111, the projections of this amplitude model on m_{Kp} and $m_{J/\psi p}$ are shown along with the data, where it is seen good descriptions are obtained. The angular distributions are reasonably reproduced as well, as shown in Fig. 112. Lastly, Fig. 113 shows the projection onto $m_{J/\psi p}$ in the usual intervals of m_{Kp}.

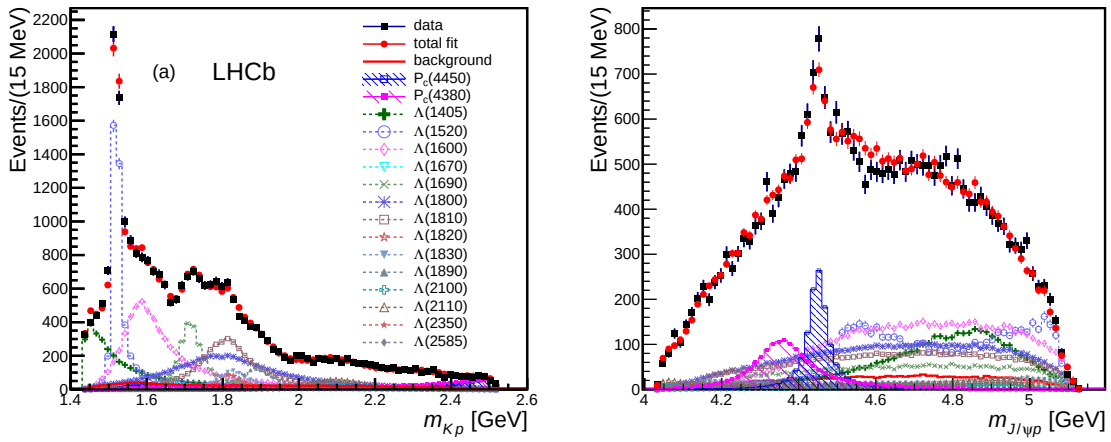

Figure 111: Fit projections of the extended Λ^* model with two P_c^+ states onto the (a) m_{Kp} and (b) $m_{J/\psi p}$ distributions. The data are shown as solid (black) squares, while the solid (red) points show the results of the fit. The solid (red) histogram shows the background distribution. The (blue) open squares with the shaded histogram represent the $P_c(4450)^+$ state, and the shaded histogram topped with (purple) filled squares represents the $P_c(4380)^+$ state. Each Λ^* component is also shown. The error bars on the points showing the fit results are due to simulation statistics.

[21] While the fits with the extended model converged, they never converged with a positive-definite error matrix. Thus it is not possible to give accurate statistical uncertainties. This is due to the number of parameters, and is another important reason for needing to have a Λ^* model with less parameters as the default.

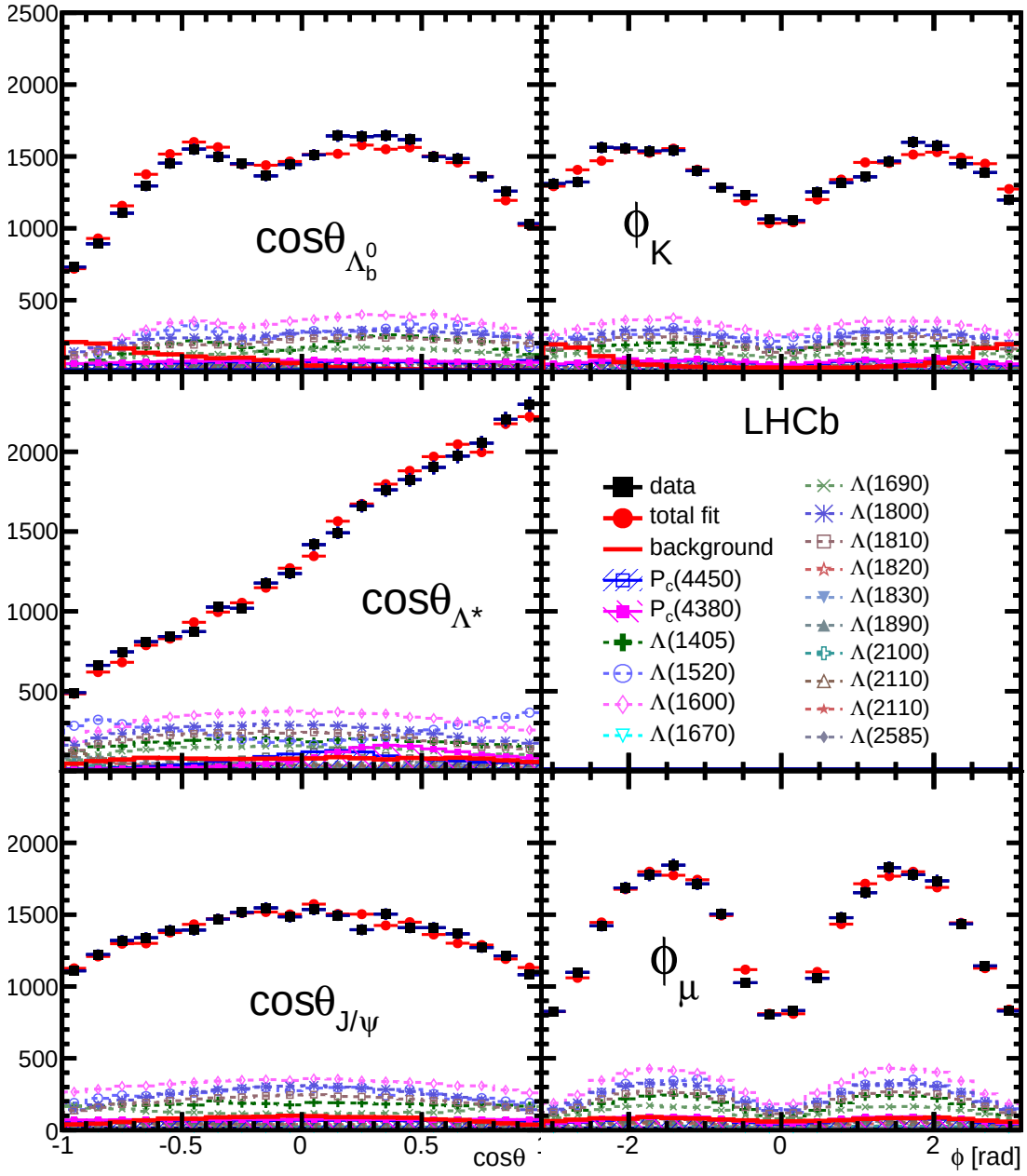

Figure 112: Fit projections of the extended Λ^* model with two P_c^+ states onto the decay angular distributions. The data are shown as (black) squares, while the (red) circles show the results of the fit. Each fit component is also shown. The angles are defined in Sec. 5.2.

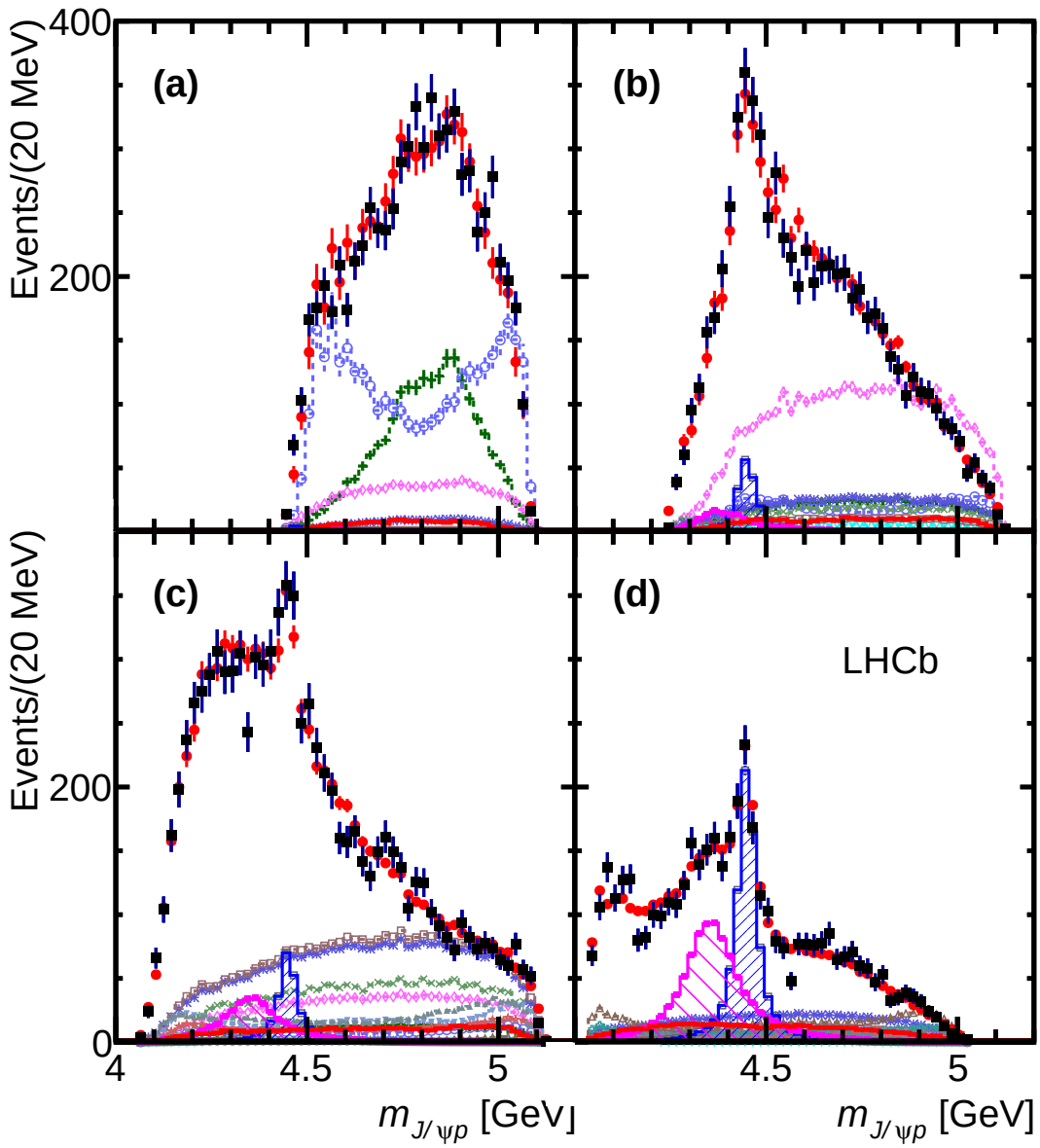

Figure 113: Fit projections of the extended Λ^* model with two P_c^+ states onto $m_{J/\psi p}$ for various intervals of m_{Kp}: (a) $m_{Kp} < 1.55$ GeV, (b) $1.55 < m_{Kp} < 1.70$ GeV, (c) $1.70 < m_{Kp} < 2.00$ GeV, an d (d) $m_{Kp} > 2.00$ GeV. The data are shown as (black) squares with error bars, while the (red) circles show the results of the fit. The blue and purple histograms show the two P_c^+ states. See Fig. 47 for the legend.

E *sFit* Results

The fit results obtained with the *sFit* method (Sec. 6.3) are given here. The attempt to fit the data with no P_c states is shown, followed by the attempts with a single P_c state. Next the fit results are shown with the default Λ^* model and two P_c states, and compared to the results obtained with the default *cFit* method. For completeness, the results with the extended Λ^* model and two P_c states are then shown.

E.1 Extended model, no P_c states

As with the *cFit* method, attempts were first made to fit the data with the extended Λ^* model and no P_c states. The projections onto m_{Kp} and $m_{J/\psi p}$ are shown in Fig. 114. As was the case with the *cFit* method (Sec. 8.1), the m_{Kp} distribution is described well by the fit, but the $m_{J/\psi p}$ distribution is described very poorly. Again, the Λ^* states show no ability to reproduce the peaking structure. The different angular distributions are

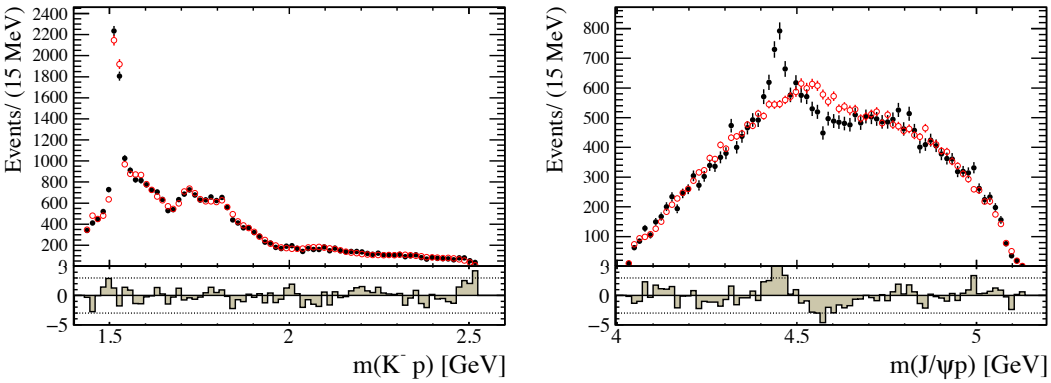

Figure 114: (*sFit*) Results of the extended Λ^* model for (a) m_{Kp} and (b) $m_{J/\psi p}$. The data are shown as (black) squares with error bars, while the open (red) circles show the projection of the fit. The error bars on the points showing the fit results are due to simulation statistics.

shown in Fig. 115. They also agree nicely with the data. The projections onto the $m_{J/\psi p}$ distribution in various bins of m_{Kp} are shown in Fig. 116. As with *cFit*, there is an inability to describe the data in the region of 4450 MeV throughout the range of m_{Kp} values.

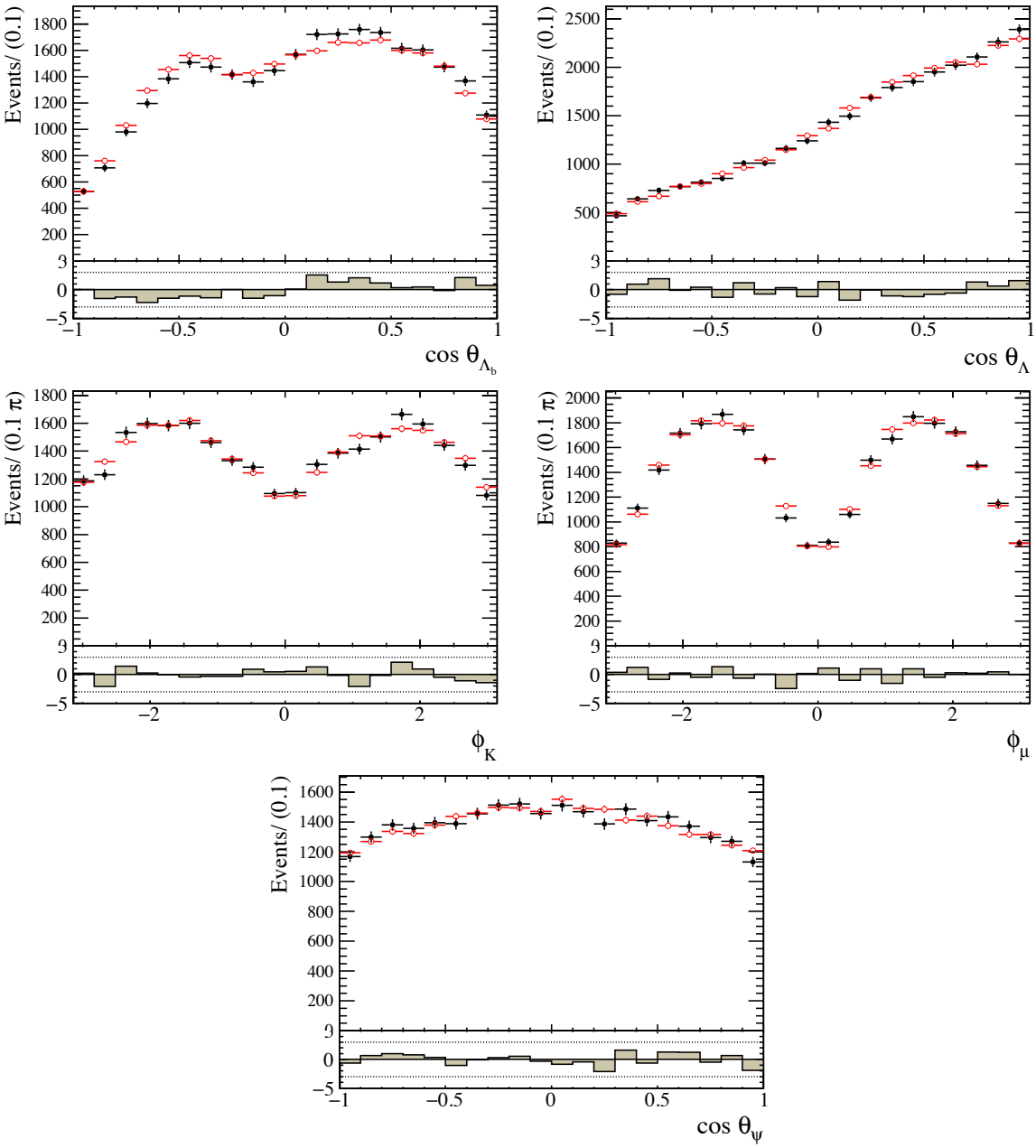

Figure 115: (*sFit*) Results of the extended Λ^* model for the different decay angular distributions. The data are shown as (black) squares, while the open (red) circles show the results of the fit. The angles are defined in Sec. 5.2.

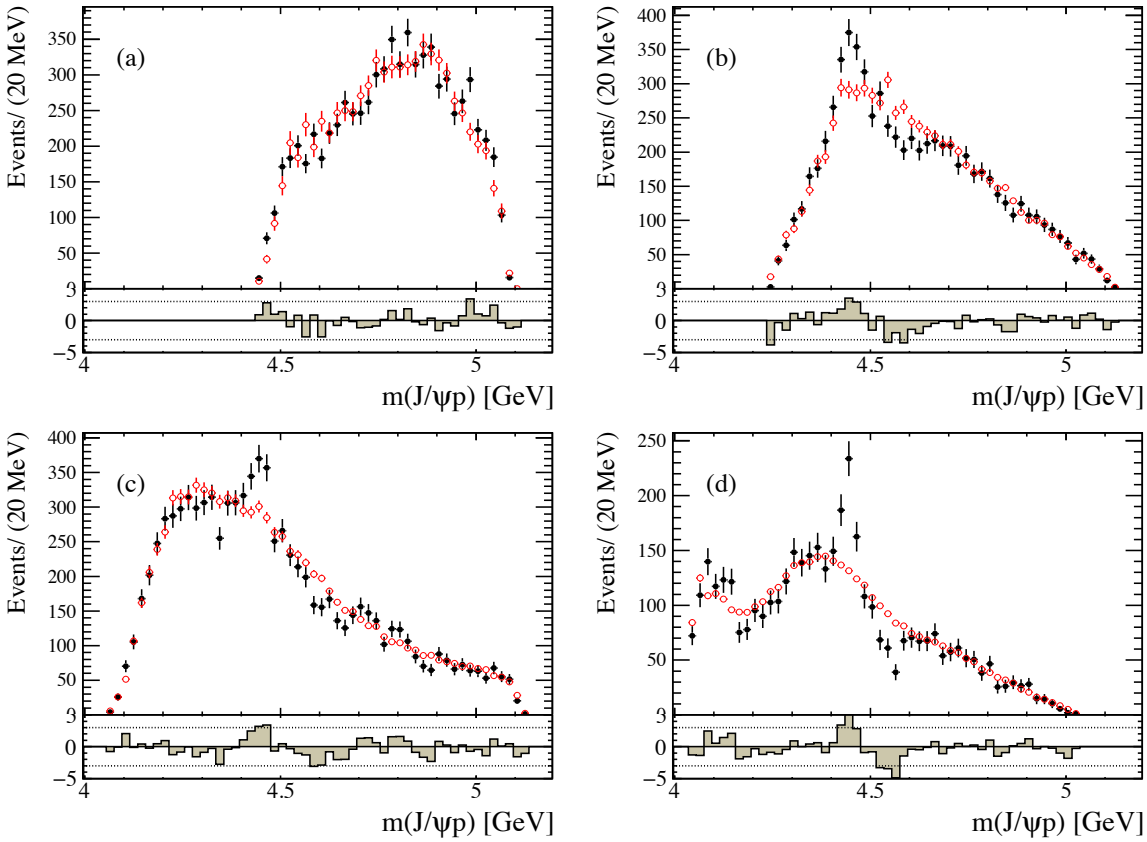

Figure 116: (*sFit*) Results of the extended Λ^* for $m_{J/\psi p}$ in various intervals of m_{Kp}: (a) $m_{Kp} < 1.55$ GeV, (b) $1.55 < m_{Kp} < 1.70$ GeV, (c) $1.70 < m_{Kp} < 2.00$ GeV, and (d) $m_{Kp} > 2.00$ GeV. The data are shown as (black) squares with error bars, while the open (red) circles show the results of the fit.

E.2 Extended model, one P_c state

Here the efforts are shown to fit the data with the extended Λ^* model and a single P_c state. Fits were performed with J^P values of $1/2^{\pm}$, $3/2^{\pm}$ and $5/2^{\pm}$. The best fit was obtained with the $3/2^+$ state. Figure 117 shows the fit projections onto the m_{Kp} and $m_{J/\psi p}$ distributions for the $J^P = 3/2^+$ best fit. Of course, the m_{Kp} distribution remains well-described. As with the *cFit* method, the $m_{J/\psi p}$ description improves somewhat, but the description of the data is still severly inadequate.

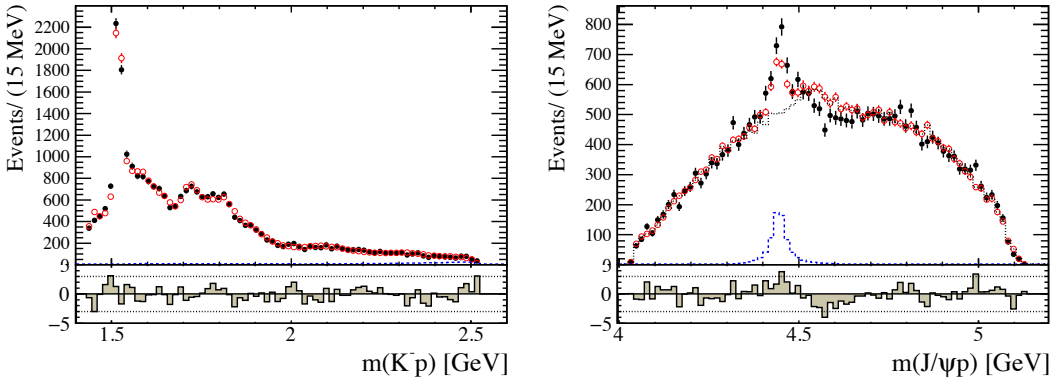

Figure 117: (*sFit*) Results of the extended Λ^* model with a $J^P = 3/2^+$ P_c for (a) m_{Kp} and (b) $m_{J/\psi p}$. The data are shown as (black) squares with error bars, while the open (red) circles show the projection of the fit. The total Λ^* contribution is shown with the dashed grey line, and the P_c contribution with the dashed blue line. The error bars on the points showing the fit results are due to simulation statistics.

The angular distributions are shown in Fig. 118. As usual, the fit is in good agreement with the data. The $m_{J/\psi p}$ mass distribution is shown in various bins of m_{Kp} in Fig. 119. The discrepancy between the fit and the peaking structures in $m_{J/\psi p}$ is much less than in the fit without a P_c, though the $1.55 < m_{Kp} < 1.70$ GeV interval is still poorly described. Thus again, the behavior mirrors that seen with the *cFit* method.

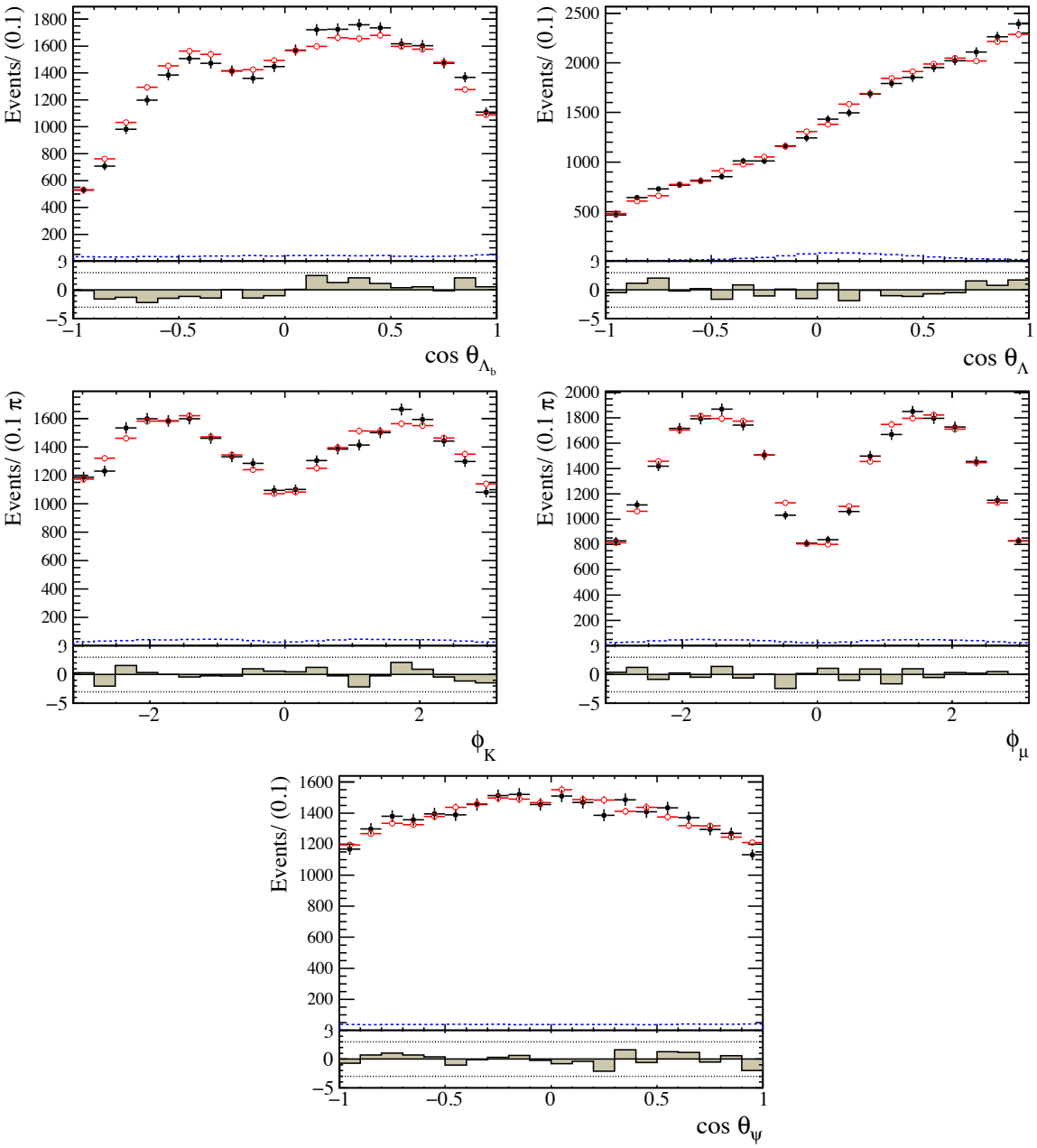

Figure 118: (*sFit*) Results of the extended Λ^* model with a $J^P = 3/2^+$ P_c for the different decay angular distributions. The data are shown as (black) squares, while the open (red) circles show the results of the fit. The total Λ^* contribution is shown with the dashed grey line, and the P_c contribution with the dashed blue line. The angles are defined in Sec. 5.2.

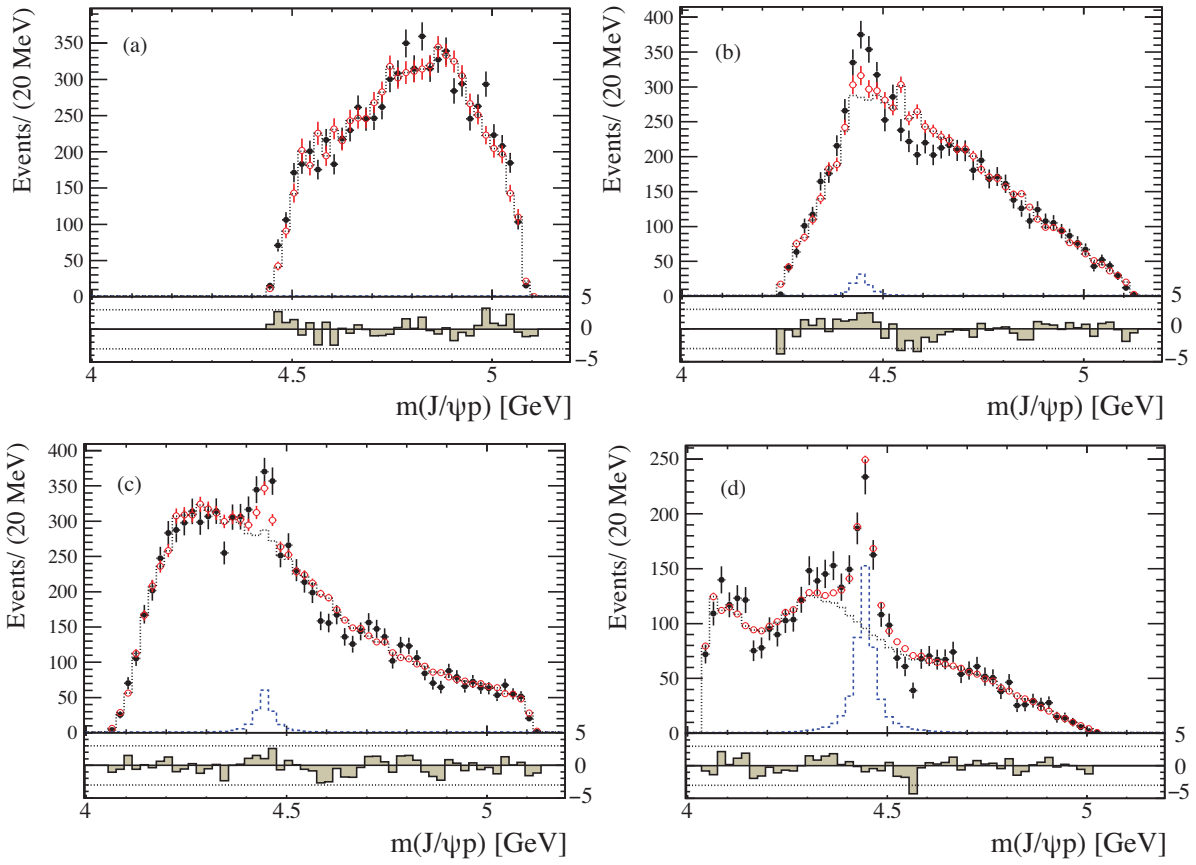

Figure 119: (*sFit*) Results of the extended Λ^* with a $J^P = 3/2^+$ P_c for $m_{J/\psi p}$ in various intervals of m_{Kp}: (a) $m_{Kp} < 1.55$ GeV, (b) $1.55 < m_{Kp} < 1.70$ GeV, (c) $1.70 < m_{Kp} < 2.00$ GeV, and (d) $m_{Kp} > 2.00$ GeV. The data are shown as (black) squares with error bars, while the open (red) circles show the results of the fit. The total Λ^* contribution is shown with the dashed grey line, and the P_c contribution with the dashed blue line.

E.3 Default model results

Clearly the same conclusion was also reached with *sFit*: the data can't be described with the extended Λ^* model and a single P_c state. The fit results are shown in this section for the default Λ^* model with a $3/2^-$ and a $5/2^+$ P_c state. Figure 120 shows the projections onto both the m_{Kp} and $m_{J/\psi p}$ distributions. The angular distributions and the $m_{J/\psi p}$

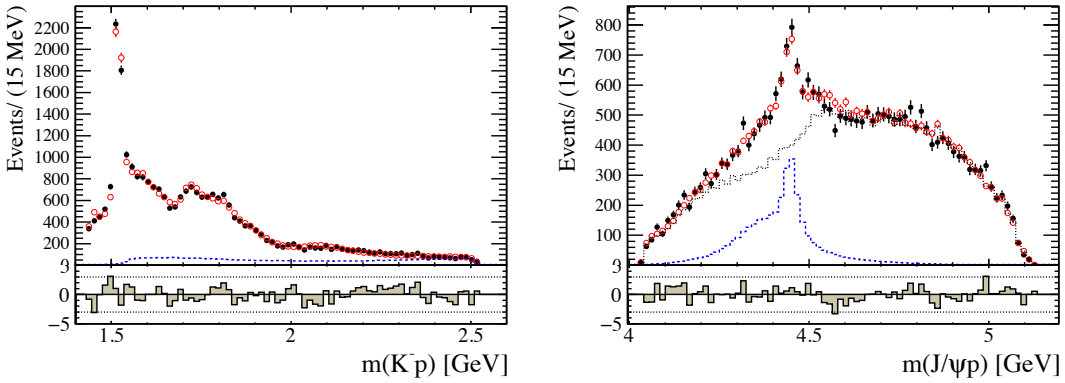

Figure 120: (*sFit*) Results of the default Λ^* and two P_c states with J^P quantum numbers of $3/2^-$ and $5/2^+$ for (a) m_{Kp} and (b) $m_{J/\psi p}$. The data are shown as (black) squares with error bars, while the open (red) circles show the projection of the fit. The total Λ^* contribution is shown with the dashed grey line, and the total P_c contribution with the dashed blue line. The error bars on the points showing the fit results are due to simulation statistics.

mass distributions in bins of m_{Kp} are shown in Fig. 121 and Fig. 122, respectively. Good agreement is seen with the data in all projections.

For $P_c(4380)$ the fit returns a mass and width of 4375 ± 8 MeV and 194 ± 16 MeV, respectively, while for $P_c(4450)$ the mass and width were found to be 4448.8 ± 1.7 MeV and 41 ± 5 MeV, respectively. These values are listed alongside those obtained with *cFit* in Tab 27. Also given in the table is a comparison of the fit fractions for each of the resonant components. Overall good agreement is seen in these as well.

The quantum number study was also done with *sFit*. Table 28 shows the changes in $-2\ln\mathcal{L}$ and P_c parameters for the different opposite parity quantum number combinations. In this case, the parity reversed $(3/2^+, 5/2^-)$ is slightly preferred over $(3/2^-, 5/2^+)$. As there is not very good discrimination between quantum number hypotheses in the *cFit* method or the *sFit* method, it is not surprising that there is some disagreement. There is fairly good agreement though, in that the same trends are seen in which the spins 3/2

Table 27: Comparison of P_c parameters and fit fractions of the resonant components which were obtained with *cFit* and *sFit* using the default Λ^* model with the two P_c's having quantum numbers $J^P(P_c(4380), P_c(4450)) = (3/2^-, 5/2^+)$.

Particle	*cFit*	*sFit*
	Mass (MeV)	
$P_c(4450)$	4449.8 ± 1.7	4448.8 ± 1.7
$P_c(4380)$	4380 ± 8	4375 ± 8
	Width (MeV)	
$P_c(4450)$	39 ± 5	41 ± 5
$P_c(4380)$	205 ± 18	194 ± 16
	Fit fraction (%)	
$P_c(4450)$	4.09 ± 0.48	4.10 ± 0.45
$P_c(4380)$	8.42 ± 0.68	7.96 ± 0.67
$\Lambda^*(1405)$	14.64 ± 0.72	14.19 ± 0.67
$\Lambda^*(1520)$	18.93 ± 0.52	19.06 ± 0.47
$\Lambda^*(1600)$	23.50 ± 1.48	24.42 ± 1.36
$\Lambda^*(1670)$	1.47 ± 0.49	1.53 ± 0.50
$\Lambda^*(1690)$	8.66 ± 0.90	8.60 ± 0.85
$\Lambda^*(1800)$	18.21 ± 2.27	16.97 ± 2.20
$\Lambda^*(1810)$	17.88 ± 2.11	17.29 ± 1.85
$\Lambda^*(1820)$	2.32 ± 0.69	2.32 ± 0.65
$\Lambda^*(1830)$	1.76 ± 0.58	2.00 ± 0.53
$\Lambda^*(1890)$	3.96 ± 0.43	3.97 ± 0.38
$\Lambda^*(2100)$	1.65 ± 0.29	1.94 ± 0.28
$\Lambda^*(2110)$	1.62 ± 0.32	1.44 ± 0.28

and 5/2 are preferred.

Table 28: (*sFit*) Changes in fit quality ($-2\ln\mathcal{L}$), masses, and widths of different J^P combinations with respect to the ($3/2^-$, $5/2^+$) solution.

		$P_c(4380)$		$P_c(4450)$	
$J^p(4380, 4450)$	$-2\ln\mathcal{L}$	M_0	Γ_0	M_0	Γ_0
$3/2^-$, $5/2^+$ Values					
$\frac{3}{2}^-$, $\frac{5}{2}^+$	–	4375 ± 8	194 ± 16	4448.8 ± 1.7	42 ± 5
Δ from $3/2^-2$, $5/2^+$					
$\frac{3}{2}^+$, $\frac{5}{2}^-$	-2.8^2	-8	9	0.5	7
$\frac{3}{2}^-$, $\frac{5}{2}^+$	–	–	–	–	–
$\frac{5}{2}^+$, $\frac{3}{2}^-$	$+0.8^2$	-3	38	-0.8	4
$\frac{3}{2}^+$, $\frac{3}{2}^-$	$+4.4^2$	-28	-35	-2.1	9
$\frac{3}{2}^-$, $\frac{3}{2}^+$	$+4.8^2$	-17	-18	-2.1	-3
$\frac{1}{2}^-$, $\frac{3}{2}^+$	$+4.8^2$	-8	44	-2.1	-6
$\frac{7}{2}^+$, $\frac{5}{2}^-$	$+5.6^2$	25	253	-1.7	4
$\frac{7}{2}^-$, $\frac{5}{2}^+$	$+6.2^2$	-32	-47	-2.8	8
$\frac{5}{2}^-$, $\frac{3}{2}^+$	$+6.4^2$	-15	-25	-2.1	10
$\frac{1}{2}^-$, $\frac{1}{2}^+$	$+6.7^2$	-25	-25	-4.3	4
$\frac{5}{2}^+$, $\frac{5}{2}^-$	$+6.8^2$	-28	-31	-3.2	-2
$\frac{7}{2}^+$, $\frac{3}{2}^-$	$+7.6^2$	-40	-43	-5.7	23
$\frac{1}{2}^+$, $\frac{3}{2}^-$	$+7.8^2$	-37	-102	-8.7	35
$\frac{7}{2}^+$, $\frac{1}{2}^-$	$+7.9^2$	-30	21	-4.8	15
$\frac{1}{2}^-$, $\frac{5}{2}^+$	$+7.9^2$	-8	4	-1.7	-8
$\frac{5}{2}^-$, $\frac{5}{2}^+$	$+8.0^2$	-25	-37	-2.9	1
$\frac{1}{2}^+$, $\frac{1}{2}^-$	$+8.3^2$	-48	-74	-3.5	19
$\frac{5}{2}^-$, $\frac{7}{2}^+$	$+8.3^2$	-2	22	-0.2	-9
$\frac{1}{2}^-$, $\frac{7}{2}^+$	$+8.9^2$	-10	-4	-1.2	-2
$\frac{7}{2}^-$, $\frac{1}{2}^+$	$+9.0^2$	-35	-41	-4.3	16
$\frac{5}{2}^+$, $\frac{7}{2}^-$	$+9.0^2$	3	54	-0.5	-3
$\frac{7}{2}^+$, $\frac{7}{2}^-$	$+9.1^2$	25	168	-2.9	-5
$\frac{5}{2}^-$, $\frac{1}{2}^+$	$+9.2^2$	-2	50	-4.1	-0
$\frac{1}{2}^+$, $\frac{5}{2}^-$	$+9.2^2$	-20	-3	-1.6	6
$\frac{3}{2}^-$, $\frac{1}{2}^+$	$+9.3^2$	-16	-17	-4.1	4
$\frac{3}{2}^+$, $\frac{7}{2}^-$	$+9.4^2$	-23	-11	-1.4	-3
$\frac{7}{2}^-$, $\frac{3}{2}^+$	$+9.6^2$	-48	-102	-5.1	18
$\frac{3}{2}^+$, $\frac{1}{2}^-$	$+10.1^2$	-34	-53	-5.6	24
$\frac{3}{2}^-$, $\frac{7}{2}^+$	$+10.1^2$	-5	10	-1.2	-4
$\frac{5}{2}^+$, $\frac{1}{2}^-$	$+10.9^2$	-35	-53	-4.6	16
$\frac{1}{2}^+$, $\frac{7}{2}^-$	$+11.1^2$	-12	27	-0.9	-4
$\frac{7}{2}^-$, $\frac{7}{2}^+$	$+11.1^2$	-36	-76	-3.2	7

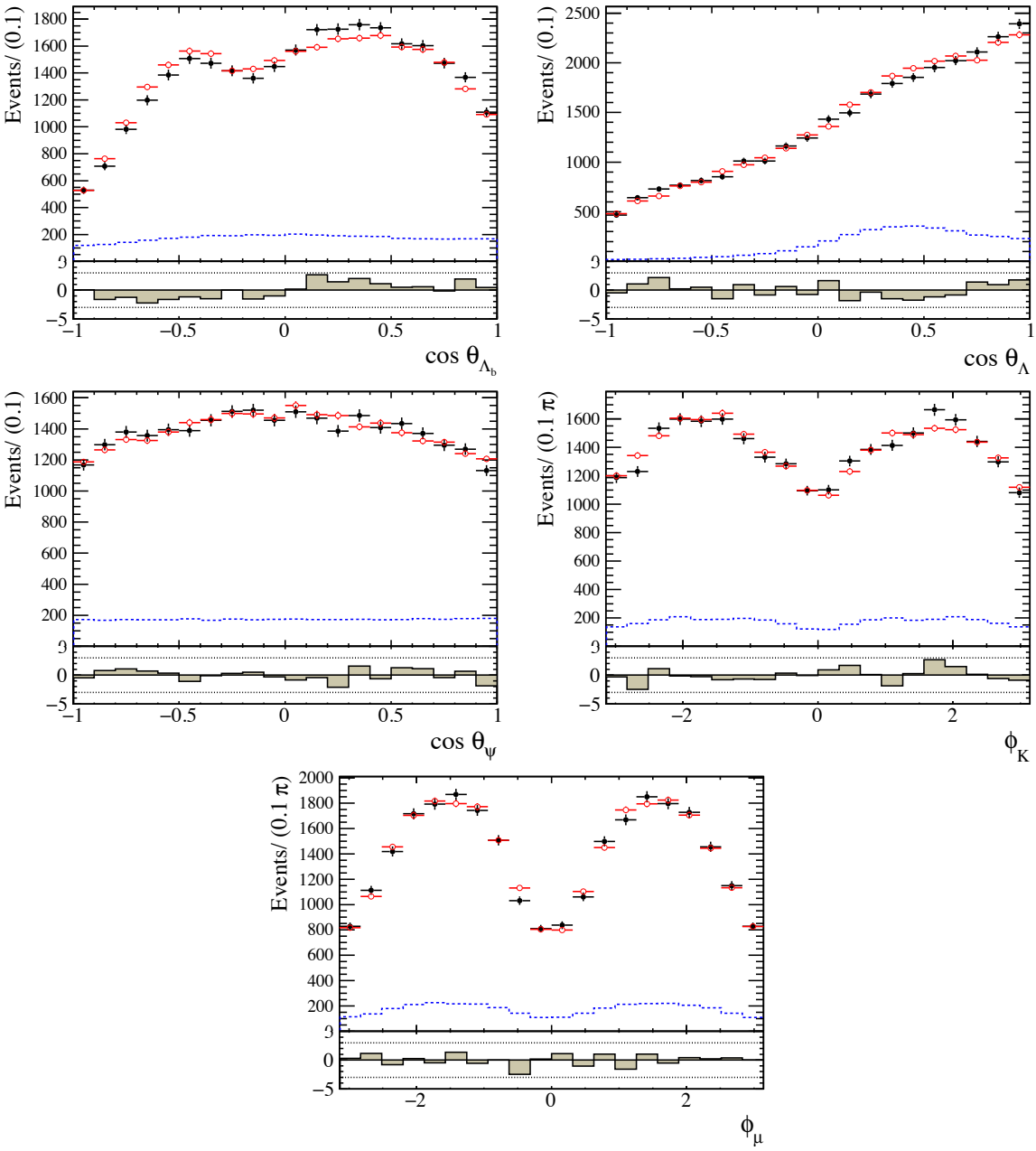

Figure 121: (*sFit*) Results of the default Λ^* and two P_c states with J^P quantum numbers of $3/2^-$ and $5/2^+$ for the different decay angular distributions. The data are shown as (black) squares, while the open (red) circles show the results of the fit. The total Λ^* contribution is shown with the dashed grey line, and the total P_c contribution with the dashed blue line. The angles are defined in Sec. 5.2.

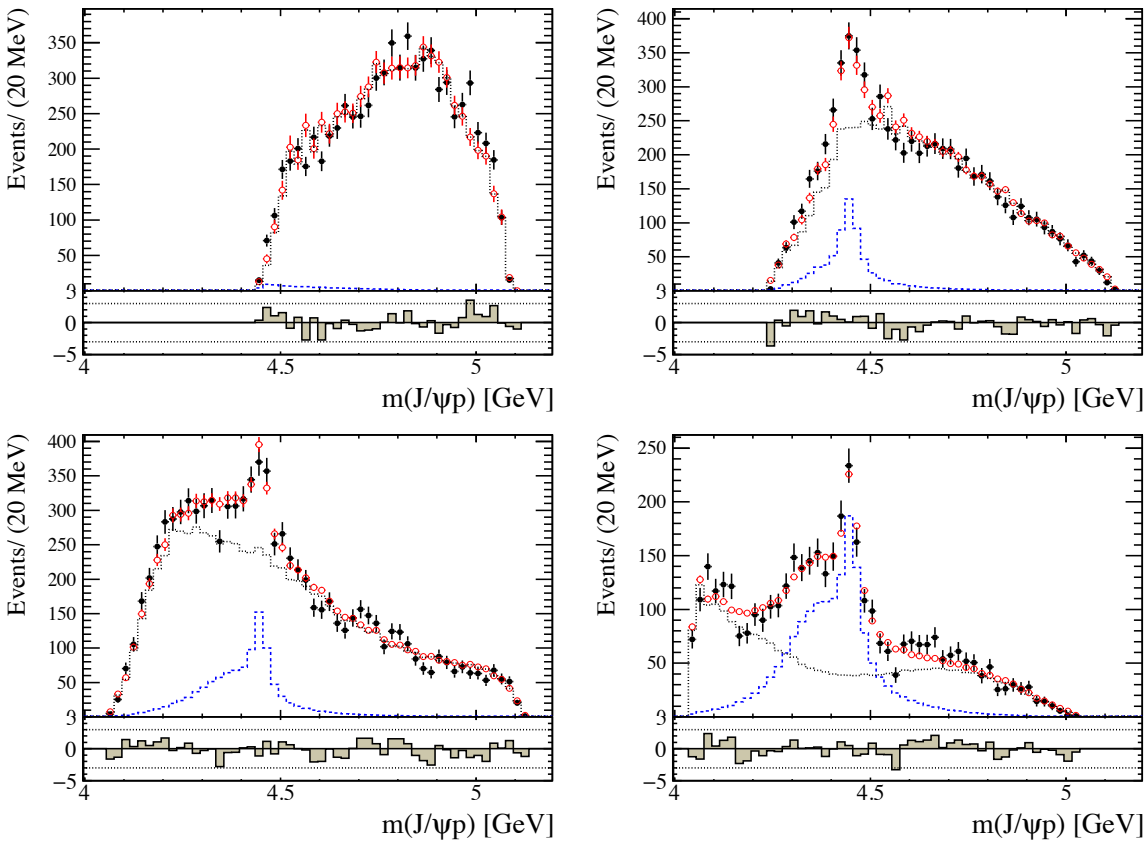

Figure 122: (*sFit*) Results of the default Λ^* and two P_c states with J^P quantum numbers of $3/2^-$ and $5/2^+$ for $m_{J/\psi p}$ in various intervals of m_{Kp}: (a) $m_{Kp} < 1.55$ GeV, (b) $1.55 < m_{Kp} < 1.70$ GeV, (c) $1.70 < m_{Kp} < 2.00$ GeV, and (d) $m_{Kp} > 2.00$ GeV. The data are shown as (black) squares with error bars, while the open (red) circles show the results of the fit. The total Λ^* contribution is shown with the dashed grey line, and the total P_c contribution with the dashed blue line.

E.4 Extended model, two P_c states

For completeness, the fit results obtained with the extended Λ^* model and two P_c states are shown here. Figure 123 shows the projections onto m_{Kp} and $m_{J/\psi p}$, where a good description of the data is seen in both. The angular distributions and $m_{J/\psi p}$ mass distri-

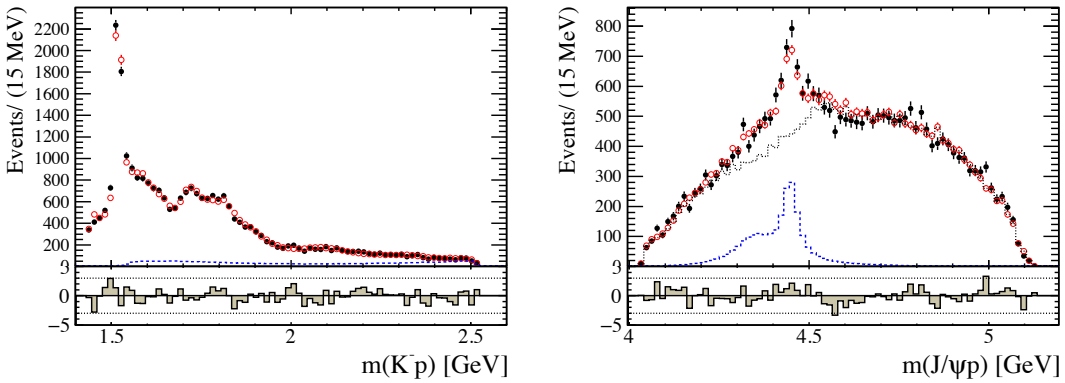

Figure 123: (*sFit*) Results of the extended Λ^* and two P_c states with J^P quantum numbers of $3/2^-$ and $5/2^+$ for (a) m_{Kp} and (b) $m_{J/\psi p}$. The data are shown as (black) squares with error bars, while the open (red) circles show the projection of the fit. The total Λ^* contribution is shown with the dashed grey line, and the total P_c contribution with the dashed blue line. The error bars on the points showing the fit results are due to simulation statistics.

bution in bins of m_{Kp} are shown in Fig. 124 and Fig. 125, respectively. Good agreement is seen.

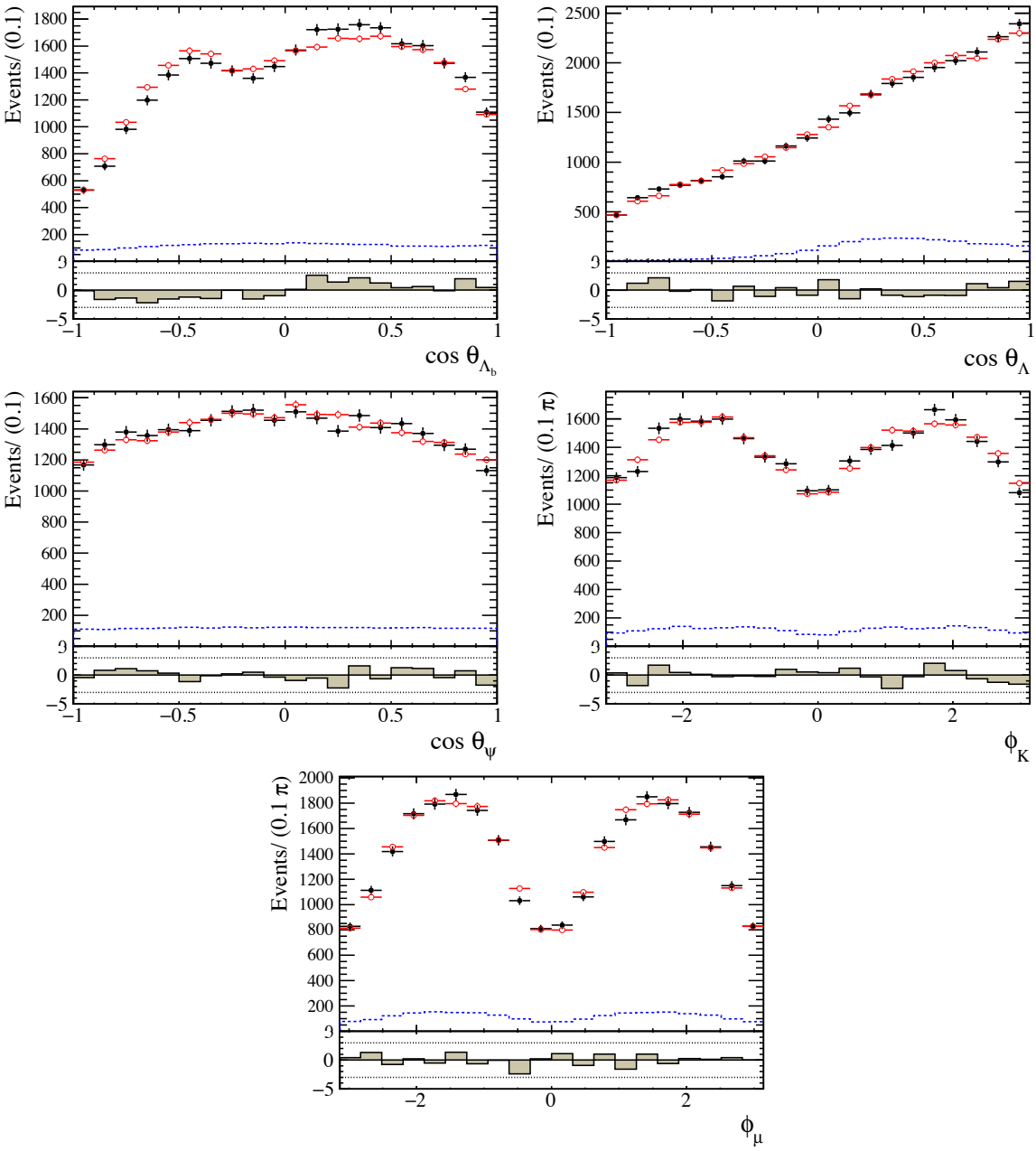

Figure 124: (*sFit*) Results of the extended Λ^* and two P_c states with J^P quantum numbers of $3/2^-$ and $5/2^+$ for the different decay angular distributions. The data are shown as (black) squares, while the open (red) circles show the results of the fit. The total Λ^* contribution is shown with the dashed grey line, and the total P_c contribution with the dashed blue line. The angles are defined in Sec. 5.2.

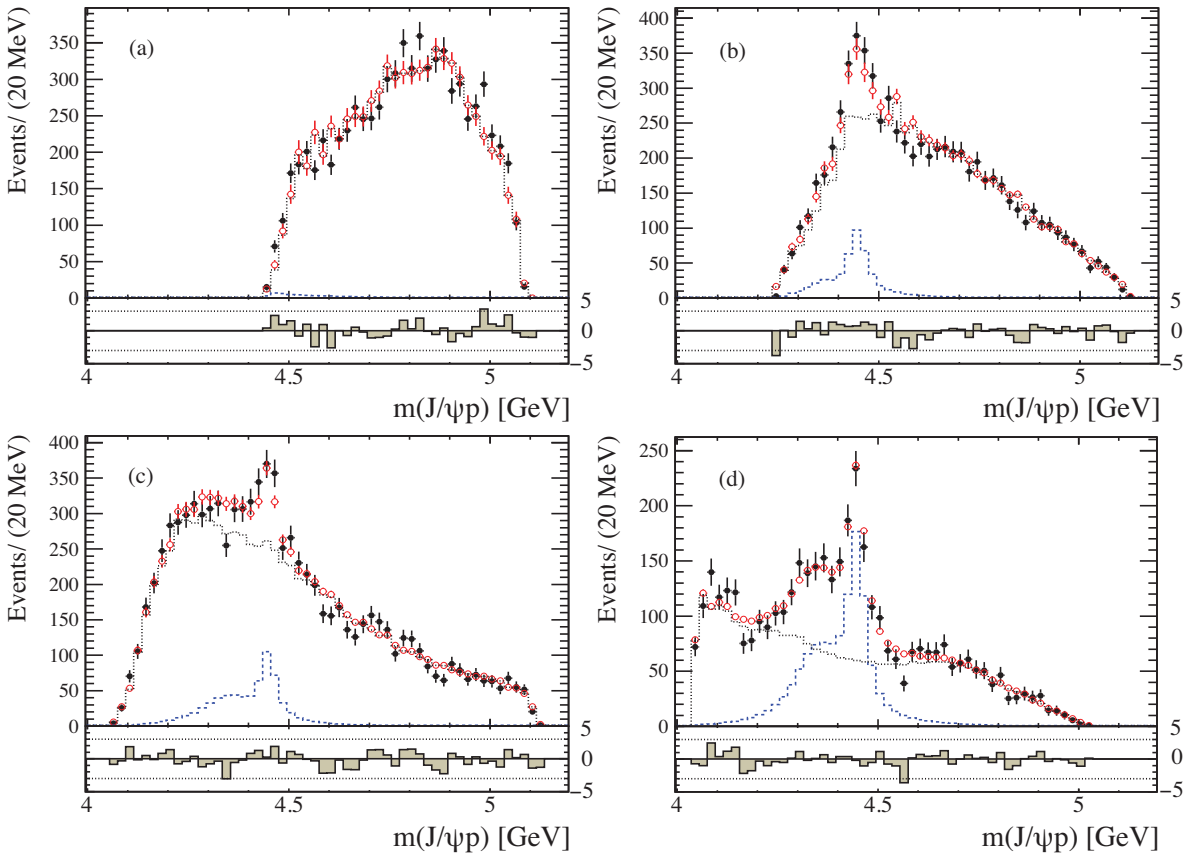

Figure 125: (*sFit*) Results of the extended Λ^* and two P_c states with J^P quantum numbers of $3/2^-$ and $5/2^+$ for $m_{J/\psi p}$ in various intervals of m_{Kp}: (a) $m_{Kp} < 1.55$ GeV, (b) $1.55 < m_{Kp} < 1.70$ GeV, (c) $1.70 < m_{Kp} < 2.00$ GeV, and (d) $m_{Kp} > 2.00$ GeV. The data are shown as (black) squares with error bars, while the open (red) circles show the results of the fit. The total Λ^* contribution is shown with the dashed grey line, and the total P_c contribution with the dashed blue line.

F Same parity fits

It was pointed out in Sec. 11 that two states with the same parity could not produce the asymmetric $\cos\theta_{P_c}$ distribution necessary to obtain good fits to the data. Nevertheless, the fits with same-parity combinations were performed. The results are listed in Table 29.

The fit with the smallest $\Delta(-2\ln\mathcal{L})$ is considerably worse than the nominal fit with $J^P(P_c(4380), P_c(4450)) = (3/2^-, 5/2^+)$. Furthermore, it does not describe the $m_{J/\psi p}$ distribution well as can be seen in Fig. 126. Indeed, the expected behavior is seen: the fit fractions of the states are prevented from growing enough to fill in the peak because doing so would cause the $\cos\theta_{P_c}$ distribution of the data to be vastly overshot at low values.

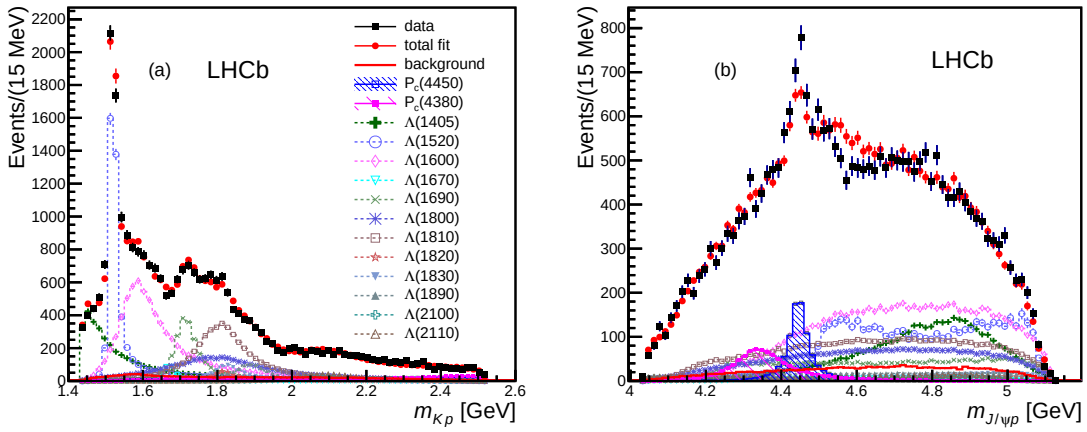

Figure 126: Fit projections of the default Λ^* model with two P_c states of quantum numbers $(5/2^+, 3/2^+)$ onto the (a) m_{Kp} and (b) $m_{J/\psi p}$ distributions. The data are shown as solid (black) squares, while the solid (red) points show the results of the fit. The solid (red) histogram shows the background distribution. The (blue) open squares with the shaded histogram represent the $P_c(4450)^+$ state, and the shaded histogram topped with (purple) filled squares represents the $P_c(4380)^+$ state. Each Λ^* component is also shown. The error bars on the points showing the fit results are due to simulation statistics.

Table 29: Changes in fit quality ($(\sqrt{-2\ln\mathcal{L}})^2$) and $P_c(4380)$ and $P_c(4450)$ mass and width from the baseline two P_c fit for different combinations of J^P states with the same parity.

		$P_c(4380)$		$P_c(4450)$	
$J^p(4380, 4450)$	$(\sqrt{-2\ln\mathcal{L}})^2$	M_0	Γ_0	M_0	Γ_0
Nominal Values					
$\frac{3}{2}^-, \frac{5}{2}^+$	–	4380	205	4449.8	39
Δ from Nominal					
$\frac{5}{2}^+, \frac{3}{2}^+$	5.1^2	−34	−57	−4.2	9
$\frac{3}{2}^-, \frac{3}{2}^-$	5.4^2	−49	−81	−6.5	19
$\frac{5}{2}^+, \frac{1}{2}^+$	5.9^2	−35	−52	−3.5	6
$\frac{3}{2}^+, \frac{1}{2}^+$	6.4^2	−43	−70	−5.1	15
$\frac{5}{2}^-, \frac{1}{2}^-$	6.7^2	−38	−43	−4.7	21
$\frac{7}{2}^-, \frac{3}{2}^-$	6.9^2	−27	−46	−5.8	18
$\frac{1}{2}^-, \frac{3}{2}^-$	7.3^2	−43	−68	−4.8	13
$\frac{5}{2}^-, \frac{7}{2}^-$	7.7^2	−23	−12	−3.4	1
$\frac{3}{2}^-, \frac{1}{2}^-$	7.7^2	−14	1	−2.3	−2
$\frac{5}{2}^-, \frac{3}{2}^-$	7.8^2	−43	−87	−5.7	14
$\frac{5}{2}^+, \frac{7}{2}^+$	8.2^2	−36	−60	−3.1	7
$\frac{1}{2}^-, \frac{1}{2}^-$	8.3^2	−16	23	1.6	1
$\frac{7}{2}^+, \frac{3}{2}^+$	8.3^2	79	586	−4.6	4
$\frac{7}{2}^-, \frac{1}{2}^-$	8.4^2	−36	−54	−3.4	22
$\frac{1}{2}^-, \frac{5}{2}^-$	8.4^2	−14	−15	−3.4	−1
$\frac{3}{2}^-, \frac{7}{2}^-$	8.4^2	−25	−28	−2.4	1
$\frac{5}{2}^+, \frac{5}{2}^+$	8.5^2	−47	−108	−4.5	14
$\frac{3}{2}^-, \frac{5}{2}^-$	8.8^2	−23	−34	−2.9	2
$\frac{7}{2}^-, \frac{7}{2}^-$	9.3^2	−25	15	5.0	4
$\frac{5}{2}^-, \frac{5}{2}^-$	9.3^2	−40	−53	−2.1	9
$\frac{1}{2}^-, \frac{7}{2}^-$	9.4^2	−2	0	−1.8	−10
$\frac{7}{2}^-, \frac{5}{2}^-$	9.6^2	−43	−103	−5.0	12
$\frac{7}{2}^+, \frac{1}{2}^+$	9.7^2	3	98	−5.4	5
$\frac{3}{2}^+, \frac{5}{2}^+$	9.8^2	−20	−23	−2.9	0
$\frac{1}{2}^+, \frac{5}{2}^+$	9.9^2	−33	−45	−4.1	10
$\frac{1}{2}^+, \frac{1}{2}^+$	9.9^2	−23	5	0.1	5
$\frac{3}{2}^+, \frac{3}{2}^+$	10.1^2	−46	−84	−4.5	13
$\frac{3}{2}^+, \frac{7}{2}^+$	10.4^2	−20	−36	−3.2	−3
$\frac{7}{2}^+, \frac{5}{2}^+$	10.8^2	9	89	−3.4	4
$\frac{1}{2}^+, \frac{3}{2}^+$	11.0^2	−18	−5	−3.1	7
$\frac{7}{2}^+, \frac{7}{2}^+$	11.0^2	121	768	2.9	−5
$\frac{1}{2}^+, \frac{7}{2}^+$	11.2^2	−20	−35	−1.5	0

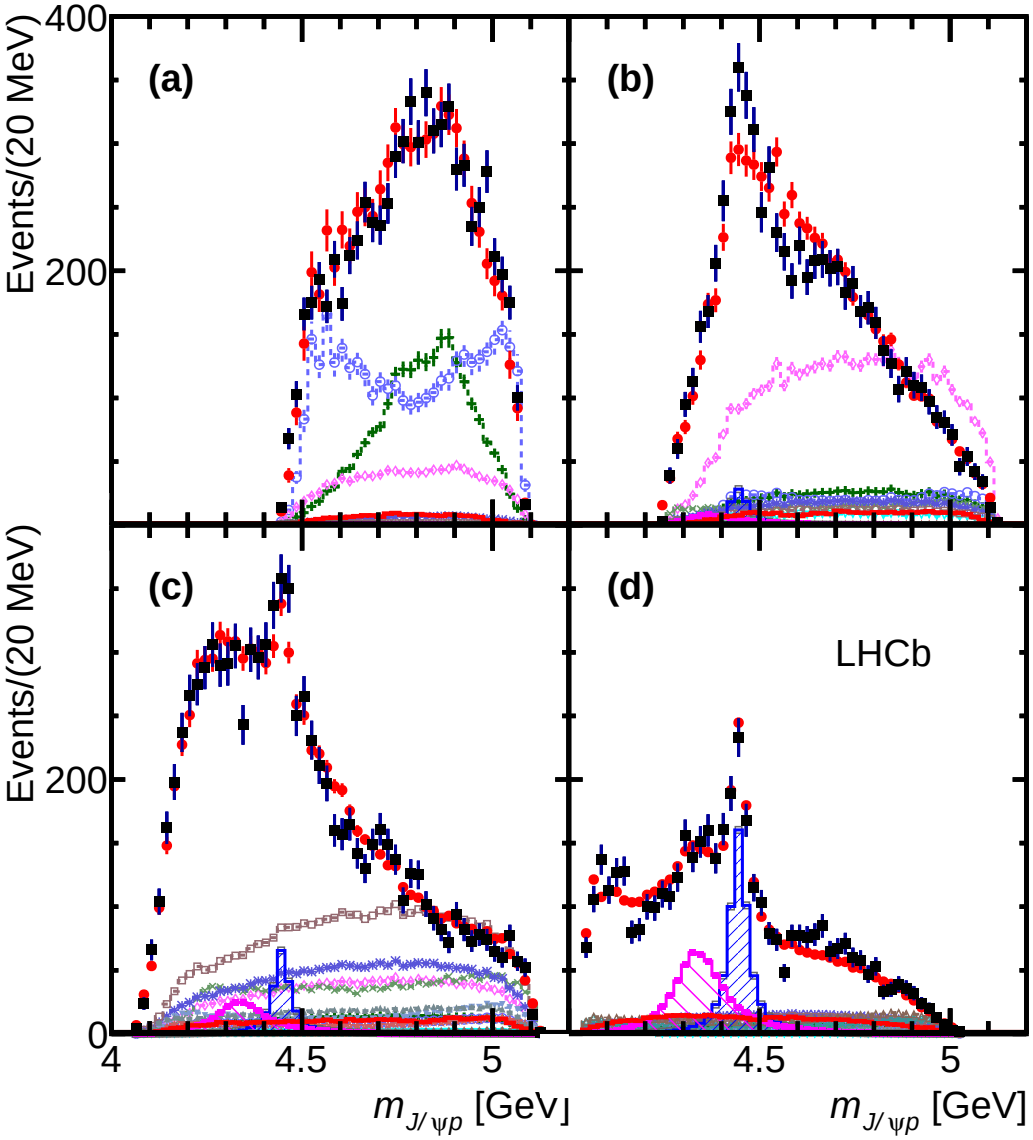

Figure 127: Fit projections of the default Λ^* model with two P_c states of quantum numbers $(5/2^+, 3/2^+)$ onto $m_{J/\psi p}$ for various intervals of m_{Kp}: (a) $m_{Kp} < 1.55$ GeV, (b) $1.55 < m_{Kp} < 1.70$ GeV, (c) $1.70 < m_{Kp} < 2.00$ GeV, an d (d) $m_{Kp} > 2.00$ GeV. The data are shown as (black) squares with error bars, while the (red) circles show the results of the fit. The blue and purple histograms show the two P_c^+ states. See Fig. 47 for the legend.

G Amplitude model based on the default fit

In this section, the numerical values are listed for all parameters obtained by the fit to the data with the default Λ^* model and two P_c states with J^P assignment of $3/2^-$ and $5/2^+$. The results are shown in Tables 31-33. The parameters without error bars were fixed in the fit. The correlation coefficients among the P_c masses and widths are shown in Table 30.

Table 30: Correlations coefficients between the P_c^+ parameters.

	$\Gamma_0(4380)$	$M_0(4380)$	$\Gamma_0(4450)$	$M_0(4450)$
$\Gamma_0(4380)$	1.000	0.272	-0.035	-0.047
$M_0(4380)$		1.000	-0.396	0.125
$\Gamma_0(4450)$			1.000	-0.073
$M_0(4450)$				1.000

Table 31: Amplitude model based on the default fit to the data - Part I

Resonance	J^P	M_0 MeV	Γ_0 MeV	$B_{L,S}$ couplings	
$P_c^+(4380)$	$3/2^-$	4380.0±8.2	205.0±17.5	$B^{\Lambda_b^0\to P_cK}_{1,\frac{3}{2}}$	$(1,0)$
				$B^{\Lambda_b^0\to P_cK}_{2,\frac{3}{2}}$	$(+0.196\pm0.078, -0.302\pm0.086)$
				$B^{P_c\to\psi p}_{0,\frac{3}{2}}$	$(-0.023\pm0.027, -1.393\pm0.022)$
				$B^{P_c\to\psi p}_{2,\frac{1}{2}}$	$(+0.181\pm0.149, +0.291\pm0.112)$
				$B^{P_c\to\psi p}_{2,\frac{3}{2}}$	$(+0.895\pm0.228, +0.811\pm0.198)$
$P_c^+(4450)$	$5/2^+$	4449.8±1.7	38.6±4.7	$B^{\Lambda_b^0\to P_cK}_{2,\frac{5}{2}}$	$(1,0)$
				$B^{\Lambda_b^0\to P_cK}_{3,\frac{5}{2}}$	$(-0.251\pm0.127, -0.595\pm0.154)$
				$B^{P_c\to\psi p}_{1,\frac{3}{2}}$	$(-7.465\pm2.678, +11.44\pm2.826)$
				$B^{P_c\to\psi p}_{3,\frac{1}{2}}$	$(+0.438\pm2.038, -7.096\pm1.866)$
				$B^{P_c\to\psi p}_{3,\frac{3}{2}}$	$(-4.156\pm2.781, -11.27\pm2.022)$
$\Lambda^*(1405)$	$1/2^-$	1405.1	50.5	$B^{\Lambda_b^0\to\Lambda^*\psi}_{0,\frac{1}{2}}$	$(+0.051\pm0.014, -0.102\pm0.013)$
				$B^{\Lambda_b^0\to\Lambda^*\psi}_{1,\frac{1}{2}}$	$(+0.054\pm0.011, -0.039\pm0.013)$
				$B^{\Lambda_b^0\to\Lambda^*\psi}_{1,\frac{3}{2}}$	$(+0.032\pm0.010, +0.042\pm0.015)$
$\Lambda^*(1520)$	$3/2^-$	1519.5	15.6	$B^{\Lambda_b^0\to\Lambda^*\psi}_{0,\frac{1}{2}}$	$(1,0)$
				$B^{\Lambda_b^0\to\Lambda^*\psi}_{1,\frac{1}{2}}$	$(-0.840\pm0.115, -0.267\pm0.138)$
				$B^{\Lambda_b^0\to\Lambda^*\psi}_{1,\frac{3}{2}}$	$(+0.559\pm0.096, -0.329\pm0.120)$
				$B^{\Lambda_b^0\to\Lambda^*\psi}_{2,\frac{3}{2}}$	$(+0.078\pm0.078, -0.048\pm0.101)$
				$B^{\Lambda_b^0\to\Lambda^*\psi}_{2,\frac{5}{2}}$	$(-0.697\pm0.112, -0.352\pm0.119)$

Table 32: Amplitude model based on the default fit to the data - Part II

Resonance	J^P	M_0 MeV	Γ_0 MeV	$B_{L,S}$ couplings	
$\Lambda^*(1600)$	$1/2^+$	1600.0	150.0	$B^{\Lambda_b^0\to\Lambda^*\psi}_{0,\frac{1}{2}}$	$(+0.223\pm0.048, -0.303\pm0.042)$
				$B^{\Lambda_b^0\to\Lambda^*\psi}_{1,\frac{1}{2}}$	$(-0.027\pm0.030, +0.038\pm0.031)$
				$B^{\Lambda_b^0\to\Lambda^*\psi}_{1,\frac{3}{2}}$	$(-0.376\pm0.043, +0.056\pm0.048)$
$\Lambda^*(1670)$	$1/2^-$	1670.0	35.0	$B^{\Lambda_b^0\to\Lambda^*\psi}_{0,\frac{1}{2}}$	$(-.0089\pm.0021, -.0035\pm.0022)$
				$B^{\Lambda_b^0\to\Lambda^*\psi}_{1,\frac{1}{2}}$	$(+.0031\pm.0019, -.0002\pm.0020)$
				$B^{\Lambda_b^0\to\Lambda^*\psi}_{1,\frac{3}{2}}$	$(-.0058\pm.0017, -.0012\pm.0022)$
$\Lambda^*(1690)$	$3/2^-$	1715.0	60.0	$B^{\Lambda_b^0\to\Lambda^*\psi}_{0,\frac{1}{2}}$	$(+0.299\pm0.084, -0.236\pm0.069)$
				$B^{\Lambda_b^0\to\Lambda^*\psi}_{1,\frac{1}{2}}$	$(+0.163\pm0.074, -0.150\pm0.063)$
				$B^{\Lambda_b^0\to\Lambda^*\psi}_{1,\frac{3}{2}}$	$(+.0026\pm0.062, -0.079\pm0.072)$
				$B^{\Lambda_b^0\to\Lambda^*\psi}_{2,\frac{3}{2}}$	$(-0.030\pm0.072, -0.427\pm0.061)$
				$B^{\Lambda_b^0\to\Lambda^*\psi}_{2,\frac{5}{2}}$	$(-0.213\pm0.076, +0.396\pm0.064)$
$\Lambda^*(1800)$	$1/2^-$	1800.0	300.0	$B^{\Lambda_b^0\to\Lambda^*\psi}_{0,\frac{1}{2}}$	$(-0.067\pm0.015, +0.070\pm0.013)$
				$B^{\Lambda_b^0\to\Lambda^*\psi}_{1,\frac{1}{2}}$	$(-0.065\pm0.012, -0.065\pm0.014)$
				$B^{\Lambda_b^0\to\Lambda^*\psi}_{1,\frac{3}{2}}$	$(+.0040\pm0.012, -0.039\pm0.010)$
				$B^{\Lambda_b^0\to\Lambda^*\psi}_{2,\frac{3}{2}}$	$(-0.013\pm0.007, +0.024\pm0.006)$
$\Lambda^*(1810)$	$1/2^+$	1810.0	150.0	$B^{\Lambda_b^0\to\Lambda^*\psi}_{0,\frac{1}{2}}$	$(-0.076\pm0.022, -0.016\pm0.023)$
				$B^{\Lambda_b^0\to\Lambda^*\psi}_{1,\frac{1}{2}}$	$(+0.034\pm0.019, +0.072\pm0.022)$
				$B^{\Lambda_b^0\to\Lambda^*\psi}_{1,\frac{3}{2}}$	$(+0.299\pm0.030, -.0002\pm0.033)$

Table 33: Amplitude model based on the default fit to the data - Part III

Resonance	J^P	M_0 MeV	Γ_0 MeV	$B_{L,S}$ couplings	
$\Lambda^*(1820)$	$5/2^+$	1820.0	80.0	$B^{\Lambda_b^0\to\Lambda^*\psi}_{1,\frac{3}{2}}$	$(-2.807\pm1.092, -5.691\pm0.958)$
$\Lambda^*(1830)$	$5/2^-$	1830.0	95.0	$B^{\Lambda_b^0\to\Lambda^*\psi}_{1,\frac{3}{2}}$	$(+1.821\pm0.330, +0.298\pm0.373)$
$\Lambda^*(1890)$	$3/2^+$	1890.0	100.0	$B^{\Lambda_b^0\to\Lambda^*\psi}_{0,\frac{1}{2}}$	$(-0.034\pm0.019, -0.011\pm0.015)$
				$B^{\Lambda_b^0\to\Lambda^*\psi}_{1,\frac{1}{2}}$	$(-0.091\pm0.017, +.0080\pm0.015)$
				$B^{\Lambda_b^0\to\Lambda^*\psi}_{1,\frac{3}{2}}$	$(+0.015\pm0.014, -0.052\pm0.016)$
$\Lambda^*(2100)$	$7/2^-$	2100.0	200.0	$B^{\Lambda_b^0\to\Lambda^*\psi}_{2,\frac{5}{2}}$	$(-116.5\pm17.70, +86.61\pm16.32)$
$\Lambda^*(2110)$	$5/2^+$	2110.0	200.0	$B^{\Lambda_b^0\to\Lambda^*\psi}_{1,\frac{3}{2}}$	$(+1.285\pm1.342, -7.745\pm0.943)$

H Addition of a third P_c state to the amplitude model

As discussed previously two P_c states are required to obtain satisfactory description of the data. In particular, while good descriptions of the other fitted variables can be obtained even without any P_c states, two P_c states are necessary to describe the $m_{J/\psi p}$ distribution. A χ^2-value for the binned $m_{J/\psi p}$ distribution between the data and the fit result performed with the default Λ^* model and no P_c states is 348.0 per 74 bins. It improves to 201.6 (a change of -146.4) with the addition of a single P_c state. It improves further to 108.5 (a change of -93.1) when a second P_c state is included in the fit. The corresponding χ^2-values obtained when using the extended Λ^* model are 265.4, 151.1 (a change of -114.2) and 109.3 (a change of -41.8) for fits with no-, one- and two-P_c states, respectively. While such χ^2-values for the fits with two P_c states are acceptable for high statistics amplitude analysis like this one, they are not perfect. This prompts the question of whether a better description of the data can be obtained by including a third P_c state in the fit. The mass region immediately above the narrow $P_c(4450)$ peak shows some disagreements between the fit and the data (see e.g. Fig. 46). Fits were performed with the default Λ^* model, $P_c(4380)$, and $P_c(4450)$, in which a third P_c state was included in this mass range, with free mass and width. Eight different J^P assignments were used, covering all quantum numbers with J ranging from 1/2 to 7/2. While the $\Delta(-2\ln\mathcal{L})$ is always improved, most of these fits make the χ^2-value of the $m_{J/\psi p}$ distributions worse (by up to +4.9). The biggest improvement in the χ^2-value is obtained with a $J^P = 3/2^-$ state, and is essentially negligible at only -1.9. In view of the lack of evidence for a third P_c state, it is not included in the fit model, or even in the evaluation of systematic uncertainties on the $P_c(4450)$ and $P_c(4380)$ parameters. [22]

Anecdotal evidence that the slight disagreement between the fits and the data in the region above the $P_c(4450)$ state may have something to do with an imperfect Λ^* model comes from the two-P_c fits with an intermediate Λ^* model, in which all possible LS couplings are allowed, but no poorly motivated Λ^* states are added. The χ^2-value for

[22] They are modest in any case. For the fit with the third state with $J^P = 3/2^-$, the masses, widths and fit fractions change by +0.8 MeV, +3.8 MeV and +0.4% for $P_c(4450)$, and by +11 MeV, +2.9 MeV and +1.8% for $P_c(4380)$, respectively.

$m_{J/\psi p}$ changes by -10.3, which is more than the gain from a third P_c state in the fit.

I Dalitz Plots

Rectangular Dalitz plots are shown in Fig 128 for both the the K^-p system variables (m_{Kp}, $\cos\theta_{\Lambda^*}$) and the $J/\psi p$ system variables ($m_{J/\psi p}$, $\cos\theta_{J/\psi p}$). Amplitude models were also used to show the contributions over the (m_{Kp}, $\cos\theta_{\Lambda^*}$) plane which could be expected from Λ^* or P_c components. A high statistics (10^7 events) sample was generated according to the extended Λ^* model (no P_c components) fit to the data. Another high statistics sample was generated according to the P_c parameters which were determined in the fit of the default amplitude model to the data. That is, the Λ^* components were zeroed out in this latter toy data set. The distributions for both of these toy data sets can be seen in Fig. 129.

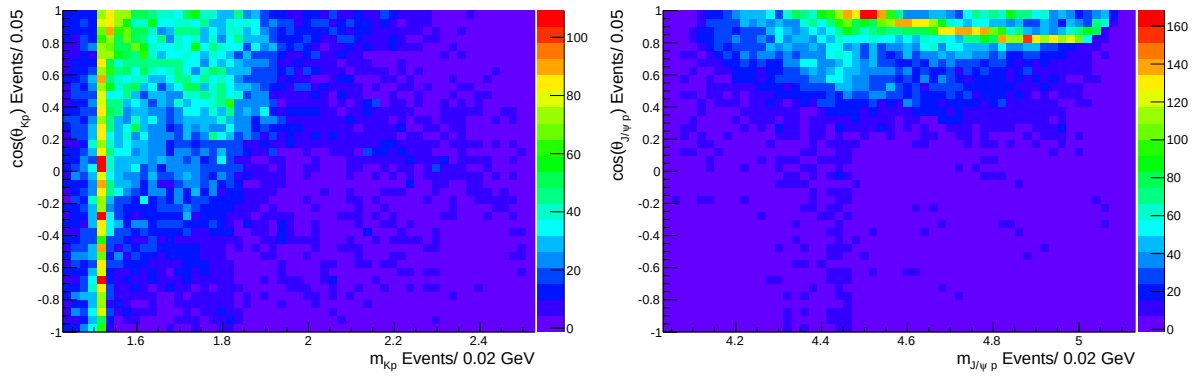

Figure 128: The rectangular Dalitz plots of the data, displaying the invariant mass versus helicity angles for the K^-p (left) and $J/\psi p$ (right) systems. The backgrounds are subtracted using sWeights.

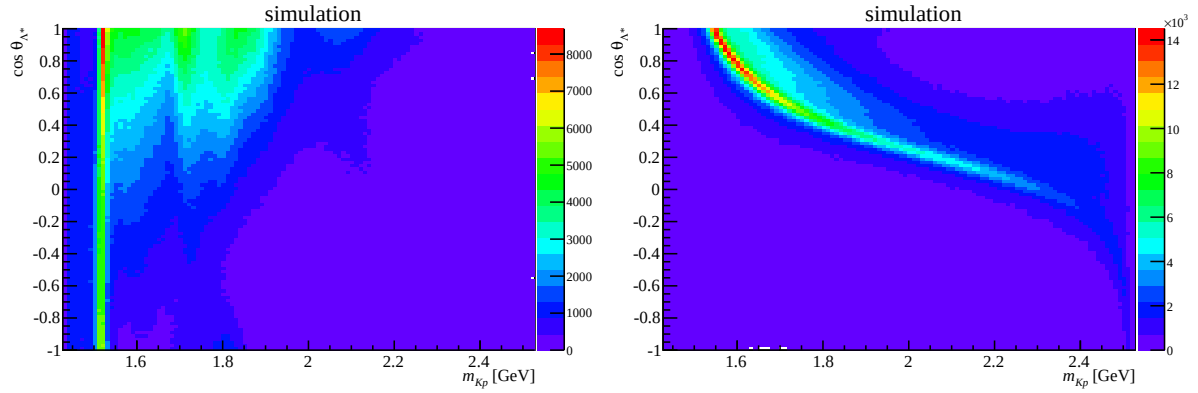

Figure 129: The rectangular Dalitz plots displaying the invariant mass versus helicity angles for the K^-p systems for the extended Λ^* model (left) and P_c components as determined in the default amplitde model (right).

J Normalized Legendre moments

The normalized Legendre moments defined by Eq. 98 are shown here. Figure 130 shows them with the m_{Kp} binning used in the analysis. In order to better see the structures, Fig. 131 shows them with bins that are four times as large.

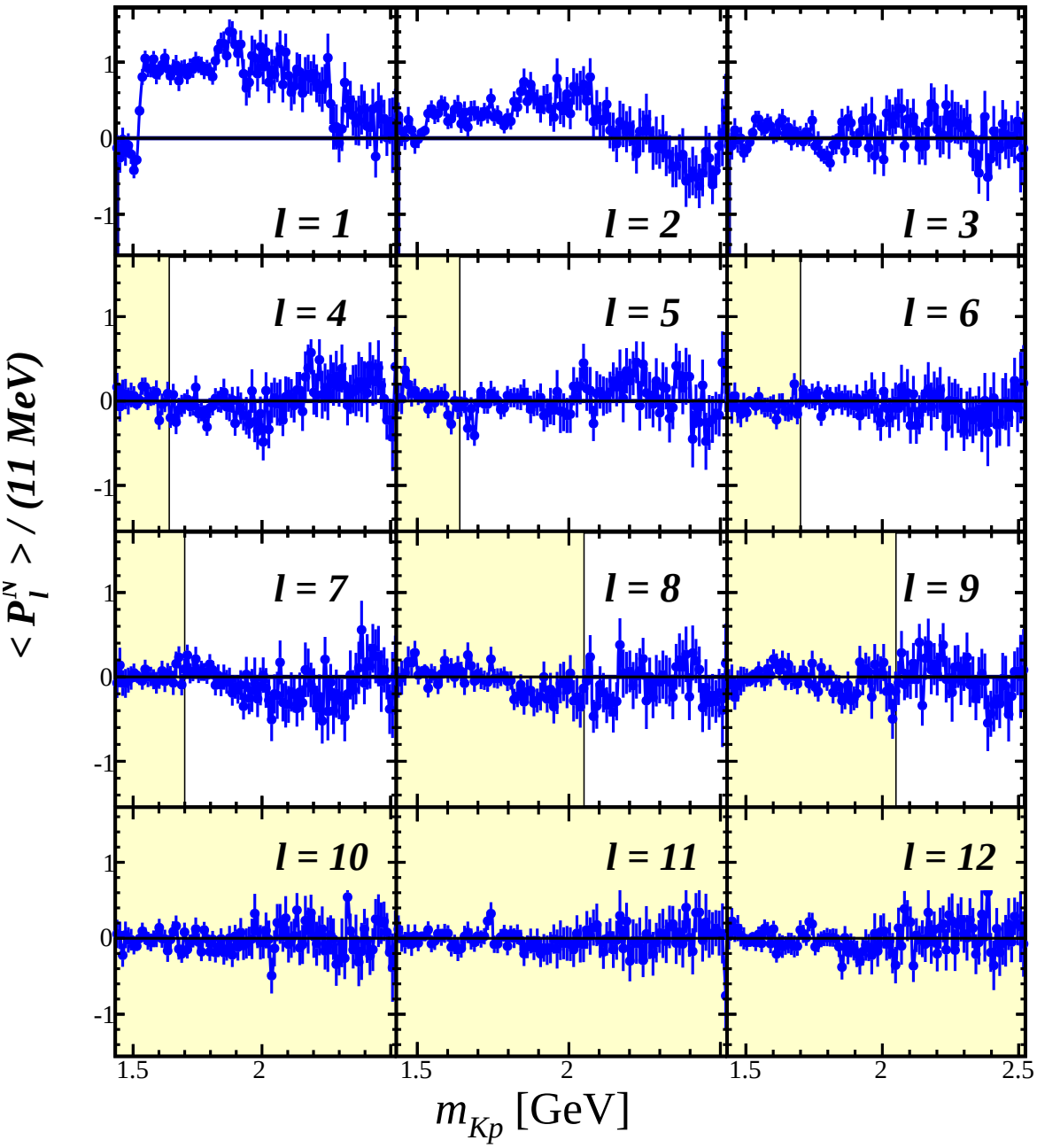

Figure 130: Normalized Legendre moments of $\cos\theta_{\Lambda^*}$ as a function of m_{Kp} in the data. Regions excluded by the $l \leq l_{\max}(m_{Kp})$ filter are shaded.

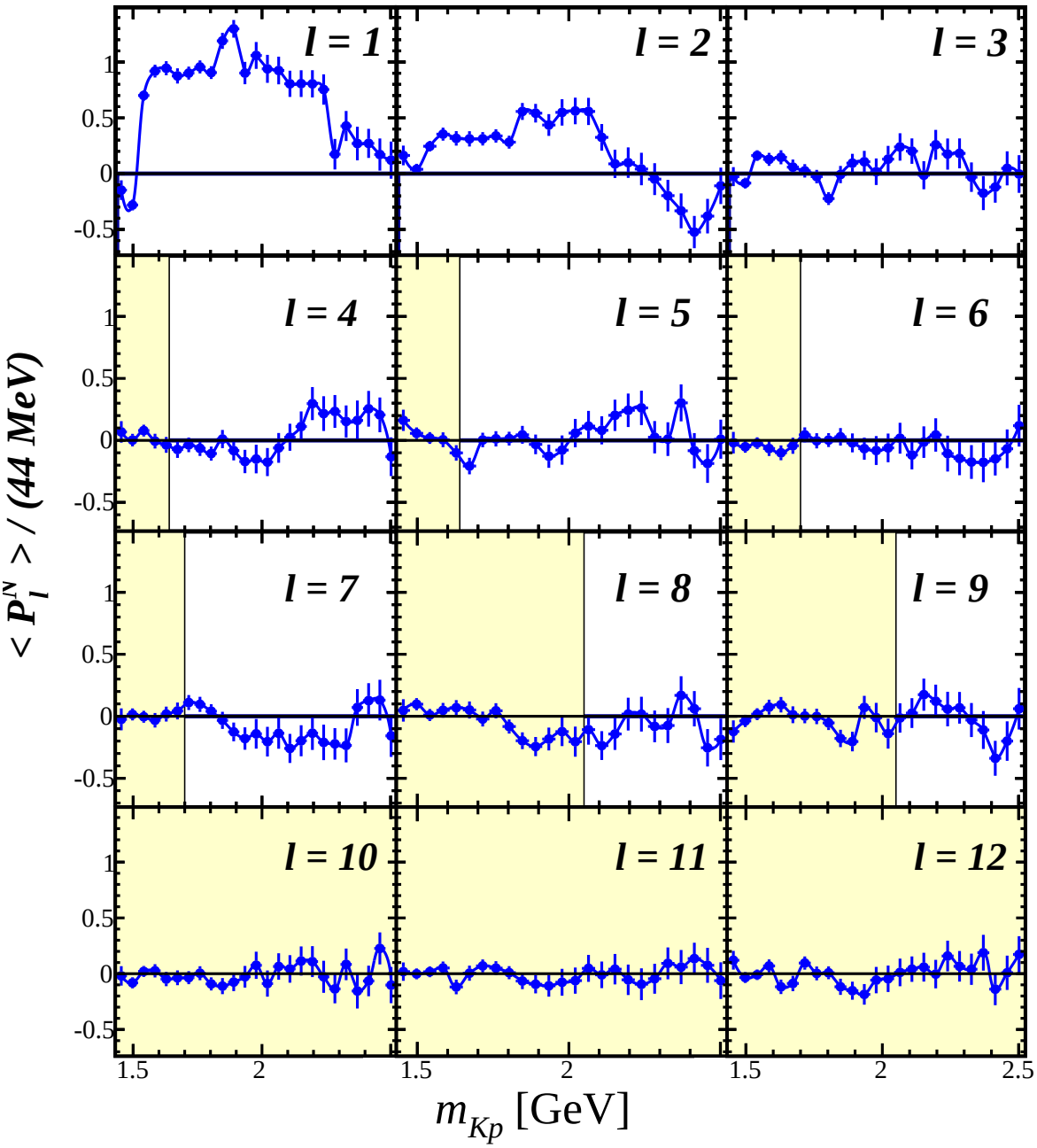

Figure 131: The normalized Legendre moments of $\cos\theta_{\Lambda^*}$ shown in Fig. 130 with four times larger bins. Regions excluded by the $l \leq l_{\max}(m_{Kp})$ filter are shaded.

K Model Dependent Hypothesis Testing

In the default analysis, H_0 hypothesis testing is performed using the 2D model independent approach based on the $(m_{Kp}, \cos\theta_{\Lambda^*})$ information. This necessarily involves neglecting dynamical correlations with the other decay angles ($\Omega_a \equiv \cos\theta_{\Lambda_b^0}$, $\cos\theta_{J/\psi}$, ϕ_K and ϕ_μ), which can affect the test results if the efficiency is not uniform in Ω_a. In the default approach, the H_0 pseudoexperiments are generated with uniform Ω_a distributions. A systematic check was discussed in Sec. 24.2, in which the Ω_a distributions were shaped according to the Λ^* amplitude model, but their correlations with $(m_{Kp}, \cos\theta_{\Lambda^*})$ were neglected in order to maintain the model independent approach to the generation of the $(m_{Kp}, \cos\theta_{\Lambda^*})$ variables under the H_0 hypothesis. In this section, the check is taken even further, these correlations are included by generating all six variables from the extended Λ^* amplitude model (no P_c states), with the parameters previously fixed by the fit to the real data. While the analysis of such generated pseudoexperiments is still performed in the default model-independent way, the pseudo-experiments themselves no longer reflect the 2D H_0 model independent hypothesis extracted from the real data. Instead, they represent just one particular 6D model-dependent implementation of the broader hypothesis that the 2D H_0 hypothesis aims to test, namely that the data are composed of K^-p contributions only. The model-dependent distribution of the model-independent χ^2 variable is shown in Fig. 132, along with the usual χ^2 value determined from the real data. The fit of the pseudoexperiment distribution with a χ^2 distribution gives ndf $= 47.9 \pm 0.1$. This then yields a rejection of the K^-p-only hypothesis of 5.4σ (vs. 5.3σ in the default approach). The model-dependent distribution of the model-independent $\Delta(-2\log\mathcal{L})$ variable is shown in Fig. 133, along with the usual value determined from the real data. The fit with a bifurcated Gaussian gives $\langle t_{\mathrm{DLL}_0}\rangle = 18.1 \pm 0.3$, a left width of $\sigma_l = 9.7 \pm 0.2$, and a right width of $\sigma_r = 12.6 \pm 0.2$. This gives a rejection of the K^-p-only hypothesis of 10.0σ (vs. 10.1σ in the default approach). This study confirms that the effects of neglecting dynamical effects in shaping Ω_a are small enough not to bias the model-independent test results in a significant way.

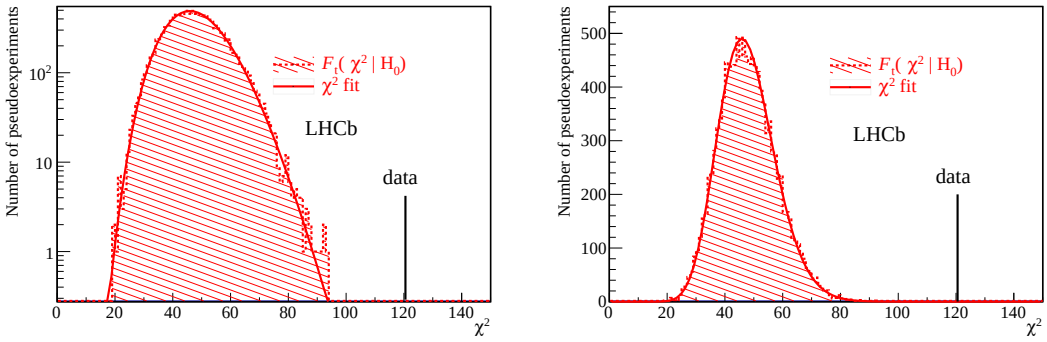

Figure 132: Distribution of t_{χ^2} in the pseudoexperiments with signal events generated according to the extended Λ^* model (red histogram) in log (left) and linear (right) scale compared to the value obtained in the data (vertical black bar). The distribution is fitted with and well described by a χ^2 distribution (solid red line).

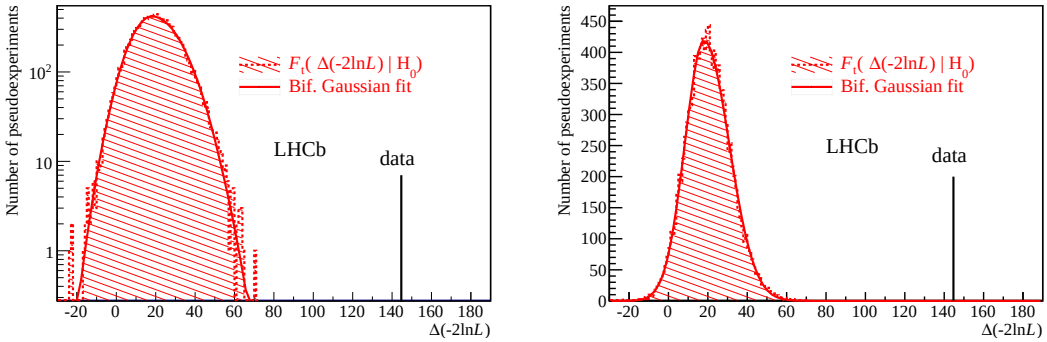

Figure 133: Distribution of t_{DLL} in the pseudoexperiments with signal events generated according to the extended Λ^* model (red histogram) in log (left) and linear (right) scale compared to the value obtained in the data (vertical black bar). The distribution is fitted with and well described by a bifurcated Gaussian distribution (solid red line).

L $l_{\max}(m_{Kp})$ Variations

In this section, the hypothesis testing is performed with variations of $l_{\max}(m_{Kp})$ (Eq. 92). In particular, the variations of $l_{\max}(m_{Kp})+1$ (but no more than 9) and $l_{\max}(m_{Kp})-1$ are tested. As an extreme test, the $l_{\max}(m_{Kp})+2$ variation is also done. Let these modified hypotheses be denoted by $H_0^{l_{\max}(m_{Kp})-1}$, $H_0^{l_{\max}(m_{Kp})+1}$, and $H_0^{l_{\max}(m_{Kp})+2}$. As usual, the distribution of the corresponding test variables generated under these different hypotheses are used to calculate the $p-$values for the values obtained from the data.

Clearly it is expected that $H_0^{l_{\max}(m_{Kp})-1}$ will be rejected with a larger significance than H_0. While this hypothesis still contains the majority of the expected Λ^* contributions some Λ^* components will not be contained. Thus its stronger rejection does not imply better evidence for non-K^-p contributions. A decrease in significance can be expected for $H_0^{l_{\max}(m_{Kp})+1}$. The goal is to see how much it decreases by, and to check that this variation won't result in any large changes and the acceptance of $H_0^{l_{\max}(m_{Kp})+1}$.

For the $H_0^{l_{\max}(m_{Kp})-1}$ pseudoexperiments, the t_{χ^2} distribution is shown in Fig. 134, where it has been fit with a nominal χ^2 distribution. The result from the data is shown as a black line. The distribution is well fit by the nominal χ^2, which returned ndf $= 49.9 \pm 0.3$. Using the value from the data, $t_{\chi^2}^{\text{data}} = 178.6$, an 8.0σ rejection of the $H_0^{l_{\max}(m_{Kp})-1}$ hypothesis is obtained.

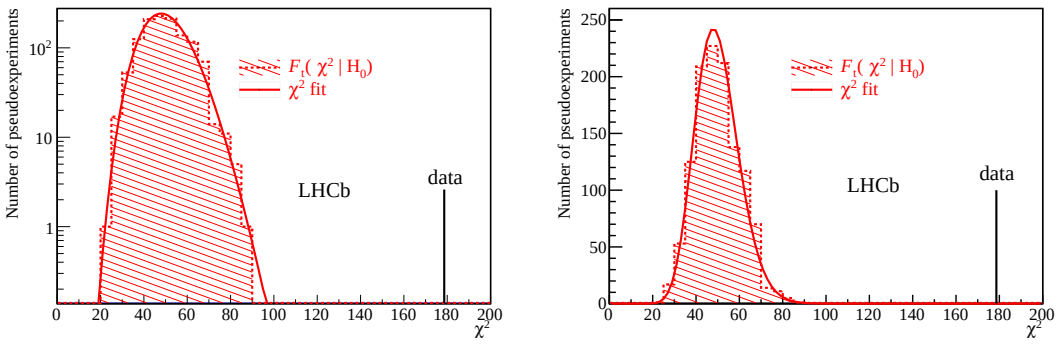

Figure 134: Distribution of t_{χ^2} in the $H_0^{l_{\max}(m_{Kp})-1}$ pseudoexperiments (red histogram) in log (left) and linear (right) scale compared to the value obtained in the data (vertical black bar). The distribution is fitted with and well described by a χ^2 distribution (solid red line).

The results of the $\Delta(-2\log\mathcal{L})$ test for the $H_0^{l_{\max}(m_{Kp})-1}$ pseudoexperiments are shown

in Fig. 135. The fit yields $\langle t_{\mathrm{DLL}_0} \rangle = 20.1 \pm 1.2$, a left width of $\sigma_l = 13.5 \pm 0.7$, and a right width of $\sigma_r = 15.2 \pm 0.8$. Using the value $t_{\mathrm{DLL}}^{\mathrm{data}} = 289.0$ determined from the data, the $H_0^{l_{\max}(m_{Kp})-1}$ hypothesis can be rejected at 17.7σ. Thus, the rejection of $H_0^{l_{\max}(m_{Kp})-1}$ is much stronger than of the default H_0 hypothesis. Interestingly, the amplitude simulations show that the isolated Λ^* resonances contribute only up to $l = 2\,J - 1$. This is due to cancellations built into the matrix element stemming from constraints in the helicity couplings from the parity conservation in the strong decay $\Lambda^* \to K^- p$. Such cancellations are not guaranteed when two different resonances overlap and interfere. Therefore, adopting $l_{\max}(m_{Kp}) - 1$ as the default approach would not be acceptable.

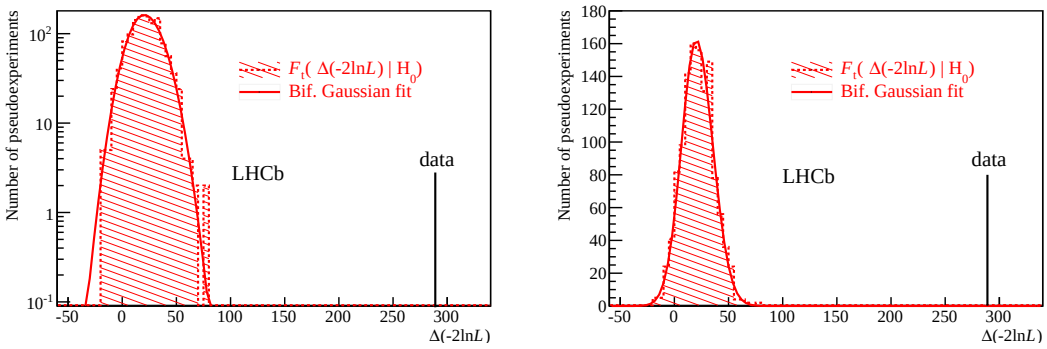

Figure 135: Distribution of t_{DLL} in the $H_0^{l_{\max}(m_{Kp})-1}$ pseudoexperiments (red histogram) in log (left) and linear (right) scale compared to the value obtained in the data (vertical black bar). The distribution is fitted with and well described by a bifurcated Gaussian distribution (solid red line).

The t_{χ^2} distribution for the $H_0^{l_{\max}(m_{Kp})+1}$ pseudoexperiments is shown in Fig. 136. The fit yields ndf $= 46.6 \pm 0.3$, and using the value from the data, $t_{\chi^2}^{\mathrm{data}} = 94.6$, a 3.9σ rejection of the $H_0^{l_{\max}(m_{Kp})+1}$ hypothesis is obtained.

The results of the $\Delta(-2\log\mathcal{L})$ test for the $H_0^{l_{\max}(m_{Kp})+1}$ pseudoexperiments are shown in Fig. 137. The fit yields $\langle t_{\mathrm{DLL}_0} \rangle = 16.7 \pm 0.9$, a left width of $\sigma_l = 8.4 \pm 0.6$, and a right width of $\sigma_r = 12.3 \pm 0.6$. Using the value from the data of $t_{\mathrm{DLL}}^{\mathrm{data}} = 98.7$, a 6.7σ rejection of the $H_0^{l_{\max}(m_{Kp})+1}$ hypothesis is obtained. As expected the rejection of the $H_0^{l_{\max}(m_{Kp})+1}$ hypothesis is lower than of the default H_0 hypothesis. With the log likelihood ratio test, it is still high enough to rule out $K^- p$-only interpretation of the data with high significance, though.

The t_{χ^2} distribution for the $H_0^{l_{\max}(m_{Kp})+2}$ pseudoexperiments are shown in Fig. 138.

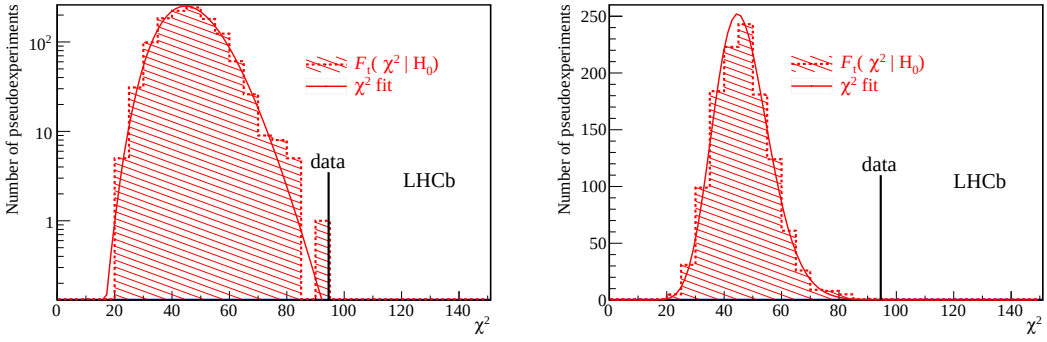

Figure 136: Distribution of t_{χ^2} in the $H_0^{l_{\max}(m_{Kp})+1}$ pseudoexperiments (red histogram) in log (left) and linear (right) scale compared to the value obtained in the data (vertical black bar). The distribution is fitted with and well described by a χ^2 distribution (solid red line).

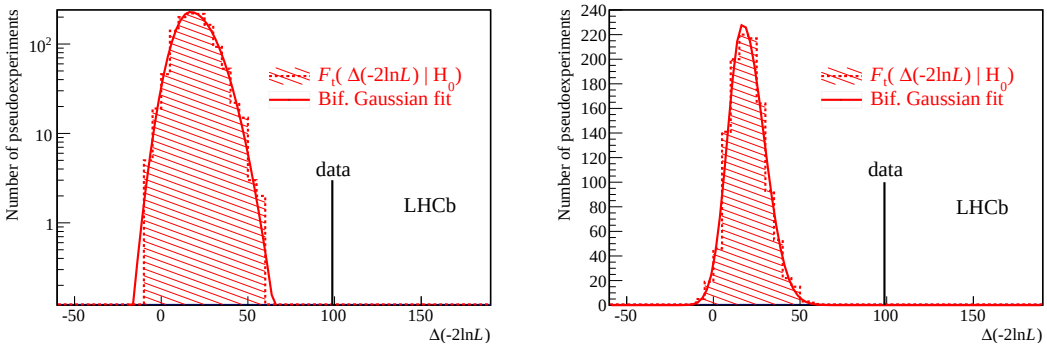

Figure 137: Distribution of $t_{\rm DLL}$ in the $H_0^{l_{\max}(m_{Kp})+1}$ pseudoexperiments (red histogram) in log (left) and linear (right) scale compared to the value obtained in the data (vertical black bar). The distribution is fitted with and well described by a bifurcated Gaussian distribution (solid red line).

The fit yields ndf $= 44.7 \pm 0.3$, and using the value from the data, $t_{\chi^2}^{\rm data} = 82.7$, a 3.2σ rejection of the $H_0^{l_{\max}(m_{Kp})+2}$ hypothesis is obtained.

The results of the $t_{\rm DLL}$ test for the $H_0^{l_{\max}(m_{Kp})+2}$ pseudoexperiments are shown in Fig. 139. The fit yields $\langle t_{\rm DLL_0} \rangle = 14.0 \pm 0.7$, a left width of $\sigma_l = 7.3 \pm 0.5$, and a right width of $\sigma_r = 12.7 \pm 0.5$. Using the value from the data of $t_{\rm DLL}^{\rm data} = 81.1$, a 5.3σ rejection of the $H_0^{l_{\max}(m_{Kp})+2}$ hypothesis is obtained. Even with this extreme variation the $H_0^{l_{\max}(m_{Kp})+2}$ hypothesis can be ruled out with a high significance. A summary of the rejections for the different variations is given in Table 34.

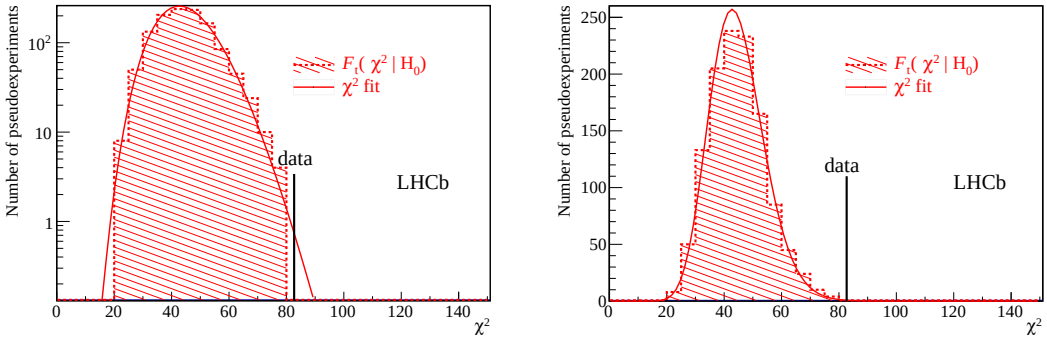

Figure 138: Distribution of t_{χ^2} in the $H_0^{l_{\max}(m_{Kp})+2}$ pseudoexperiments (red histogram) in log (left) and linear (right) scale compared to the value obtained in the data (vertical black bar). The distribution is fitted with and well described by a χ^2 distribution (solid red line).

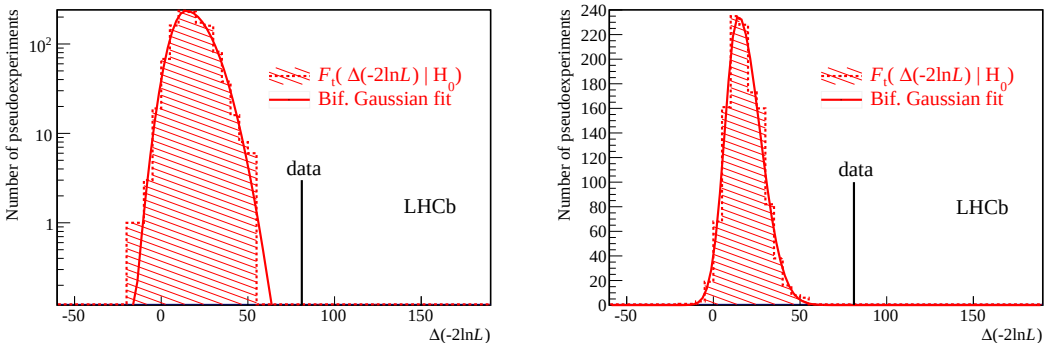

Figure 139: Distribution of $t_{\rm DLL}$ in the $H_0^{l_{\max}(m_{Kp})+1}$ pseudoexperiments (red histogram) in log (left) and linear (right) scale compared to the value obtained in the data (vertical black bar). The distribution is fitted with and well described by a bifurcated Gaussian distribution (solid red line).

Table 34: Significances of rejection in standard deviations, obtained for both test variables under the different $l_{\max}(m_{Kp})$ variations

	$t = \chi^2$	$t = \Delta(-2\log\mathcal{L})$
$H_0^{l_{max}(m_{Kp})-1}$	8.0σ	17.7σ
H_0 (nominal)	5.3σ	10.1σ
$H_0^{l_{max}(m_{Kp})+1}$	3.9σ	6.7σ
$H_0^{l_{max}(m_{Kp})+2}$	3.2σ	5.3σ

M Variations of $l_{\rm large}$

The choice of $l_{\rm large}$ must be large enough to capture the features of $m_{J/\psi p}$ (or $m_{J/\psi K}$). However, if it is made too large, the discriminating power of the likelihood ratio test is expected to deteriorate. This is because after a certain point the higher moments serve more to capture statistical fluctuations than they do to capture actual physics. Indeed, in the $l_{\rm large} \to \infty$ limit, it is expected that the power will deteriorate to that of the χ^2 test. While it is important to choose the value of $l_{\rm large}$ independently of the actual data set [23], it is interesting to study how its value affects the strength with which H_0 can be rejected. The pseudoexperiments and test on the data were repeated with varying values of $l_{\rm large}$. The resulting levels of rejection of H_0 are shown in Fig. 140.

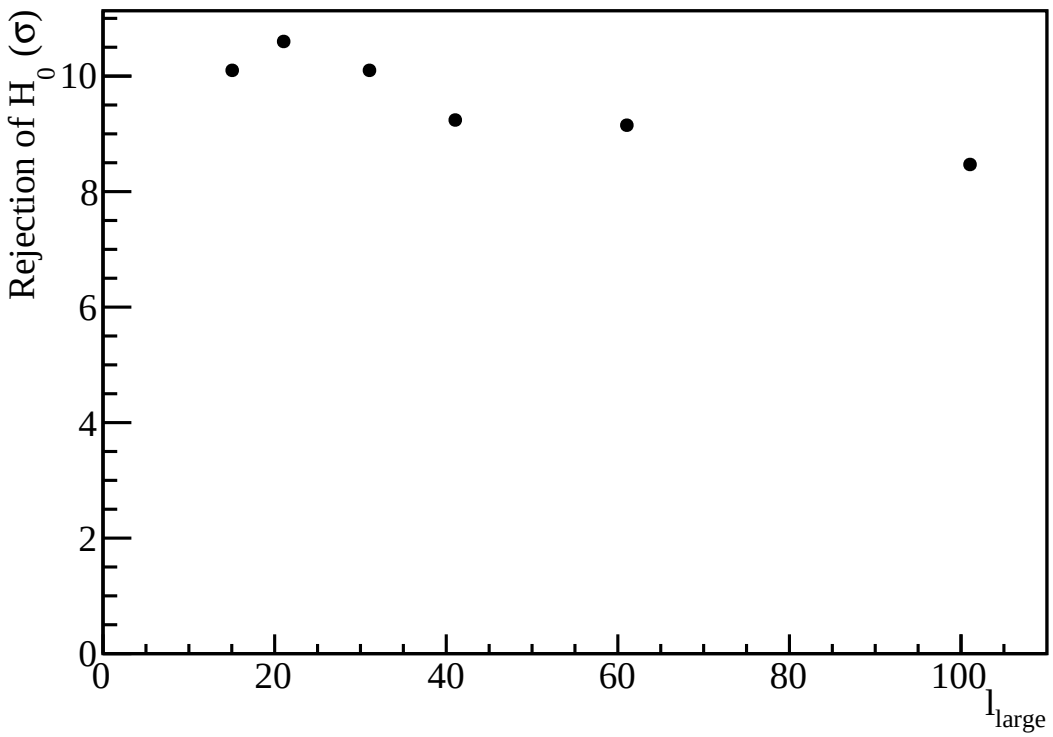

Figure 140: Levels of rejection of H_0 obtained when the hypothesis testing is repeated with various values of $l_{\rm large}$.

The expected deterioration of the power of the test for very high values of $l_{\rm large}$ is clearly seen. Also, the level of rejection of H_0 obtained with the nominal choice of

[23] If the $l_{\rm large}$ value is tuned to the data set, then this procedure must also be simulated in the pseudo-experiments. This would require a well defined numerical procedure, and would be overly cumbersome.

$l_{\text{large}} = 31$ is actually close to the optimal level. While the test could be strengthened somewhat by tuning l_{large}, this is unnecessary and undesirable to do.

N Measurement of the ratio of B_c^+ branching fractions to $J/\psi\pi^+$ and $J/\psi\mu^+\nu_\mu$ final states

This Appendix covers an analysis which was done during the period of the dissertation work, but does not fit into the main narrative of the study. The analysis resulted in a paper, which will be briefly summarized here. For more details, Ref. [100] should be consulted.

N.1 Introduction

The B_c^+ meson is the ground state of the $\bar{b}c$ quark-pair system and thus has the unique status of being the lightest doubly-heavy, open-flavor bound state. It must decay weakly, and is further unique in that the decays of both constituents compete with each other. The $c \to s$ and $b \to c$ transitions are expected to contribute about 70% and 20% of the decay width, respectively, with the remaining 10% being from weak annihilation [101]. These features make the B_c^+ meson a good system for studying both the weak and strong interactions, and a means for refining effective models. While its decays to several channels have previously been observed, there had been no experimental determination of the relative size of semileptonic and hadronic decay rates. The goal of this work is a measurement of the ratio of branching fractions,

$$\mathcal{R} \equiv \frac{\mathcal{B}(B_c^+ \to J/\psi\,\pi^+)}{\mathcal{B}(B_c^+ \to J/\psi\,\mu^+\nu_\mu)}, \tag{116}$$

and to test various theoretical models of B_c^+ meson decays, for which predictions of $\mathcal{R}$ vary over a wide range, 0.050–0.091 [102–109]. The analysis was performed on the data sample collected during 2011 by the LHCb experiment, corresponding to an integrated luminosity of $1.0\,\text{fb}^{-1}$.

N.2 Analysis Summary

The mass of $B_c^+ \to J/\psi\pi^+$ signal candidates peaks at the B_c^+ mass within the experimental resolution, which allows for a straightforward signal yield extraction in the presence of relatively small backgrounds under the signal peak. An extended maximum likelihood fit to the unbinned distribution of observed $m_{J/\psi\pi}$ values yields $N_{J/\psi\pi} = 839 \pm 40$ $B_c^+ \to J/\psi\pi^+$ signal events and is shown in Fig. 141. The signal is represented in the fit

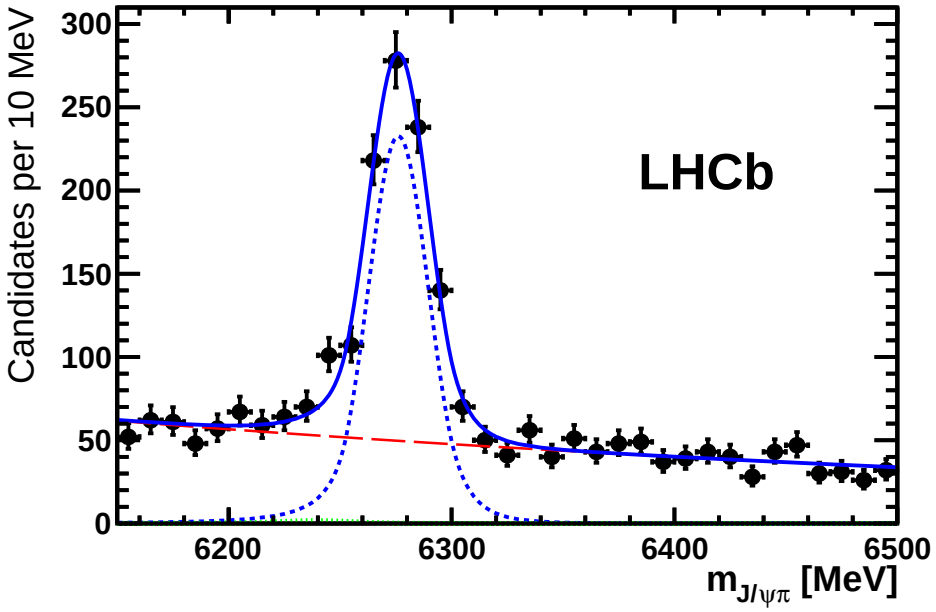

Figure 141: Invariant-mass distribution of $B_c^+ \to J/\psi\pi^+$ candidates (black data points). The maximum likelihood fit of the B_c^+ signal is superimposed (blue solid line). Individual fit components are also shown: (dashed blue line) the signal, (red long-dashed line) the background and (green dotted line) $B_c^+ \to J/\psi K^+$ feeddown.

by a double-sided Crystal Ball (CB) function [110], with the parameters describing small non-Gaussian tails fixed by a fit to a simulated signal distribution. The background is smoothly distributed and modeled by an exponential function. A small background from $B_c^+ \to J/\psi K^+$ decays, peaking 37 MeV below the signal peak, is also included in the fit with all shape parameters fixed from the simulation. Its normalization is constrained to be 1% of the fitted signal amplitude, as predicted by the measured ratio of the branching fractions [111] scaled by an efficiency ratio of 15% obtained from the simulation.

The main challenge in this analysis is the signal yield extraction for the $B_c^+ \to J/\psi\mu^+\nu_\mu$ decay mode, as the unreconstructed neutrino results in a broad $J/\psi\mu^+$ mass

($m_{J/\psi\,\mu}$) distribution amidst multiple difficult-to-model backgrounds. The dominant background source is from $B_{u,d,s}$ decays to J/ψ plus hadrons, with one of the hadrons misidentified as a muon. The $B_{u,d,s}$ production rates are orders of magnitude higher than for B_c^+, resulting in the large backgrounds. Since many exclusive decay modes with various hadron multiplicities and unknown branching ratios contribute, the $m_{J/\psi\,\mu}$ shape of such backgrounds is difficult to predict. Additionally, feeddown from other $B_c^+ \to f$, $f \to J/\psi\,\mu^+\nu_\mu\,X$ decays must be accounted for, many of which have unknown $m_{J/\psi\,\mu}$ distributions and decay rates, and thus require theoretical input. Decays to excited charmonium states ($f = \psi_f\mu^+\nu_\mu$, with $\psi_f = \chi_{cJ}$ or $\psi(2S)$) and states containing τ leptons ($f = J/\psi\,\tau^+\nu_\tau$) are the dominant contributions.

To suppress these dominant backgrounds, the analysis is restricted to the $m_{J/\psi\,\mu} > 5.3\,\text{GeV}$ endpoint region, and uses the mass-shape difference between the signal and the remaining background to extract the $B_c^+ \to J/\psi\,\mu^+\nu_\mu$ signal yield. This endpoint value is then extrapolated to the full phase space using theoretical predictions. Since the B_c^+ and J/ψ are both $1S$ heavy quarkonia states, the form factors involved in predicting the extrapolation factor and the shape of the mass distribution at the endpoint have only modest model dependence. The 5.3 GeV lower limit on $m_{J/\psi\,\mu}$ is above the kinematic limit for $B_u^+ \to J/\psi\,h^+$ decays, with h^+ denoting a charged kaon or pion. Thus the $B_{u,d,s}$ backgrounds in the selected region are much smaller, and are from $B_{u,d,s} \to J/\psi\,X$ decays paired with a bachelor μ^+ originating from some other decay. This is illustrated in Fig. 142, where the simulated $B_{u,d,s} \to J/\psi\,X$ distribution is shown with the simulated signal distribution. The shape of such combinatorial backgrounds is less sensitive to the details of the composition of b-hadron decay modes, and thus is easier to predict. The feeddown contributions are also easier to model, as unreconstructed decay products in the $\psi_f \to J/\psi\,X$ transitions ($X = \gamma$, $\pi\pi$, π^0, η, $\gamma\gamma$) or $\tau^+ \to \mu^+\nu_\mu\bar{\nu}_\tau$ decays carry energy away, lowering the $J/\psi\,\mu^+$ mass relative to that from direct $B_c^+ \to J/\psi\,\mu^+\nu_\mu$ decays. This is also shown in Fig. 142.

The signal yield is determined from the fit to the $m_{J/\psi\,\mu}$ distribution, and has a signal, background, and feeddown component, each of which will be discussed in turn. The

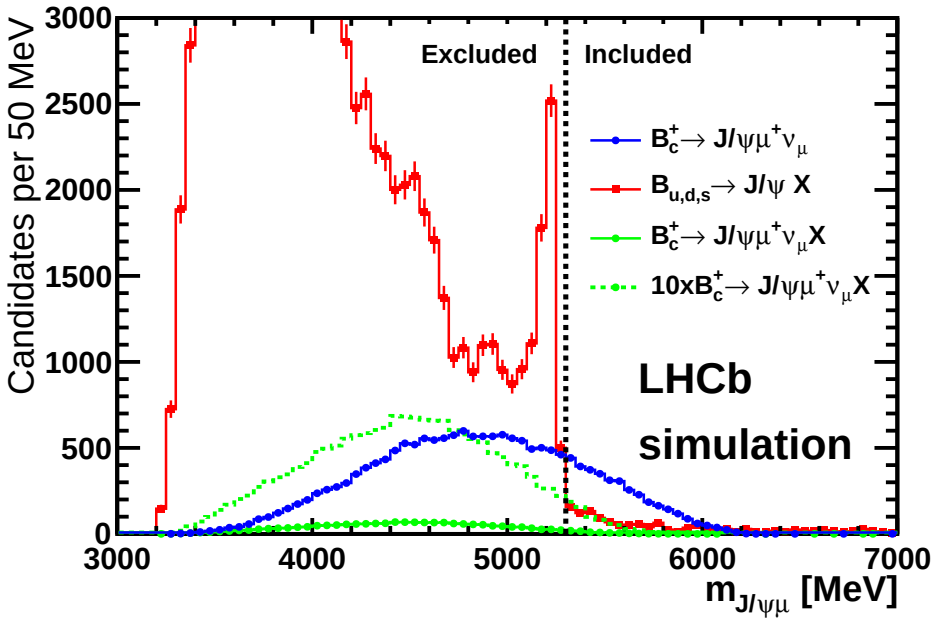

Figure 142: Distribution of $m_{J/\psi\,\mu}$ for $B_c^+ \to J/\psi\,\mu^+\nu_\mu$ candidates selected in simulated event samples of (blue filled points) the signal, (green filled points) the B_c^+ feeddown and (red filled squares) the $B_{u,d,s}$ backgrounds. Relative normalization is derived from the fit to the data described later in the text. The part of the spectrum included in the fit is indicated with a vertical dashed black line. The B_c^+ feeddown distribution is also shown after magnifying its normalization by a factor of ten (green dashed histogram).

$m_{J/\psi\,\mu}$ signal shape is dominated by the endpoint kinematics, and is described by the $B_c^+ \to J/\psi\,\mu^+\nu_\mu$ three-body phase-space distribution multiplying a linear polynomial to accound for distortions resulting from the dynamics of the decay. The combinatorial background is smooth and extends beyond the kinematic limit for the $B_c^+ \to J/\psi\,\mu^+\nu_\mu$ decays, which is used to set the background level in the signal region. The combinatorial $B_{u,d,s}$ background is parameterized with an exponential function which is quadratic in its argument. The tail of the $B_u^+ \to J/\psi\,h^+$ distribution, with a light hadron misidentified as a muon, may enter the signal region because of detector resolution. This is parameterized with a Gaussian function, with a mean value and width fixed to the results of the fit to the simulated $B_u^+ \to J/\psi\,h^+$ distribution. The relative contributions of the combinatorial and misidentified backgrounds is a free parameter in the fit. The feeddown background is small, and its shape is fixed by simulations of the contributing channels mixed in the expected proportions. It is parametrized with a $J/\psi\,\mu^+\nu_\mu$ three-body phase space distribution multiplying a quadratic polynomial, where an effective B_c^+ mass is used in

the phase space distribution due to the unreconstruced decay products. The ratio of the feeddown yield to the signal yield is fixed to the expectations obtained using theoretical predictions for the decay rates and simulated samples for the efficiencies.

An unbinned maximum likelihood fit is performed simultaneously to the $m_{J/\psi\,\mu}$ distributions of the data and the signal and background simulations. The fitted $m_{J/\psi\,\mu}$ range of 5.3 to 8.0 GeV yields $N_{J/\psi\,\mu} = 3537 \pm 125$ signal events. The $m_{J/\psi\,\mu}$ distributions and the fit results are displayed in Fig. 143.

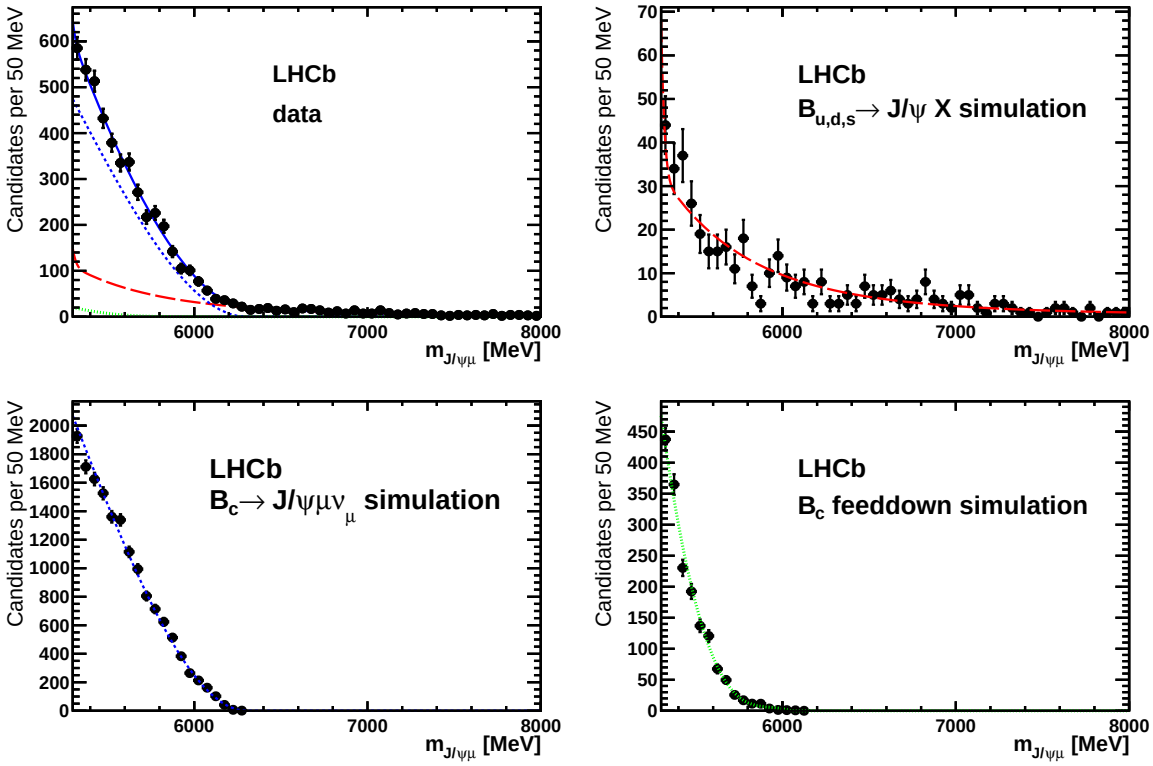

Figure 143: Invariant-mass distribution of $J/\psi\,\mu^+$ pairs from $B_c^+ \to J/\psi\,\mu^+\nu_\mu$ candidates (black data points) for (top left) the data, (bottom left) $B_c^+ \to J/\psi\,\mu^+\nu_\mu$ signal simulation, (top right) $B_{u,d,s} \to J/\psi\,X$ background simulation and (bottom right) B_c^+ feeddown simulation. The unbinned maximum likelihood fit of the B_c^+ signal is superimposed (blue solid line). Individual fit components are also shown: (blue short-dashed line) the signal, (red long-dashed line) the background and (green dotted line) B_c^+ feeddown.

The result for the ratio of the branching fractions restricted to decays with $m_{J/\psi\,\mu} > 5.3\,\text{GeV}$ is found to be

$$\mathcal{R}(m_{J/\psi\,\mu} > 5.3\,\text{GeV}) = 0.271 \pm 0.016 \pm 0.016, \tag{117}$$

where the first uncertainty is statistical and the second is systematic. This ratio is extrapolated to the full phase space using the predictions of various phenomenological models [106,107,109,112–114]. The result obtained using the model of Kiselev *et al.* [106] is near the average of all models, and is used for the default value. The largest deviation from this model is taken as an estimate of the extrapolation systematic error. The final result over the full mass range is

$$\mathcal{R} = 0.0469 \pm 0.0028 \pm 0.0046. \tag{118}$$

N.3 Summary

The ratio of hadronic and semileptonic decay branching fractions of the B_c^+ meson is measured for the first time. A comparison between the measured and the predicted values of $\mathcal{R}$ is shown in Fig. 144. The measured value is slightly below the lowest predicted value. The predictions by the relativistic quasipotential Schrödinger model of Ebert *et al.* [107] and the model of El-Hady *et al.*, based on a nonrelativistic reduction of the Bethe-Salpeter equation [104], are in good agreement with the experimental value. The model of Ke *et al.* [109], based on the modified harmonic oscillator wave function in light-front quark model, is also consistent with the data. The other models [102, 103, 105, 106, 108] significantly overestimate $\mathcal{R}$.

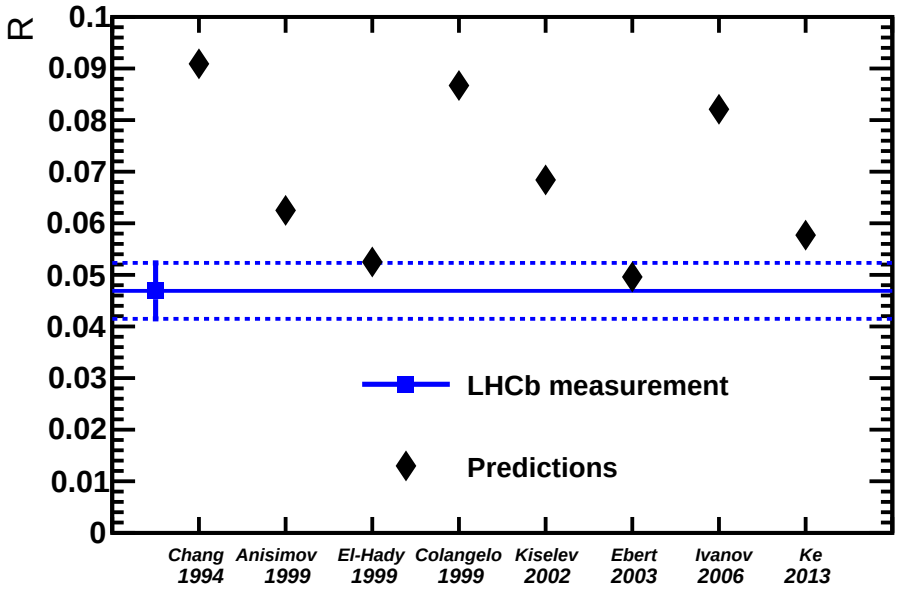

Figure 144: The measured value of $\mathcal{R}$ (horizontal solid line) and its $\pm 1\sigma$ uncertainty band (dashed lines) compared to the predictions (diamonds). A nonrelativistic reduction of the Bethe-Salpeter equation is used in the predictions of Chang *et al.* [102], El-Hady *et al.* [104], and Colangelo *et al.* [105], while the latter also utilizes heavy quark symmetry. A light-front constituent quark model is used by Anisimov *et al.* [103] and Ke *et al.* [109]. QCD sum rules are used by Kiselev *et al.* [106], a relativistic quasipotential Schrödinger model is used by Ebert *et al.* [107], and a relativistic constituent quark model is used by Ivanov *et al.* [108].

References

[1] M. Gell-Mann, *A schematic model of baryons and mesons*, Phys. Lett. **8** (1964) 214.

[2] G. Zweig, *An SU_3 model for strong interaction symmetry and its breaking*, CERN-TH-401, 1964.

[3] Particle Data Group, T. G. Trippe *et al.*, *Review of Particle Properties. Particle Data Group*, Rev. Mod. Phys. **48** (1976) S1, [Erratum: Rev. Mod. Phys.48,497(1976)].

[4] Particle Data Group, K. Hikasa *et al.*, *Review of particle properties. Particle Data Group*, Phys. Rev. **D45** (1992) S1, [Erratum: Phys. Rev.D46,5210(1992)].

[5] M. Praszalowicz, *Skyrmions and Anomalies, p.112, M. Jezabek Ed.*, World Scientific Publishing, 1987.

[6] D. Diakonov, V. Petrov, and M. V. Polyakov, *Exotic anti-decuplet of baryons: Prediction from chiral solitons*, Z. Phys. **A359** (1997) 305, `arXiv:hep-ph/9703373`.

[7] K. H. Hicks, *On the conundrum of the pentaquark*, Eur. Phys. J. **H37** (2012) 1.

[8] LEPS, T. Nakano *et al.*, *Evidence for a narrow $S = +1$ baryon resonance in photoproduction from the neutron*, Phys. Rev. Lett. **91** (2003) 012002, `arXiv:hep-ex/0301020`.

[9] DIANA, V. V. Barmin *et al.*, *Observation of a baryon resonance with positive strangeness in K^+ collisions with Xe nuclei*, Phys. Atom. Nucl. **66** (2003) 1715, `arXiv:hep-ex/0304040`.

[10] CLAS, S. Stepanyan *et al.*, *Observation of an exotic $S = +1$ baryon in exclusive photoproduction from the deuteron*, Phys. Rev. Lett. **91** (2003) 252001, `arXiv:hep-ex/0307018`.

[11] SAPHIR, J. Barth *et al.*, *Evidence for the positive strangeness pentaquark Theta+ in photoproduction with the SAPHIR detector at ELSA*, Phys. Lett. **B572** (2003) 127, arXiv:hep-ex/0307083.

[12] S. Stone, *Pathological science*, in *Flavor physics for the millennium. Proceedings, Theoretical Advanced Study Institute in elementary particle physics, TASI 2000, Boulder, USA, June 4-30, 2000*, pp. 557–575, 2000. arXiv:hep-ph/0010295.

[13] Particle Data Group, W. M. Yao *et al.*, *Review of Particle Physics*, J. Phys. **G33** (2006) 1.

[14] Belle, S. K. Choi *et al.*, *Observation of a narrow charmonium-like state in exclusive $B^{\pm} \to K^{\pm}\pi^{+}\pi^{-}J/\psi$ decays*, Phys. Rev. Lett. **91** (2003) 262001, arXiv:hep-ex/0309032.

[15] LHCb, R. Aaij *et al.*, *Determination of the X(3872) meson quantum numbers*, Phys. Rev. Lett. **110** (2013) 222001, arXiv:1302.6269.

[16] LHCb, R. Aaij *et al.*, *Quantum numbers of the $X(3872)$ state and orbital angular momentum in its $\rho^{0}J\psi$ decay*, Phys. Rev. **D92** (2015), no. 1 011102, arXiv:1504.06339.

[17] Belle collaboration, S. K. Choi *et al.*, *Observation of a resonance-like structure in the $\pi^{\pm}\psi'$ mass distribution in exclusive $B \to K\pi^{\pm}\psi'$ decays*, Phys. Rev. Lett. **100** (2008) 142001, arXiv:0708.1790.

[18] Belle collaboration, K. Chilikin *et al.*, *Experimental constraints on the spin and parity of the $Z(4430)^{+}$*, Phys. Rev. **D88** (2013) 074026, arXiv:1306.4894.

[19] LHCb, R. Aaij *et al.*, *Observation of the resonant character of the $Z(4430)^{-}$ state*, Phys. Rev. Lett. **112** (2014), no. 22 222002, arXiv:1404.1903.

[20] LHCb collaboration, R. Aaij *et al.*, *A model-independent confirmation of the $Z(4430)^{-}$ state*, Phys. Rev. **D92** (2015) 112009, arXiv:1510.01951.

[21] CDF, T. Aaltonen *et al.*, *Evidence for a Narrow Near-Threshold Structure in the $J/\psi\phi$ Mass Spectrum in $B^+ \to J/\psi\phi K^+$ Decays*, Phys. Rev. Lett. **102** (2009) 242002, arXiv:0903.2229.

[22] LHCb, R. Aaij *et al.*, *Amplitude analysis of $B^+ \to J/\psi\phi K^+$ decays*, arXiv:1606.07898.

[23] LHCb, R. Aaij *et al.*, *Observation of $J/\psi\phi$ structures consistent with exotic states from amplitude analysis of $B^+ \to J/\psi\phi K^+$ decays*, arXiv:1606.07895.

[24] LHCb collaboration, R. Aaij *et al.*, *Precision measurement of the Λ_b^0 baryon lifetime*, Phys. Rev. Lett. **111** (2013) 102003, arXiv:1307.2476.

[25] LHCb collaboration, R. Aaij *et al.*, *Observation of $J/\psi p$ resonances consistent with pentaquark states in $\Lambda_b^0 \to J/\psi p K^-$ decays*, Phys. Rev. Lett. **115** (2015) 072001, arXiv:1507.03414.

[26] LHCb, R. Aaij *et al.*, *Model-independent evidence for $J/\psi p$ contributions to $\Lambda_b^0 \to J/\psi p K^-$ decays*, arXiv:1604.05708.

[27] Particle Data Group, K. A. Olive *et al.*, *Review of Particle Physics*, Chin. Phys. **C38** (2014) 090001.

[28] R. L. Jaffe, *Multiquark hadrons. I. Phenomenology of $Q^2\overline{Q}^2$ mesons*, Phys. Rev. **D15** (1977) 267.

[29] D. Strottman, *Multi-quark baryons and the MIT bag model*, Phys. Rev. **D20** (1979) 748.

[30] Högaasen, H. and Sorba, P. , *The systematics of possibly narrow quark states with baryon number one*, Nucl. Phys. **B145** (1978) 119.

[31] H. J. Lipkin, *New possibilities for exotic hadrons: Anticharmed strange baryons*, Phys. Lett. **B195** (1987) 484.

[32] M. Karliner, H. J. Lipkin, and N. A. Tornqvist, *Heavy Baryon Spectrum and New Heavy Exotics*, in *Proceedings, 14th International Conference on Hadron spectroscopy (Hadron 2011)*, 2011. arXiv:1109.3472.

[33] M. Karliner, H. J. Lipkin, and N. A. Tornqvist, *New states with heavy quarks*, Nucl. Phys. Proc. Suppl. **225-227** (2012) 102.

[34] X.-Q. Li and X. Liu, *A possible global group structure for exotic states*, Eur. Phys. J. **C74** (2014), no. 12 3198, arXiv:1409.3332.

[35] LHCb collaboration, A. A. Alves Jr. *et al.*, *The LHCb detector at the LHC*, JINST **3** (2008) S08005.

[36] LHCb collaboration, R. Aaij *et al.*, *LHCb detector performance*, Int. J. Mod. Phys. **A30** (2015) 1530022, arXiv:1412.6352.

[37] C. Lefvre, *The CERN accelerator complex. Complexe des acclrateurs du CERN*, Dec, 2008.

[38] CMS, S. Chatrchyan *et al.*, *The CMS experiment at the CERN LHC*, JINST **3** (2008) S08004.

[39] ATLAS, G. Aad *et al.*, *The ATLAS Experiment at the CERN Large Hadron Collider*, JINST **3** (2008) S08003.

[40] ALICE, K. Aamodt *et al.*, *The ALICE experiment at the CERN LHC*, JINST **3** (2008) S08002.

[41] T. Sjöstrand, S. Mrenna, and P. Z. Skands, *PYTHIA 6.4 Physics and manual*, JHEP **05** (2006) 026, arXiv:hep-ph/0603175; T. Sjöstrand, S. Mrenna, and P. Skands, *A brief introduction to PYTHIA 8.1*, Comput. Phys. Commun. **178** (2008) 852, arXiv:0710.3820.

[42] I. Belyaev *et al.*, *Handling of the generation of primary events in* Gauss*, the LHCb simulation framework*, Nuclear Science Symposium Conference Record (NSS/MIC) **IEEE** (2010) 1155.

[43] GEANT4 collaboration, S. Agostinelli *et al.*, *GEANT4: A simulation toolkit*, Nucl. Instrum. Meth. **A506** (2003) 250.

[44] M. Clemencic *et al.*, *The LHCb simulation application, Gauss: design, evolution and experience*, Journal of Physics: Conference Series **331** (2011) 032023.

[45] D. Martínez Santos and F. Dupertuis, *Mass distributions marginalized over per-event errors*, Nucl. Instrum. Meth. **A764** (2014) 150, arXiv:1312.5000.

[46] R. H. Dalitz, *On the analysis of τ-meson data and the nature of the τ-meson*, Phil. Mag. **44** (1953) 1068.

[47] M. Pivk and F. R. Le Diberder, *sPlot: A statistical tool to unfold data distributions*, Nucl. Instrum. Meth. **A555** (2005) 356, arXiv:physics/0402083.

[48] J. M. Blatt and V. F. Weisskopf, *Theoretical Nuclear Physics*, Springer-Verlag, 1979.

[49] S. M. Flatté, *Coupled-channel analysis of the $\pi\eta$ and $K\overline{K}$ systems near $K\overline{K}$ threshold*, Phys. Lett. **B63** (1976) 224.

[50] LHCb collaboration, R. Aaij *et al.*, *Measurements of the $\Lambda_b^0 \to J/\psi\Lambda$ decay amplitudes and the Λ_b^0 polarization in pp collisions at $\sqrt{s} = 7$ TeV*, Phys. Lett. **B724** (2013) 27, arXiv:1302.5578.

[51] Belle collaboration, R. Mizuk *et al.*, *Observation of two resonance-like structures in the $\pi^+\chi_{c1}$ mass distribution in exclusive $\bar{B}^0 \to K^-\pi^+\chi_{c1}$ decays*, Phys. Rev. **D78** (2008) 072004, arXiv:0806.4098.

[52] J. F. Donoghue, E. Golowich, W. A. Ponce, and B. R. Holstein, *Analysis of ΔS=1 nonleptonic weak decays and the ΔI=1/2 rule*, Phys. Rev. **D21** (1980) 186.

[53] LHCb collaboration, R. Aaij *et al.*, *Observation of overlapping spin-1 and spin-3 $\bar{D}^0K^-$ resonances at mass* 2.86 GeV/c^2, Phys. Rev. Lett. **113** (2014) 162001, arXiv:1407.7574; LHCb collaboration, R. Aaij *et al.*, *Dalitz plot analysis of $B_s^0 \to \bar{D}^0K^-\pi^+$ decays*, Phys. Rev. **D90** (2014) 072003, arXiv:1407.7712.

[54] L. Roca, M. Mai, E. Oset, and U.-G. Meiner, *Predictions for the $\Lambda_b^0 \to J/\psi\,\Lambda(1405)$ decay*, Eur. Phys. J. **C75** (2015) 218, arXiv:1503.02936.

[55] F. James, *Statistical methods in experimental physics*, World Scientific Publishing, 2006.

[56] R. N. Faustov and V. O. Galkin, *Strange baryon spectroscopy in the relativistic quark model*, Phys. Rev. D. **92** (2015) 054005, arXiv:1507.04530.

[57] S. Capstick and N. Isgur, *Baryons in a relativized quark model with chromodynamics*, Phys. Rev. D. **34** (1986) 2809.

[58] U. Loring, B. C. Metsch, and H. R. Petry, *The Light baryon spectrum in a relativistic quark model with instanton induced quark forces: The Strange baryon spectrum*, Eur. Phys. J. **A10** (2001) 447, arXiv:hep-ph/0103290.

[59] T. Melde, W. Plessas, and B. Sengl, *Quark-model identification of baryon ground and resonant states*, Phys. Rev. D. **77** (2008) 114002.

[60] E. Santopinto and J. Ferretti, *Strange and nonstrange baryon spectra in the relativistic interacting quark-diquark model with a Gürsey and Radicati-inspired exchange interaction*, Phys. Rev. C. **92** (2015) 025202, arXiv:1412.7571.

[61] G. P. Engel, C. B. Lang, D. Mohler, and A. Schaefer, *QCD with Two Light Dynamical Chirally Improved Quarks: Baryons*, Phys. Rev. D. **87** (2013) 074504, arXiv:1301.4318.

[62] C. Fernandez-Ramirez *et al.*, *Coupled-channel model for $\bar{K}N$ scattering in the resonant region*, Phys. Rev. **D93** (2016), no. 3 034029, arXiv:1510.07065.

[63] H. Zhang, J. Tulpan, M. Shrestha, and D. M. Manley, *Partial-wave analysis of $\bar{K}N$ scattering reactions*, Phys. Rev. C. **88** (2013) 035205.

[64] H. Kamano, S. X. Nakamura, T.-S. H. Lee, and T. Sato, *Dynamical coupled-channels model of K^-p reactions (II): Extraction of Λ^* and Σ^* hyperon resonances*, Phys. Rev. C. **92** (2015) 025205, arXiv:1506.01768.

[65] BaBar collaboration, B. Aubert *et al.*, *Search for the $Z(4430)^-$ at BABAR*, Phys. Rev. **D79** (2009) 112001, arXiv:0811.0564.

[66] T. J. Burns, *Phenomenology of $P_c(4380)^+$, $P_c(4450)^+$ and related states*, Eur. Phys. J. **A51** (2015), no. 11 152, arXiv:1509.02460.

[67] H.-X. Chen, W. Chen, X. Liu, and S.-L. Zhu, *The hidden-charm pentaquark and tetraquark states*, Phys. Rept. **639** (2016) 1, arXiv:1601.02092.

[68] M. Karliner and J. L. Rosner, *New Exotic Meson and Baryon Resonances from Doubly-Heavy Hadronic Molecules*, Phys. Rev. Lett. **115** (2015), no. 12 122001, arXiv:1506.06386.

[69] R. Chen, X. Liu, X.-Q. Li, and S.-L. Zhu, *Identifying exotic hidden-charm pentaquarks*, Phys. Rev. Lett. **115** (2015), no. 13 132002, arXiv:1507.03704.

[70] H.-X. Chen *et al.*, *Towards exotic hidden-charm pentaquarks in QCD*, Phys. Rev. Lett. **115** (2015), no. 17 172001, arXiv:1507.03717.

[71] L. Roca, J. Nieves, and E. Oset, *LHCb pentaquark as a $\bar{D}^*\Sigma_c - \bar{D}^*\Sigma_c^*$ molecular state*, Phys. Rev. **D92** (2015), no. 9 094003, arXiv:1507.04249.

[72] J. He, *$\bar{D}\Sigma_c^*$ and $\bar{D}^*\Sigma_c$ interactions and the LHCb hidden-charmed pentaquarks*, Phys. Lett. **B753** (2016) 547, arXiv:1507.05200.

[73] H. Huang, C. Deng, J. Ping, and F. Wang, *Possible pentaquarks with heavy quarks*, arXiv:1510.04648.

[74] L. Roca and E. Oset, *On the hidden charm pentaquarks in $\Lambda_b \to J/\psi K^- p$ decay*, arXiv:1602.06791.

[75] Q.-F. L and Y.-B. Dong, *Strong decay mode $J/\psi p$ of hidden charm pentaquark states $P_c^+(4380)$ and $P_c^+(4450)$ in $\Sigma_c\bar{D}^*$ molecular scenario*, Phys. Rev. **D93** (2016), no. 7 074020, arXiv:1603.00559.

[76] Y. Shimizu, D. Suenaga, and M. Harada, *Coupled channel analysis of molecule picture of $P_c(4380)$*, Phys. Rev. **D93** (2016), no. 11 114003, arXiv:1603.02376.

[77] C.-W. Shen, F.-K. Guo, J.-J. Xie, and B.-S. Zou, *Disentangle the hadronic molecule nature of the $P_c(4380)$ pentaquark-like structure*, arXiv:1603.04672.

[78] L. Maiani, A. D. Polosa, and V. Riquer, *The New Pentaquarks in the Diquark Model*, Phys. Lett. **B749** (2015) 289, arXiv:1507.04980.

[79] V. V. Anisovich *et al.*, *Pentaquarks and resonances in the pJ/ψ spectrum*, arXiv:1507.07652.

[80] G.-N. Li, X.-G. He, and M. He, *Some Predictions of Diquark Model for Hidden Charm Pentaquark Discovered at the LHCb*, JHEP **12** (2015) 128, arXiv:1507.08252.

[81] R. Ghosh, A. Bhattacharya, and B. Chakrabarti, *The masses of $P_c^*(4380)$ and $P_c^*(4450)$ in the quasi particle diquark model*, arXiv:1508.00356.

[82] Z.-G. Wang, *Analysis of $P_c(4380)$ and $P_c(4450)$ as pentaquark states in the diquark model with QCD sum rules*, Eur. Phys. J. **C76** (2016), no. 2 70, arXiv:1508.01468.

[83] A. Ali, I. Ahmed, M. J. Aslam, and A. Rehman, *Heavy quark symmetry and weak decays of the b-baryons in pentaquarks with a $c\bar{c}$ component*, arXiv:1607.00987.

[84] R. F. Lebed, *The Pentaquark Candidates in the Dynamical Diquark Picture*, Phys. Lett. **B749** (2015) 454, arXiv:1507.05867.

[85] R. Zhu and C.-F. Qiao, *Pentaquark states in a diquark-triquark model*, Phys. Lett. **B756** (2016) 259, arXiv:1510.08693.

[86] F.-K. Guo, U.-G. Meissner, W. Wang, and Z. Yang, *How to reveal the exotic nature of the $P_c(4450)$*, Phys. Rev. **D92** (2015), no. 7 071502, arXiv:1507.04950.

[87] U.-G. Meissner and J. A. Oller, *Testing the $\chi_{c1}\,p$ composite nature of the $P_c(4450)$*, Phys. Lett. **B751** (2015) 59, arXiv:1507.07478.

[88] X.-H. Liu, Q. Wang, and Q. Zhao, *Understanding the newly observed heavy pentaquark candidates*, Phys. Lett. **B757** (2016) 231, arXiv:1507.05359.

[89] M. Mikhasenko, *A triangle singularity and the LHCb pentaquarks*, arXiv:1507.06552.

[90] C. Schmid, *Final-state interactions and the simulation of resonances*, Phys. Rev. **154** (1967) 1363.

[91] X.-H. Liu, M. Oka, and Q. Zhao, *Searching for observable effects induced by anomalous triangle singularities*, Phys. Lett. **B753** (2016) 297, arXiv:1507.01674.

[92] F.-K. Guo, U.-G. Meiner, J. Nieves, and Z. Yang, *Remarks on the P_c structures and triangle singularities*, arXiv:1605.05113.

[93] Q. Wang, X.-H. Liu, and Q. Zhao, *Photoproduction of hidden charm pentaquark states $P_c^+(4380)$ and $P_c^+(4450)$*, Phys. Rev. **D92** (2015) 034022, arXiv:1508.00339.

[94] V. Kubarovsky and M. B. Voloshin, *Formation of hidden-charm pentaquarks in photon-nucleon collisions*, Phys. Rev. **D92** (2015), no. 3 031502, arXiv:1508.00888.

[95] M. Karliner and J. L. Rosner, *Photoproduction of Exotic Baryon Resonances*, Phys. Lett. **B752** (2016) 329, arXiv:1508.01496.

[96] A. N. H. Blin *et al.*, *Studying the $P_c(4450)$ resonance in J/ψ photoproduction off protons*, arXiv:1606.08912.

[97] LHCb, R. Aaij *et al.*, *Evidence for exotic hadron contributions to $\Lambda_b^0 \to J/\psi p\pi^-$ decays*, arXiv:1606.06999.

[98] Belle, K. Chilikin *et al.*, *Observation of a new charged charmoniumlike state in $\bar{B}^0 \to J/\psi K^-\pi^+$ decays*, Phys. Rev. **D90** (2014), no. 11 112009, arXiv:1408.6457.

[99] A. Hoecker *et al.*, *TMVA: Toolkit for Multivariate Data Analysis*, PoS **ACAT** (2007) 040, arXiv:physics/0703039.

[100] LHCb, R. Aaij *et al.*, *Measurement of the ratio of B_c^+ branching fractions to $J/\psi\pi^+$ and $J/\psi\mu^+\nu_\mu$*, Phys. Rev. **D90** (2014), no. 3 032009, arXiv:1407.2126.

[101] I. P. Gouz *et al.*, *Prospects for the B_c studies at LHCb*, Phys. Atom. Nucl. **67** (2004) 1559, arXiv:hep-ph/0211432.

[102] C.-H. Chang and Y.-Q. Chen, *Decays of the B_c meson*, Phys. Rev. **D49** (1994) 3399.

[103] A. Y. Anisimov, I. M. Narodetskii, C. Semay, and B. Silvestre-Blac, *The B_c meson lifetime in the light-front constituent quark model*, Phys. Lett. **B452** (1999) 129, arXiv:hep-ph/9812514; A. Y. Anisimov, P. Y. Kulikov, I. . M. Narodetskii, and K. A. Ter-Martirosyan, *Exclusive and inclusive decays of the B_c meson in the light-front ISGW model*, Phys. Atom. Nucl. **62** (1999) 1739, arXiv:hep-ph/9809249.

[104] A. A. El-Hady, J. H. Muñoz, and J. P. Vary, *Semileptonic and nonleptonic B_c decays*, Phys. Rev. **D62** (1999) 014019, arXiv:hep-ph/9909406.

[105] P. Colangelo and F. De Fazio, *Using heavy quark spin symmetry in semileptonic B_c decays*, Phys. Rev. **D61** (1999) 034012, arXiv:hep-ph/9909423.

[106] V. V. Kiselev, *Exclusive decays and lifetime of B_c meson in QCD sum rules*, arXiv:hep-ph/0211021.

[107] D. Ebert, R. N. Faustov, and V. O. Galkin, *Weak decays of the B_c meson to charmonium and D mesons in the relativistic quark model*, Phys. Rev. **D68** (2003) 094020, arXiv:hep-ph/0306306.

[108] M. A. Ivanov, J. G. Körner, and P. Santorelli, *Exclusive semileptonic and nonleptonic decays of the B_c meson*, Phys. Rev. **D73** (2006) 054024, arXiv:hep-ph/0602050.

[109] H.-W. Ke, T. Liu, and X.-Q. Li, *Transitions of $B_c \to \psi(1S, 2S)$ and the modified harmonic oscillator wave function in LFQM*, Phys. Rev. **D89** (2014) 017501, arXiv:1307.5925.

[110] T. Skwarnicki, *A study of the radiative cascade transitions between the Upsilon-prime and Upsilon resonances*, PhD thesis, Institute of Nuclear Physics, Krakow, 1986, DESY-F31-86-02.

[111] LHCb collaboration, R. Aaij *et al.*, *First observation of the decay* $B_c^+ \to J/\psi K^+$, JHEP **09** (2013) 075, arXiv:1306.6723.

[112] W. Wang, Y.-L. Shen, and C.-D. Lü, *Covariant light-front approach for* B_c *transition form factors*, Phys. Rev. **D79** (2009) 054012, arXiv:0811.3748.

[113] W.-F. Wang, Y.-Y. Fan, and Z.-J. Xiao, *Semileptonic decays* $B_c \to (\eta_c, J/\psi)\ell\nu$ *in the perturbative QCD approach*, arXiv:1212.5903.

[114] D. Scora and N. Isgur, *Semileptonic meson decays in the quark model: an update*, Phys. Rev. **D52** (1995) 2783, arXiv:hep-ph/9503486.

Vita

Nathan Jurik

Education

Ph.D. in Physics, Syracuse University, 2016:

Concentration: Experimental High Energy Physics

Dissertation: Observation of $J/\psi p$ resonances consistent with pentaquark states in $\Lambda_b \to J/\psi K^- p$ decays

Advisor: Prof. Tomasz Skwarnicki

B.Sc. in Engineeering Physics, University of Illinois at Urbana-Champaign, 2011

Experience

Teaching Assistant, 2011-2012:

Teaching assistant for undergraduate Classical Mechanics course.

Research Assistant, 2012-2016:

Physics Analysis: Semileptonic B_c decays and exotic hadrons.

Electronics: Readout system for Upstream Tracker

Talks

USLUO Annual Meeting, Fermilab, Batavia, USA

Date: November 13, 2015

Title: Pentaquarks at LHCb

LNS Seminar, MIT, Boston, USA

Date: October 20, 2015

Title: Observation of $J/\psi p$ resonances consistent with pentaquark states in $\Lambda_b \to J/\psi K^- p$ decays

IVICFA's Fridays: Experimental Physics, IFIC, Valencia, Spain

Date: October 2, 2015

Title: Pentaquarks and Tetraquarks at LHCb

CERN-LHC Seminar, CERN, Geneva, Switzerland

Date: September 22, 2015

Title: Observation of $J/\psi p$ resonances consistent with pentaquark states in $\Lambda_b \to J/\psi K^- p$ decays at LHCb

XHADRONS Conference, Mimar Sinan, Istanbul, Turkey

Date: September 05, 2015

Title: Exotic Hadrons At LHCb

DPF Conference, University of Michigan, Ann Arbor, USA

Date: August 05, 2015

Title: Exotic hadron spectroscopy in LHCb

USLUO Annual Meeting, Fermilab, Batavia, USA

Date: November 13, 2014

Title: Results in B_c physics at LHCb

Publications

A full publication list can be retrieved at the INSPIRE-HEP database. I have been on the LHCb Collaboration author list since 2013, and am listed as an author on all physics and upgrade publications since then. Listed here are the publications I have been directly involved in.

LHCb Collaboration, R. Aaij *et al.*, *Model-independent evidence for $J/\psi p$ contributions to $\Lambda_b^0 \to J/\psi p K^-$ decays*, arXiv:1604.05708

LHCb Collaboration, R. Aaij *et al.*, *Observation of $J/\psi p$ resonances consistent with pentaquark states in $\Lambda_b^0 \to J/\psi K^- p$ decays*, Phys. Rev. Lett. **115** (2015) 072001, arXiv:1507.03414

LHCb Collaboration, R. Aaij *et al.*, *Measurement of the ratio of B_c^+ branching fractions to $J/\psi\pi^+$ and $J/\psi\mu^+\nu_\mu$*, Phys. Rev. D **90** (2014) 032009, arXiv:1407.02126